DISSERTATION

MEASUREMENT OF THE INCLUSIVE ELECTRON-NEUTRINO CHARGED-CURRENT CROSS SECTION IN THE NOνA NEAR DETECTOR

Submitted by

Matthew A. Judah

Department of Physics

In partial fulfillment of the requirements

For the Degree of Doctor of Philosophy

Colorado State University

Fort Collins, Colorado

Fall 2019

Doctoral Committee:

Advisor: Norm Buchanan

Martin Gelfand
John Harton
Sangmi Pallickara

ABSTRACT

MEASUREMENT OF THE INCLUSIVE ELECTRON-NEUTRINO CHARGED-CURRENT CROSS SECTION IN THE NOνA NEAR DETECTOR

This thesis describes the methods used to extract the inclusive ν_e charged-current cross section in the NOνA near detector using data collected from November 2014 to February 2017, corresponding to an exposure of 8.09 $\times 10^{20}$ protons-on-target of a primarily neutrino beam. The near detector is located at Fermilab, 800 m from the primary target. The neutrino beam peaks near 2 GeV and is able to probe a variety of different neutrino-nucleus interactions through their final-state characteristics. The flux-integrated double-differential cross section is measured with respect to the final-state electron kinematics, as well as the total cross-section as a function of neutrino energy integrated over the same phase space used for the double-differential measurement.

ACKNOWLEDGEMENTS

The majority of the work presented in this thesis is the result of the support and guidance of many people how have helped me throughout my graduate career. The first round of thanks goes to my wife, Amber, and my family. Without their constant support and encouragement, this work would not have been possible.

Next, I would like to thank my advisor and mentor Norm Buchanan. He was instrumental in mentoring me through this thesis and all of the work throughout my graduate career. It was also a great help to have many great people to work with on NOvA throughout my time at Colorado State including Shih-Kai Lin, Paul Rojas, Steven Calvez, Connor Johnson, and Derek Doyle. My deep appreciation goes to Biswaranjan Behera and Ivan Lepetic for providing me a friendly environment and excellent sounding board in our shared cubicle.

I would also like to thank the NOvA collaboration. Everyone has played a role in making the experiment and the work presented in this thesis a success. Through the countless meetings, they've taught me to defend my ideas and to leave no stone unturned throughout the experimental process. I would like to thank Jon Paley and Mat Muether who have provided a substantial amount of feedback on each step of the electron neutrino cross section analysis as the conveners for the near detector cross section group. Additionally, I would like to thank everyone in the Data Acquisition group in particular Andrew Norman and Pengfei Ding for their discussions on all aspects of the experiment and their advice. Finally, I'd like to thank a few of the fantastic scientists I've had the pleasure of working with on NOvA: Evan Niner, Michael Baird, Gavin Davies, Jeremy Wolcott, Peter Shanahan, Louise Suter, Alex Himmel, Leo Aliaga, and Reddy Pratap Gandrajula.

TABLE OF CONTENTS

LIST OF TABLES

LIST OF FIGURES

Introduction

The study of elementary particles and the interactions between them defines the Standard Model of particle physics (SM). This model has been tested for the past half century and continues to be one of the most successful theories in physics. Although this model is successful, it does have known limitations. Neutrinos were hypothesized to solve an energy/momentum mystery in beta decay. In the SM they are massless particles, however, the discovery that at least two neutrino flavors have a non-zero mass came in stark contrast to the construction of the SM. Over the past two decades the study of neutrinos has been focused on oscillation measurements, as well as the study of neutrino interactions with matter.

Due to the tiny magnitude of the weak interaction and the inability to produce neutrinos with precisely known energy, modern neutrino oscillation experiments rely on intense neutrino beams and detectors that are large, dense, and have good energy resolution. Such experiments depend on the precise understanding of neutrino interactions with the detector materials. The importance of neutrino-nucleus interactions and the models used to predict them have become increasingly important as oscillation experiments are used to probe fundamental questions in physics, such as the origin of matter/anti-matter imbalance in the universe. In addition to the importance to neutrino oscillations, neutrino-nucleus scattering is also interesting in its own right. Neutrino interactions can provide information about nuclear structure that is not easily accessible through charged lepton-nucleus scattering. Weak interactions and the intra-nuclear scattering that follows provide an immense amount of information that will lead to a better understanding of the nucleus, and how neutrinos interact with matter.

The NOνA experiment, based at Fermi National Accelerator Laboratory in Batavia, Illinois, is a two-detector neutrino oscillation experiment designed for precision studies of electron-neutrino (ν_e) appearance from a predominately muon-neutrino (ν_μ) beam in the far detector located 810 kilometers away in Ash River, Minnesota. The NOνA near detector is a rich environment for studying neutrino-nucleus interactions. This thesis presents a measurement of ν_e scattering on a

primarily hydrocarbon target within the NOνA near detector. The charged-current ν_e cross section is not well measured in the range of energies sampled by the NOνA near detector, and this measurement will provide valuable data. Measurements of the ν_e cross section will help improve oscillation measurements by reducing systematic errors related to the neutrino-nucleus interaction models, and by constraining the beam flux. As neutrino energy can only be reconstructed using the kinematics of final-state charged particles, this measurement will provide valuable information pertaining to the ν_e cross section as a function of electron kinematics with the first measurement of the ν_e double-differential cross section at energies relevant to accelerator-based neutrino oscillation experiments.

Chapter 1 gives a brief history of neutrino physics and an overview of neutrino-nucleus interactions, including a discussion of the importance of electron neutrino interactions to neutrino oscillation measurements. Details of the NOνA experiment are contained in Chapter 2. The simulation, reconstruction, and calibration techniques used within the NOνA experiment are discussed in Chapter 3. 4 details the methods used to extract the electron neutrino cross section. The results of the electron neutrino cross section measurement are presented in Chapter 5. Additional contributions to the NOνA experiment are discussed within Chapter 6. Conclusions from this work and the presented results are given in Chapter 7

Chapter 1

Neutrino Physics

Despite the fact that neutrinos are one of the most abundant particles in the universe, their existence was only first theorized in 1930 by Wolfgang Pauli [1]. This theory was a "desperate" remedy to explain the apparent violation of energy and angular momentum conservation in β-decay [2]. Pauli explained the continuous β-decay spectrum with the existence of an extremely light, weakly interacting, neutral particle that was emitted with the electron during β-decay. In Pauli's theory, the existence of this particle explained not only why the β-decay spectrum was continuous but also that the maximal β ray energy was guaranteed to be less than the parent and daughter nucleus mass-difference. However, Pauli feared that this particle would never have any hope of being detected experimentally. It took 26 years to have the experimental evidence necessary to shown the direct detection of neutrinos. Experimental evidence was provided by Clyde Cowan and Frederick Reins with Project Poltergeist that was designed to observe inverse β-decay initiated through interactions of neutrinos produced in a nuclear reactor [3]. Since this discovery, the study of neutrinos, along with their interactions, has become important in providing the verification of weak interaction theory, and the first evidence showing that the Standard Model (SM) is incomplete in its original form. This chapter briefly discusses the standard model, the history of neutrino physics, and the current understanding of neutrino interactions important to the context of the research presented within this document.

1.1 Standard Model of Particle Physics

The Standard Model of particle physics (SM) is the theoretical framework that describes the elementary particles and the interactions between them [4]. The SM includes 12 elementary particles of spin $1/2$, known as fermions. Each of these fermions has a corresponding antiparticle. The fermions are further classified according to their interactions as quarks (up, down, charmed,

strange, top, and bottom) and leptons (electron, muon, tau, electron neutrino, muon neutrino, and tau neutrino), as shown in Figure 1.1.

The defining trait of a quark is that they carry "color" charge and interact through the strong force. Color charge comes in three different types, red, green, and blue. Quarks combine with each other to form color-neutral composite particles called hadrons. These composite states come in two basic varieties: baryons, which are made up of three quarks, and mesons, which are made up of quark and antiquark pairs. In addition to color charge, quarks also carry an electric charge and weak isospin, thus quarks also interact via electromagnetic and weak interactions.

Leptons differ from quarks in that they do not carry a color charge, thus they do not interact via the strong force. There are also two different types of leptons, those with electromagnetic charge and those without. The three leptons that carry electromagnetic charge are the electron, muon, and tau. These three particles are able to interact via the electromagnetic force. The three neutral leptons are the neutrinos. As these do not carry an electric charge, they only interact through the weak force.

Figure 1.1 also illustrates the three generations of matter. Most matter is made up of only first-generation particles, for example, all atomic nuclei consist of protons and neutrons which are made of up and down quarks. Second and third generation particles have greater masses than the corresponding particles of the lower generations and are unstable against decay into first-generation particles. This results in particles with short half-lives which are only produced in high energy interactions.

The interactions between the fermions are mediated through the exchange of gauge bosons, which have a spin value of 1. Photons mediate the electromagnetic force between electrically charged particles, the $W^{\pm}$ and Z bosons mediate weak interactions, and gluons mediate the strong interactions between particles that carry color charge. The weak interaction will be discussed further in the context of neutrino interactions with nuclei later in this chapter.

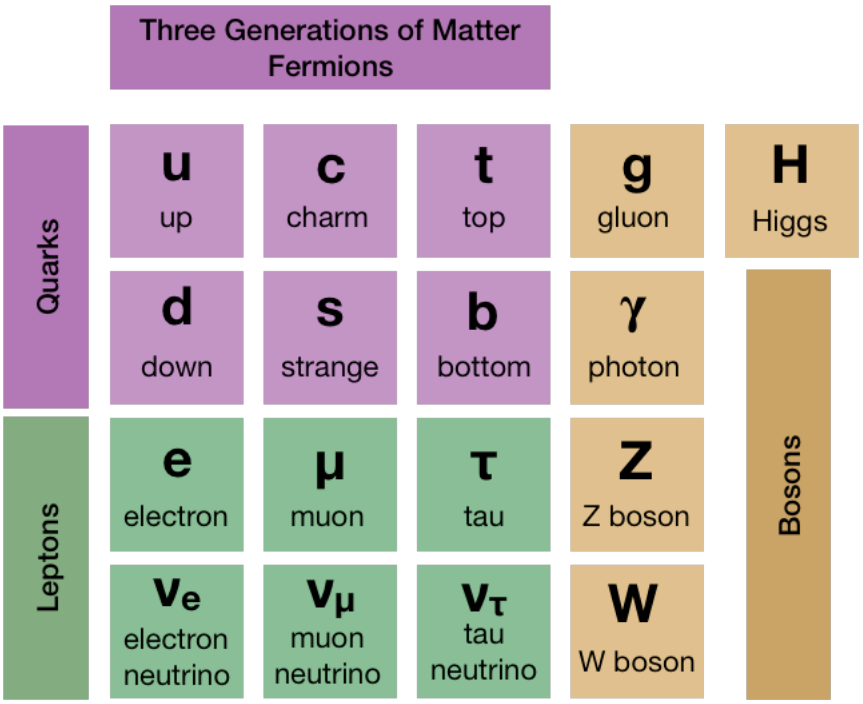

Figure 1.1: The Standard Model of elementary particles in diagram form showing the 12 fundamental fermions and the 5 bosons.

The final particle contained in the SM is the massive scalar boson, with spin 0 called the Higgs boson. The Higgs boson is responsible for the Higgs mechanism which explains how the other elementary particles have a mass through spontaneous symmetry breaking [5] [6].

1.2 Brief History of Neutrino Physics

The story of the neutrino begins with the experimental evidence that the energy spectrum of electrons emitted in β decay was continuous rather than the prediction of a discrete spectrum [2]. Pauli postulated the existence of a light, neutral, and weakly interacting particle that was emitted with the electron during β decay [1]. This postulation was taken further by Femi in 1934 when he developed the theoretical framework necessary to describe β-decay [7]. He postulated that β-decay was mediated by the decay process $n \rightarrow p + e^- + \overline{\nu}_e$. Fermi's framework not only enabled the computation of nuclear β-decay but also provided a means for the computation of the cross section of inverse beta decay, $\bar{\nu_e} + p \rightarrow e^+ + n$. It was this interaction that led to the direct detection

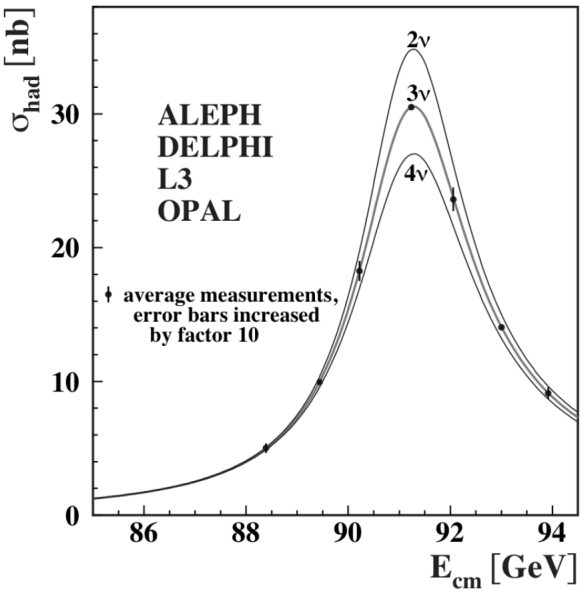

Figure 1.2: Measurement of the hadron production cross section around the Z resonance, shows a combined result from four linear electron positron collider experiments. The curves indicate the predicted cross section for two, three, and four neutrino species with SM couplings and negligible mass. Figure taken from [12]

of neutrinos by Reines and Cowan [3]. The energy-averaged cross section for the reaction was measured to be $11 \pm 2.6 \times 10^{-44}\text{cm}^2$.

In 1962 the AGS neutrino experiment at Brookhaven national lab utilized the first neutrino beam to observe the muon neutrino (ν_μ). The experiment used a 15 GeV proton beam incident on a beryllium target to produce pions and kaons, which would decay into hadrons, muons, and neutrinos creating the first neutrino beam [8]. This experiment pioneered many different techniques that are still used in modern accelerator-based neutrino experiments, like NOνA, which will be discussed in great detail in Chapter 2. The discovery of the tau lepton in 1975 [9] led to the prediction of the associated tau neutrino (ν_τ). The first indirect evidence for the ν_τ came in 1989 when the ALEPH collaboration made measurements of the mass and decay width of the Z gauge boson [10]. From the width of the mass peak (shown in Figure 1.2), they were able to place a limit on the number of light ($m_\nu < m_Z/2$) neutrinos to be 2.9840 ± 0.0082 corresponding to the three generations of leptons that had been discovered. The direct detection of ν_τ occurred in 2000 at Fermilab's DONUT experiment [11].

Following their discovery, it was realized that neutrinos could be used to study a variety of topics that other forms of probes cannot. One such example is the study of the ν_e flux coming nuclear reactions in the Sun to verify solar models. The Homestake experiment led by R. Davis measured this flux, and over the 30 year running period found about one-third of the predicted number of ν_e from the Standard Solar Model [13]. At the time, the differences between the experiment and the theory were attributed to issues with the experimental technique or failure of the model for the prediction of the solar neutrino flux. Other experiments, like Kamiokande-II, GALLEX, and SAGE, were designed to address this problem, but their results corroborated the Homestake observations [14] [15] [16].

A solution to this "solar neutrino problem", had first been offered in 1957 [17] and was later expanded upon in the 1960s by Pontecorvo [18], Maki, Nakagawa, and Sakata [19]. They suggested that neutrinos could oscillate between flavor states as they propagate, which would result in a diminished flux of ν_e from the sun as measured on Earth. In 2002, the SNO experiment was able to directly test the theory of neutrino oscillations. This was done by directly measuring the electron neutrino flux and the total neutrino flux through charged- and neutral- current weak interactions, respectively. The results showed that the electron neutrino flux was about a third of the solar model predictions, but that the total neutrino flux was in agreement with the predictions [20]. Further evidence to support the neutrino oscillation hypothesis was provided by the Super Kamiokande experiment, which measured the flux of electron and muon neutrinos from interactions between cosmic rays and the Earth's atmosphere. It was found that the muon neutrino flux was dependent on the distance these neutrinos traveled prior to their interaction within the detector [21]. This disappearance of muon neutrinos was consistent with the predictions of neutrino oscillations.

Since the 1950s much has been learned about neutrinos, including that there are three flavors, their oscillations, and the verification of electroweak theory through neutrino interactions. Current- and next-generation neutrino experiments will make increasingly accurate measurements of neutrino oscillation parameters. These precise characterizations require both an understanding of neutrino fluxes from nuclear reactors and accelerator-based neutrino beams and the interac-

tions between neutrinos and the nuclei that comprise neutrino experiments. The next sections describe the basic foundations of neutrino oscillations (Section 1.3) and the current understanding of neutrino-nucleus interactions necessary to describe the bulk of this thesis (Section 1.4).

1.2.1 Motivations for the Study of Neutrino-Nucleus Interactions

Before discussing some of the theoretical foundations for the work presented in this thesis, it is important to have an understanding of how neutrino-nucleus interactions play an important role in the current and future landscape of neutrino physics. This will be done through a discussion of neutrino-nucleus interactions and their importance in neutrino oscillation measurements as well as their role in weak interactions through the current levels of agreement of neutrino-nucleus interaction models to experimental measurements (see Section 1.4).

Role of Neutrino-Nucleus Interaction Physics on Oscillation Physics Analyses

Neutrino oscillation experiments require two things: a high-intensity source of a single flavor of neutrino, ν_μ in this example, and a way to detect these neutrinos after they have propagated some distance. By comparing the rate of ν_μ interactions in the detector to the expected rate based on the neutrino flux and the probability that a neutrino will interact within the detector the oscillation parameters of the neutrinos can be characterized. Even in this simplified example, the impact of our current understanding of neutrino-nucleus interactions plays a key role in our ability to accurately measure and characterize neutrino oscillations.

Additional information can be extracted if the oscillations are characterized by some additional parameter, like the energy of the neutrinos (see Section 1.3 for how this impacts neutrino oscillations). The total event rate then becomes dependent on the neutrino energy. Because the neutrino energy is unknown prior to their interaction within the detector, oscillation experiments must be able to determine the neutrino energy indirectly through the outgoing kinematics of particles created in the neutrino interaction. Any unobserved energy, like that coming from neutral particles in the final-state, particles below the detection threshold of the detector, and inefficiencies in charged particle detection, must be fully accounted for to reconstruct the neutrino energy. The measured

neutrino energy within detectors typically differs from the true energy of the neutrino. To fully characterize the neutrino energy requires further input from our neutrino-nucleus interaction models to relate the observed quantities back to the true neutrino energy.

The measured event rate can also be impacted by the types of materials that comprise neutrino detectors. Thus, neutrino interactions can occur on a variety of target nuclei that will need to be understood. The differences in the nuclei (ranging from H to Ti, in the NOνA detector), can have wide-ranging impacts on the possible interactions and the kinematics of outgoing particles.

Limitations of Current Neutrino-Nucleus Interaction Models

Neutrino-nucleus interactions and the models used to predict them play an important role in the characterization of neutrino oscillations. The current level of understanding of these interactions introduces uncertainties in a variety of ways throughout an oscillation analysis. One way to reduce these uncertainties is through continued study of neutrino-nucleus interactions.

The largest systematic uncertainty in NOvA's first published muon neutrino disappearance measurement [22] was a 15% uncertainty in the absolute scale of energy observed in the hadronic recoil systems of neutrino interactions. This uncertainty was designed to cover the discrepancy seen in the NOνA near detector (see Chapter 2) between data and the predicted hadronic energy, which is any energy within a candidate neutrino event not associated with the final-state lepton in the NOνA detector. This discrepancy is shown in Figure 1.3. It is only important to know that each of the colored histograms, QE (blue), RES (green), DIS (grey), and Other (black), refer to different types of neutrino-nucleus interactions that can occur within the NOνA experiment. There is clearly a deficiency in the number of predicted neutrino interactions near Visible $E_{had} \approx 0.1$ GeV.

The issue with this prediction was the fact that the default neutrino-nucleus interaction models did not include a variety of scattering processes that occur exclusively on multi-nucleon nuclei, like carbon in the NOνA detector. Due to the lack of understanding in the underlying physics, agreement was reached using a semi-empirical approach. This was done through the inclusion of an additional interaction model, called Meson Exchange Currents (MEC), that was further tuned to give a better description of the ND data. The improved agreement is shown in Figure 1.4, but

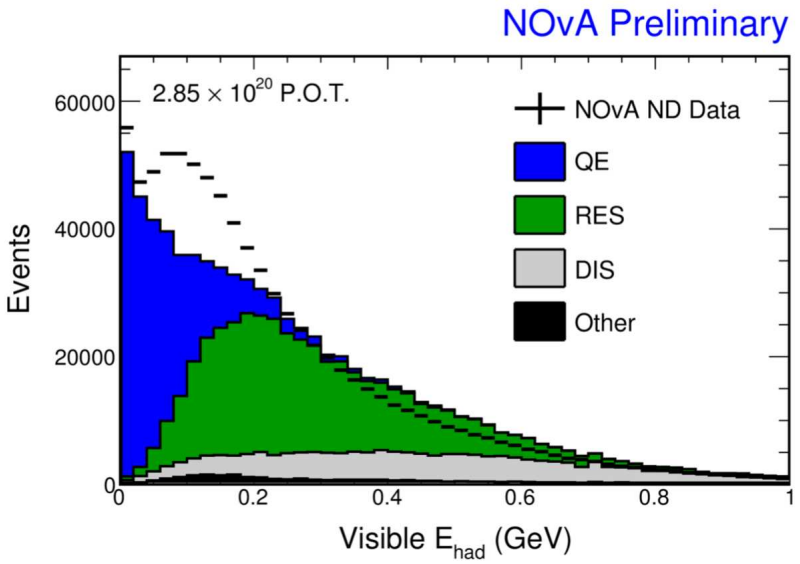

Figure 1.3: Plot of visible hadronic energy in selected charged-current muon neutrino interactions in the near detector. Colored histograms correspond to the predicted true interaction types from GENIE 2.10.2 ("QE" is quasi-elastic scattering; "RES" is resonant production; "DIS" is deep inelastic scattering). The data points are data taken in the NOνA near detector with statistical uncertainties (2.85×10^{20} P.O.T.)

this method still does not adequately describe the data spectrum. These types of discrepancies require additional measurements to probe the fundamental questions that still remain about weak interactions between neutrinos and nuclei, and can even provide additional information about the nuclear environment itself.

1.3 Neutrino Oscillations

The theory of neutrino oscillations describes two sets of orthogonal neutrino states. The first set describes the flavor eigenstates of the weak interaction. These are labeled by the charged lepton associated with the neutrino such that ν_α is associated with the α charged lepton, where $\alpha = e, \mu, \tau$. The other set describes the neutrino mass states ν_i, where $i = 1, 2, 3$. The mass states are the eigenstates of the free neutrino Hamiltonian, thus they describe the state of propagating neutrinos. There is no reason for each of the neutrino states to be equivalent, in fact, the neutrino flavor states are linear combinations of the neutrino mass eigenstates,

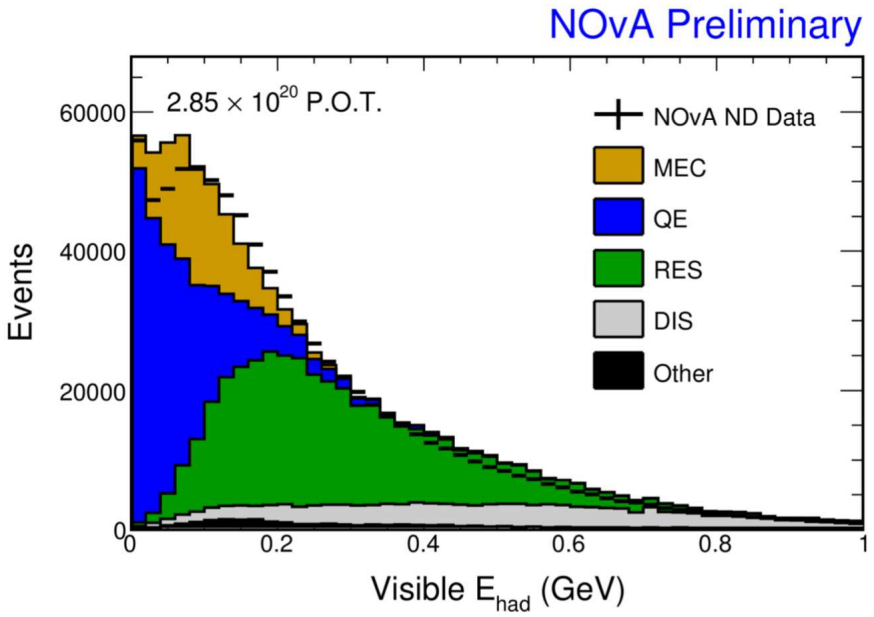

Figure 1.4: Measured visible hadronic energy (compare Figure 1.3) compared to the model with an added GENIE MEC component.

$$|\nu_\alpha\rangle = \sum_{i=1}^{n} U^*_{\alpha i} |\nu_i\rangle \ , \tag{1.1}$$

where n is the number of light neutrino species and U is the unitary mixing matrix describing the lepton section neutrino mixing. The lepton sector mixing matrix is commonly referred to as the PMNS matrix (Pontecorvo-Maki-Nakagawa-Sakata) [23] and is given by:

$$\begin{aligned} U_{PMNS} &= \begin{bmatrix} U_{e1} & U_{e2} & U_{e3} \\ U_{\mu 1} & U_{\mu 2} & U_{\mu 3} \\ U_{\tau 1} & U_{\tau 2} & U_{\tau 3} \end{bmatrix} \\ &= \begin{bmatrix} 1 & 0 & 0 \\ 0 & c_{23} & s_{23} \\ 0 & -s_{23} & c_{23} \end{bmatrix} \begin{bmatrix} c_{13} & 0 & s_{13}e^{-i\delta_{CP}} \\ 0 & 1 & 0 \\ -s_{13}e^{i\delta_{CP}} & 0 & c_{13} \end{bmatrix} \begin{bmatrix} c_{12} & s_{12} & 0 \\ -s_{12} & c_{12} & 0 \\ 0 & 0 & 1 \end{bmatrix} \begin{bmatrix} e^{i\alpha_1/2} & 0 & 0 \\ 0 & e^{i\alpha_2/2} & 0 \\ 0 & 0 & 1 \end{bmatrix} , \end{aligned} \tag{1.2}$$

where $c_{ij} = \cos(\theta_{ij})$ and $s_{ij} = \sin(\theta_{ij})$. The PMNS matrix is required to be an unitary matrix and is parametrized by three mixing angles $(\theta_{12}, \theta_{13}, \theta_{23})$, one Dirac CP-violating phase (δ_{CP}) and two Majorana CP-violating phases (α_1, α_2). Where Majorana describes the possibility that the particle is its own antiparticle. The two Majorana phases will be measurable and have physical meaning if neutrinos are Majorana particles. Majorana phases have no effect on neutrino oscillation probabilities, as oscillation probabilities depend on UU^* in which the Majorana phases cancel. Off-diagonal terms in U represent the fact that neutrinos created in a specific flavor state are also in a superposition of mass states. As neutrinos travel, the superposition of mass states causes the neutrinos to change flavor. Thus, neutrinos created in a definite flavor state have a finite probability of being observed as a different flavor state after propagation.

Implicit in the definition shown in Equation 1.1 is the dependence of $|\nu\rangle$ on its propagation through space and time, such that a neutrino originally produced with flavor α traveling a distance L (or time t for relativistic neutrinos) evolves according to:

$$|\nu_\alpha(t)\rangle = \sum_{i=1}^{n} U^*_{\alpha i} \, |\nu_i(t)\rangle \ , \tag{1.3}$$

where $|\nu_i\rangle$ is the state of the neutrino with mass m_i and energy E_i of the neutrino is given by:

$$E_i = \sqrt{p^2 + m_i^2} \simeq p + \frac{m_i^2}{2p} \approx E + \frac{m_i^2}{2E} \, , \tag{1.4}$$

p_i is the momentum of the propagating neutrino. The last approximation in Equation 1.4 reflects the fact that propagating neutrino is relativistic as neutrino masses are so small that $|p_i| >> m_i$ is effectively always true.

According to the Schrodinger equation, for a neutrino produced in flavor state ν_α at the production point at time, $t = 0$, the mass eigenstates will evolve in time as:

$$|\nu_\alpha(t)\rangle = \sum_{i=1}^{n} U^*_{\alpha i} e^{-iE_k t} \, |\nu_i(0)\rangle \, . \tag{1.5}$$

Using the approximations from Equation 1.4 and for an ultra relativistic particles $t \approx L$ (in natural units $c = 1 = \hbar$), the mass eigenstates evolve in time as:

$$|\nu_\alpha(t)\rangle = \sum_{i=1}^{n} U^*_{\alpha i} e^{-im_i^2 L/2E} |\nu_i(0)\rangle . \tag{1.6}$$

Each neutrino mass eigenstate propagates with a different phase, thus the flavor content of the final-state will differ from the initial state of the neutrino. The probability of a neutrino having started in some flavor state α, being found in some flavor state β at time t is calculated:

$$P_{\alpha\to\beta} = |\langle\nu_\beta(t)|\nu_\alpha(0)\rangle|^2 = \left|\sum_{i=1}^{n} U^*_{\alpha i} U_{\beta i} e^{-im_i^2 L/2E}\right|^2 . \tag{1.7}$$

Given the fact that U is a unitary matrix Equation 1.7 can be expanded to:

$$\begin{aligned} P_{\alpha\to\beta} &= \delta_{\alpha\beta} - 4\sum_{i>j} Re[U^*_{\alpha i} U_{\alpha j} U_{\beta i} U^*_{\beta j}] \sin^2\left(\frac{\Delta m^2_{ij}}{4E} L\right) \\ &\quad +2\sum_{i>j} Im[U^*_{\alpha i} U_{\alpha j} U_{\beta i} U^*_{\beta j}] \sin^2\left(\frac{\Delta m^2_{ij}}{2E} L\right) \end{aligned} \tag{1.8}$$

where $\delta_{\alpha\beta}$ is the Kroenecker delta defined as $\delta_{\alpha\beta} = 1$ when $\alpha = \beta$ and 0 when $\alpha \neq \beta$. The survival probability ($\nu_\beta = \nu_\alpha$) can be further simplified to:

$$P_{\alpha\to\alpha}(L, E) = 1 - 4\sum_{i>j} |U_{\alpha i}|^2 |U_{\alpha j}|^2 \sin^2\left(\frac{\Delta m^2_{ij}}{4E} L\right) \tag{1.9}$$

where $\Delta m^2_{ij} = m^2_i - m^2_j$. Equation 1.9 can be shown in an approximate form as:

$$P_{\mu\to\mu} \approx 1 - (\sin^2(2\theta_{13}) \sin^2(\theta_{23}) + \cos^4(\theta_{13}) \sin^2(2\theta_{23}) \sin^2(\frac{\Delta m^2 L}{4E}) \tag{1.10}$$

It can be seen from Equation 1.10 that three-flavor neutrino oscillations probabilities are described by both the mixing angles and the mass squared differences between the mass eigenstate values. Higher-order corrections to equation 1.10 show additional dependence of the oscillation

probability on the CP-violating phase present in the PMNS matrix. The measurement of these parameters is the goal of modern long-baseline neutrino experiments.

1.3.1 Neutrino Oscillations in Matter

The previous section considered neutrinos propagating through a vacuum, but most neutrino experiments involve neutrinos propagating through some form of matter. In accelerator-based neutrino experiments this medium is the Earth. The effects of matter on neutrino oscillations can make a substantial difference to neutrino oscillation physics due to the fact matter is electron dominated. This leads to additional interactions with matter via coherent forward scattering through weak interactions. Wolfenstein, Mikheyev, and Smirnov [24] [25] were the first to calculate the effects of these interactions on neutrino oscillations.

While vacuum oscillations are sensitive to the square of the neutrino mass splittings (δm^2_{ij}), matter effects are sensitive to the signs of the mass splittings. Matter effects allow the determination of the ordering of the neutrino mass states such that $m_1 < m_2 < m_3$ or $m_3 < m_1 < m_2$ which are called the normal or inverted neutrino mass hierarchy, respectively*. Whether the neutrino mass hierarchy is normal or inverted is one of the most prominent unanswered questions within neutrino physics. Additionally, matter effects impact the oscillation differently for neutrinos and antineutrinos. This can lead to a measured CP violation $P(\nu_\alpha \to \nu_\beta) \neq P(\bar{\nu}_\alpha \to \bar{\nu}_\beta)$, that needs to be accounted for to determine if leptonic sector CP violation (δ_{CP} from the PMNS matrix) exists. A further discussion of this topic can be found in [27]. Accounting for matter effects, the oscillation probability of ν_μ to ν_e can be written as [28]:

*The sign of Δm^2_{12} is obtained through the observation of matter effects in the sun. This experiments constrain the product of $\Delta m^2_{21} \cos 2\theta_{12}$ to be positive [26].

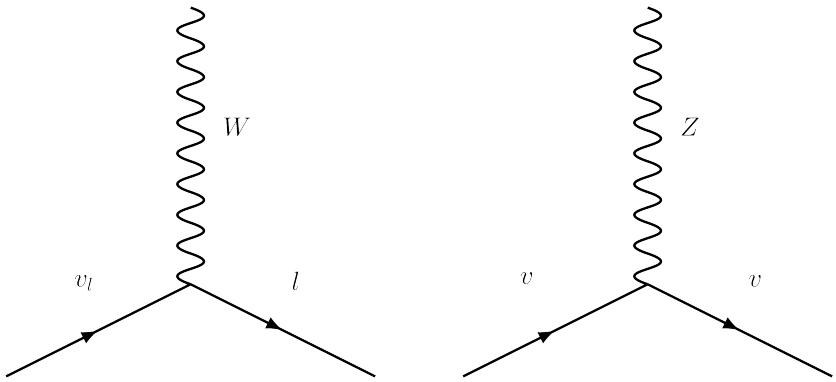

Figure 1.5: Feynman diagram vertices for weak interactions. Left: Charged current weak interaction vertex. Right: Neutral current weak interaction vertex, where ν_l corresponds to one of the neutrino flavors, with l being the associated charged lepton.

$$\begin{aligned} P(\nu_\mu \to \nu_e) &= \sin^2\theta_{23}\sin^2 2\theta_{13}\frac{\sin^2(\Delta_{31}-aL)}{(\Delta_{31}-aL)^2}\Delta_{31}^2 \\ &\quad + \sin 2\theta_{23}\sin 2\theta_{13}\sin 2\theta_{12}\frac{\sin(\Delta_{31}-aL)}{(\Delta_{31}-aL)}\Delta_{31}\frac{\sin(aL)}{(aL)}\Delta_{21}\cos(\Delta_{31}+\delta_{\text{CP}}) \\ &\quad + \cos^2\theta_{23}\sin^2 2\theta_{12}\frac{\sin^2(aL)}{(aL)^2}\Delta_{21}^2 \end{aligned} \tag{1.11}$$

where $\Delta_{ij} = \Delta_{ij}^2 L/4E$, and a is the density of electrons in the medium.

1.4 Neutrino - Nucleon Interactions

The theory describing electroweak interactions was developed by Glashow, Weinberg, and Salam in the late 1950s and early 1960s [29–31]. They predicted the existence of two massive gauge bosons, the W and Z, that mediate the weak force. Neutrinos, being electrically neutral and almost massless, interact with matter almost entirely through weak interactions. Thus, the study of neutrinos has been extensively linked to the development of electroweak theory and the current understanding of the weak force. With the prediction of these two gauge bosons, electroweak theory predicted the existence of two types of weak interactions charged- and neutral- current interactions mediated by the W and Z bosons, respectively. Figure 1.5, shows neutrino interactions via the W and Z bosons.

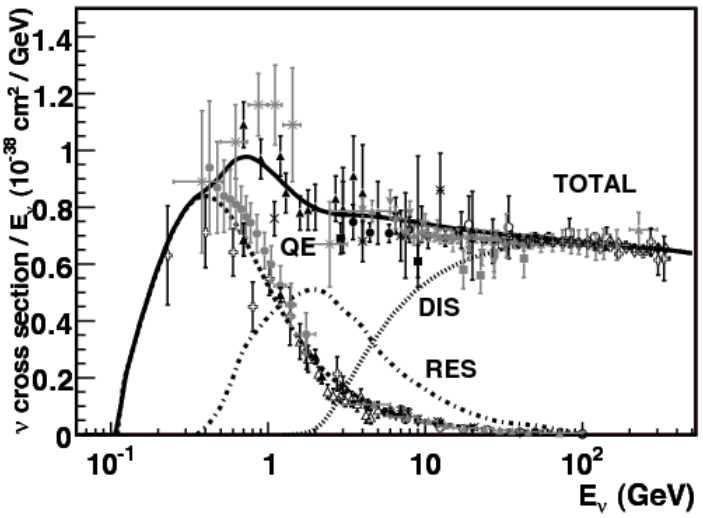

Figure 1.6: Total neutrino per nucleon charged current cross sections divided by neutrino energy and plotted as a function of energy. Figure taken from [33].

Charged-current neutrino interactions, mediated by the charged W boson, are flavor neutral, meaning that neutrino that underwent the interaction is of the same flavor as the charged lepton produced in the final-state. Electron neutrinos generate electrons, muon neutrinos produce muons, and tau neutrinos produce tau leptons in the interaction. These final-state leptons are the only way to identify the flavor of the neutrino. These interactions have been studied since the first detection of the electron antineutrino by Reines and Cowan in the late 1950s [3]. The first experimental evidence for neutral current interactions was discovered in the Gargamelle bubble chamber experiment at CERN [32]. These interactions are observed through the presence of neutrino-induced hadronic activity. Due to the lack of a charged lepton in the final-state, it is impossible to determine the flavor of the neutrino that underwent the interaction.

Neutrino interactions depend on the energy of the neutrino undergoing the interaction, as shown in Figure 1.6. At higher energies the neutrino can interact at smaller length scales, ranging from entire nucleus down to individual quarks within a nucleon. The next sections discuss interaction types that are important to charged-current cross section measurements at the energy scale of a few GeV.

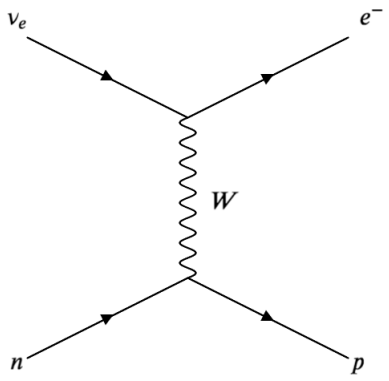

Figure 1.7: A Feynman diagram illustrating a charged-current QE interaction.

1.4.1 Quasi-Elastic (QE) Interactions

Quasi-elastic (QE) scattering is the main interaction mechanism for neutrinos with energies below about 1-2 GeV. Current models describe QE scattering as the neutrino interacting with an entire nucleon bound within a nucleus. Although the neutrino interaction is with an individual quark within a nucleon, this is a reasonable description because a W-boson (in charged current interactions) is exchanged between the neutrino and nucleon and a charged lepton and nucleon with altered isospin is produced. The process is referred to as quasi-elastic because the neutrino is translated to a charged lepton during the W-exchange with the nucleus. In neutral current (NC) interactions the process is elastic. In charged-current interactions for neutrino-nucleon scattering, the target neutron is converted into a proton, while for antineutrino scattering the target proton is converted into a neutron. This is illustrated in Figure 1.7 for an interaction between an electron neutrino and a neutron.

Calculating the exact cross section for this relatively simple looking interaction is actually quite difficult due to the fact that a nucleon is a composite object. Current theoretical calculations parameterize the cross section in terms of a set of parameters that can be measured using other types of interactions namely β-decay and electron scattering experiments. The basic model of QE interactions used by modern neutrino event generators is the Llewellyn-Smith model [34]. This

model focuses on the simplified case of QE scattering off of free nucleons, where the differential cross section with respect to four-momentum transfer to the nucleon, Q^2, is:

$$\frac{d\sigma}{dQ^2} = \frac{\mathrm{G_F^2} M^2 \cos^2\theta_c}{8\pi E_\nu^2}\left(A(Q^2) \mp B(Q^2)\frac{s-u}{M^2} + C(Q^2)\frac{(s-u)^2}{M^4}\right) \tag{1.12}$$

where -(+) refers to neutrino(antineutrino) scattering, $\mathrm{G_F}$ is the Fermi coupling constant, M is the nucleon mass, E_ν is the incident neutrino energy, $(s-u) = 4ME_\nu - Q^2 - m^2$, m is the lepton mass, and θ_c is the Cabibo angle[†] ($\cos\theta_c = 0.9742$). The factors A, B, and C are functions of Q^2 built from the several vector, axial-vector, and pseudo-scalar coupling terms:

$$\begin{aligned} A(Q^2) =& \frac{m^2+Q^2}{M^2}[(4+\frac{Q^2}{M^2})F_A^2 - (1-\zeta)\left|F_V^1\right|^2 + \frac{Q^2}{M^2}\zeta\left|F_V^2\right|^2(1-\frac{Q^2}{4M^2}) \\ &+ \frac{4Q^2 ReF_V^{1*}\zeta F_V^2}{M^2} - \frac{Q^2}{M^2}\left(4+\frac{Q^2}{M^2}\right)\left|F_A^3\right|^2 - \frac{m^2}{M^2}(\left|F_V^1+\zeta F_V^2\right|^2 \\ &+ \left|F_A+2F_P\right|^2 - (4+\frac{Q^2}{M^2})\left|F_A^3\right|^2 + \left|F_P\right|^2))] \end{aligned} \tag{1.13}$$

$$B(Q^2) = \frac{Q^2}{M^2}ReF_A^*\left(F_V^1+\zeta F_V^2\right) - \frac{m^2}{M^2}Re\left[\left(F_V^1 - \frac{Q^2}{4M^2}\zeta F_V^2\right)^* F_V^3 - \left(F_A - \frac{Q^2F_P}{2M^2}\right)^* F_A^3\right] \tag{1.14}$$

$$C(Q^2) = \frac{1}{4}\left(\left|F_A\right|^2 + \left|F_V^1\right|^2 + \frac{Q^2}{M^2}\left|\frac{\zeta F_V^2}{2}\right|^2 + \frac{Q^2}{M^2}\left|F_A^3\right|^2\right), \tag{1.15}$$

where F_V^1, F_V^2, and F_V^3 are the vector and F_A and F_A^3 are the axial-vector form factors and F_P is the pseudo-scalar form factor, and ζ is the difference between the anomalous magnetic moment of the proton and neutron ($\zeta = (\mu_p/\mu_N - \mu_n/\mu_N) - 1$). In practice, F_V^1 and F_V^2 have been determined by observing electromagnetic interactions in electron scattering experiments. Unlike the other form-factors, $F_{V,A}^3$ are associated second-class currents, which require the existence of charge and time

[†] The Cabibbo angle is the mixing angle between the first two generations of quarks. It is used to describe the violation of flavour in weak interactions in the quark sector [35].

symmetry violations that, based on β-decay experiments, are considered small and are typically assumed to be zero in neutrino analyses [36]. The only form factors left for neutrino experiments to determine are the axial-vector and pseudo-scalar form factors. The axial-vector form factor is typically parameterized to have a dipole form:

$$F_A(Q^2) = \frac{g_A}{\left(1 + \frac{Q^2}{M_A^2}\right)^2} \tag{1.16}$$

$$F_P(Q^2) = \frac{2M^2}{Q^2 + m_\pi^2} F_A(Q^2) \tag{1.17}$$

where $g_A = 1.267$, the axial vector constant, and is measured by β-decay experiments [37]. The only parameter left to constraint in the Llewellyn-Smith model is M_A. This parameter is called the axial mass and its average value is $M_A = 1.014 \pm 0.014$ GeV/c^2. It has been measured using both neutrino-deuterium and neutrino-hydrogen scattering [38]. However, more recent neutrino scattering experiments using heavier nuclei have measured differences from the original extracted axial mass from neutrino-deuterium scattering experiments [39].

1.4.2 Resonant Pion Production

In resonant (RES) inelastic interaction, given enough energy, neutrinos can excite the interacting nucleon to an excited state. The excited state produces a baryon resonance, with the main decay mode being the emission of one (or more) pions. The energy range of interest for these types of interaction is between 1 and 3 GeV and is typically characterized by an hadronic mass, W, less than 2 GeV.

In the lower energy range, pions are typically produced through the $\Delta_{33}(1232)$ resonance. For higher neutrino energies a range of resonances can be produced including $P_{11}(1440)$, $S_{11}(1535)$, and $D_{13}(1520)$. The higher energy resonances can decay to multiple pions, kaons, or other final-states. The main channels of charged current single pion production interactions on free nucleons are:

$$\nu_l + p \rightarrow l^- + p + \pi^+ \tag{1.18}$$

$$\nu_l + n \rightarrow l^- + p + \pi^0 \tag{1.19}$$

$$\nu_l + n \rightarrow l^- + n + \pi^+ \tag{1.20}$$

The main channels of neutral current single pion production interactions on free nucleons are:

$$\nu_l + p \rightarrow \nu_l + p + \pi^0 \tag{1.21}$$

$$\nu_l + p \rightarrow \nu_l + n + \pi^+ \tag{1.22}$$

$$\nu_l + n \rightarrow \nu_l + n + \pi^0 \tag{1.23}$$

$$\nu_l + n \rightarrow \nu_l + p + \pi^- \tag{1.24}$$

An example of a resonance interaction is shown in Figure 1.8.

Current neutrino experiments use the Rein-Sehgal model to describe resonant production processes [40]. The model gives predictions for both the charged and neutral current resonance processes and corrects for interference between overlapping resonances. These models use form factors to describe the nuclear target that are similar to those seen in the Llewellyn Smith model used for QE scattering. However, these form factors are not as well constrained by electron scattering interactions and require more precise inputs from resonant neutrino interaction measurements.

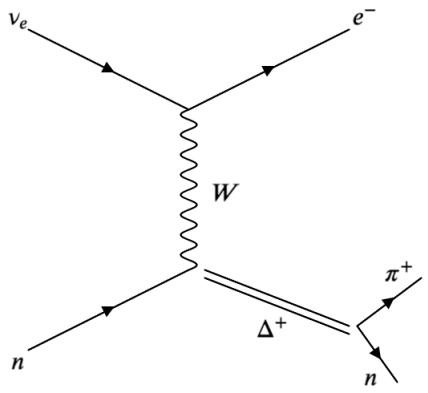

Figure 1.8: A Feynman diagram illustrating a charged-current RES interaction.

1.4.3 Deep Inelastic Scattering

Deep inelastic scattering (DIS) occurs when the neutrino has a sufficiently high energy to interact with individual quarks through the exchange of a W or Z boson. The interaction breaks apart the nucleon producing a hadronic jet in the final-state. An example of this is shown in Figure 1.9. Deep inelastic scattering becomes the dominant interaction channel for neutrino energies above 10 GeV. Deep inelastic scattering interactions in this energy regime have been used as both a probe of nuclear structure and as a validation of the Standard Model of Particle Physics [33].

These interactions can be described using three parameters:

$$Q^2 = -q^2 = (p_\nu - p_l)^2 \tag{1.25}$$

$$y = \frac{p_t \cdot q}{p_t \cdot p_\nu} \tag{1.26}$$

$$x = \frac{Q^2}{2p_t \cdot q} \tag{1.27}$$

where Q^2 is the 4-momentum transfer of the interaction, defined as the squared difference between the 4-momentum of the incoming neutrino, p_ν and outgoing lepton p_l, and y is the inelasticity of

the interaction. This parameter relates the initial 4-momentum of the target, to the 4-momentum of the incoming neutrino and the momentum transferred during the interaction. The Bjorken scaling variable, x, describes how strongly interacting particles (like hadrons) behave as a collection of point particles when probed at high energies [41]. Using these parameters the inclusive cross section for DIS scattering of neutrinos and antineutrinos is written [33]:

$$\frac{d^2\sigma}{dxdy} = \frac{\mathrm{G_F^2} M E_\nu}{\pi \left(1 + Q^2/M_\mathrm{W}^2\right)^2} \times \left[\frac{y^2}{2} 2xF_1\left(x, Q^2\right) + \left(1 + y - \frac{Mxy}{2E}\right) F_2\left(x, Q^2\right) \pm y\left(1 - \frac{y}{2}\right) xF_3\left(x, Q^2\right)\right] \tag{1.28}$$

where +(-) refers to neutrino(antineutrino) scattering, $\mathrm{G_F}$ is the Fermi coupling constant, M is the nucleon mass, and M_W is the mass of the W boson for CC scattering. $F_i\left(x, Q^2\right)$ are nucleon structure functions that characterize the underlying structure of the target nucleus. Although Equation 1.28 provides a clear look at the predicted DIS scattering cross section for CC events, it is missing additional information necessary to correctly predict the cross section. These corrections include the final-state lepton mass, higher order QCD corrections, as well as additional nuclear effects and other processes.

While the typical kinematic region considered for DIS interactions ($W \geq 2.0$ GeV and $Q^2 \geq 1$ GeV^2) has been well studied as a verification of the Standard Model, the transition region from RES to DIS has not been as well-researched. This transition region is typified by shallow inelastic scattering (SIS). This energy region is of particular interest for current neutrino interaction experiments as it is the typical energy range used in neutrino oscillation experiments. A lack of data at lower energies makes the extrapolation of well-characterized DIS interactions at higher energies problematic, thus this is an area of active study in neutrino-interaction physics.

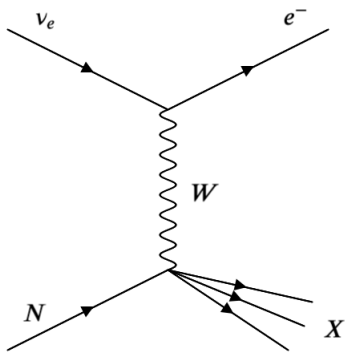

Figure 1.9: A Feynman diagram illustrating a charged-current DIS interaction.

1.4.4 Coherent Pion Production

Coherent pion scattering is a process by which the incoming neutrino scatters with the entire nucleus. The nucleus recoils but is left in the same final-state as in the initial state and a characteristic forward-going pion (co-linear with the incoming neutrino) is produced. This process is possible at low values of Q^2 and is possible through both CC and NC interactions:

$$\nu_l + A \rightarrow l^- + A + \pi^+ \tag{1.29}$$

$$\nu_l + A \rightarrow \nu_l + A + \pi^0 \tag{1.30}$$

The description of coherent pion production is commonly based on the Partially Conserved Axial Current (PCAC) theorem developed by Adler [42]. The PCAC theorem relates neutrino-induced coherent pion production to pion-nucleus elastic scattering in the limit $Q^2 = 0$. This limit is then extrapolated to non-zero values of Q^2 using nuclear form-factors similar to those described previously.

Figure 1.10 shows a Feynman diagram for a coherent pion production interaction. Coherent pion production is characterized by the variable $|t|$ which is the squared momentum transfer to the nucleus from the neutrino-pion system, or $|t| = |\,(q - p_\pi)^2\,|$, where q is defined in Equation 1.25

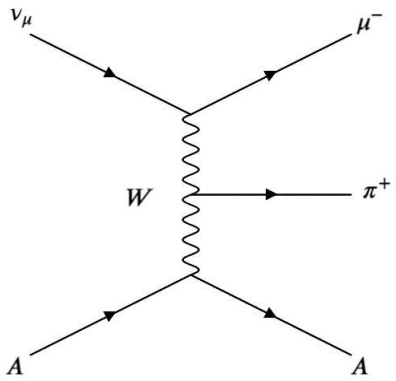

Figure 1.10: A Feynman diagram of a charged-current coherent pion production.

and p_π is the momentum of the outgoing pion. The momentum transfer to the nucleus in coherent pion production is small. The differential cross section for CC coherent pion production is given by [43]:

$$\frac{d^3\sigma}{dQ^2 d\nu dt} = \frac{\mathrm{G_F^2}\cos^2\theta_C f_\pi^2}{2\pi^2}\frac{uv}{|\mathbf{q}|}\left[\left(\mathrm{G_A} - \frac{1}{2}\frac{Q_m^2}{(Q^2+m_\pi^2)}\right)^2 + \frac{\nu}{4E_\nu}\left(Q^2 - Q_m^2\right)\frac{Q_m^2}{(Q^2+m_\pi^2)}\right] \times \frac{d\sigma(\pi^+ A \to \pi^+ A)}{dt} \tag{1.31}$$

where $\mathrm{G_F}$ is the Fermi coupling constant, θ_c is the Cabibo angle ($\cos\theta_c = 0.9742$), u and v are kinematic factors given by $u, v = \left(E_\nu + E_\mu \pm |\mathbf{q}|\right)/2E_\nu$, $\mathrm{G_A}$ is the axial vector form factor given in Equation 1.16 (but with different notation), the pion decay constant, f_π(= 0.93 m_π), and $\frac{d\sigma(\pi^+A\to\pi^+A)}{dt}$ is the elastic pion-nucleon differential cross section. The factor $Q_m^2 = \frac{m_\mu^2\nu}{E_\nu - \nu}$ and is described as the high energy approximation of the true minimum of four momentum transfer. The neutrino-nucleus interaction simulations used in this thesis are based on a model for coherent pion production following on the work by Rein-Seghal [44].

1.5 Impact of Nuclear Effects on Neutrino-Nucleus Scattering

The previous section focused mainly on neutrino-nucleon interactions. Modern neutrino interaction experiments typically do not use free nucleons as the primary target, instead they rely on a detector made up of a variety of target nuclei. While the previous discussion on the different types of neutrino-nucleon interactions still applies to light nuclei, interactions with heavier nuclei (like carbon, oxygen, argon, etc.) can substantially impact the final-state products of the different interactions through "nuclear effects".

Nuclear effects can broadly be separated into two categories initial-state and final-state effects. Initial-state effects are conditions within the nucleus that impact the nucleon prior to and as a part of the neutrino interaction. Final-state effects consist of hadronic interactions that impact the outgoing final-state particles prior to their exit from the nucleus. These processes can impact the outgoing kinematics or even affect the outgoing hadronic products from the neutrino interaction as they propagate through the nucleus. Brief summaries of these different nuclear effects on neutrino-nucleus scattering are discussed in this section.

1.5.1 Initial-State Effects

Fermi-Motion

The Pauli Exclusion Principle states that no two identical fermions can occupy the same quantum state. As protons and neutrons inside a nucleus are fermions, they must obey and be distributed according to Fermi-Dirac statistics. Assuming that the nucleons are non-interacting and that each energy state of the nucleus is filled sequentially, all nucleons bound within the nucleus occupy states in a Fermi-gas up to the Fermi level. This is illustrated in Figure 1.11. This so-called Fermi Gas Model allows for the bound nucleons to move independently within the volume of the nucleus under a constant nuclear binding potential. The combined motion of the nucleons is called Fermi-motion. This initial state momenta for the nucleons in the nucleus cause neutrino interactions to experience a boost in the lab-frame that differs event-by-event. Although the Fermi Gas Model is fairly simplistic it gives insight into the dynamics of nucleons within the nucleus.

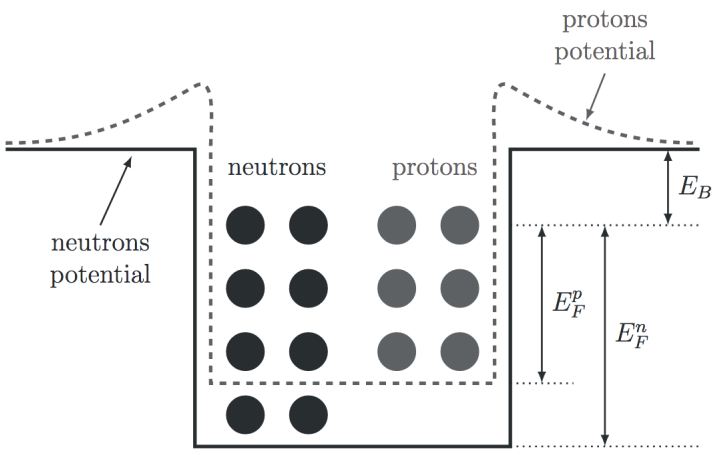

Figure 1.11: A cartoon of nuclear potential well for protons and neutrons bound within nucleus with constant nuclear potential for each nucleon. E_F^p and E_F^n are the Fermi energies of protons and neutrons. E_B is the nuclear binding energy. Figure taken from [45]

.

Another model of initial state effects used in neutrino event generators is known as the Relativistic Fermi Gas Model and includes an increase in complexity. This model introduces the concept of Pauli blocking, where a lower energy state nucleon cannot be given enough momentum (through interactions) to achieve an energy level that is equal to a state that is already filled by another nucleon. These "blocked" energy levels require that the nucleon receives enough energy that it will be above the Fermi level. If a neutrino interaction transfers enough energy to a nucleon to put it above the Fermi level and the binding energy, the nucleon can be ejected from the nucleus and the remainder of the nucleus does not take part in the interaction. If these conditions are not met the interaction is suppressed through Pauli blocking and the outgoing kinematic distributions of final-state products are additionally impacted.

The Relativistic Fermi Gas model and Fermi Gas model belong to a class of models known as Global Fermi Gases (GFG). These models assume that all nucleons feel the same constant binding potential. A more sophisticated approach assumes that the binding potential depends on the local density of the nucleons. This position-dependent nuclear density has previously been observed in electron scattering data [46]. Models that make use of this type of nuclear potential are known as "local Fermi gasses" (LFG). In these models, the local nuclear density is used to build a nuclear

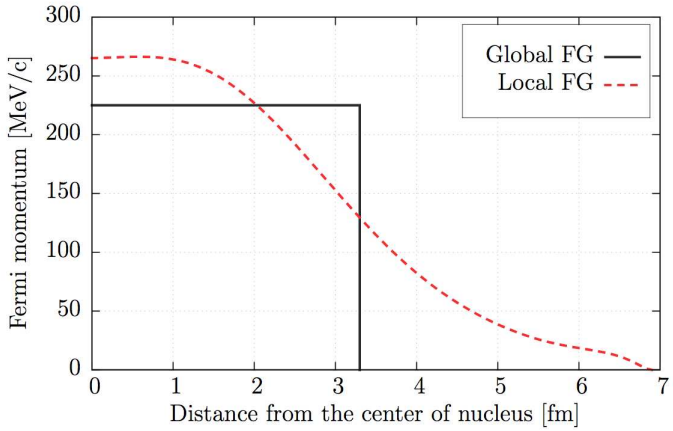

Figure 1.12: Comparison of Global to Local Fermi Gas models. Plots shows nucleon momentum as a function of distance from center of the nucleus. Figure taken from [45].

.

potential that is dependent on the radial position of a nucleon within a nucleus [45]. A comparison of the nucleon momentum as a function of the radial position is shown in Figure 1.12.

Each model discussed previously assumes that nucleons within the nucleus are non-interacting. However, electron scattering experiments show that this assumption is not well motivated [47] [48]. Nucleon-nucleon interactions within the nucleus can have additional effects on the momenta of nucleons. Models that incorporate these effects are known as spectral function (SF) models (see [49] for an example). Spectral function models consider modifications to nuclear potentials due to the inclusion of two- and three-nucleon interaction potentials. Sometimes these additional potentials can include repulsive interactions. These interactions lead to a probability that nucleons can have a momentum above the Fermi momentum.

Nucleon-Nucleon Correlations

As discussed above many nuclear models do not take nucleon-nucleon interactions within the nuclear medium into account. In addition to the correlations discussed above another mechanism called short-range correlations can also affect the momentum of the correlated nucleons [50]. These types of nucleon-nucleon correlations are additionally motivated by neutrino experiments [51].

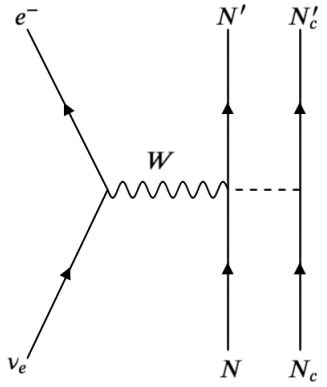

Figure 1.13: A Feynman diagram illustrating a charged-current MEC interaction.

In addition to interactions between correlated nucleon pairs within the nucleus, there is another scattering mechanism that can contribute to neutrino-nucleus interactions. In Meson Exchange Current(MEC) interactions two correlated nucleons are modeled as interacting through the exchange of a meson. When one of the correlated nucleons interacts with a neutrino through the exchange of a W boson both nucleons can be ejected from the nucleus. This interaction mode is illustrated in Figure 1.13. New models used to describe these types of multi-nucleon interactions have been proposed [52][53]. The interactions between neutrinos and correlated nucleon pairs are called two-particle two-hole interactions (2p-2h), while quasi-elastic scattering interactions are referred to as one-particle one-hole (1p-1h) interactions.

Random Phase Approximation (RPA)

The previous section detailed the effects of short-range correlations between nucleons within a nucleus. Although these short-range correlations do have a noticeable effect in the prediction of neutrino scattering experiments, they do not adequately describe heavy-target neutrino scattering data [52][53]. In addition to the short-range correlations discussed previously, these models include a nuclear screening potential known as the random phase approximation (RPA). This model describes the excitation of many-body systems assuming that each excited state is effectively described by linear combinations of 1p-1h and 1h-1p excitations. The collective excitations of each

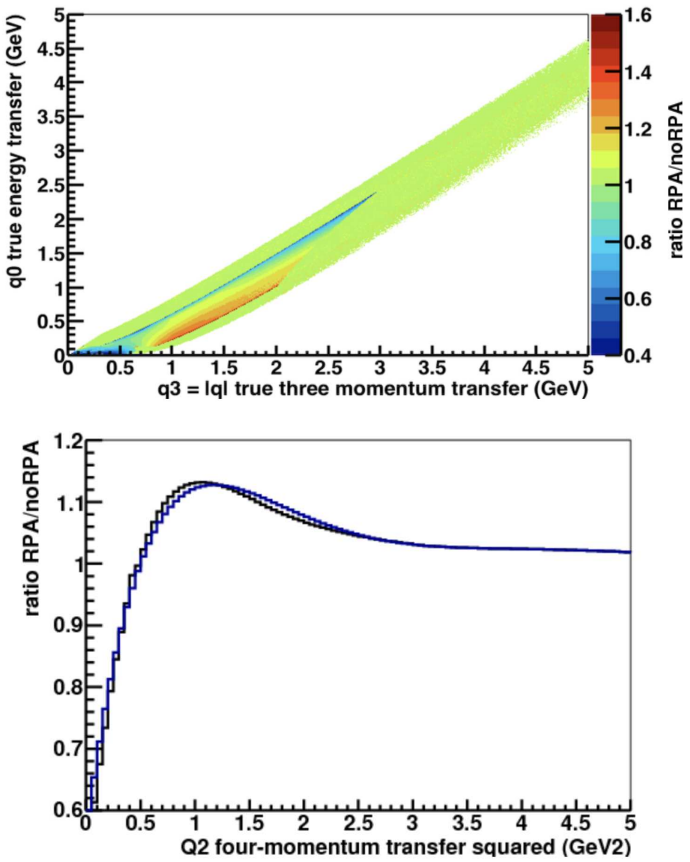

Figure 1.14: The 2D ratio of RPA to no RPA for GENIE neutrino events in (q_0, q_3) (top). The ratio of RPA to no RPA events are binned in true Q^2 (bottom). Figures adapted from [56].

excited state are orthogonal and the phases are treated as "random". These models have been used effectively to describe nuclear excitations in nuclei with more than 10 nucleons over the QE region where the emission of single nucleon processes are dominant [54].

The RPA model also takes into account modifications of the electroweak coupling strength due to the presence of strongly interacting nucleons [55]. As shown in Figure 1.14, RPA corrections vary in strength as a function of four-momentum transfer. At low four-momentum transfer, the effects of the RPA correction is suppressed due to the modification of the electroweak coupling strengths coming from the presence of strongly interacting nucleons within the nuclear potential of the nucleus.

1.5.2 Final-State Effects

As shown in all of the interactions modes described in Section 1.4, neutrino-nucleus interactions can produce a variety of hadronic products including protons, neutrons, and pions. As these interactions take place within the nucleus, the ejected hadrons must escape the nucleus before the particles can be experimentally detected. Before the hadrons can be detected it is possible for them to undergo interactions within the nuclear environment. These re-interactions inside the nucleus can result in the hadronic products being absorbed, having their kinematics altered, or can stimulate additional nuclear emissions (such as additional pions) through the excitation of the nucleus via internal interactions. These hadronic interactions within the nucleus are collectively known as final-state interactions (FSI).

Final-state interaction effects are extremely difficult to model and constrain with current experimental data. Most neutrino interaction simulations make use of a cascade model to account for FSI effects [57]. The cascade model allows for hadrons to interact within the nucleus based on the mean-free path, allowing for multiple interactions as the hadron traverses the nucleus. If additional hadrons are created through one of these re-interactions, they are allowed to re-interact as they traverse the nuclear medium. Each of these steps is repeated until all hadronic particles exit the nucleus or are absorbed. FSI processes in the cascade model are depicted in Figure 1.15.

Experimentally, products of neutrino interactions are detected after FSIs take place. Thus, neutrino interaction measurements utilize specific event topologies within a detector rather than a specific type of interaction (QE, RES, DIS, etc.). An example of this would be an experimental measurement of a charged-current quasi-elastic-like cross section measurement. The final-state of this measurement would consist of a charged lepton and proton being detected within the detector, as would be seen in a typical QE interaction. Such a detected final-state could have been produced by a true QE interaction or by more complicated RES interaction where the pion was re-absorbed within the nucleus.

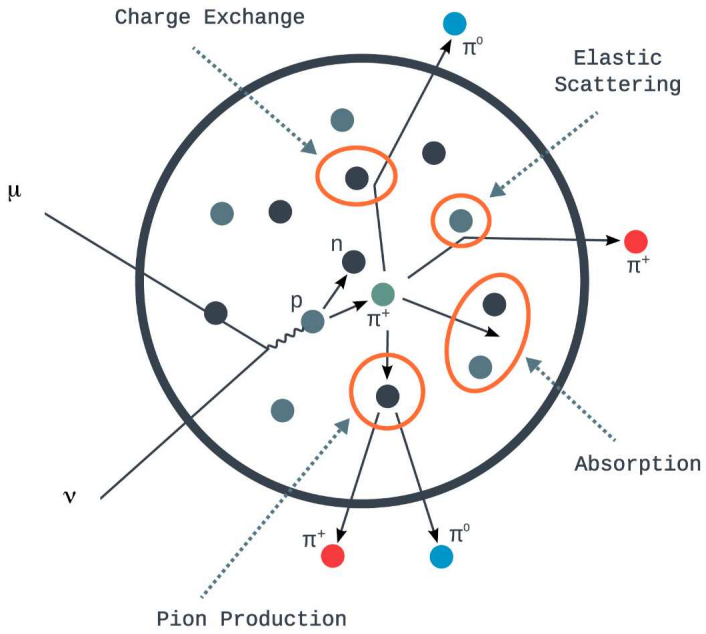

Figure 1.15: A schematic of hadronic showers produced by the neutrino interaction must traverse the nucleus and may undergo final-state Interactions before detection within the detector. The interactions include nucleon-nucleon interactions as well as pion-nucleon interactions as illustrated. Figure taken from [58].

1.6 Electron Neutrino - Nucleus Interaction Cross Section

Although the electron neutrino was the first neutrino to be discovered there have been relatively few measurements of its cross section, or the interaction probability, at the energy scale relevant for long-baseline neutrino oscillation experiments (around 1 GeV). Natural sources of electron neutrinos have fluxes primarily centered around the MeV energy scale from fusion processes in the sun and fission in nuclear reactors. While numerous neutrinos are produced from accelerators, only a small fraction of these are electron neutrinos. This section details the results of electron neutrino cross section measurements at the GeV energy scale.

Theoretical Differences Between ν_e and ν_μ CC Interactions

Numerous muon neutrino charged-current cross sections have been measured using neutrino beams. Select measurements of the total charged-current muon neutrino cross section measure-

ments are shown in Figure 1.6, with the predictions of the various interaction types (QE, Res, DIS) that contribute to the total charged-current cross section.

When neutrinos interact with fundamental particles, like quarks in the interaction $\nu_l + d \rightarrow l^- + u$, there are no expected differences in the reactions for electron or muon neutrinos, as the coupling of leptons to gauge bosons are flavor independent [36]. The effect of the final-state lepton mass on this two-body reaction can be definitively calculated. The major contributors to differences in the ν_e and ν_μ CC interactions are expected to be due to the different masses of the charged leptons and radiative corrections. The charged lepton masses can cause significant differences in the interaction cross section near the kinematic thresholds for charged-current QE interactions. The final-state lepton mass is accounted for in modern neutrino event generators allowing for slight differences in the predictions for ν_e and ν_μ CC event rates.

Radiative corrections from a particle of mass m in an interaction with momentum transfer Q are of order $\frac{\alpha}{\pi} log \frac{Q}{m}$, where α is the fine structure constant, leading to significant changes in interaction cross sections due to the differences in the final-state lepton masses [59]. Radiative corrections are not currently taken into account in neutrino event generators but can distort the scattering kinematics. An approximation of how radiative corrections would effect the cross section was calculated and the differences in ν_e to ν_μ charged current quasi-elastic cross sections are shown in Figure 1.16 [36]. In the figure, Δ is the fractional difference between the ν_μ and ν_e cross sections:

$$\Delta = \frac{\sigma_{\nu_\mu} - \sigma_{\nu_e}}{\sigma_{\nu_\mu}} \tag{1.32}$$

Figure 1.16 shows an estimate of the fractional difference between the electron and muon neutrino total charged-current quasi-elastic cross sections with Δ as defined above, as a function of neutrino energy. The negative difference means that the electron neutrino cross section is larger than the muon neutrino cross section, the effects of this correction are roughly 10% at the energies relevant to neutrino oscillation experiments.

Understanding the differences between the ν_μ and ν_e cross sections will lead to better predictions for oscillation analyses. Improved predictions can help with the determination of δ_{CP} and the

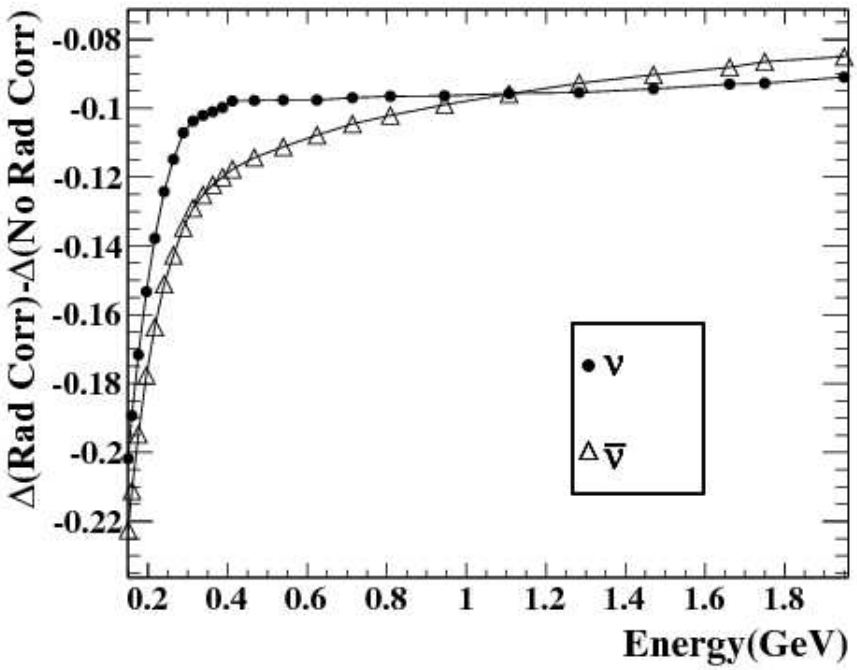

Figure 1.16: Plot of the estimated of the fractional difference between the electron and muon neutrino total charged-current quasi-elastic cross sections due to radiative corrections. Results shown using Δ from Equation 1.32, as a function of neutrino energy. Figure taken from [36].

correct ordering of the neutrino mass states by lowering the uncertainty on neutrino interactions with nuclei. Understanding the weak force through neutrino interaction measurements is of great importance to basic physics by refining our understanding of Standard Model predictions. The only way these differences can continue to be quantified is through continued study of ν_e charged current interactions including at the few GeV energy scale which forms the main study of this thesis.

Existing ν_e Cross Section Measurements

Experiments determine a cross section through a measurement of the rate of a specific type of interactions. This rate is then related back to the interaction probability

The first measurement of the electron neutrino cross section performed at the GeV scale was made using the Gargamelle bubble chamber in 1978 [60]. About 200 ν_e event candidates were

selected with an extracted cross section that was in close agreement with the predicted cross section of ν_μ charged current interactions.

A more recent measurement of the inclusive electron neutrino cross section was made by T2K [61]. The cross section was measured in the ND280 detector which is made of primarily carbon (86%) and hydrogen (7%) with small amounts of heavier elements present. In total, 315 ν_e CC interaction candidates were selected. The T2K analysis was able to produce the first flux-averaged single differential cross section measurements with respect to electron momentum, electron angle, and Q^2. The total flux-averaged cross section was measured as $1.11 \pm 0.20 \times 10^{-38}\text{cm}^2/\text{nucleon}$ at the mean beam neutrino energy of electron neutrinos (approximately 1.2 GeV) with 16% systematic uncertainty. Figure 1.17 shows the full-phase space results of the T2K cross section measurements, where the full phase-space refers to the fact that no kinematic cuts were placed on the electron. The Gargamelle results are superimposed on the plot of the total flux averaged measurement.

The MINERνA collaboration produced the first measurement of the electron neutrino charged-current quasi-elastic-like cross section on hydrocarbon in the few GeV region of neutrino energy [62]. The total number of selected candidate signal events was 2,105 with an exposure of 3.49×10^{20} protons on target (POT)[‡] The results were reported as single differential measurements with respect to electron energy, angle, and Q^2 with systematic uncertainties ranging from 10-15%.

Using the same detector and a similarly selected sample of ν_μ CCQE interactions, a ratio measurement of the ν_μ CCQE to ν_e CCQE differential cross sections with respect to Q^2 was also produced. This result showed good agreement between the measured ratio and that predicted from the GENIE neutrino event generator [63]. The MINERvA measurement has been important in confirming the predictions of neutrino event generators. As more precise measurements of the inclusive ν_e cross section are made, further probes of the differences between the inclusive ν_μ

[‡]Protons on target refers to the number of protons delivered by the accelerator to the neutrino generating target. It is a performance indicator for the amount of data collected by accelerator-based neutrino experiments.

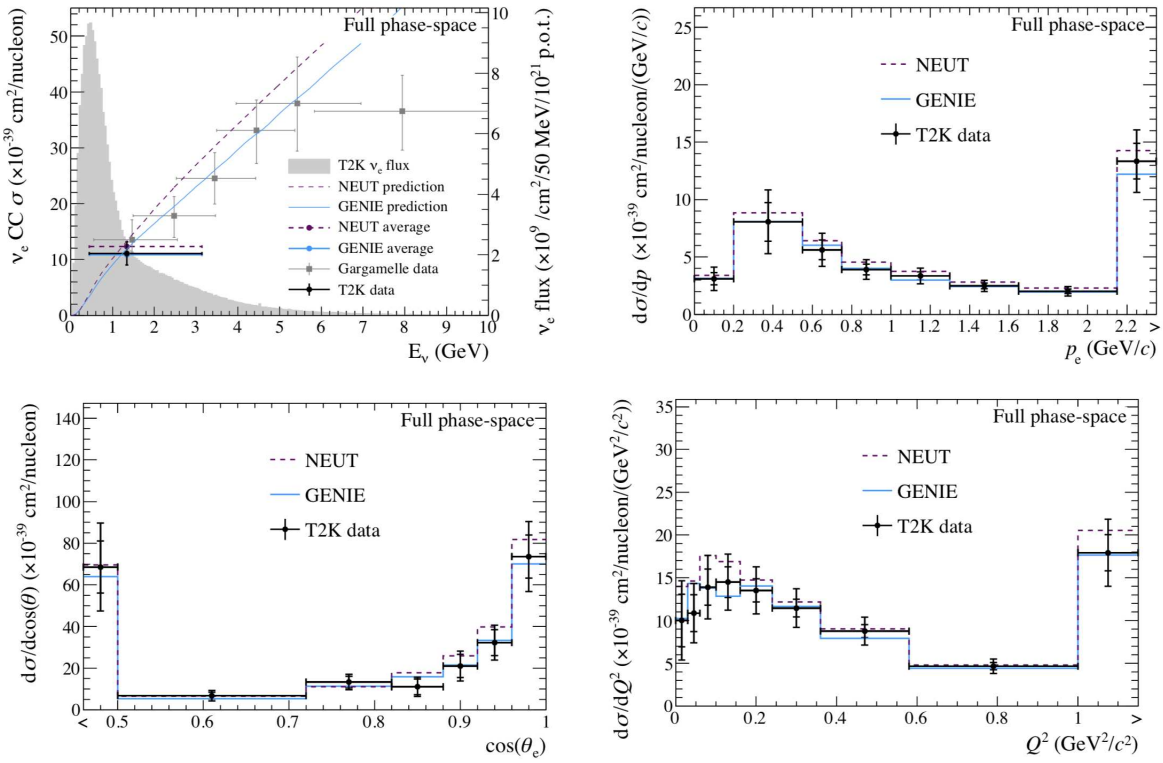

Figure 1.17: Plots of the T2K inclusive ν_e cross section measurements. Total ν_e CC inclusive cross section measurement, with T2K data point placed at the ν_e flux mean energy with the Gargamelle data is overlayed in the top left plot. The remaining plots show the inclusive ν_e single-differential cross section measurements as a function of p_e, $\cos\theta_e$, and Q^2. The figures are taken from [61]

.

and ν_e cross sections can be made and can impact the predictions used for neutrino oscillation measurements. These results are shown in Figure 1.18.

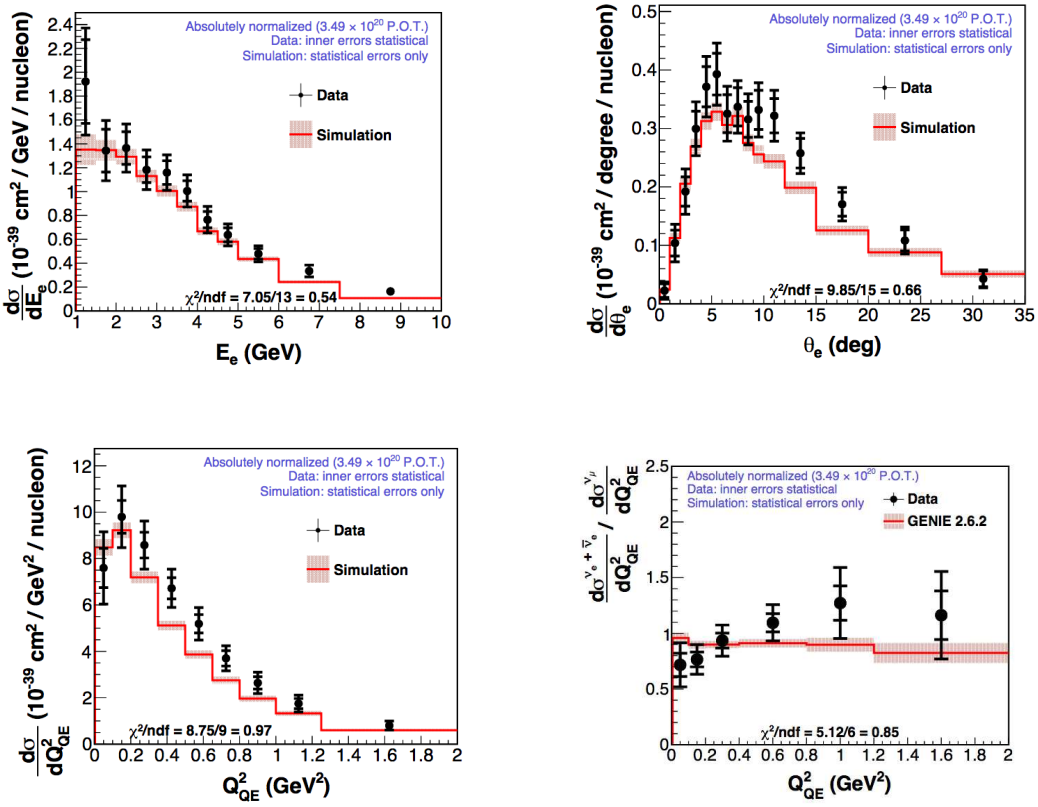

Figure 1.18: Plots of the flux averaged ν_e CCQE single-differential cross section measurements from the MINERvA collaboration. The figures are taken from [62]

.

Chapter 2

The NOvA Experiment

The NuMI Off-axis ν_e Appearance (NOνA) experiment is a long baseline neutrino oscillation experiment designed for the precise measurement of ν_e appearance from a primarily ν_μ beam. The experiment makes use of two functionally equivalent detectors and a high-intensity neutrino source using Fermilab's Neutrinos at the Main Injector (NuMI) beam. The detectors are constructed from PVC cells filled with liquid scintillator and utilize a segmented tracking region to distinguish neutrino interactions from background events. The 300 ton near detector (ND) lies 1 km from the NuMI target and is used to measure the neutrino composition of the beam prior to oscillations and to make neutrino-nucleus cross section measurements. The 14 kiloton far detector (FD) lies 810 km from the NuMI target and measures the neutrino energy and flavor composition of the beam after oscillations have occurred. Both detectors lie 14 mrad off of the beam axis. The NuMI beamline can operate in both a neutrino and antineutrino beam modes allowing for separate measurements of neutrino and antineutrino oscillation probabilities.

This chapter discusses the details of the NOνA experiment including the neutrino beam and the near and far detectors.

2.1 Long Baseline Neutrino Oscillation Experiments

Equation 1.10 demonstrates that the probability of neutrinos having oscillated from their original flavor state is dependent on both the neutrino energy and the distance traveled. Modern long baseline neutrino oscillation experiments exploit this by utilizing a proton accelerator to produce a neutrino beam. The experiments then observe the altered flavor composition of the beam hundreds of kilometers away using a far detector. This allows for the determination of the oscillation parameters using the rate of the detection of the different neutrino flavors. Additionally, these experiments make use of a near detector, to constrain the properties of the neutrino beam prior to any

Figure 2.1: An illustration of a typical long baseline neutrino oscillation experiment.

flavor oscillations. Each of these components are illustrated in Figure 2.1. The following sections discuss the neutrino beam, near detector and far detectors that comprise the NOνA experiment.

2.2 Fermilab Accelerator Complex

Fermilab's accelerator complex is comprised of several particle beams for use by high energy physics experiments. A diagram of the complex is shown in Figure 2.2. The proton beam begins as hydrogen atoms at the ion source. After the electron is removed from the atom, the remaining proton is accelerated to 0.4 GeV in the Linear Accelerator (LINAC). The protons are then fed into the Booster ring. Here the protons are accelerated up to 8 GeV until protons are removed from the Booster and sent into the Recycler. The Recycler combines the protons into batches to form a more intense beam, where intensity refers to large values of protons/cm^{2}s. From the Recycler batches of protons are sent to the Main Injector (MI) synchrotron accelerator. In the 3.3 km ring, the protons are accelerated to 120 GeV. From here the proton batches are extracted and directed onto the targets used to produce the beams for high energy neutrino experiments.

2.3 NuMI Beam

The neutrino source of the NOνA experiment is the NuMI beam [65]. The major beam components, including the target, magnetic horns, decay pipe, hadron monitor, absorber, and the muon monitors, are shown in Figure 2.3. The 120-GeV protons are directed onto a graphite target during a beam spill. Each beam spill is 10 μs in length with a typical interval of 1.3 seconds between

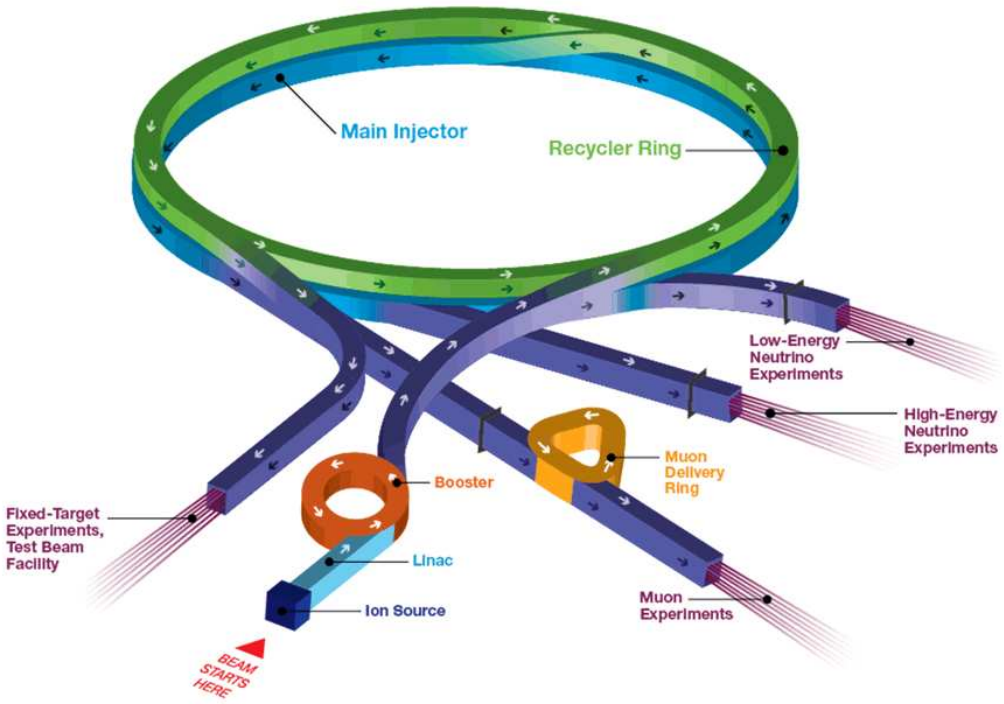

Figure 2.2: A diagram of the Fermilab Accelerator Complex, taken from [64].

each spill. The beam spill is further divided into several bunches, as shown in Figure 2.4. The segmented nature of the beam allows for the isolation of neutrino interactions in time, which is useful in the elimination of cosmogenic backgrounds within the detectors but also introduces the pile-up, or multiple interactions occurring at nearly the same time, as seen within the near detector.

Each beam spill involves approximately 4.8×10^{13} protons interacting with the graphite target resulting in the production of charged mesons that are focused into a beam by magnetic horns. The magnetic horns select the charge of the mesons that are focused into the beam based on the sign of the current used to generate the magnetic field. This allows the creation of a primarily neutrino or antineutrino beam. The beam of focused charged mesons enter a 675 m helium-filled decay pipe, where the mesons decay into charged leptons and neutrinos. Following the decay pipe, the beamline consists of the hadron monitor, absorber, muon monitors and approximately 240 m of rock. The remaining hadrons and muons are absorbed by the absorber and rock, respectively, leaving only a beam of neutrinos. The neutrinos then are detected in various neutrino experiments.

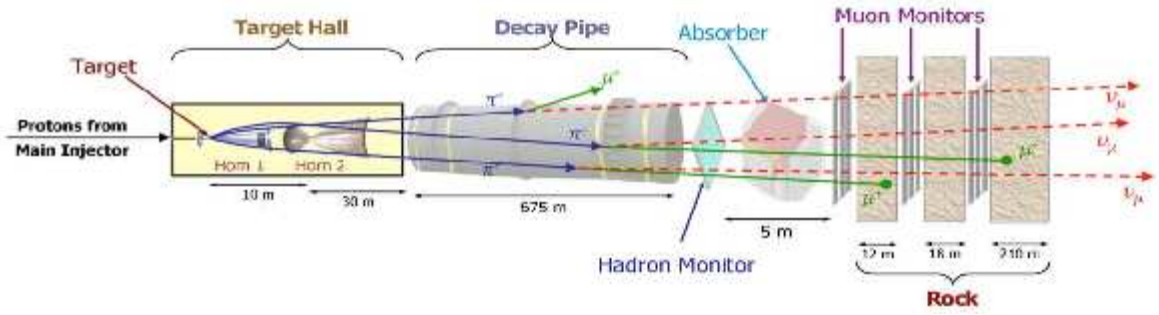

Figure 2.3: A diagram of the NuMI beamline, taken from [65].

The charged mesons, primarily pions and kaons, decay to neutrinos via :

$$\pi^+ \rightarrow \mu^+ + \nu_\mu \tag{2.1}$$

$$K^+ \rightarrow \mu^+ + \nu_\mu \tag{2.2}$$

The neutrino beam flux at the NOνA near detector is shown in Figure 2.5. Although the neutrino beam is primarily made of muon-type neutrinos, there is a small amount of antineutrino contamination due to inefficiency in magnetic focusing leading to some of the oppositely charged mesons remaining. There is also a small amount of electron neutrino and antineutrino production through other decay channels like:

$$\mu^+ \rightarrow e^+ + \nu_e + \overset{(-)}{\nu}_\mu \tag{2.3}$$

$$K^+ \rightarrow \pi^0 + e^+ + \nu_e \tag{2.4}$$

2.3.1 Off-Axis Experimental Approach

The NOνA detectors are located off-axis by 14 mrad from the NuMI beam. This approach is used to exploit the kinematics of two-body pion decay which is used to produce a majority of

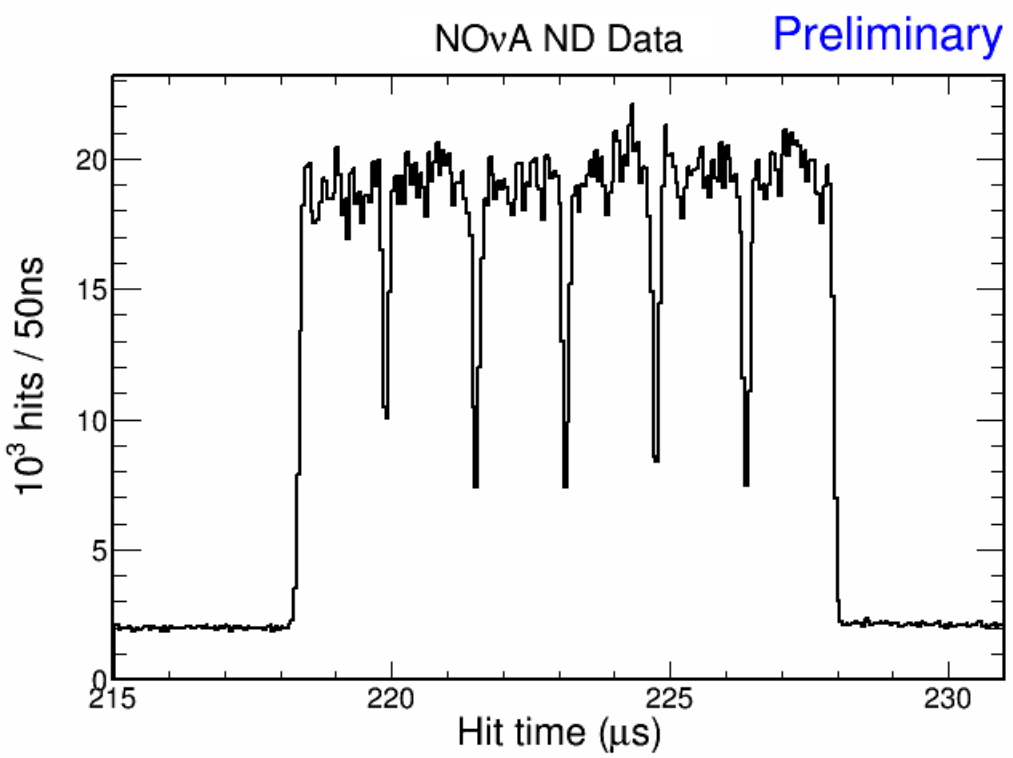

Figure 2.4: The times of all hits in the NuMI beam spill from the Near Detector. Timing resolution within the near detector shows the timing structure of the beam.

the neutrinos in the beam. In the center of mass frame, a two-body decay occurs as an isotropic process. In the lab frame, the parent particle is not at rest, resulting in the neutrinos being boosted in the direction of the parent particle. For small angles, the flux of neutrinos from pion decay and their energy is given by:

$$\Phi = \left(\frac{2\gamma}{1+\gamma^2\theta^2}\right)^2 \frac{A}{4\pi L^2} \tag{2.5}$$

$$E_\nu = \frac{0.43 E_\pi}{1+\gamma^2\theta^2} \tag{2.6}$$

where Φ is the neutrino flux, E_ν is the neutrino energy, $\gamma = E_\pi/m_\pi$, A is the cross sectional area of the detector, L is the distance to the detector from the neutrino source, and θ is the angle between the muon and the neutrino direction.

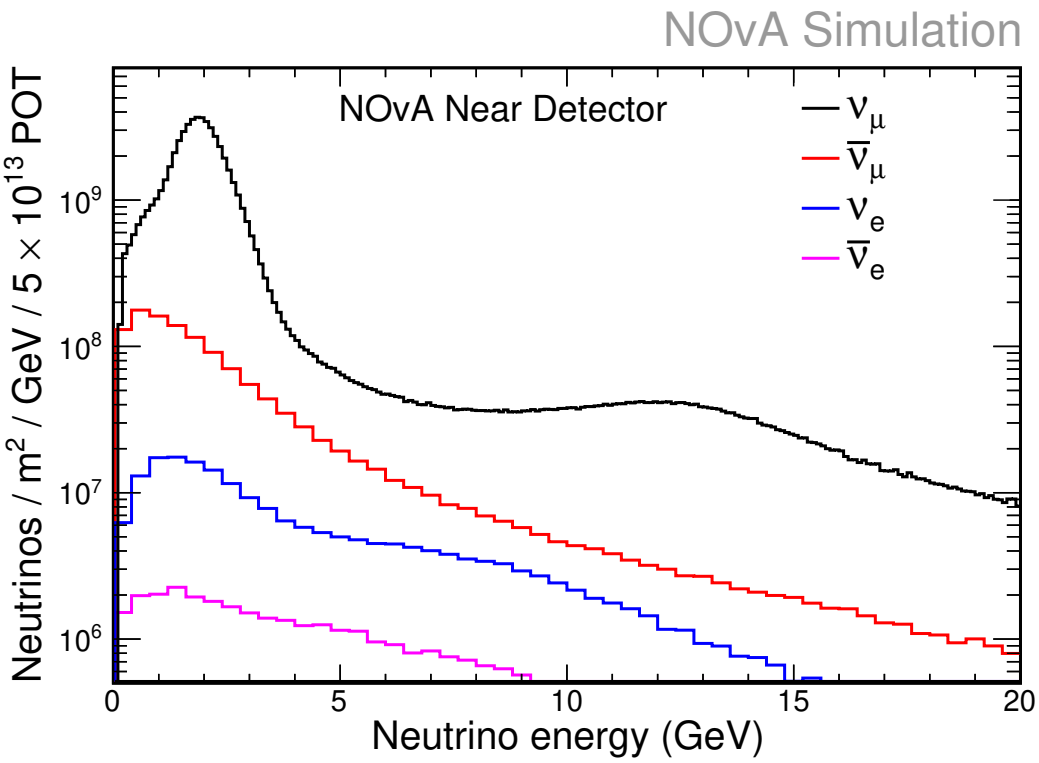

Figure 2.5: Plot of the neutrino components of the NuMI beam at the NOνA near detector.

Equations 2.5 and 2.6 are plotted in Figure 2.6. The figure shows that for a neutrino produced 14 mrad from the parent particle direction, the neutrino energy is not strongly dependent on the energy of the parent pion. Figure 2.7 shows the predicted ν_μ charged-current event rates for a detector that is 800 km from the NuMI target at various off-axis angles. At 14 mrad, the event rate at 2 GeV is about five times higher than an on-axis experiment at the same distance. The peak at 2 GeV is situated near the first oscillation maximum for NOνA's baseline, resulting in higher statistic measurements of neutrino oscillation parameters. Additionally, the narrow energy range of the off-axis beam reduces background events. Neutral current, NC, events are an important background for oscillation measurements which increase at higher energies. For NC events, the neutrino carries a significant amount of the energy away leading to visible energy within the detector being reconstructed at lower energy. This tends to shift NC backgrounds from the oscillation narrow-band peak to lower reconstructed energies, which is away from the energy of the charged-current interactions used to measure neutrino oscillations.

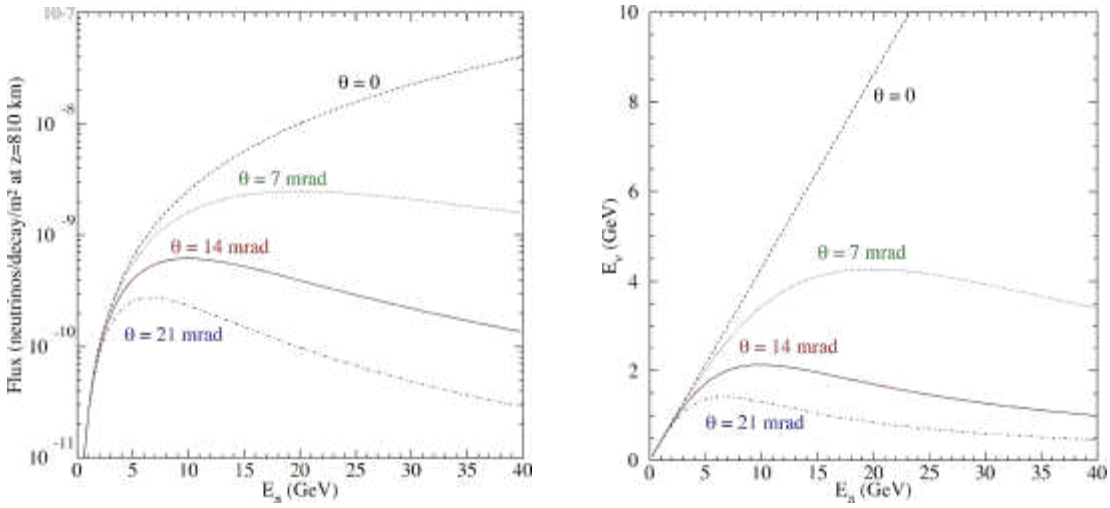

Figure 2.6: Left: The neutrino flux from a pion of energy E_π viewed from a site that is an angle θ from the main beam axis. Right: The energy of neutrinos produced at an angle θ relative to the pion direction as a function of pion energy. Figures taken from [66].

2.4 The NOvA Detectors

The two NOνA detectors are the ND and the FD which lie 1 km and 810 km from the beam source, respectively. The ND lies 105 meters underground on the Fermilab campus. The FD is located on the surface and is shielded by a 6-inch layer of barite overburden to absorb some cosmic ray particles from the atmosphere and the photon background from cosmic showers.

The NOνA detectors are made from low Z materials (mostly carbon) to aid in the discrimination between neutrino interactions and backgrounds within the detector. The detectors have a 40 cm radiation length* and a Moliere radius† of about 7 cm [67] [68]. This design allows for electromagnetic showers to be distinguished from particle tracks within the detector.

Drawings of the two detectors are shown in Figure 2.8. Despite the functional equivalence of the two detectors, there are a few characteristic differences between the two detectors based on the differences in location of each of the detectors. The ND utilizes a muon catcher to increase the

*The radiation length is a characteristic of a material, related to the energy loss of high energy particles electromagnetically interacting with it. It is the mean distance over which a high-energy electron loses all but $1/e$ of its energy by bremsstrahlung.

†The Molier radius is a characteristic of a material, related to the transverse dimension of electromagnetic showers, by definition it is the radius of a cylinder containing 90% of the shower's energy deposition.

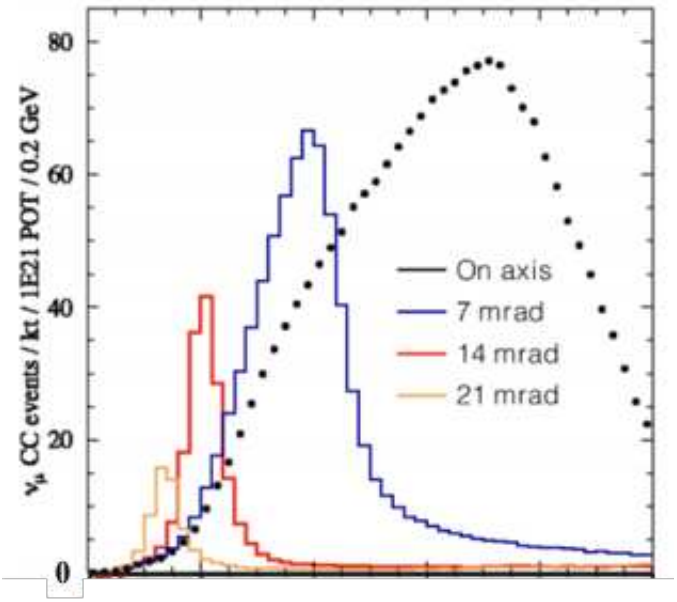

Figure 2.7: Charged current ν_μ event rates vs. neutrino energy with no oscillations. The distributions are shown for a detector which is 800 km from the NuMI target and for various off-axis angles. Figure taken from [66].

stopping power of the ND and to allow for the better detection of muon-type neutrino interactions. Due to the much higher event rates, the ND has a higher readout sampling rate. As illustrated in Figure 2.8, the FD is much larger than the ND. This design is used to increase the neutrino interaction rate at the increased distance from the neutrino source.

2.4.1 Fundamental Detector Components

The entire NOνA design is based upon a simple rectangular PVC plastic extrusion that contains liquid scintillator and a wavelength-shifting fiber. This basic design element is illustrated in Figure 2.9.

The PVC cells are made of a highly reflective titanium dioxide coated PVC with 5.0 mm thick walls. The width of the cell parallel to the beam direction is 5.9 cm, while the transverse width is 3.8 cm. The length of the cells differs between the far and near detector where they measure 15.5 m and 3.6 m, respectively. Charged particles traversing a cell produce scintillation light in the liquid. The light reflects in the rectangular cell until it is captured by the wavelength-shifting fiber

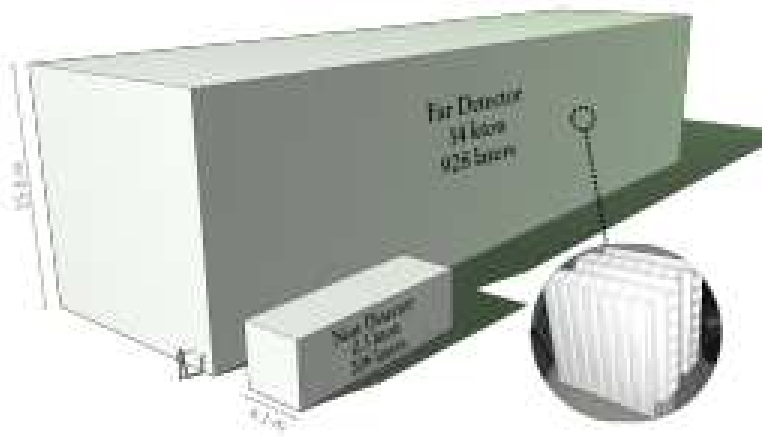

Figure 2.8: The relative sizes of the NOνA Far and Near Detectors. The inset shows the structure of the NOνA detector layers. Figure taken from [69].

or is absorbed by the PVC or liquid scintillator. The wavelength shifting fiber is twice the length of the cell and is looped at the bottom. This allows captured light to move in two directions to the end of the fiber (at the top of the illustration) towards the instrumented end of the cell. Each end of the fiber is directed to a single pixel of an Avalanche Photodiode (APD) photodetector array, where the captured light is converted to an electronic signal. The ND contains 20,192 such cells, and the FD contains 344,064 cells.

Liquid Scintillator

Liquid scintillator accounts for approximately 60 percent (31 tons) of the NOνA near detector mass. The composition of the liquid scintillator is detailed in Table 2.1. The primary constituent of the liquid scintillator is mineral oil with 4.1 % pseudocumene [1,2,4-Trimethlybenzene] as the scintillant. Pseudocumene produces light with a spectrum peaked at 360 - 390 nanometers (nm). The liquid also contains additional chemicals to shift the initial scintillation light to the 400 - 450 nm necessary for the wavelength-shifting fiber absorption spectrum. The additional wavelength shifting chemicals are PPO [2,5-diphenyloxazole] and bis-MSB [1,4-di(methylstyryl)benzene]. The attenuation length of the liquid scintillator is measured to be greater than 20 m, but light is typically capture within 1 m in a NOνA cell.

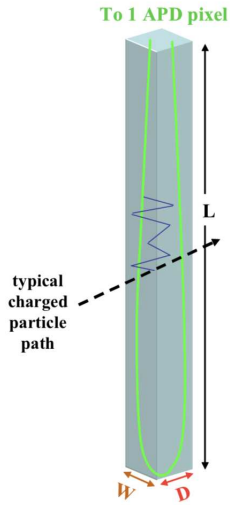

Figure 2.9: A NOvA cell consisting of an extruded PVC tube filled with liquid scintillator and a looped wavelength-shifting fiber. Figure taken from [66].

Table 2.1: The composition of NOνA Liquid Scintillator. Table adapted from [66].

Component	Purpose	Mass Fraction
Mineral Oil	Solvent	95.8%
Pseudocumene	Scintillant	4.1%
PPO	Waveshifter	0.091%
bis-MSB	Waveshifter	0.0013%
Stadis-425	Antistatic agent	0.0003%
tocopherol (Vit.E)	Antioxidant	0.0010%

Wave-length Shifting Fiber

The fiber in each cell captures the 400 - 450 nm (blue) and wavelength shifts to a green light in the range of 490 - 550 nm. The fiber is 0.7 mm in diameter with a core of polystyrene mixed with R27 dye which acts as the wave-shifter. The polystyrene core only contains R27 at a concentration of about 300 parts per million. The coatings are a thin acrylic layer of polymethylmethacrylate (PMMA) and fluoracrylic, with both coatings accounting for about 3% of the fiber diameter. The internally reflected light is attenuated by about a factor of ten along the entire length of the fiber. Green light (520 - 550 nm) preferentially survives this process.

Figure 2.10: Photograph of a NOνA APD pixel array. Figure taken from [70].

Avalanche Photo Diode

The NOνA photodetector is an Avalanche Photodiode (APD) that detects light exiting the end of the wavelength shifting fiber and converts it to an electronic signal pulse. The APD has an 85% quantum efficiency for the 520 - 550 nm light exiting the fiber. Thermal noise produced in the APD is reduced by cooling the APD using a thermo-electric cooler to a temperature of -15°celcius. A water cooling system is used to remove the heat from the thermoelectric coolers.

Figure 2.10 shows a photograph of a NOvA APD array of 32 pixels. Each APD pixel is connected to both ends of a single wavelength-shifting fiber. The signal from the APD is read, shaped, and digitized by a Front End Board (FEB). This process uses multiple correlated sampling to reduce the noise level and increase the timing resolution of the detector.

Detector Geometry

The NOνA detectors are made up of collections of many different cells. 16 cells are extruded together in a single unit to form an extrusion. An extrusion module consists of two extrusions placed side by side to form a 32 cell unit, along with an end plate, side seal, manifold cover, snout and electronics bow. The end-plate caps the module ends to seal the detector. The manifold cover

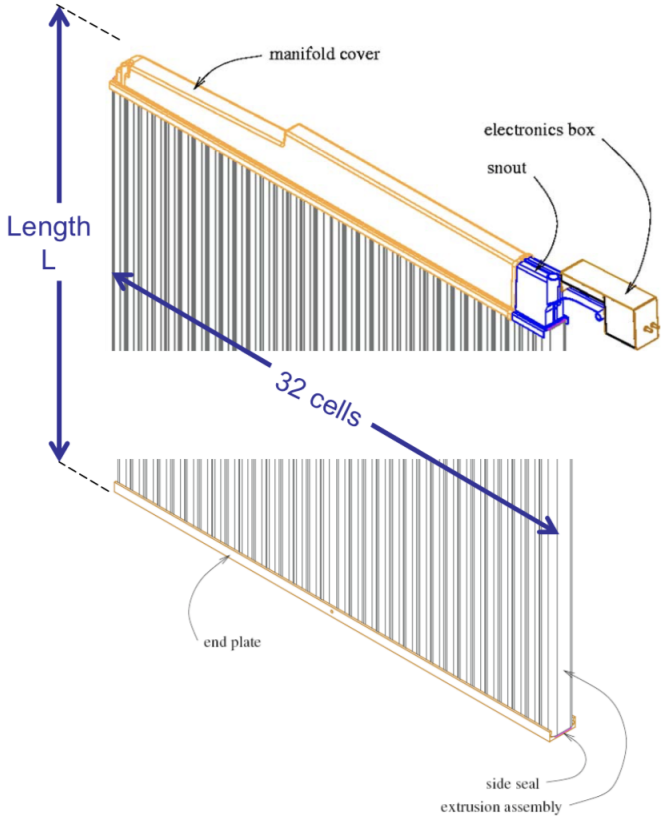

Figure 2.11: Schematic of an extrusion module, constructed from two extrusions, an end plate, manifold cover, snout, and electronics box. Figure taken from [66].

caps the other end of the extrusion module and is used to direct the 32 fiber end pairs from each of the cells to the APD pixels. Figure 2.11 depicts an extrusion module.

Multiple extrusion models are installed side-by-side to form a plane. Figure 2.12 shows a cross section of multiple plane layers. The planes are layered together in an alternating pattern using orthogonal orientations of the cells that make up an individual plane. If tracks pass through multiple planes, this pattern allows for the reconstruction of particle tracks in three dimensions. The planes are glued together in this alternating arrangement to form a single detector piece called a block. A block consists of 32 (24) planes in the far (near) detector.

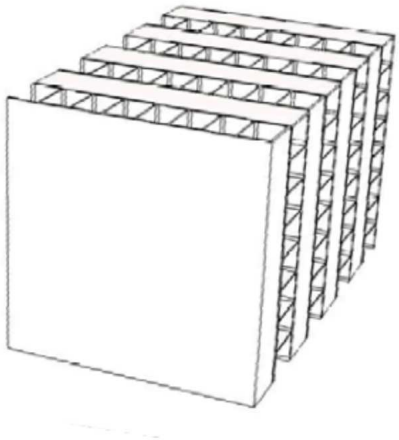

Figure 2.12: A cross-sectional view of the NOνA detector showing the alternating orientation of the planes of cells. Figure taken from [66].

2.4.2 Far Detector

The far detector is located 810 km from the NuMI target, approximately 10 m below ground level, at an elevation of 372 m above sea-level in Ash River, Minnesota. The detector is constructed from 896 planes perpendicular to the neutrino beam direction. Figure 2.13 shows a photograph of the completed NOνA far detector. The top and sides of the detector are outfitted with all electronics described previously for the readout of the entire detector.

The 14 kiloton detector consists of approximately 65% liquid scintillator and 35% PVC by mass. The detector is built on the surface so cosmic rays are a major source of background events. The far detector building includes a 122 cm thick concrete enclosure and a 15 cm thick overburden of barite on top of the enclosure. These provide 12 radiation lengths of shielding to the detector to eliminate photons coming from cosmic ray interactions above the detector.

2.4.3 Near Detector

The 290 ton NOνA near detector (shown in Figure 2.14) is located on the Fermilab campus, 1.05 km from the NuMI target, and approximately 105 m below the surface, thus the near detector sees a higher flux of NuMI neutrino events and a lower flux of cosmic rays than the far detector.

Figure 2.13: A photograph of the NOνA far detector. The far detector height and width are 15.6 m long. The detector is 63.0 m long. The beam direction is away from the camera in this photo.

The neutrino beam enters the detector at a downward angle of 3° and like the far detector, it is situated 14.5 mrad off of the NuMI beam axis.

The near detector is functionally equivalent to the far detector except in the scale of the extrusion modules, corresponding to the space limitations of and cost of expanding the NuMI underground area. The ND is made up of 20,192 cells arranged into 214 planes. The detector is 4.2 m in width and height and has a length of 15.8 m. In order to enhance the physics capabilities of the detector, a muon catcher is placed at the downstream end of the near detector to help range out, or stop, muons. Muons generated from the few GeV charged current ν_μ interactions of interest for neutrino oscillation experiments would not typically stop within the detector. The muon catcher is constructed from layers of steel and liquid scintillator planes. The steel planes are 10 cm thick and are separated by two scintillator planes, one in each of the two orthogonal positions. The vertically aligned planes consist of three extrusion modules while the horizontal planes are made from two extrusion modules. The muon catcher is therefore as wide as the rest of the detector but not as tall.

Figure 2.14: A photograph of the NOνA near detector, in the NuMI underground campus at Fermilab. The beam propagates away from the camera in this photo.

The muon catcher is shown in Figure 2.15. The difference in height between the muon catcher and the main active region of the detector can clearly be seen. In total, the muon catcher is made up of ten steel and 20 liquid scintillator planes.

Due to the location of the near detector in relation to the neutrino source, the ND lies in a high event rate location. To deal with the high rate of interactions within the detector the near detector electronics are set to sample each channel about four times more frequently than in the far detector, or every 125 ns. This allows for better handling of data pileup, or the number of interactions occurring within the detector in a specific time window. During a typical beam spill (10 μs in length) the near detector sees about 5 neutrino interactions as shown in Figure 2.16. The figure shows the activity from several charged particles colored by the time of each hit within the detector readout window. The time window shown corresponds to a single NuMI beam spill. The faster sampling rate of the ND improves the timing resolution of the hits within the detector, allowing for the separation of distinct interactions within the detector.

Figure 2.15: A photograph of the muon catcher seated at the downstream end of the NOνA near detector. The beam is directed toward the camera in this photo.

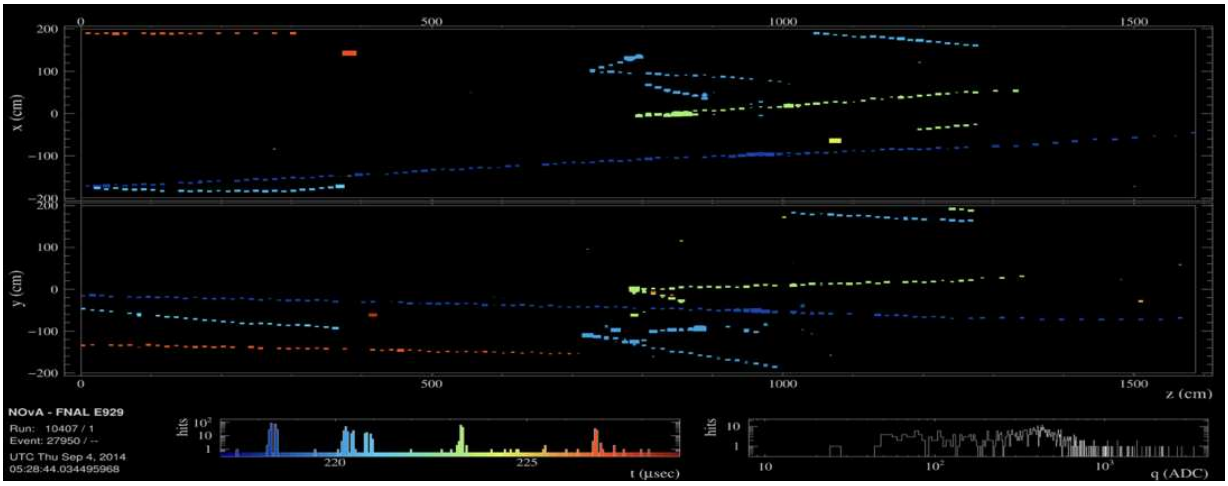

Figure 2.16: NOνA event display showing a typical the typical detector activity during a NuMI beam spill. The event display shows the XZ view of the detector in the top pane. The YZ view is shown in the bottom pane. All hits within the detector are colored by time of the hit within the detector readout window.

2.4.4 Data Acquisition System

Data are continuously read out during every beam spill. The data acquisition (DAQ) system allows for the aggregation and processing of all data taken continuously by the detector. A single FEB reads out the data from 32 cells of the detector (one for each pixel of an APD). The signals from up to 64 FEBs are sent to a data concentrator module (DCM) corresponding to a localized geographic region of the detector.

The DCM time orders the input data streams into 50-microsecond time intervals. These time windows are referred to as "microslices". A series of microslices are then organized into a "millislice", which corresponds to 5 milliseconds of data. Every DCM sends a millislice corresponding to a particular window of time to a circular buffer. The circular buffer consists of a farm of machines with the capability to store approximately 20 minutes worth of data. While the data are stored within the buffer nodes, the DAQ waits for a trigger to determine if a certain window of time should be recorded. Figure 2.17 shows each of the individual elements of the detector readout and DAQ systems and how the data progress from the detector through the DAQ system to the writing of the data to disk.

There are three trigger types, clock triggers, signal triggers, and data-driven triggers (DDT). Clock triggers are triggers that occur at specific time intervals, an example of this would be the calibration pulser that writes out activity within the detector ten times each second. Signal triggers occur whenever an external source triggers the DAQ to write out a certain window of time. These types of triggers include beam triggers, which cause the DAQ to write out any data associated with the arrival of neutrinos from a beam spill at either of the detectors. The final type of trigger is called a Data-Driven Trigger (DDT). This type of trigger signals the presence of specific event topologies and will be discussed in more detail in Section 2.4.5.

2.4.5 Data Driven Trigger

One of the unique features of the NOνA readout is that is operates in a trigger-less readout mode, meaning all detector data is transmitted to and actively buffered in an online computing

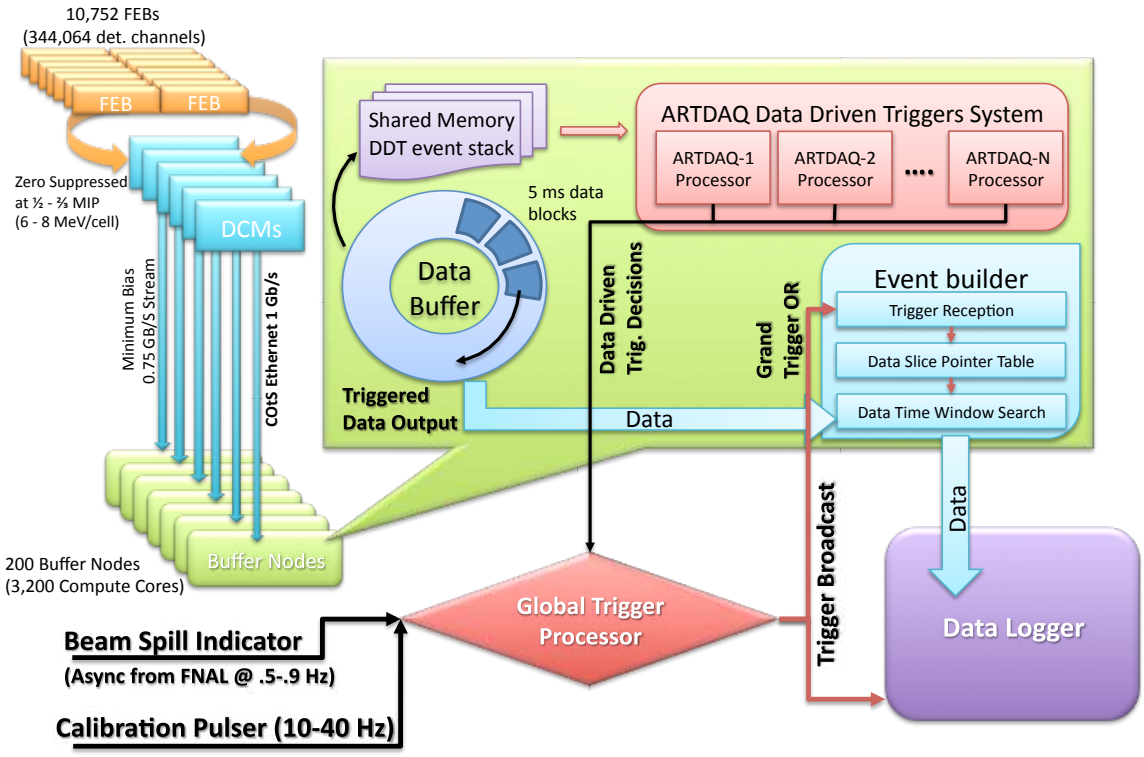

Figure 2.17: Schematic of the NOνA DAQ system. Figure taken from [71].

farm prior to any data being recorded. The NuMI beam spill occurs once every second with a spill length of 10 μs. The amount of data that are recorded for the neutrino oscillation measurements represents only a fraction of the amount of data that is read out and buffered by the DAQ system. Therefore, the detector is basically "idle" for more than 99% of the time. Although the beam associated data contains all of the information necessary to perform the core oscillation analyses, it is too small to be used for performing many types of detector calibration or for physics searches outside of beam-related measurements. To obtain additional samples of the detector readout, the DDT analyzes all of the buffered raw data looking for events that can be utilized at a later time.

The depth of the buffers currently allows for twenty minutes of raw data to be held before a decision to record the data must be issued. This allows the DDT system to make use of the same (or similar) reconstruction algorithms used to process NOνA data during physics analyses. Any time a specific condition, such as a particular event topology, is met the DDT system issues a trigger causing the DAQ system to record data associated with the corresponding time window.

The DDT provides the opportunity to examine non-beam data for interesting physics. The DDT greatly enhances the physics capabilities of the NOνA experiment. The current trigger suite includes a number of triggers ranging from supernova and magnetic monopole searches to calibration triggers identifying electrons from cosmic muon decays in the far detector.

Chapter 3

NOvA Software

This chapter provides an overview of the analyses methods used by the NOνA collaboration. A simple overview of this procedure is shown in Figure 3.1. Each analysis begins with the simulation of each aspect of the experiment, from the neutrino beam to the response of the detector to the charged particles produced following a neutrino interaction. The neutrino interactions from simulation and real detector data are then reconstructed using the same algorithms. It is from this point that a blind analysis is developed. Each analysis is developed using only simulated events in order to reduce or eliminate the biasing of the measured answer in a particular direction. Only after the developed analysis has been thoroughly tested is real detector data used to perform the measurement. This chapter discusses the simulation, event reconstruction, and detector calibration techniques used within the NOνA experiment.

3.1 Simulation

The NOνA experiment uses a series of simulated processes from several Monte Carlo (MC)-based packages. The stages of the simulation are the creation of neutrinos in the NuMI beamline, the neutrino interactions within the detector, the propagation of final-state particles through the detector geometry, and the response of the detector to these particles.

3.1.1 Neutrino Beam Flux Simulation

The predicted neutrino flux from the NuMI beam is simulated using a package called G4NuMI [72]. This package combines the output of two MC-based packages FLUKA [73], which describes the interactions of all particles generated from the 120 GeV proton interactions on the NuMI target, and Geant4 [74], which is used to simulate the geometry of the beamline.

The simulation of resultant hadrons continues through the eventual decay of the hadrons into neutrinos and other particles that are eventually stopped within the beamline or the down-stream

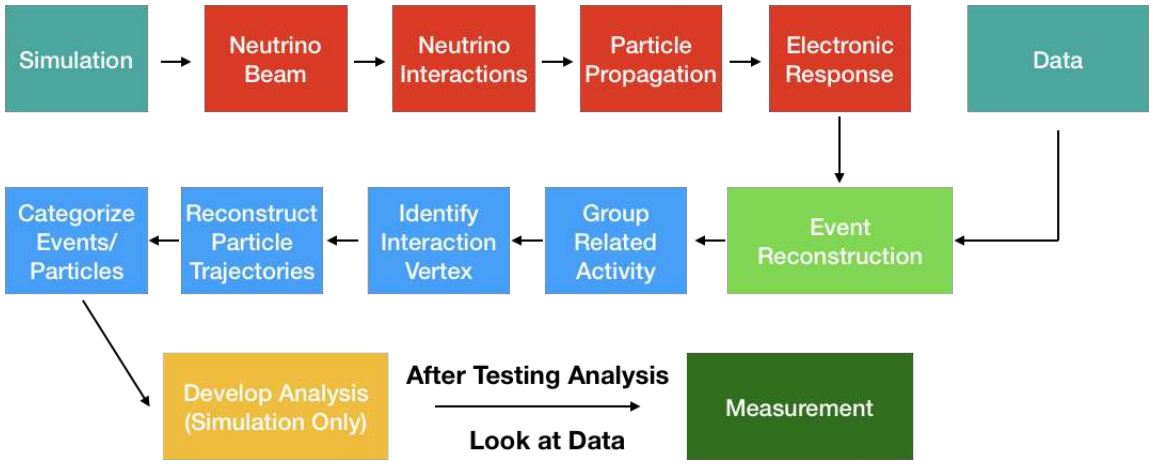

Figure 3.1: Illustration of the simulation and reconstruction chain used within the NOνA experiment.

absorbers. The neutrinos are saved for further use in the simulation by storing the neutrino flavor, direction, decay point, momentum, and energy for each neutrino. Additionally, the hadron parent information is also stored to allow for additional event re-weighting based on hadronic model studies.

3.1.2 Neutrino Interactions

The simulated beam neutrino interactions within the NOνA detectors are modeled by GENIE version 2.12.2 [63]. GENIE simulates interactions in the detector using the neutrino energy as simulated in the previous step and models used for the neutrino-nucleon interactions as detailed in Section 1.4. The output of the GENIE code is a list of the final-state particles of the neutrino-nucleus interaction in the detector with the kinematics of each of the final-state particles. The GENIE software also provides methods to determine systematic uncertainties for various parameters, like the axial mass in the dipole form factor used in the Llewellyn-Smith formalism of QE scattering [34], used in the cross section models.

In addition to neutrino interactions within the detector, GENIE is also used to simulate interactions that occur in the rock upstream of the detector. The final-state particles of these interactions can interact in the detector material at the same time as neutrino interactions. Rock interactions

are simulated independently from the detector interactions and are overlaid * on the detector interactions due to the complexity of simulating the interactions. Due to the computational limitations of simulating rock interactions, the event samples are smaller in number and are overlaid on top of detector events so that the total number of interactions in the detector is consistent with what is predicted during data taking.

3.1.3 Simulation of Particle Propagation Through Detector

The output of the GENIE simulation is both the final-state particles and their corresponding 4-momenta for each neutrino interaction within the detector. Using the 4-momenta and particle identity Geant4 is used to simulate the propagation and energy deposition of each particle. From each of these primary particles, secondary particles can be created and are also simulated.

In addition to Geant4, NOνA uses specific software modules to simulate the response of the detectors to energy depositions. One such module simulates the process of energy depositions within the cell being converted to photons arriving at the APD. The APD signal is simulated as a combination of both the signal photons and the model of APDs response to noise. Another software package simulates the response of the front end board (FEB) to the APD signals. This package includes the simulation of the electronic pulse produced by the APD in response to the photons, incident on the APD pixels.

3.1.4 Tuning of the Simulation

To account for recent experimental results that suggest the existence of additional processes, the standard NOνA simulation is tuned to these measurements in order to improve the agreement between external measurements and the ND data. The quasielastic dipole form factor, M_A, is set to 1.04 GeV/c^2 [75], rather than 0.99 GeV/c^2 used within the nominal simulation. Further corrections to the charged-current quasielastic cross section derived from the random phase ap-

*Overlaying is the procedure where specific features that are time consuming to generate are placed "on-top" of the nominal detector simulation. In the far detector, samples of comsic particles are obtained during non-beam time windows. This non-beam data is then placed into the same time window as a simulated neutrino interaction to mimic true data-taking conditions within the simulation.

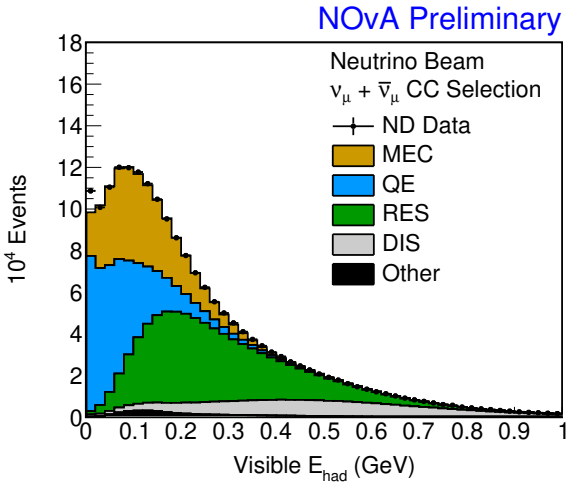

Figure 3.2: Visible hadronic energy distribution of ν_μ CC selected ND data and MC simulation after the cross section tuning procedure.

proximation (RPA) are also applied [54] [55]. Currently, calculations for the RPA effect only exist for quasielastic scattering. However, is is believed that the same (or a similar) phenomenon may also influence other interaction channels at low momentum transfer [76–78]. At the neutrino energies seen in NOνA this would primarily effect pion production through resonances. A correction based on this theory is applied to the RES model used in NOνA.

Several corrections to the simulation are also obtained from comparing NOνA ND data samples to the nominal GENIE simulation. The data shows an excess rate of short track-length ν_μ CC events. This is accounted for by increasing the rate of deep-inelastic scattering interactions with a hadronic mass $W > 1.7\text{GeV}/c^2$ by 10%. The largest modification to the central value prediction comes from the tuning of the Dytman empirical MEC model used in GENIE v2.12.2. The tuning is done using a fit in q^0-q^3 space, which results in weights of MEC that achieve better agreement with the ND data. A plot showing the data-MC agreement of visible hadronic energy after the full tuning procedure is shown in Figure 3.2. While each of these tuning procedures were done using selected ν_μ CC interactions, the tuned values are also applied to ν_e CC interactions within the NOνA simulation.

3.2 Reconstruction of Interactions in the NOνA ND

The NOνA detectors are essentially sampling, or tracking, calorimeters with a segmented structure designed to provide information to distinguish between different particle track and shower topologies. The reconstruction of neutrino events relies on the ability to identify the different types of particle necessary to identify the type of neutrino interaction and reconstruct the unknown energy of the neutrino.

Figure 3.3 illustrates three types of neutrino interactions commonly measured within the NOνA detectors. The shown interactions are simulated interactions with a simulated neutrino energy of 2 GeV. The top pane shows a charged current ν_μ interaction, which is typically identified through the presence of a long, straight, minimally ionizing[†] muon track within the the detector. The middle pane shows a charged current ν_e interaction. The reconstruction and identification of the electromagnetic shower induced by the electron is vital to the identification of this type of neutrino interaction. The bottom pane shows a neutral current interaction. These interactions lack a charged lepton in the final-state but can contain a variety of non-leptonic activity like the photons from π^0 decay shown here, which can mimic ν_e events.

3.2.1 Neutrino Interaction Selection

Interactions resulting from NuMI beam spills are recorded as a set of hits within the detector occurring within a 550 μs readout window. Neutrino-induced interactions within the detector take place within a shorter time frame than the detector readout window. Only charge depositions within detector cells, or hits, above a minimum threshold energy are recorded in each readout window. The collection of hits are clustered, into sets of contiguous hits, using spatial and timing information. These reconstructed objects are called slices [79] [80].

Figures 3.4 and 3.5 show the results of the slicing procedure in both the far and near detectors. Figure 3.4 shows a typical NOνA event display for a cosmic trigger taken in the far detector. The

[†]A minimum ionizing particle is a particle whose mean energy loss rate while propagating through matter is close to the minimum.

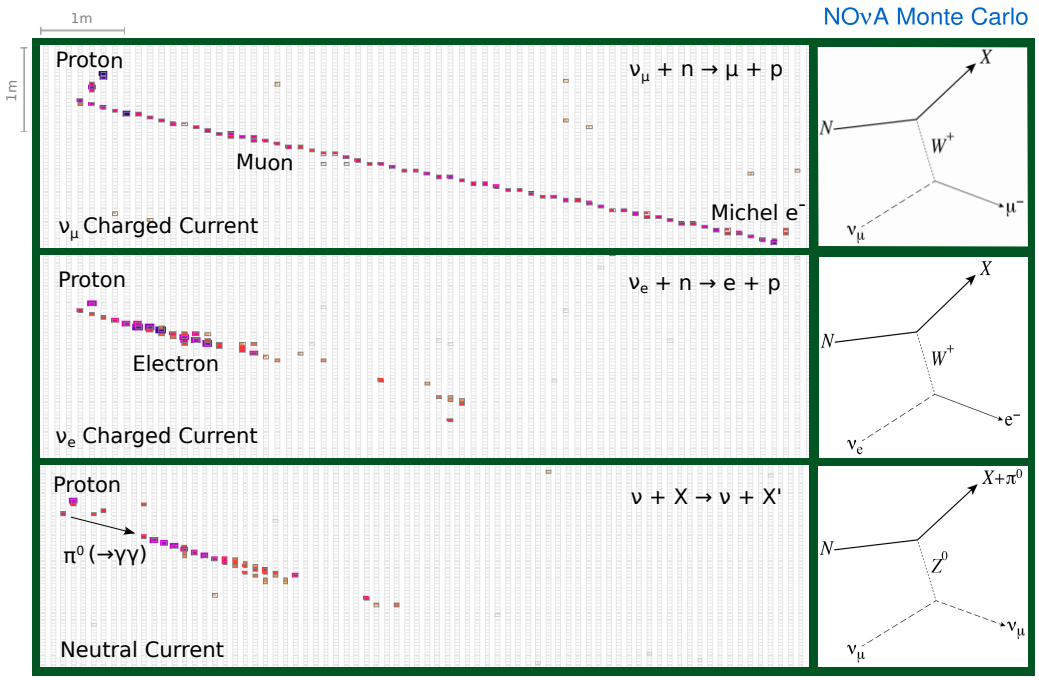

Figure 3.3: Simulated event displays of neutrino interaction event topologies in the NOνA detectors using a true simulated neutrino energy of 2 GeV. Top: ν_μ CC interaction. Middle: ν_e CC interaction. Bottom: NC interaction.

top pane shows what would be seen looking down through the top of the detector (XZ view). The bottom pane shows a picture of the detector as seen from the side (YZ view). Additionally, the timing and charge deposition distributions of all hits in the readout window can be seen at the bottom of the figure. Each of the colored segments represent a single slice that has been view-matched forming a three-dimensional collection of related hits within the detector. Figure 3.5 shows the results of the slicing procedure on an detector readout associated with a single NuMI beam spill in the near detector. In this case the slicing algorithm has separated a candidate neutrino interaction in orange, from various charged particles coming from from rock interactions outside the detector.

Identifying the Neutrino Interaction Vertex

After an individual slices have been separated from the other activity within the detector, reconstruction of the neutrino interaction can begin. The first step in this process is identifying the

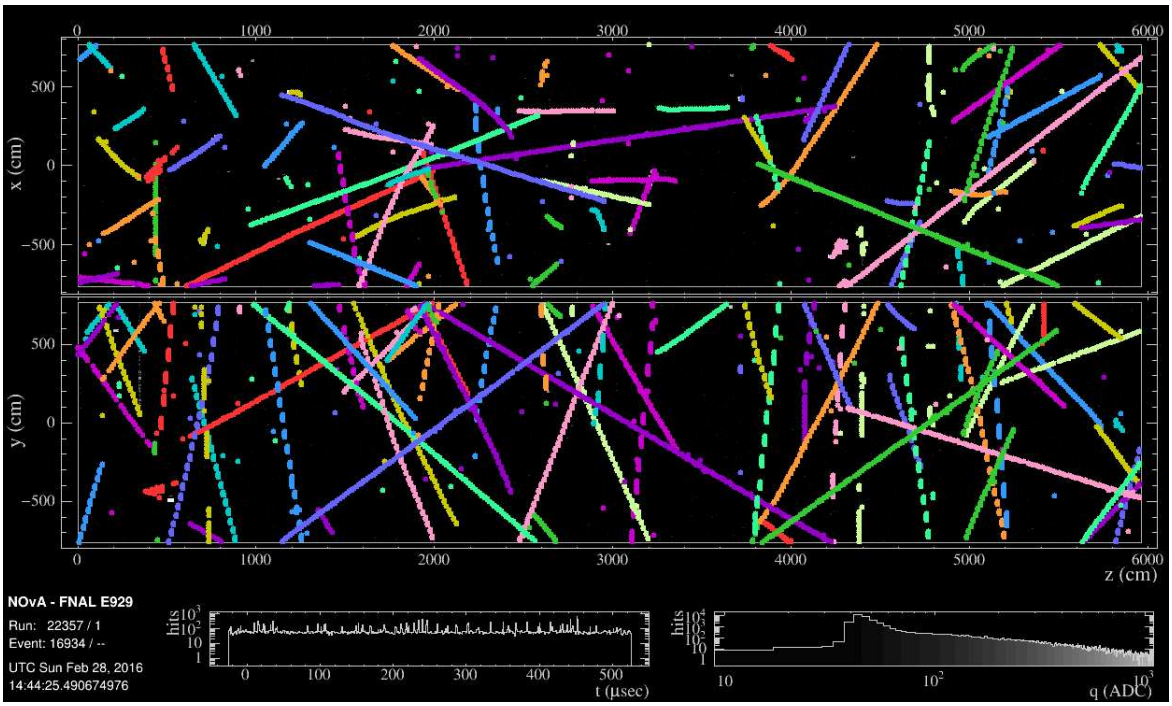

Figure 3.4: Example of cosmic ray distribution throughout the 550 μs time window in the far detector. The reconstructed slices are drawn.

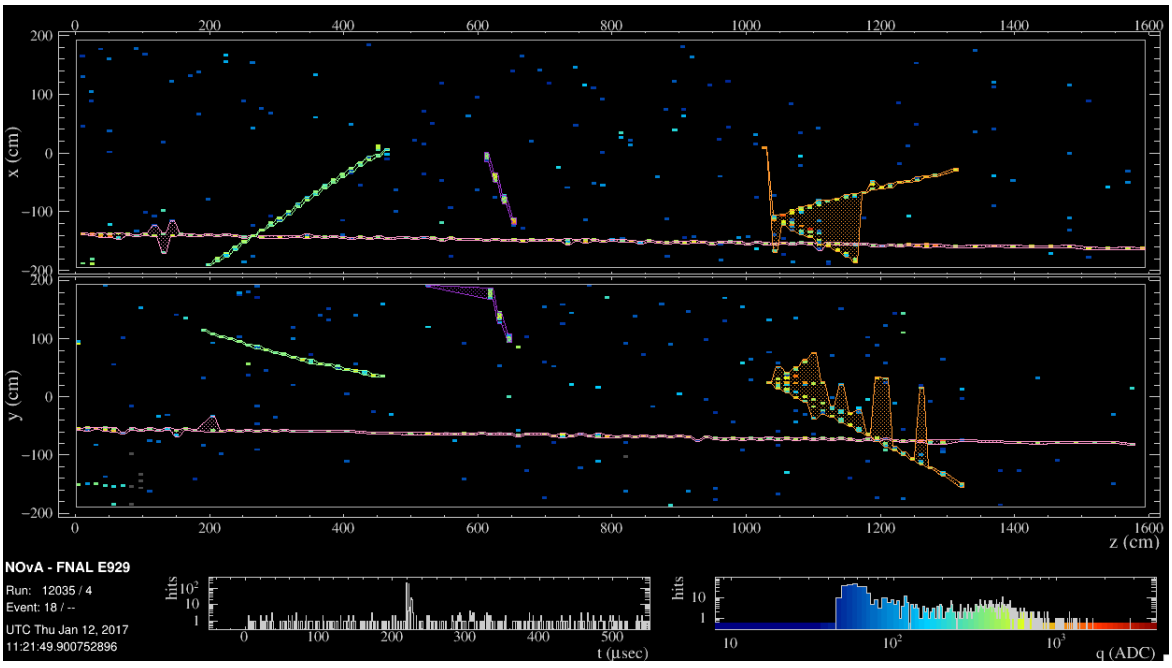

Figure 3.5: Example of reconstructed slices on a 550 μs time window around the NuMI beam spill in the near detector.

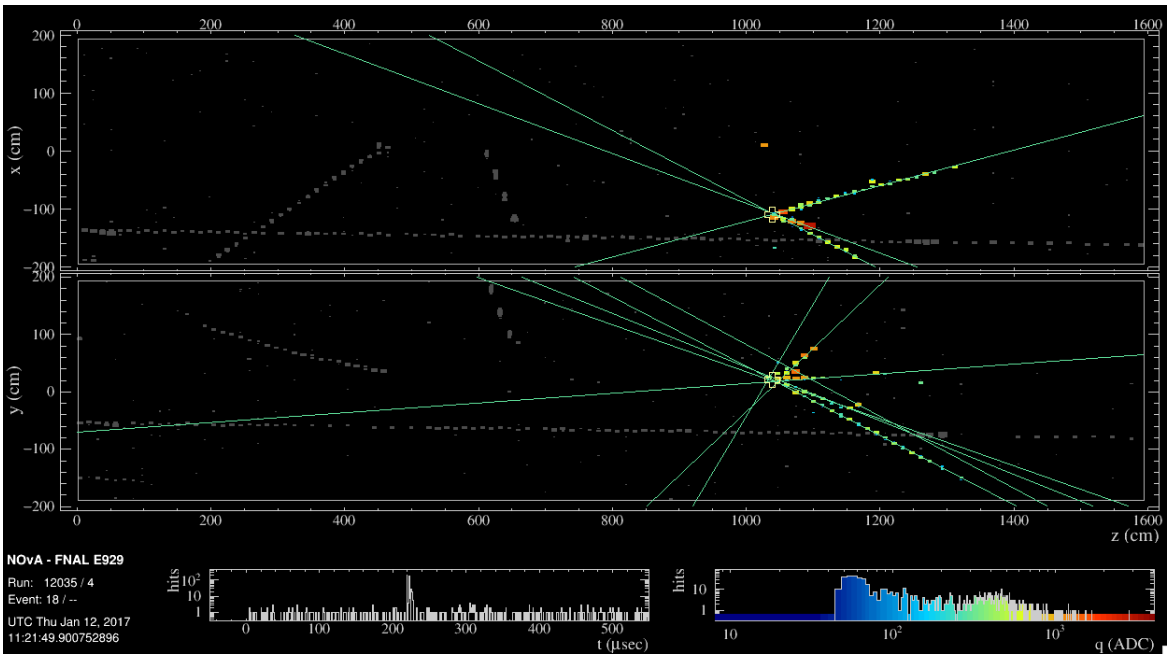

Figure 3.6: Example of reconstructed event vertex (orange cross) in the NOνA near detector. The Hough lines used to determine the vertex are depicted in green.

location of the candidate neutrino interaction. This process starts with the assumption that final-state particles propagate outward from a single interaction vertex [81] [82]. The vertex is identified through the creation of Hough lines, which are lines connecting each pair of hits separated by some minimum distance. Hough lines are characterized by an (r, θ) coordinate. The Hough lines are used in a minimization procedure to arrive at the location of the vertex. The reconstructed interaction vertex and the Hough lines used to determine its location are shown in Figure 3.6.

3.2.2 Reconstructed Particle Trajectories

Once the event vertex has been identified, individual particle trajectories emanating from this vertex are reconstructed, these reconstructed objects fall into two categories, tracks and prongs. Track reconstruction is optimized on identifying charge depositions within the detector that lie along a line. Prongs reconstruction allows for a looser collection of hits, such as would be seen in an electromagnetic shower. Prongs are reconstructed using a fuzzy-k algorithm [80]. The idea behind the fuzzy-k algorithm is that individual particle trajectories should appear as peaks of de-

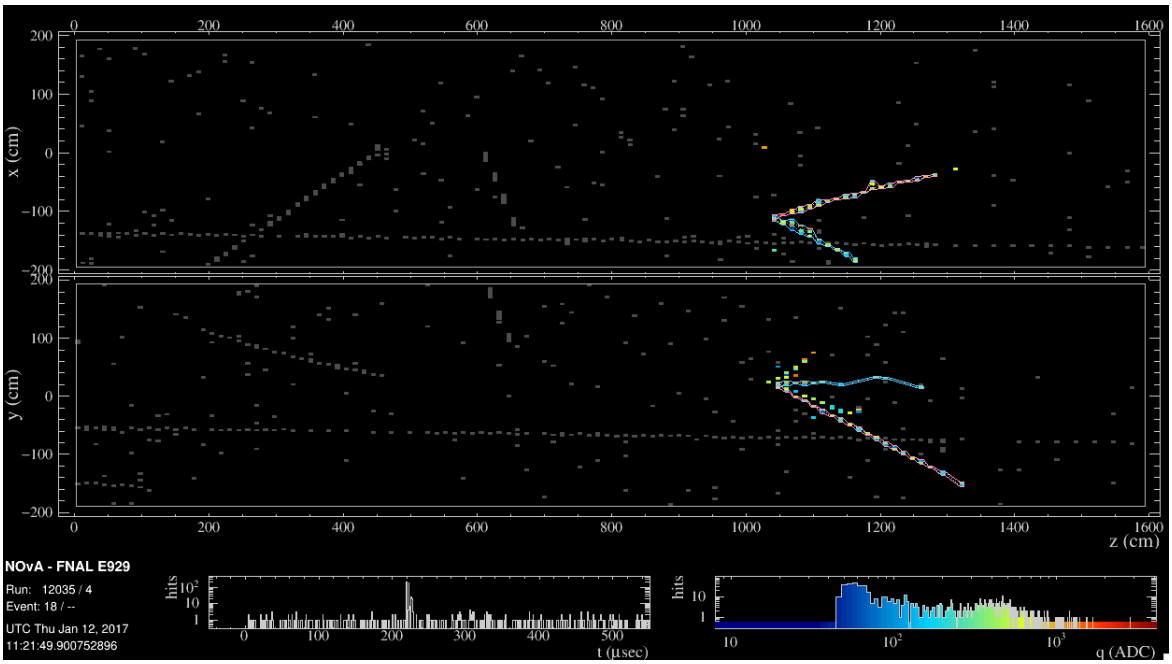

Figure 3.7: An event display illustrating reconstructed prongs in the NOνA near detector. The three-dimensional reconstructed prongs are shown as the collection of hits outlined by the colored lines.

posited energy when looking outward from the event vertex. As with the previously described reconstruction techniques, prongs are initially reconstructed separately in the XZ and YZ views. The two-dimensional prongs are then matched between each of the views to create three-dimensional prongs. Figure 3.7 shows the results of fuzzy-k prong reconstruction algorithm for a single neutrino interaction. Prongs with matching colors in the XZ and YZ views of the detector have been matched in three dimensional space. Additional hits can be seen outside of the three-dimensional prongs, these typically belong to two-dimensional prongs that were not matched between the two detector views.

3.3 Reconstruction of Electron Kinematics

Electron kinematics in the NOνA ND are characterized by the energy and direction of the electron candidate prong within a slice (further particle identification is discussed in Section 3.5). Measured electron energy is defined to be the calorimeteric energy of the identified prong which is defined as the sum of the deposited energy for each hit in the reconstructed prong. Figure 3.8

shows the fractional resolution for reconstructed electron energy when averaged over the energy range of interest for the analysis presented in this thesis ($0 <$ Electron Energy$(E_e)(GeV) < 6.0$), where fractional resolution is defined as:

$$\text{Fractional Resolution} = \frac{E_{\text{reco}} - E_{\text{true}}}{E_{\text{true}}} \tag{3.1}$$

where E_{reco} and E_{true} are the reconstructed and true energy of the reconstructed electron prong from simulation. A Gaussian fit to the fractional resolution shows a shift of about 15% in the reconstructed value of electron energy, which is interpreted as a bias in the reconstructed electron energy. A positive shift in this distribution means that the calibrated energy associated with the electron prong over-predicts the amount of actual amount of energy deposited by electron produced electromagnetic showers in the ND. Figure 3.9 is a plot of the absolute resolution[‡] of electromagnetic calorimetric energy. The black markers in the figure represent the mean value and vertical error bars represent the width of each Gaussian fit to 1D projections of true electron energy. The black points correspond to a reconstruction bias of at least +150 MeV across all true energy values.

To achieve better agreement between the reconstructed and true distributions of electron energy, a correction was applied to the reconstructed value to reduce the bias. This technique assumes that the detector response to electromagentic showers is modeled correctly within the simulation. This is checked using several techniques including those show in Sections 3.6 and 4.6. The application of the bias correction was done using the plot shown in Figure 3.10. The figure shows the absolute electron energy resolution as a function of reconstructed electron energy. A polynomial was fit to the to the profile of this distribution as a function of reconstructed electron energy. This polynomial function is then subtracted from the reconstructed value to reduce the observed intrinsic bias.

Multiple polynomials were explored as shown in Figure 3.10. This was done to ensure that there the bias correction function was adequate to cover the energy range of interest. The bias and resolution (defined as the central value and width of each Gaussian fit to 1D projections of true

[‡]Absolute resolution is the difference between the reconstructed and true quantity as predicted by simulation

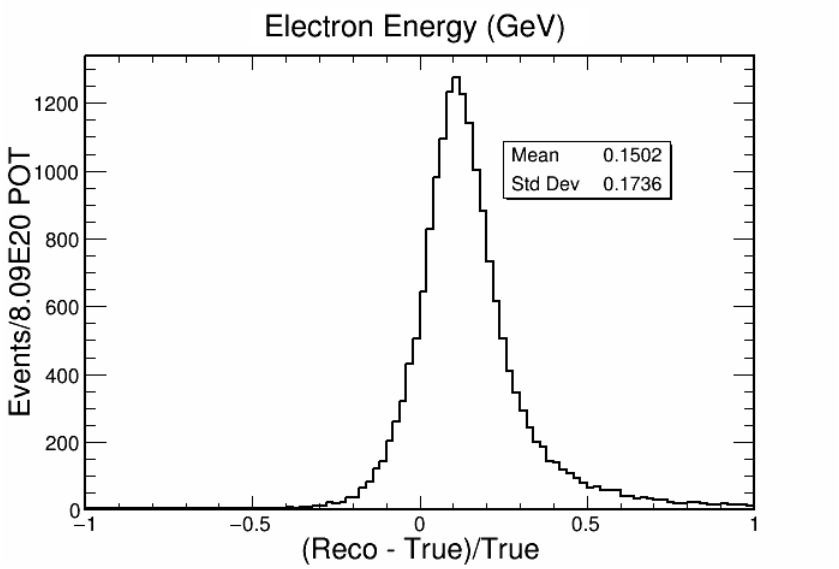

Figure 3.8: The fractional resolution of reconstructed electron energy. (Before bias correction)

electron energy space) after the correction is shown in Figure 3.11 for several of the polynomials. The results of this study suggest that a polynomial of at least order three is necessary to adequately describe the bias correction needed for reconstructed electron energy.

The second reconstructed kinematic variable used to characterize the electron is the angle between the reconstructed prong associated with the electron and the average neutrino beam direction. The average beam direction is calculated using the simulated neutrino flux discussed in Section 3.1.

A comparison of each reconstructed variable to truth in simulated events is shown in Figure 3.12. Reasonably good agreement is seen between the true and reconstructed quantities for electron energy, particularly in the 1 to 5 GeV region. For the distribution of electron angle a shift is seen showing that electrons are reconstructed to be at higher angles with respect to the average beam direction, than is simulated. This shift will be dealt with using unfolding techniques to correct the reconstructed distribution. Unfolding will be discussed in more detail in Chapter 4.

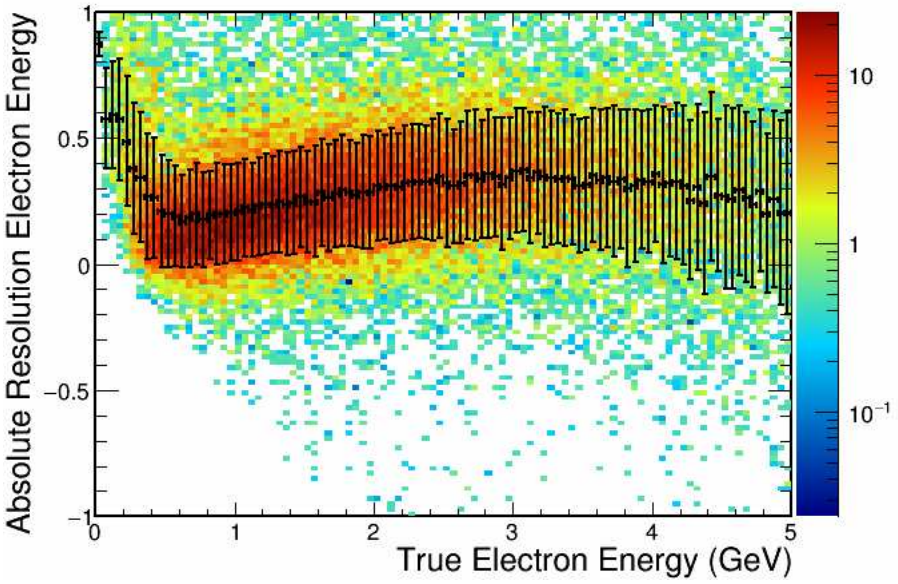

Figure 3.9: The absolute resolution of reconstructed electron energy as a function of true electron energy. The central value and width of Gaussian fits to 1D projections to true electron energy are reported by the central black marker and vertical error bars, respectively. (Before bias correction)

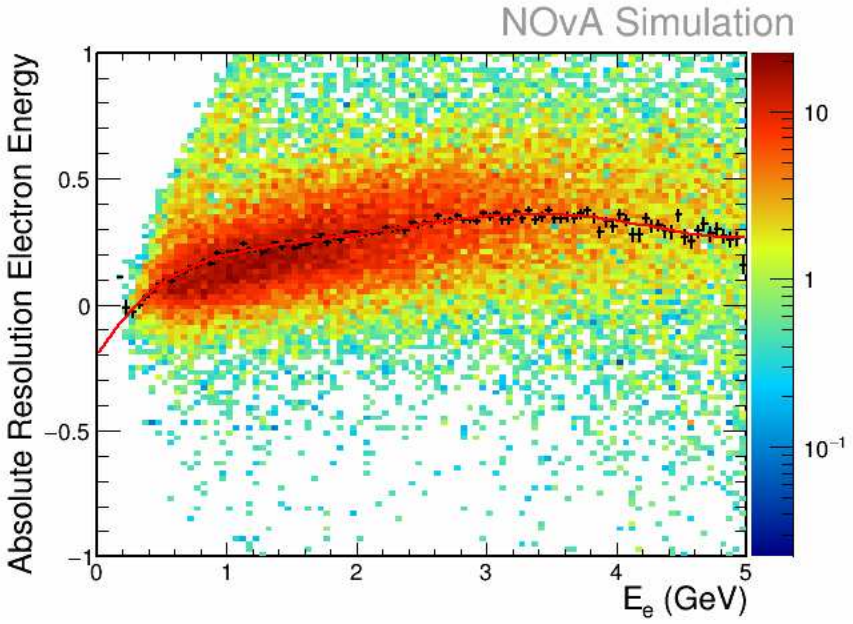

Figure 3.10: Absolute resolution versus reconstructed electron energy. Black points on the plot represent the average value of (Reco. - True), in each of the reconstructed energy bins. The red line shows the results of a polynomial fit to the black points. The polynomial shown is a fifth order polynomial.

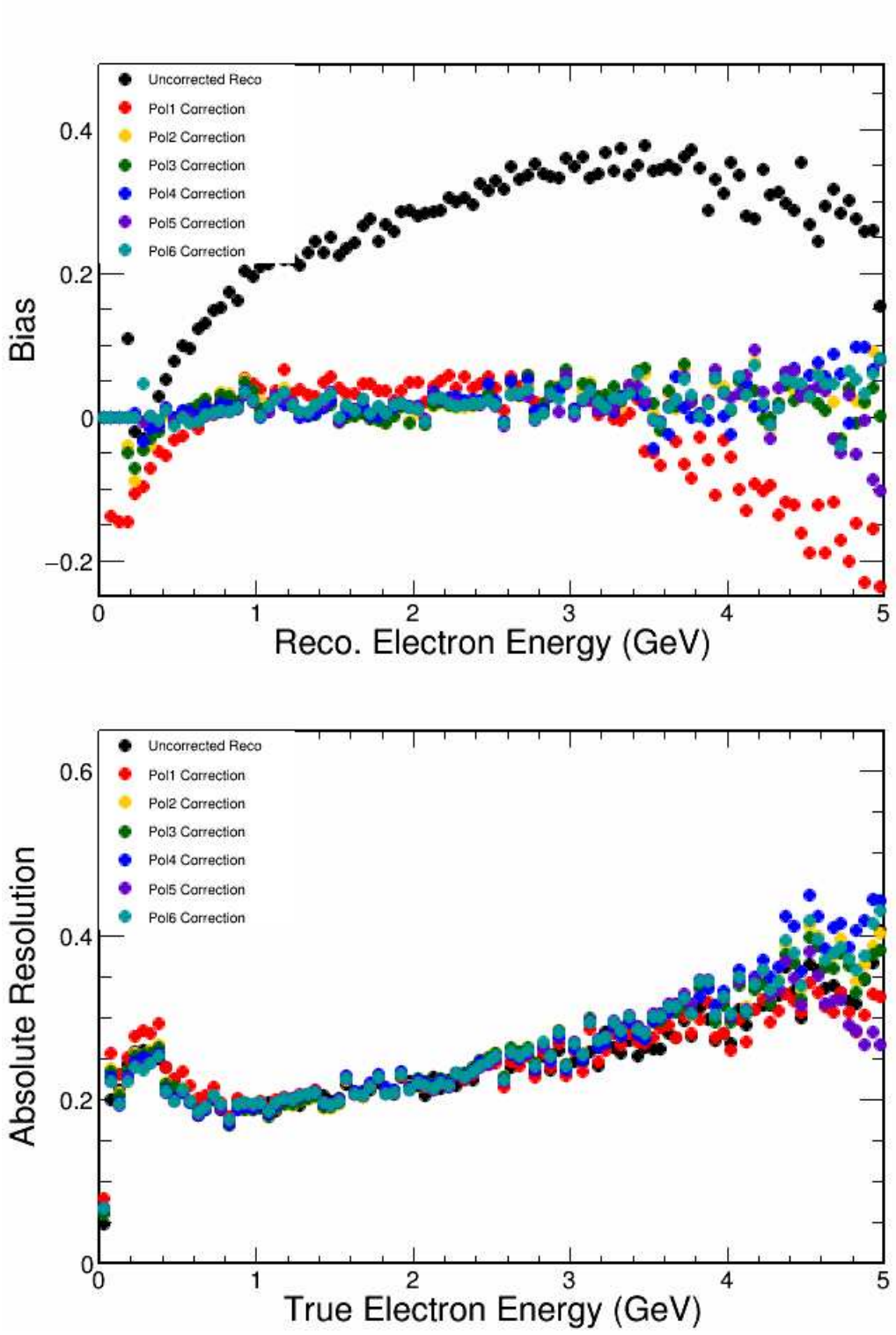

Figure 3.11: The bias and absolute resolution of reconstructed electron energy before and after bias corrections using polynomials. PolX in the legend refers to a bias correction using an X order polynomial. Top: Reconstruction bias. Bottom: Absolute electron energy resolution.

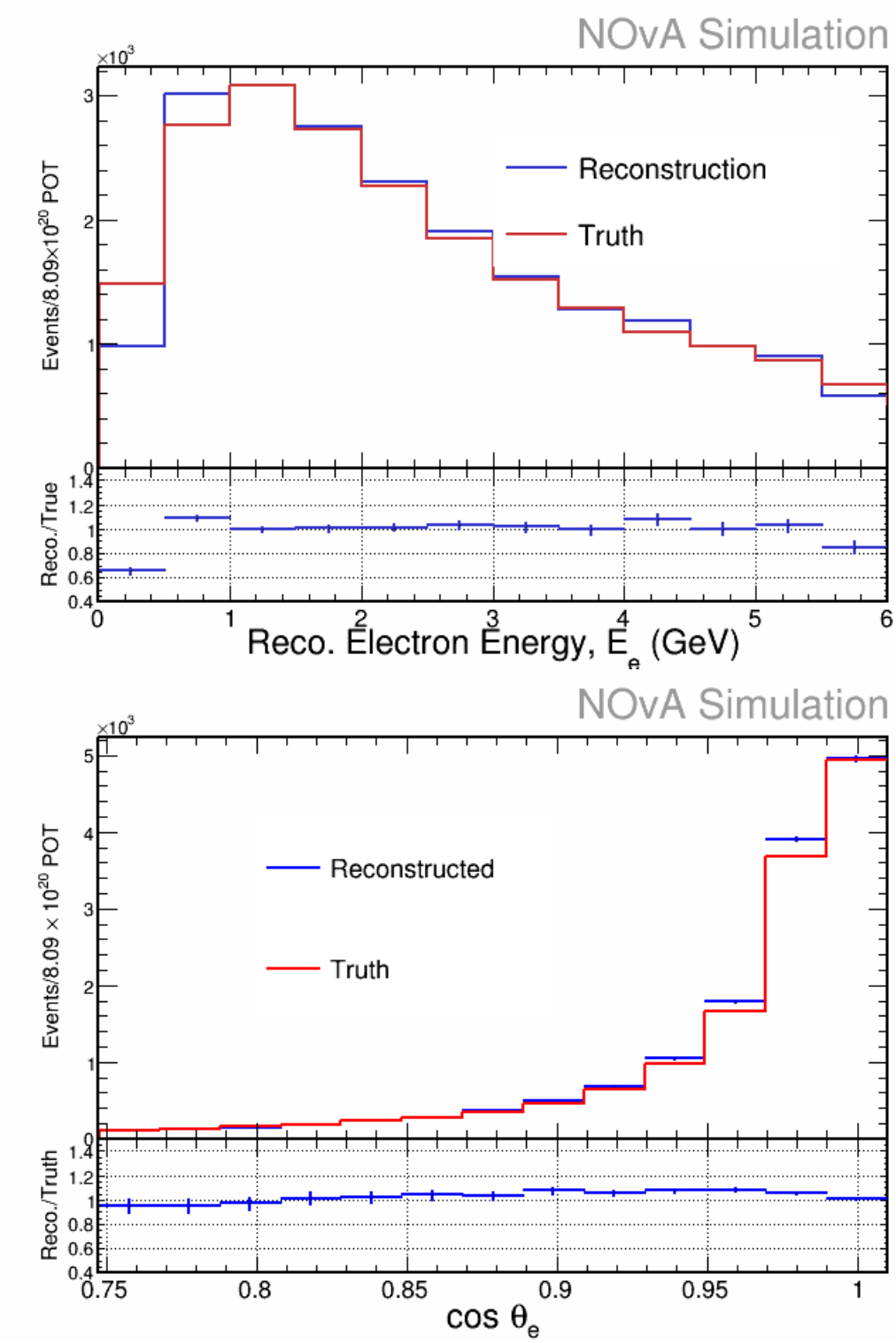

Figure 3.12: The comparison of reconstructed electron energy(top) and $\cos\theta_e$ (bottom) to truth from simulation. Number of events are normalized to the 8.09×10^{20} POT.

3.4 Neutrino Energy Estimation

The reconstruction of neutrino energy for ν_e CC events is based on the assumption that the detector response is different for electromagnetic and hadronic energy depositions, which are both present in signal interactions. Hadrons can be reconstructed as tracks or showers depending on the relative importance of energy loss due to Coulomb and strong interactions. Uncertainties on the production rate of secondary particles result in significantly worse energy resolution for hadronic particles when compared to the lepton induced activity.

To first order, neutrino energy is reconstructed as the addition of lepton energy and all hadronic energy recorded within the slice containing the interaction. However, neutrino energy reconstruction is complicated by any missing energy. Missing energy can result from the presence of "dead" material within the detector, like energy depositions within uninstrumented regions of the detector (e.g. interactions within the PVC itself), or the lack of a charged particle in the final-state. To account for these losses reconstructed electromagnetic and hadronic energy components are fit to the true neutrino distribution predicted by the ND simulation. To achieve this all 3D reconstructed prongs are first classified as either electromagnetic or hadronic energy depositions. This is done by through the use a convolutional neural network trained to classify reconstructed prongs (this will be discussed in more detail in Section 3.5). The reconstructed energy of the classified prongs are then fit to the true neutrino energy distribution from simulation to produce a polynomial to provide an estimate of the neutrino's energy.

Figure 3.13 is a plot of the true neutrino energy as a function of both hadronic energy and EM shower energy. In order to avoid bias in the energy estimator to the expected beam peak (near 2 GeV), a weight is applied to the neutrino energy distribution to flatten the distribution from 1 to 5 GeV. The reconstructed hadronic and electromagnetic energies are then fit to the true neutrino energy using:

$$E_\nu = aE_{EM} + bE_{Had} + cE_{EM}^2 + dE_{Had}^2 \tag{3.2}$$

where a, b, c, and d are normalization parameters.

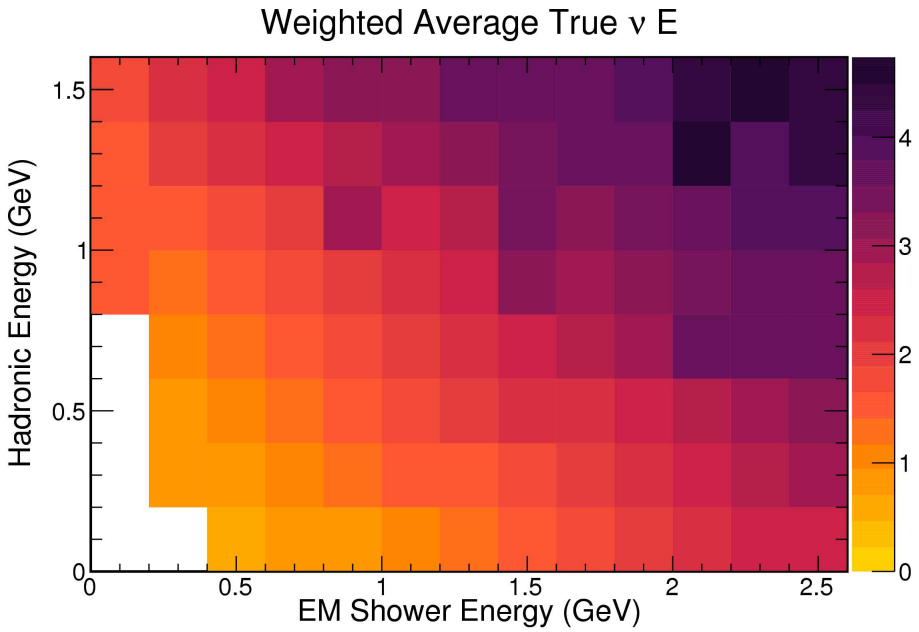

Figure 3.13: The true neutrino energy distribution as a function of reconstructed electromagnetic energy and hadronic energy. The Z-axis is the weighted average of the true simulated neutrino energy.

A comparison of reconstructed and true neutrino energies is shown in Figure 3.14. Although the fitting procedure described above is performed using a flat distribution of true neutrino energy, the figure shows that there is good agreement between the reconstructed and true neutrino energy spectra from the NOνA ND simulation, although, as energy decreases a clear shift can be seen when comparing reconstructed to true values. For this analysis, the energy shift is dealt with using unfolding techniques to correct for reconstruction/detector effects. These techniques will be discussed in more detail in Chapter 4.

3.5 Electron Neutrino Event Identification

The primary goal of the NOνA experiment is to measure ν_μ to ν_e oscillations. Several tools have been developed to aid in the identification of events containing electron neutrino interactions and the final-state electron within them. This section describes these techniques. A comparison of the performance of these techniques is discussed within the context of the analysis presented in Chapter 4.

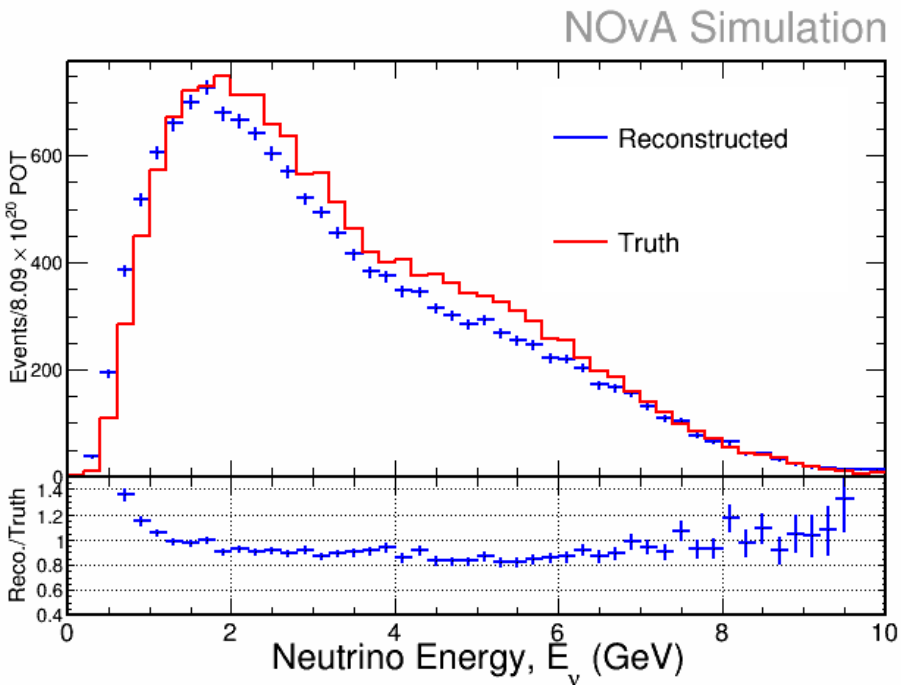

Figure 3.14: Comparison of reconstructed neutrino energy to true energy from simulation. The number of events are normalized to the 8.09×10^{20} POT.

3.5.1 Likelihood-based Identifier

The basic idea of the Likelihood-based Identifier (LID) is to exploit differences in the energy deposition in electromagnetic showers compared to hadronic showers or track-like depositions to discriminate between electrons, muons, photons, and hadrons. Different types of particles will generally leave different energy depositions within the detector, as illustrated in Figure 3.3. In the case of high-energy electrons, energy is predominantly deposited through bremsstrahlung[§]. These interactions are typically characterized by the radiation length. Photons, on the other hand, typically induce an electromagnetic shower after they have traveled one radiation length. Therefore photon showers tends to leave a gap between a reconstructed interaction vertex and the first hits that make up a reconstructed prong. These types of differences make it possible to develop tech-

[§]Bremmstrahlung is electromagnetic radiation produced by the acceleration of a charged particle when deflected by another charged particle

niques to identify particles by comparing different particle hypotheses to the characteristics of an individual shower or track.

Simulated interactions are used to define the specific particle hypotheses used in the LID algorithm. These hypotheses are compared to the measured characteristics of a reconstructed prong in order to obtain likelihoods, which are then used to train an artificial neural network, which is applied to the identification of ν_e events. The likelihoods are obtained by comparing the measured longitudinal and transverse differential energy loss (dE/dx) to those predicted by simulations of electron, photon, muon, π^0, proton, neutrino, and charged pions in the detector. In addition to this likelihood information five other inputs are used:

- π^0 mass: the invariant mass of the most energetic prong is computed iteratively with each of the other prongs in the event The pair that produces an invariant mass most similar to the π^0 mass is used to select candidate π^0, which are rejected then rejected.
- Shower energy fraction: the fraction of total event energy that is contained in the most energetic prong.
- Vertex energy: calorimetric energy within eight planes of the reconstructed interaction vertex, excluding the energy from the most energetic prong.
- Shower gap: the distance of the starting point of the shower to the reconstructed event vertex.
- Shower Angle: the angle between the most energetic prong within an event and the average beam direction.

The output of the neural network is shown in Figure 3.15. The identifier typically selects ν_e-like interactions in the highest scoring region of the LID distribution (near 1). As there is no way to distinguish ν_e and $\bar{\nu}_e$ CC interactions within the NOνA detector, the identifier places both types of interactions in the highest scoring region of the LID distribution. Besides $\bar{\nu}_e$ interactions the main background components in the signal region (LID score > 0.8) are NC interactions with final-state π^0s. At NOνA energies, the decay of these π^0s often result in decays with a single

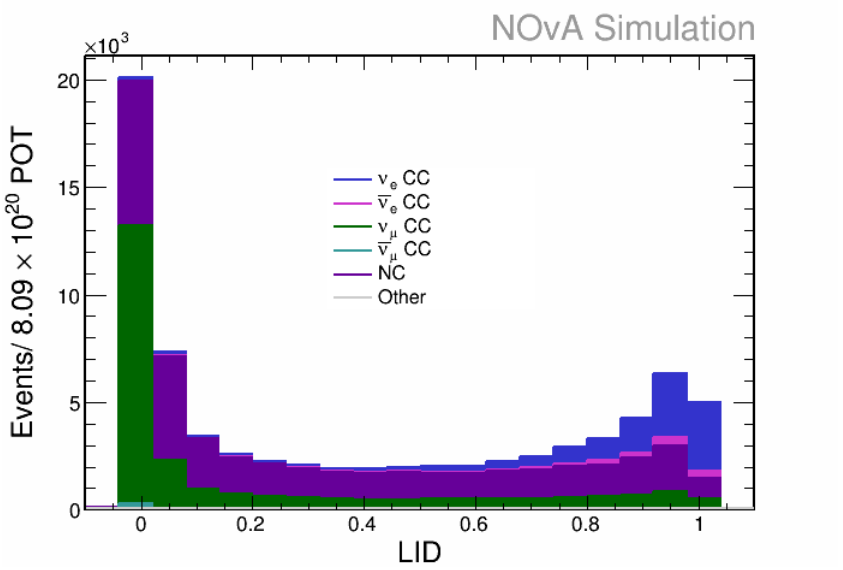

Figure 3.15: The likelihood-based Identifier distribution of the simulated ND sample after all selection cuts used within the inclusive ν_e cross section analysis (Chapter 4). The number of events is normalized to 8.09×10^{20} POT

photon obtaining a large fraction of the π^0 energy or both emitted photons being very forward and reconstructed into a single prong. The LID ν_e classifier was used in the first ν_μ to ν_e oscillation analysis [83], thus it is used a baseline PID metric within this analysis.

3.5.2 Convolutional Neural Network Classifiers

Multi-variate based classifiers, like the one used in the development of LID, have had wide use throughout the experiment particle physics community and beyond. Although such classifiers are extremely powerful, there are still limitations to their use [84]. Some examples of these limitations are the inability to scale to a large number of raw inputs. Additionally, large (and even small) numbers of free parameters run the risk of over-training[¶] within large networks.

Deep learning, or the use of network architectures with many layers, has had considerable success in mitigating some of the limitations of traditional multi-variate classifiers. The architecture of a simple neural is illustrated in Figure 3.16. The most basic unit of an artificial neural network is

[¶]Over-training is when the network "learns" to reproduce the training sample too well, and fails to generalize to inputs it has not yet seen.

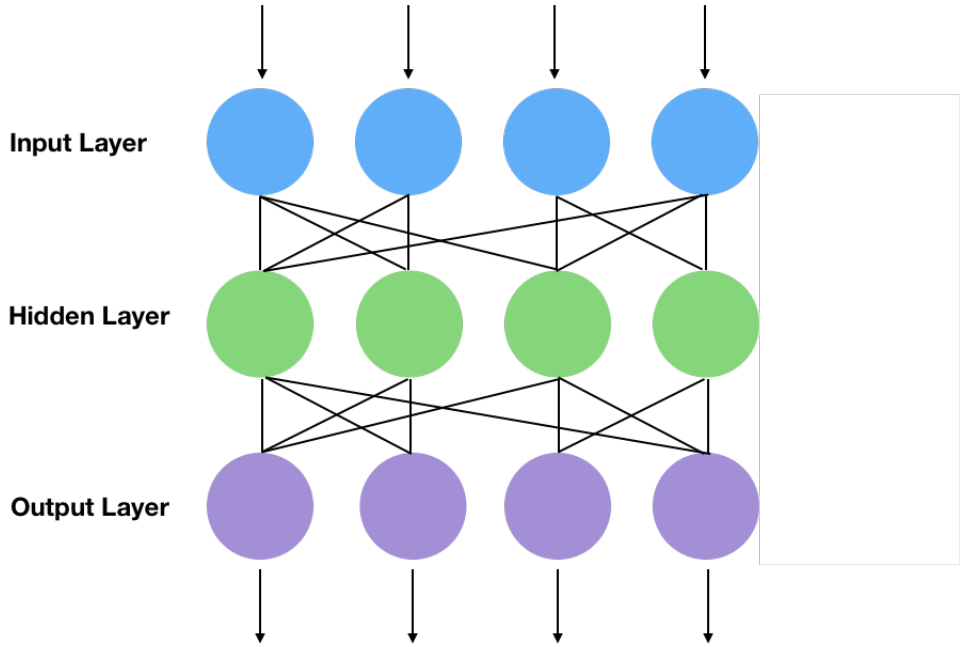

Figure 3.16: The illustration the information flow through an artificial neural network.

is called a neuron, or node. A neuron receives input from another node or from an external source, like the likelihood information used within LID, and calculates an output. The input commonly is associated with a weight, or the relative importance of input when compared to the other inputs. Sets of nodes are arranged into layers, where nodes in adjacent layers have connections between them. Each of the connections have weights associated with them. Layers are classified as input, hidden, and output layers. Input layers receive information from outside the neural network, hidden layers have no direct connection with information outside of the network, and the output layer is responsible for transferring information from within the network to the outside world.

Deep learning networks have shown considerable success in tasks like image recognition [85]. They have also been adapted to many other types of classification problems, such as the identification of events or particles within physics experiments [86]. The NOνA experiment makes use of a machine learning algorithm known as a convolutional neural network (CNN). These networks do not use specifically constructed features, like longitudinal and transverse dE/dx, but instead rely on the extraction of features through the machine learning algorithm itself.

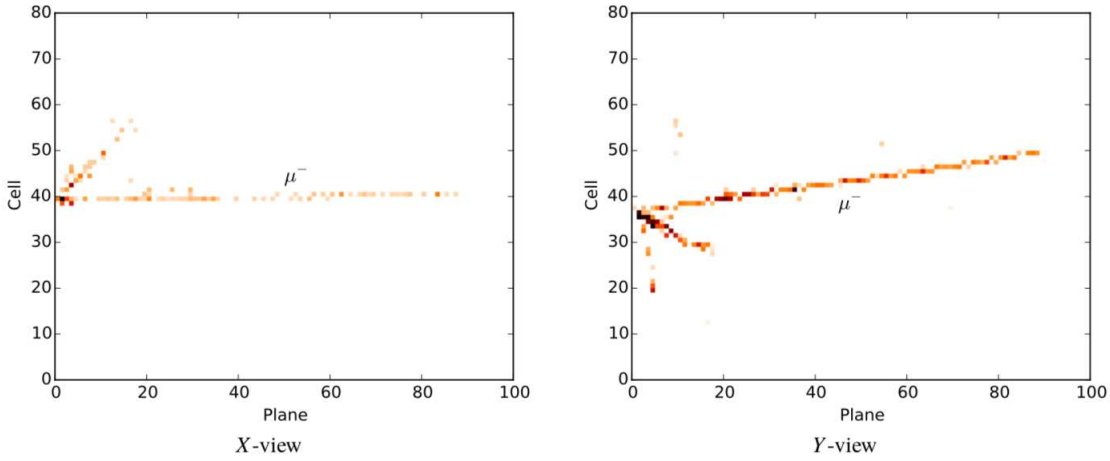

Figure 3.17: Examples of pixel maps for a simulated ν_μ interaction from the XZ (left) and YZ (right) views.

CNNs take advantage of the fact that any image can be mapped onto matrices using the pixels of the image. Thus images are treated as $w \times h \times d$ arrays where the width, w, and the height h are the dimensions of the image in pixels and the depth, d, is the number of channels. For image recognition the depth is colors in RGB space. The content of the matrix corresponds to the colors in an image, which preserve the features and spatial correlations necessary to identify objects within the image.

Event Classification

The input to the event classification convolution neural network used by NOνA are matrices produced directly from the readout of the detector. These matrices are called pixel maps which correspond to cell locations in the XZ and YZ views of the detector. The location of a hit within an event is directly mapped to a single element of the pixel map, mimicking the dimensions of the detector. A pixel map generated from a simulated ν_μ charged charged current interaction is shown in Figure 3.17.

Convolutional neural networks are used to analyze images by applying matrix filter operations across it. The filters, also called kernels, are different matrix operations that are used to extract unique image features. Convolutions refer to the application of these matrix filters across the image. The features that these matrix filters extract are learned by the network through the training

process. The kernels are not set by the user, but rather they evolve through the training. This means that the set of features that the network uses to classify objects is not limited to extracted physical quantities, like those used in the training of LID. This process is completely decoupled from traditional reconstruction and any inefficiencies that may result from the reconstruction process. This also means that studies must be performed to identify any inefficiencies in the training of a CNN.

The convolutional neural network used for event identification of NOνA ND ν_e events is called a Convolutional Visual Network (CVN) [86]. CVN was designed to identify energy depositions characteristics of neutrino interaction topologies that are commonly seen within the NOνA detectors. It was trained on approximately 4.7 million events. The training sample consisted of neutrino interactions from simulated events and cosmic rays from out-of-beam data. The inputs for the network were two pixel maps, one for both the XZ and YZ projections, and the output is the likelihood that an event is a certain interaction type (ν_μ, ν_e, ν_τ, or NC) and interaction mode (QE, RES, DIS, Other).

The ν_e CC event CVN classifier distribution in the near detector is shown in Figure 3.18. This event classifier shows a clear enhancement of signal and background discrimination as compared to the LID classifier shown in Figure 3.15. When the CVN technique was first implemented in NOνA 's 2016 ν_e appearance analysis [87], its use resulted in an 30% increase in effective exposure for signal events as compared to the results of the analysis using the LID classifier.

Convolutional Neural Network Prong Classifier

The convolutional visual network described above can only give the likelihood that an event is from a specific interaction type. There is no additional output that identifies the individual particles within the neutrino interaction. NOνA employs the use of a more targeted CNN to classify individual reconstructed objects within an event. This allows for the selection of a particle type for a given reconstructed prong.

The implementation of the particle classifier, or Flat Flux Prong CVN, is similar to the event CVN described in the previous section. The differences come from training on single objects simulated within the near detector. Prong CVN was designed to identify energy depositions char-

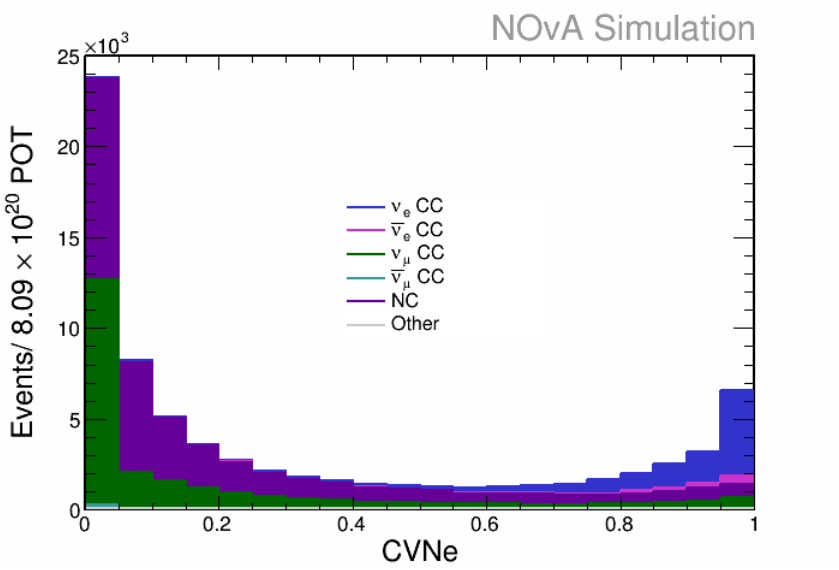

Figure 3.18: The CVN ν_e CC classifier distribution of the simulated ND sample after all selection cuts used within the inclusive ν_e cross section analysis (Chapter 4). The number of events is normalized to 8.09×10^{20} POT

acteristics of specific particles types within the NOνA detector. To avoid any bias towards the particular final-state particle kinematics, the training sample was generated by drawing all kinematic variables from "flat" distributions. The inputs to this network are pixel maps of the XZ- and YZ- views of 3D reconstructed prongs. Due to the inefficiencies associated with prong reconstruction, the classifier only attempts to classify the particle that contributes the most energy to the prong. The output of the classifier are several likelihoods that a reconstructed prong is a muon, electron, charged pion, photon or proton.

Electron neutrino interactions are identified through the presence of highly scoring electron prongs from the prong classifier. Figure 3.19, shows the classification of interaction types by the highest scoring electron prong in an event. Events with electromagnetic showers typically score highly when ranked in this fashion. The inefficiencies in identifying ν_e CC interactions is due to the lack of contextual information about the individual prong within an event. The training of Prong CVN has no additional information like the presence of a gap between the interaction vertex and the start of a prong.

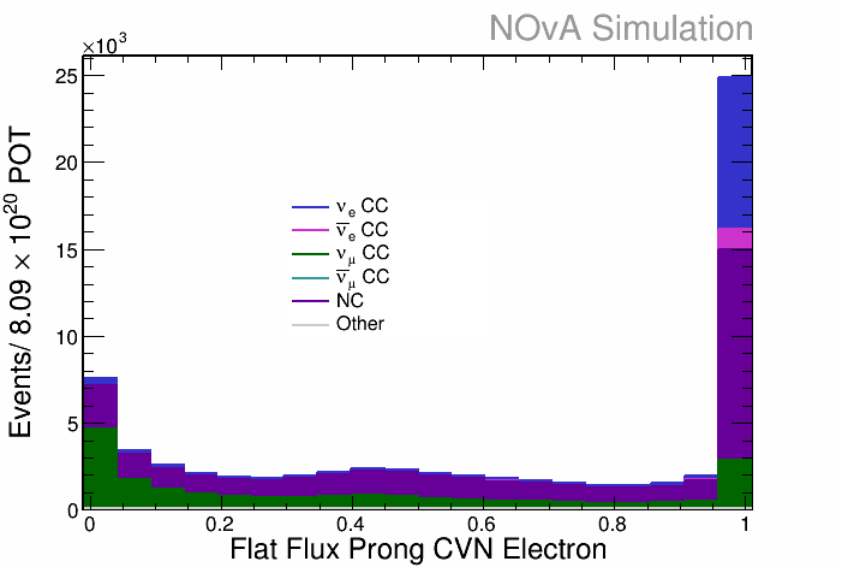

Figure 3.19: The Flat Flux Prong CVN ν_e CC classifier distribution of the simulated ND sample after all selection cuts used within the inclusive ν_e cross section analysis (Chapter 4).. Each event is ranked by the highest scoring electron prong within the event. The number of events is normalized to 8.09×10^{20} POT

3.5.3 Multivariate-based Electron Identifier

Figures 3.18 and 3.19 show that prong CVN would select more background events that event CVN. This is primarily driven by the lack of contextual information, like the presence of gap between a reconstructed interaction vertex and the beginning of a reconstructed prong, in the training of the network. This contextual information can be used to enhance the output of the Flat Flux Prong CVN classifier through the use of multivariate techniques [88]. The inputs for the multivariate-based electron identifier (ElectronID) are:

- Flat Flux Prong CVN classification scores:
  - Electron score
  - Photon score
  - Non-EM score = muon + charged pion + proton scores
- Reconstructed shower width
- Reconstructed gap from vertex to prong/shower starting hit

The distribution of each of these input variables is shown in Figure 3.20. Each distribution is decomposed into the signal-like (electron and positron) and various background prongs. Differences between particle types can be seen. The shower gap distribution clearly shows distinctions between electron and photon prongs, where the photon prongs have a clear secondary peak near 6 cm. Correlations between the input variables are plotted in Figure 3.21. The highest correlations are between the prong CVN variables. The prong CVN classifier is normalized for an individual prong the sum of all prong likelihoods is one. For example, highly scoring non-EM prongs always have low electron scores. This results in correlations between each of the prong CVN scores used as inputs to the multi-variate classifier.

An important consideration for the development of this electron identifier was minimizing model dependence. Multiple studies were performed to ensure that the variables did not exhibit dependence on outgoing electron kinematics. For example, reconstructed shower width was studied for any potential kinematic bias. As the detector was designed for the discrimination of electromagnetic showers from particles tracks it has a well-characterized Molier radius[37], defined as:

$$R_M = X_0 \frac{E_s}{E_c} \approx 0.0265 X_0 (Z + 1.2) \tag{3.3}$$

which describes the transverse development of electromagnetic showers using the radiation length, X_0, and critical energy, E_c, of the medium. The EM energy scale is defined as $E_s = \sqrt{4\pi/\alpha} m_e c^2$. The approximate definition also relies on the atomic number, Z, of the medium. The Moliere radius is not dependent on the electron kinematics, this can also be observed in Figure 3.22, where a well-defined peak in reconstructed shower width is observed to only vary slightly as a function of electron energy.

The multivariate technique used to develop the ElectronID identifier is called a Boosted Decision Tree (BDT) [88]. An example decision tree is illustrated in Figure 3.23. Decision trees use a tree structure to classify an object. This is done by breaking down a data set into smaller subsets at each of the nodes (shown as a yellow box within the figure) through if-then statements.

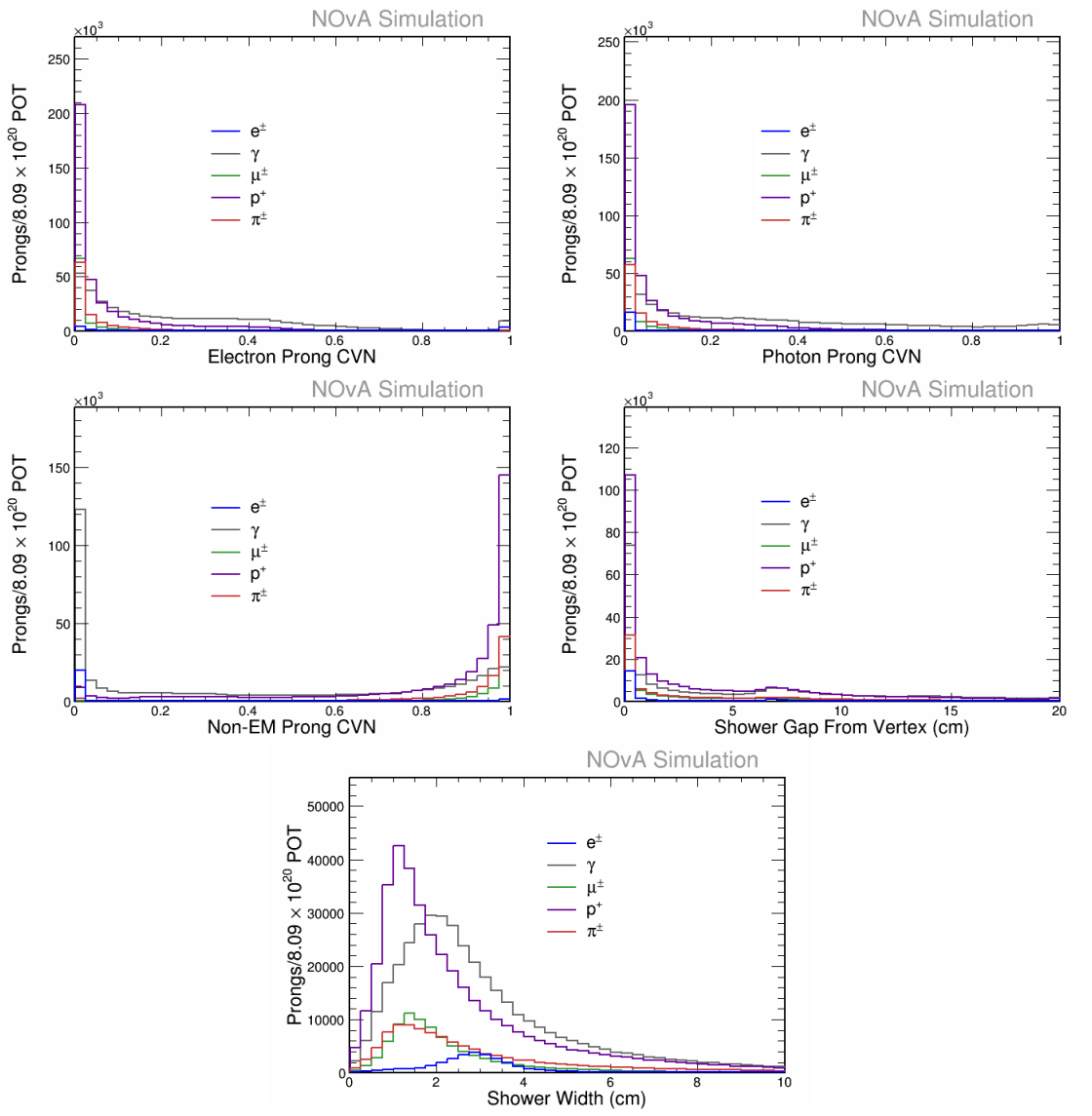

Figure 3.20: Distributions of input variables to ElectronID, broken down by true prong identity. (Top Left) Electron Prong CVN score, (Top Right) Photon Prong CVN score, (Middle Left) Non-EM Prong CVN score, (Middle Right) Shower Gap from vertex, (Bottom) Prong Width.

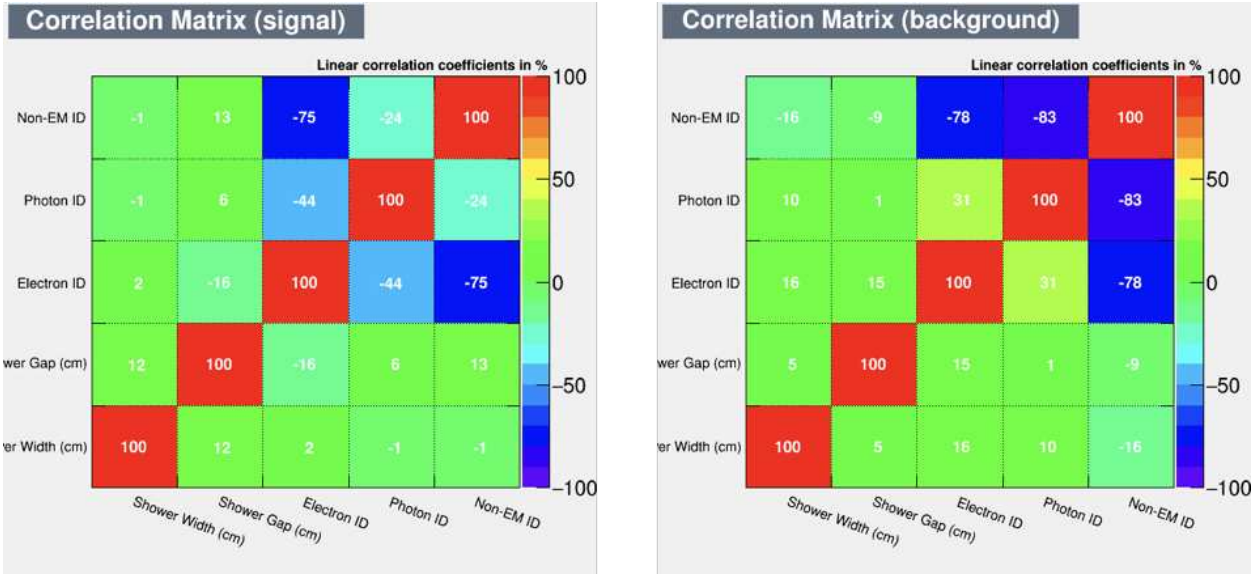

Figure 3.21: Correlation matrix of ElecronID input variables for signal prongs (left) and correlation matrix of input variables for background prongs (right)

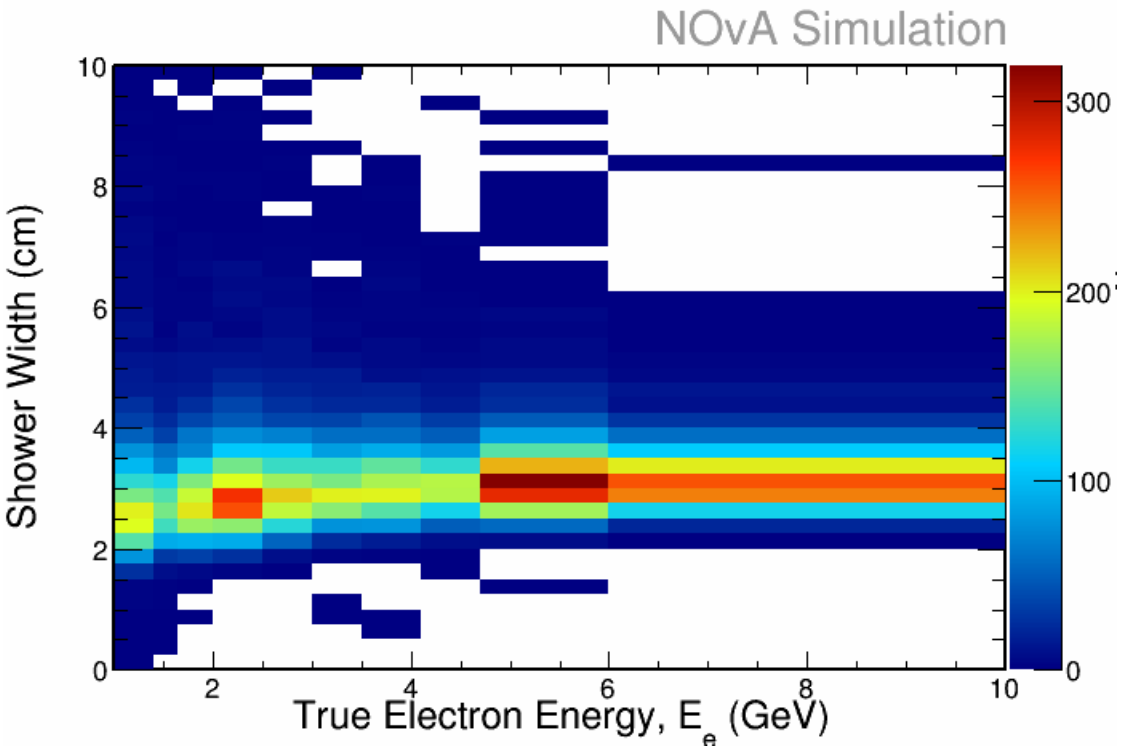

Figure 3.22: Plot of the reconstructed shower width as a function of true electron energy.

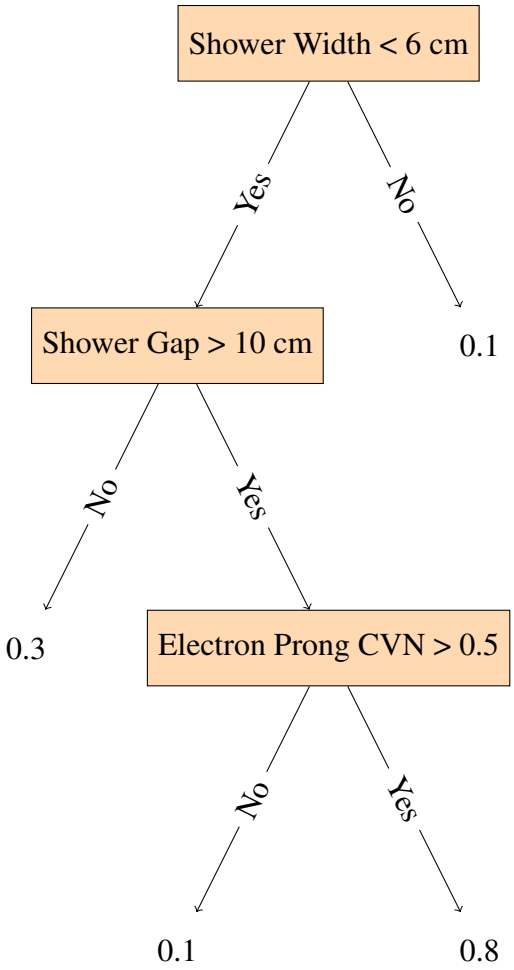

Figure 3.23: A diagram of an example decision tree. Individual nodes are identified with yellow boxs, and the leaves are identified by the numerical values.

Based on the decision of an individual node the tree either terminates at a leaf, which represents an output label or identification probability, or continues to another node within the tree. Decision trees typically consist of several layers of nodes[‖] to build up the strength of the classifier. Boosting refers to a method for coming the output of many weaker trees to form a strong classifier.

The multivariate-based identifier was trained multiple times in an attempt to optimize the discrimination of signal from background, using the ROC integral[**] and minimize the amount of

[‖]The number of layers that make up a decision tree is sometimes referred to as tree depth. For the example shown in Figure 3.23, the tree depth is 3).

[**]A ROC curve is a graphical plot that illustrates the efficiency of a classifier system by plotting the true positive and false positive rates of the classifier as the discrimination threshold is varied.

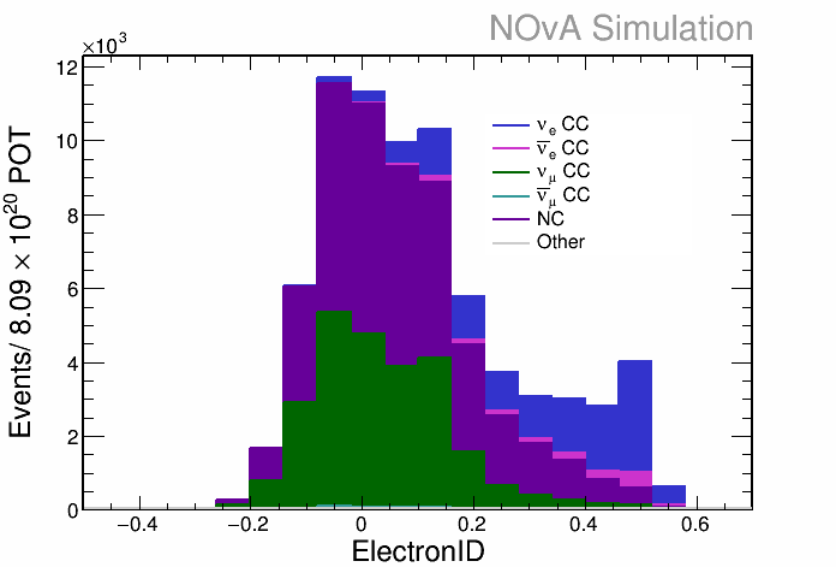

Figure 3.24: The distribution of the highest scoring ElectronID prong in each event of the simulated ND sample after all selection cuts used within the inclusive ν_e cross section analysis (Chapter 4). Numbers normalized to 8.09×10^{20} POT

over-training through the use of the Kolmogorov-Smirnov test[††] to compare the BDT performance on the training and a test data sets. The optimization of each of these metrics was performed with respect to multiple training parameters. The parameters that had the largest impact on the two figures of merit where the minimum node size, which is the percentage of the training data set that the tree is trained using, and the tree depth. The optimal training method was determined to be a BDT consisting of 700 trees, with a tree depth of 3, and a minimum node size of 1 %.

The output of the BDT is called ElectronID, and is related to the likelihood that a reconstructed prong is an electron. The distribution of the highest scoring ElectronID prong in simulated neutrino events is shown in Figure 3.24. The main backgrounds in the signal region of this distribution are NC events with final-state π^0s.

[††]The Kolmogorov-Smirnov test is a statistical test that tries to determine if two data sets differ significantly, by looking at the cumulative probability distributions of the data sets.

3.6 Calorimetric Energy Scale Calibration

The calibration calorimetric energy for the NOνA ND is preformed in two distinct steps. The first characterizes the the response of each cell for the attenuation of photons as they travel from one end of a cell to the APD readout on the opposite end. The second characterizes the absolute energy scale of the detector accounting for the conversion of electronic signals to energy.

3.6.1 Attenuation and Threshold Calibration

Calibration of light attenuation is performed in each cell of the NOνA ND detector. This calibration is data-driven using cell-hits from comic ray muon energy depositions. The paths of these comic ray muons are tracked allowing for an uncalibrated measurement of the energy loss per centimeter within the detector. As cosmic muons are minimum-ionizing particles with a well defined dE/dx, they can be used for energy calibration.

Figure 3.25 shows the uncalibrated detector response per unit path length along the length of a NOνA ND cell. The detector response correction is provided by the light attenuation calibration constants obtained by a fit to the data distribution as shown in the figure.

3.6.2 Absolute Energy Scale Calibration

Absolute energy scale calibration uses the energy deposited by stopping muons as a standard candle process to find the absolute energy scale in the detector. These are studied by looking at the deposited energy one to two meters away from the end of tracks where the dE/dx is close to minimum ionizing for muons. The mean detector response distribution is found for data and simulated cosmic muon tracks in both the near and far detectors and is used to convert between detected and true energy. The results of the absolute energy scale calibration are shown in Figure 3.26. The remaining differences between the data and simulation are accounted with systematic uncertainties.

3.6.3 Electromagnetic Shower Energy Calibration

Electromagnetic showers, which are key to this analysis, must also be calibrated. Due to the low number of electron neutrino induced electromagnetic showers occurring in the NOνA ND,

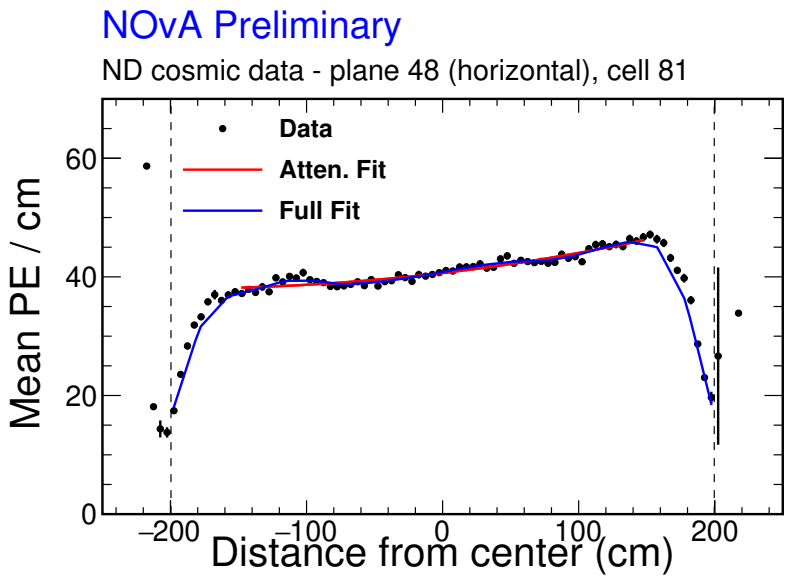

Figure 3.25: An example of how the detector response (PE/cm) varies along the length of a cell in the NOνA ND. The distance is measured relative to the center of the cell. The black points depict the measured data. A fit to the data is shown by the blue curve.

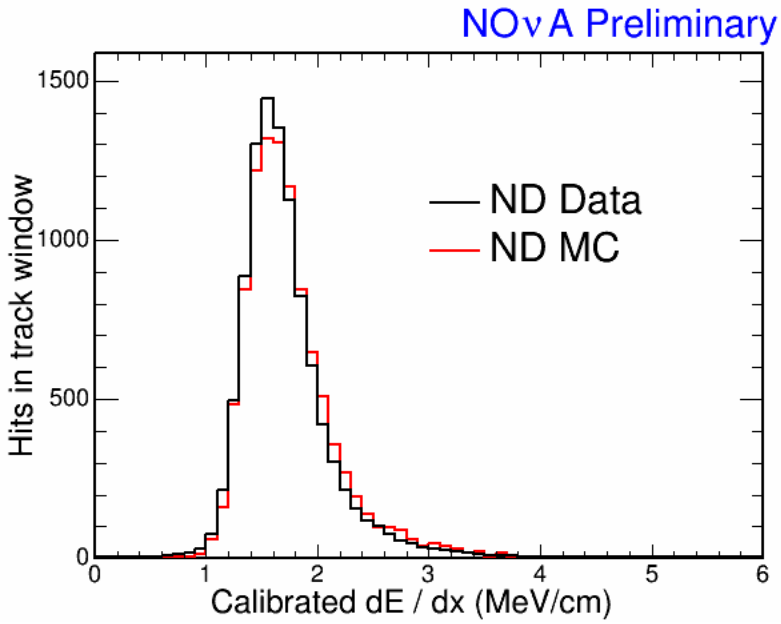

Figure 3.26: The calibrated dE/dx for hits near the end of a stopping muon track in the NOνA ND.

other data samples must be used. A technique that utilizes Bremsstrahlung showers resulting from cosmic muon tracks is used to study the detector response to EM showers.

The process begins with the identification of reconstructed cosmic muon candidates. The reconstructed tracks are required to enter and exit the detector and cross at least 30 planes within the detector. As a relativistic muon will deposit energy in the detector that is consistent with a minimum ionizing particle, an algorithm is used to find excess energy along the length the reconstructed track. This excess energy is assumed to be associated with a muon Bremsstrahlung photon that is depositing additional energy near the muon track. After identifying the regions with excess EM shower related energy all of the energy associated with only the muon are removed from the event, leaving behind a pure electromagnetic shower. This process is referred to as Muon Removed Cosmic Bremsstrahlung (MRBrem). An example illustrating the procedure is shown in the event displays of Figure 3.27.

This procedure is performed in both data and simulation to allow for a cross-check in the detector response to electromagnetic showers. As such no calibration constants are derived from this procedure. A comparison of deposited shower energy from data and simulated MRBrem events is shown in Figure 3.28. The differences between the data and MC shower distributions are accounted for with the systematic uncertainties derived from the absolute calibration procedure.

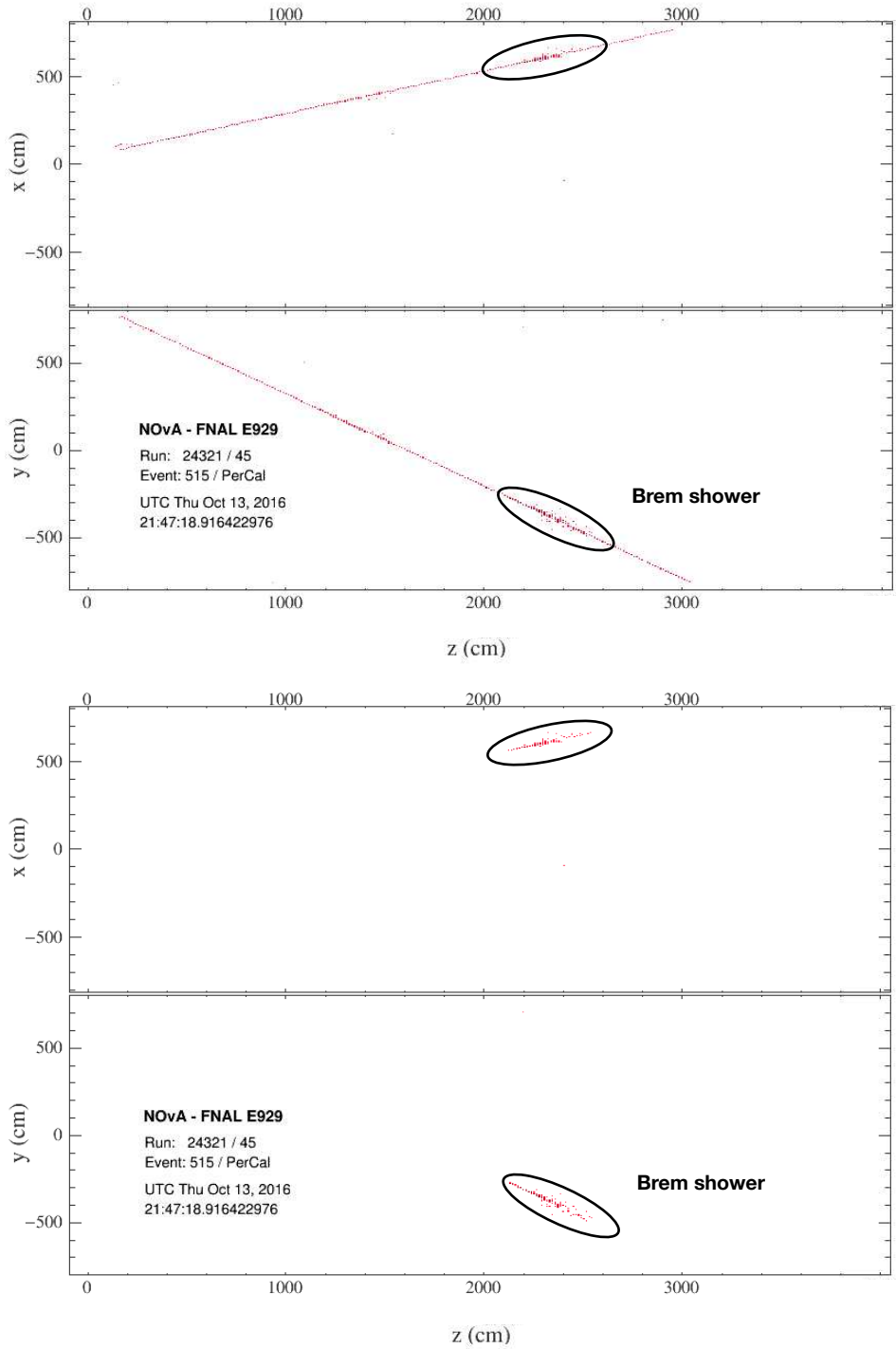

Figure 3.27: (Top)Comic muon track candidate with associated Bremsstrahlung shower in the NOνA FD. (Bottom) Results of the MRBrem procedure.

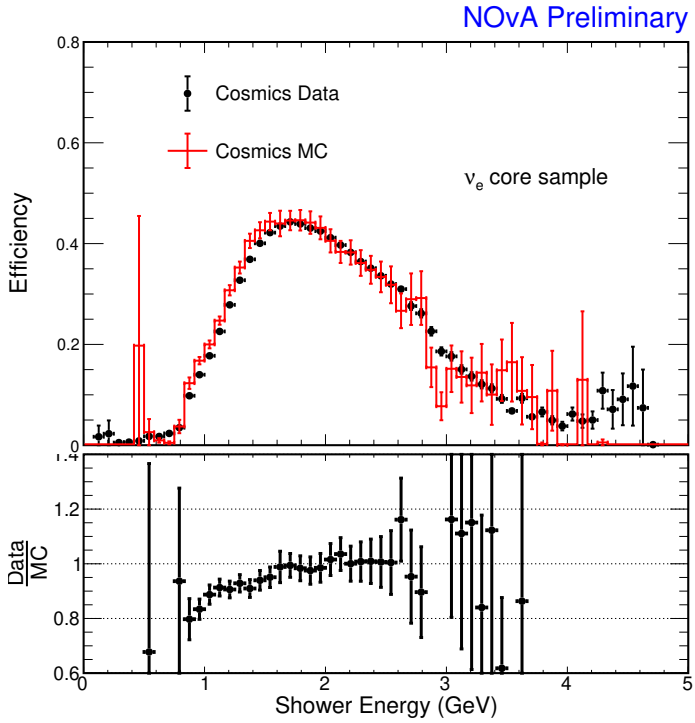

Figure 3.28: The reconstructed shower energy distribution of MRBrem events in data and simulation in the far detector after ν_e core selection (nominal ν_e selection used in the oscillation analysis).

Chapter 4

Inclusive ν_e Cross Section Analysis

The analysis presented in this thesis is a measurement of the inclusive ν_e- nucleus interaction cross section. An improved understanding of this interaction will lower uncertainties in oscillation analyses, as ν_e-nucleus interactions are the signal of electron neutrino appearance measurements. This measurement will also add to the overall understanding of neutrino-nucleus interactions. A measurement of the ν_e CC differential cross section is presented as a function of final-state electron kinematics. This chapter provides the background to how cross section measurements are made and the techniques used to extract the electron neutrino cross section using the NOνA detector.

4.1 Scattering Cross Section

A scattering cross section, σ, is a measure of the rate at which a particular particle-target interaction occurs. For a hard inelastic sphere, like that occurring between billiard balls, this probability is directly related to the geometric area of the balls, or the effective area for the collision to occur. In physics, this effective area is called a cross section. For billiard balls, the cross section can easily be measured and determined but if particles interact through an action-at-a-distance force the measurement becomes more complicated.

Consider an experiment where a beam composed of some small point-like particles is directed at a thin sheet of some material. If the beam particles are scattered only when they interact with a nucleus in the thin sheet, the overall scattering cross section for each of the target nuclei is defined as:

$$\sigma = \frac{\text{\# Scattered Particles}}{\text{Beam particles per unit area} \times \text{Total \# of Target Particles}} \tag{4.1}$$

where σ is defined as the total cross section, which has units of area. Although cross sections are given in units of area, for semi-transparent targets (like weak interactions of neutrinos with a

nucleus) the measured cross section will typically be much smaller than the actual size of scattering particles.

Once the total cross section is defined, additional questions may be considered such as: does the total cross section vary with the energy of the incoming particle, or how often does the scattered particle get ejected at a particular angle? When a cross section is specified in terms of a final-state variable, like particle energy or angle, it is called a differential cross section. An example of the measurement of a differential cross section is shown in Figure 4.1. In this illustration, the incoming particle is incident on a stationary target, with an impact parameter, b, which is the perpendicular offset of the incoming particle from the center of the target. After the interaction the outgoing particle exits at scattering angle, θ, which is the angle measured between the direction of incoming particle and the scattered particle. The probability of scattering through solid angle, $d\Omega$, is given by $d\sigma$, or the differential cross section. The differential cross section can be found as $d\sigma/d\Omega$, giving insight into how the cross section varies with the scattering angle. The total cross section can be obtained from the differential cross section by integrating over the full solid angle:

$$\sigma = \int_0^{2\pi} \int_0^{\pi} \frac{d\sigma}{d\Omega} \sin\theta d\theta d\phi \tag{4.2}$$

4.2 Measuring a Cross Section

In essence, this thesis is concerned with the question of: what is the probability that an electron neutrino will undergo a charged-current interaction with a nucleus and produce a particular result? This will be answered through a measurement of the ν_e CC event rate. This rate is then used to calculate the total and differential cross sections. The total cross section is measured using the following definition of the the cross section:

$$\sigma = \frac{N_{\text{sel}} - N_{\text{bkg}}}{\epsilon N_{\text{t}} \Phi} \tag{4.3}$$

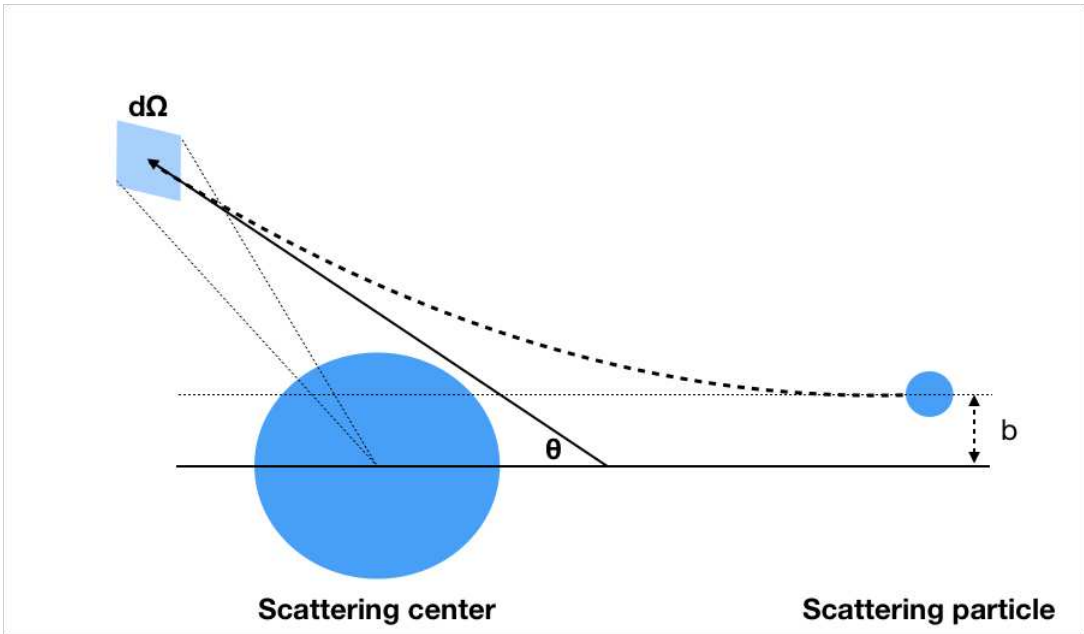

Figure 4.1: A diagram of a two-particle scattering process. One particle is scattered off of a single scattering center. The impact parameter and the solid angle element in the exit direction are marked.

where N_{sel} is the total number of selected events, N_{bkg} is the estimated number of background events, N_{t} is the number of target nucleons in the detector, Φ is the flux of electron neutrinos, and ϵ is the signal selection efficiency defined as:

$$\epsilon = \frac{\text{\# Selected Signal Events}}{\text{\# True Signal Events}} \tag{4.4}$$

Equation 4.3 is equivalent to Equation 4.1. $N_{\text{sel}} - N_{\text{bkg}}$, gives the total number of signal scattering interactions that we are interested in measuring. This value is corrected by the signal selection efficiency, which is a measurement of the ability to reconstruct and identify signal interactions in the experiment. Additionally, the definition of flux and the number of targets carry over exactly from the previous equation.

Although the total cross section is important, additional information can be obtained by measuring is the total cross section as a function of incoming neutrino energy. This is measured as:

$$\sigma(E_i) = \frac{\sum_j U_{ij}(N_{sel,j}(E_j) - N_{bkg,j}(E_j))}{N_t \Phi(E_i)\epsilon(E_i)} \tag{4.5}$$

where all of the previous factors from Equation 4.3 depend on neutrino energy, E. Additionally, the subscripts i and j refer to the true bin, i and reconstructed bin, j. This reflects the fact that the reconstructed quantities, like neutrino energy, will in general differ from their true value due to various detector and reconstruction effects. These are related through what is called an unfolding matrix, U, which maps reconstructed quantities to the true quantities predicted through detector and neutrino event simulations.

Measuring the cross section as a function of outgoing electron kinematics provides the most information to help improve neutrino-nucleus interaction models. This is done through the measurement of a flux-integrated differential cross section as a function of the kinematics of the final state electron:

$$\left(\frac{d^2\sigma}{dE_e d\cos\theta_e}\right)_i = \frac{\sum_j U_{ij}(N_{\text{sel},j}(E_e,\cos\theta_e) - N_{\text{bkg},j}(E_e,\cos\theta_e))}{N_t \Phi \epsilon(E_e,\cos\theta_e)_i \Delta(E_e)_i \Delta(\cos\theta_e)_i} \tag{4.6}$$

where besides the the dependence on electron energy and angle, the only additional terms are $\Delta(E_e)$ and $\Delta(\cos\theta_e)$ which are the bin widths to define the electron kinematic variables.

The signal for this measurement is defined to be all charged-current electron neutrino interactions of the form $\nu_e + N \rightarrow e^- + X$ that occur within the fiducial region of the detector, where "fiducial" region refers to a central area of the detector where the detector response is well understood. In the signal definition X can include any number of nucleons, pions, or kaons in the final state. All interactions that do not fit this criteria are regarded as background interactions. This includes ν_e CC interactions that do not occur inside the fiducial region of the detector, all neutral current (NC), ν_μ CC, and any $\bar{\nu}_e$ or $\bar{\nu}_\mu$ interactions.

It is of particular importance that the extracted cross section is not biased by assumptions, such as the neutrino-nucleus interaction simulation. To reduce the bias as much as possible, the analysis avoids any substantial dependence on the input interaction simulation. This is done through several careful considerations. The first is requiring that the cross section is measured as a function of directly observable quantities from the NOνA detector that do not require any particular assumptions about a specific type of model, such as the reconstruction of neutrino energy, which

requires making assumptions about the outgoing kinematics of final-state particles. The cross section is only measured in a region of electron kinematic phase-space* that the NOνA near detector is sensitive to. The extracted cross section signal definition is defined as an inclusive measurement with the only requirement being that the final-state lepton is an electron from the primary neutrino interaction. This requirement ensures that there is no dependence on a nuclear model being used to predict the correct FSI effects on final-state hadronic particles. Finally, the analysis is based on extensive fake data studies to ensure that the methods used to extract the cross section remain unbiased across a wide range of possible scenarios that may reflect those found using the real data. Additionally, no signal-region data were used throughout the development of the analysis. This is referred to as a blind analysis. Blind analyses provide a way to reduce or eliminate the potential of biasing a result in a particular direction based on features observed in data.

An overview of the ν_e inclusive analysis is shown in Figure 4.2. The strategy is to develop the entire analysis using the nominal ND simulation. This process begins with determining the event selection criteria to determine the rate of ν_e CC interactions in the ND. After the selection criteria is developed the selected signal events are evaluated to determine the detector resolution of electron kinematic variables that define the binning that the analysis will be measured in. The event selection efficiency is then studied using the nominal ND simulation, as well as a data-driven correction to the efficiency calculation through the use of ND sideband data†. Similarly, this analysis makes use of a data-driven technique to provide estimates of signal and background events. The development of this technique is done through the use of simulated events, called fake data. The final step of the analysis is the examination of all systematic uncertainties, which are then used to optimize several steps throughout the analysis framework. After a thorough assessment of the analysis procedure using fake data, which is a simulated set of proxy data events that differ from the simulated events used to develop the analysis, the near detector data is used and the cross section measurement is made.

*A mathematical space of all possible momenta of the outgoing electron.

†A sideband describes a set of selected events in the ND data that are not in the primary selected sample used for the cross section analysis

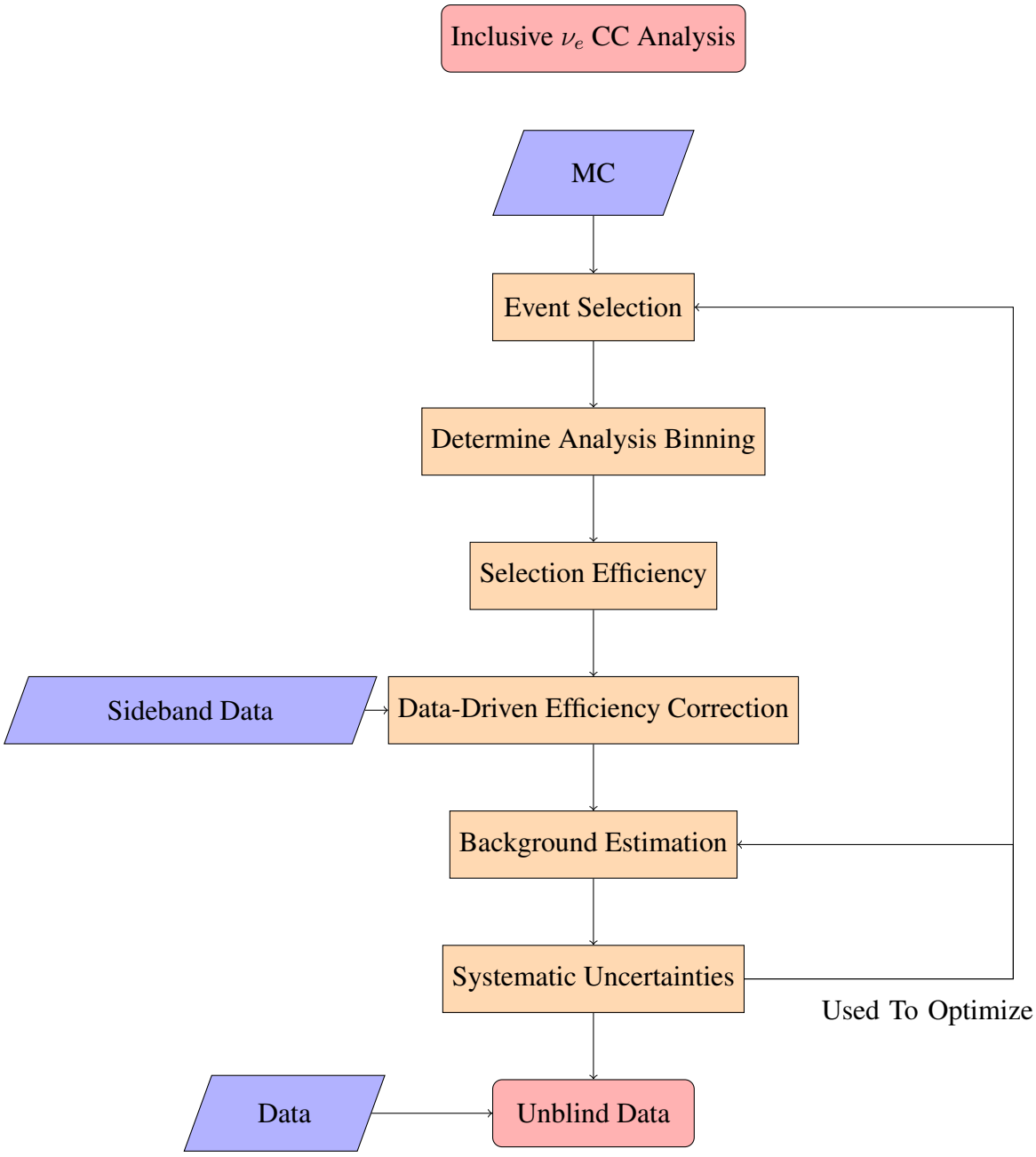

Figure 4.2: A simplified schematic of the steps of the inclusive ν_e CC analysis

The following sections will describe each of the techniques used to extract the cross section measurement. The signal selection criteria are outlined in Section 4.3. The resolution studies used to determine the binning used for the measurements are described in Section 4.4. A data-driven technique for background estimation is described in Section 4.9. The final measurement will be made as a function of true quantities requiring unfolding techniques to be used to relate reconstructed quantities to truth. The description of studies relating to unfolding and determination of the unfolding technique to be used are described in Section 4.10. Efficiency corrections are detailed in Section 4.5. Systematic uncertainties are described in Section 4.11.

4.3 Event Selection

The first step in the analysis is to develop a set of selection criteria that obtain a sample of ν_e CC-like interactions from the total sample of simulated interactions. Events with any activity in the muon catcher (where active planes are interlayed with steel planes) are not considered in the analysis. Selected events with one electron and any number of final state particles and a reconstructed vertex within the fiducial volume of the detector are considered to be true signal events.

The two main sources of background events are beam induced backgrounds from neutral current and ν_μ charged-current interactions, particularly, those with one or more π^0s in the final state. An additional source of background interactions is events coming from interactions that occur outside of the detector but that produce activity within the detector. This latter type of interaction includes through-going muons that are produced via a ν_μ charged-current interaction occurring in the rock surrounding the detector. These muons can produce bremsstrahlung showers within the detector that can mimic signal interactions.

4.3.1 Minimization of Cross Section Uncertainties

The general selection strategy in this analysis is to determine selection criteria that minimize both the systematic and statistical uncertainties on the total cross section, as given in Equation 4.3. The figure of merit used in this analysis is derived from that Equation 4.3, by making the as-

sumption that uncertainties on the flux and the number of targets are only slightly dependent on the selection criteria. Furthermore, any correlations between the estimated number of background events and the total selection efficiency are additionally ignored. The figure of merit is the fractional uncertainty on the cross section and is defined as:

$$\frac{\delta\sigma}{\sigma} = \sqrt{\frac{N_{\text{sel}}^{\text{stat}} + N_{\text{bkg}}^{\text{stat}} + (\delta N_{\text{bkg}}^{\text{syst}})^2}{(N_{\text{sel}} - N_{\text{bkg}})^2} + \left(\frac{\delta\epsilon}{\epsilon}\right)^2} \tag{4.7}$$

The systematic uncertainties are represented by each δ term, these uncertainties include cross section model, detector modeling, and detector calibration. Each of these sources of uncertainty are discussed in Section 4.11.

4.3.2 Preselection

Preselection is a set of selection criteria that is defined before looking at any of the physical characteristics of an event. A preselection defines a baseline sample of interest, and is used to remove any events associated with poor detector running conditions, events outside of the fiducial volume of the detector, and events with particles that exit the detector. This section defines the preselection criteria used within this analysis.

Data Quality

The data quality selection reflects the data taking conditions of both the detector and beam when the data were recorded. This selection ensures that a standard of quality is met for the collected data before of the event reconstruction is performed. The cuts are standard across all NOvA analyses.

The quality selection of the detector running conditions:

- **Number of active diblocks[‡] = 4**: Ensures that a region of the detector sufficiently large to contain events was active during data collection.

[‡]A physical unit of a number of planes on a NOνA detector. For the near detector there are only 4 diblocks: three composed of 64 planes, and 1 (the muon catcher) composed of 22 planes

- **Timestamp**: The time that the data were taken is correctly synchronized with the NuMI beam spills.

- **Hit Rate**: Overall hit rate within the detector is stable with respect to the average recorded values. This is designed to ensure that the noise rate is within the expected range.

- **Tracking**: A high fraction of tracks reconstructed in 2D are able to be view matched in 3D. If this was not true it would indicate a region of the detector was not correctly synchronized with the rest of the detector.

- **Average Number of Slices**: Ensured that the entire detector was successfully read out and that the timing resolution was stable across the detector.

The following set of cuts[§] ensure that the quality of the beam being delivered to the experiment meets a minimum set of standards:

- **Fraction of hits occurring outside the beam peak < 0.45**: Ensures that the taken data corresponds to the time of the beam spill. The number of hits collected in the beam window has a strong dependence on the beam intensity. The hits outside of the beam window are directly related to electronics noise in the ND.

- **Time Delay between NuMI time stamp and spill < 0.5 ns**: Ensures that the taken data correspond to the time of the beam spill.

- **-202 < Horn current (kA) < -198**: Ensures that the magnetic horn current is within the nominal expected value to produce the focusing necessary to properly predict the neutrino flux at the NOνA detectors.

- **2.0 < Beam x and y position on target (mm) < 2.0**: Ensures that the beam was correctly positioned on the target such that the interactions produce the expected flux.

[§]Selection criteria are commonly referred to as "cuts" in high energy physics

- **0.57 < Beam width in x and y < 1.58**: Ensures that the beam was correctly focused such that the target interactions produce the expected flux.

Event Reconstruction Quality

These selection criteria are designed to ensure that data were not taken when the detector was in a sub-optimal condition or that there are events with reconstruction failures. One additional detector issue is the presence of "FEB Flashers" within reconstructed slices. FEB Flashers are induced by high energy cosmic rays that interact with in the APD, these are observed as multiple contiguous hits on the same plane. The event reconstruction quality selection criteria are:

- **Number of Hits in a Single Plane < 8**: Designed to cut out FEB flashers.
- $\mathbf{N_{vtx} > 0}$: Requires a reconstructed vertex
- $\mathbf{N_{prong} > 0}$: Requires at least 1 reconstructed prong.
- $\mathbf{N_{shw} > 0}$: Requires at least 1 reconstructed shower.
- $\mathbf{N_{shw,hit,x} > 6}$ **or** $\mathbf{N_{shw,hit,y} > 6}$: Require greater than 6 hits in a single view of the reconstructed shower.
- **Distance from leading reconstructed shower to event vertex < 100 cm**: A gap of this distance is greater than 3 times the radiation length of EM showers within the NOνA detectors. Such a gap is most likely due to reconstruction failures.
- **Cosine of angle between the two leading showers < -0.95**: This criterion removes events where the most energetic prongs have a large angle with respect to each other. This is a remedy for a reconstruction artifact where an event with a gap (which could be do to bad channels on the detector) has its leading prong reconstructed into two separate prongs going in opposite directions.
- $\mathbf{(N_{shw,hit,x} - N_{shw,hit,y})/(N_{shw,hit,x} + N_{shw,hit,y}) > 0.40}$: This criterion removes events with a large difference between the number of hits in 3D reconstructed showers. If a large difference

between the number of hits in each view is observed it likely indicates an issue with 3D view matching.

- **Fraction of Hits in Showers < 0.7**: Removes events where small fraction of hits are reconstructed into a shower, as such showers potentially have a high contamination of noise hits

Fiducial Volume

The charged-current inclusive ν_e cross section is measured per nucleon and thus the determination of the number of nucleons in the fiducial volume directly impacts the cross section measurement. The determination of the fiducial volume was based on the figure of merit described previously using cuts placed on the reconstructed interaction vertex. Figure 4.3, shows the individual terms of the FOM (Equation 4.7), and their sum. The detector coordinate system is defined by placing the center of the detector at 0 cm, in the X and Y directions, with the sides of the detector at ± 200 cm. The figure of merit is calculated in each bin independently, and thus the plots in the figure show the fractional uncertainties on a bin-by-bin basis. The plots are used to determine the regions of the detector that contribute most significantly to the uncertainties on the cross section measurement. The statistical uncertainties on selected signal and background events are seen in the upper-most row of plots. These plots show that the number of reconstructed events with vertices near the edges of the detector falls off rapidly, and that the fractional statistical uncertainty increases accordingly. The middle row plots contain the systematic uncertainties on the selected background events and the efficiency of signal event selection. The calibration and light-model systematics contribute highly at the edges of the detector (near ± 200 cm), while the neutrino-nucleus interaction uncertainties are the largest contribution to the systematic uncertainties as seen in the "flat" portion of the distribution. The sum of all the terms shows a relatively flat distribution from -130 to 150 cm in the X-view, while the uncertainties outside of this region rise rapidly. The fiducial region was chosen to be in the region where the uncertainties were flat. Optimization of cuts on the figure of merit is always done using minimum regions of $\delta\sigma/\sigma$, and by avoiding regions where the value is changing rapidly.

The optimization of the fiducial volume using the reconstructed vetex in the Y dimension is shown in Figure 4.4. The features seen in these distributions are similar to the what were seen in the distributions discussed above. For both the X and Y vertices the distributions are asymmetric when comparing across the origin, in terms of the vertex position. This is primarily due to particles coming from the +y and -x from events in the rock surrounding the detector. This corresponds to the direction of the NuMI target from the near detector.

Figure 4.5 shows the Z-position fractional uncertainties used in the figure of merit. One of the requirements of the analysis was to ensure that no activity from a neutrino-induced event would have final-state particles entering the muon catcher region of the detector. Such events result in a rapid increase in fractional uncertainty as it approaches the muon catcher. A relatively flat region of fractional uncertainty is seen from 150 to 800 cm, and this defines the fiducial region of the detector in the Z view.

The final selection regions of the vertex position are shown by the region in-between the black arrows in Figures 4.3- 4.5. The exact values used to define the event vertex cuts and the fiducial volume of the detector are:

- -130.0 $<$ X(cm) $<$ 150.0
- -140.0 $<$ Y(cm) $<$ 140.0
- 150.0 $<$ Z(cm) $<$ 800.0

4.3.3 Containment Volume

To ensure that electron energy was completely reconstructed for all selected events, the analysis required that all neutrino-induced activity be contained within the a predefined volume in the detector, called the containment volume. The containment volume is determined by calculating the fractional cross section uncertainty as a function of the minimum distance of a prong from each face of the detector, which is the distance of the closest cell hit within a prong to a face of the detector wall.

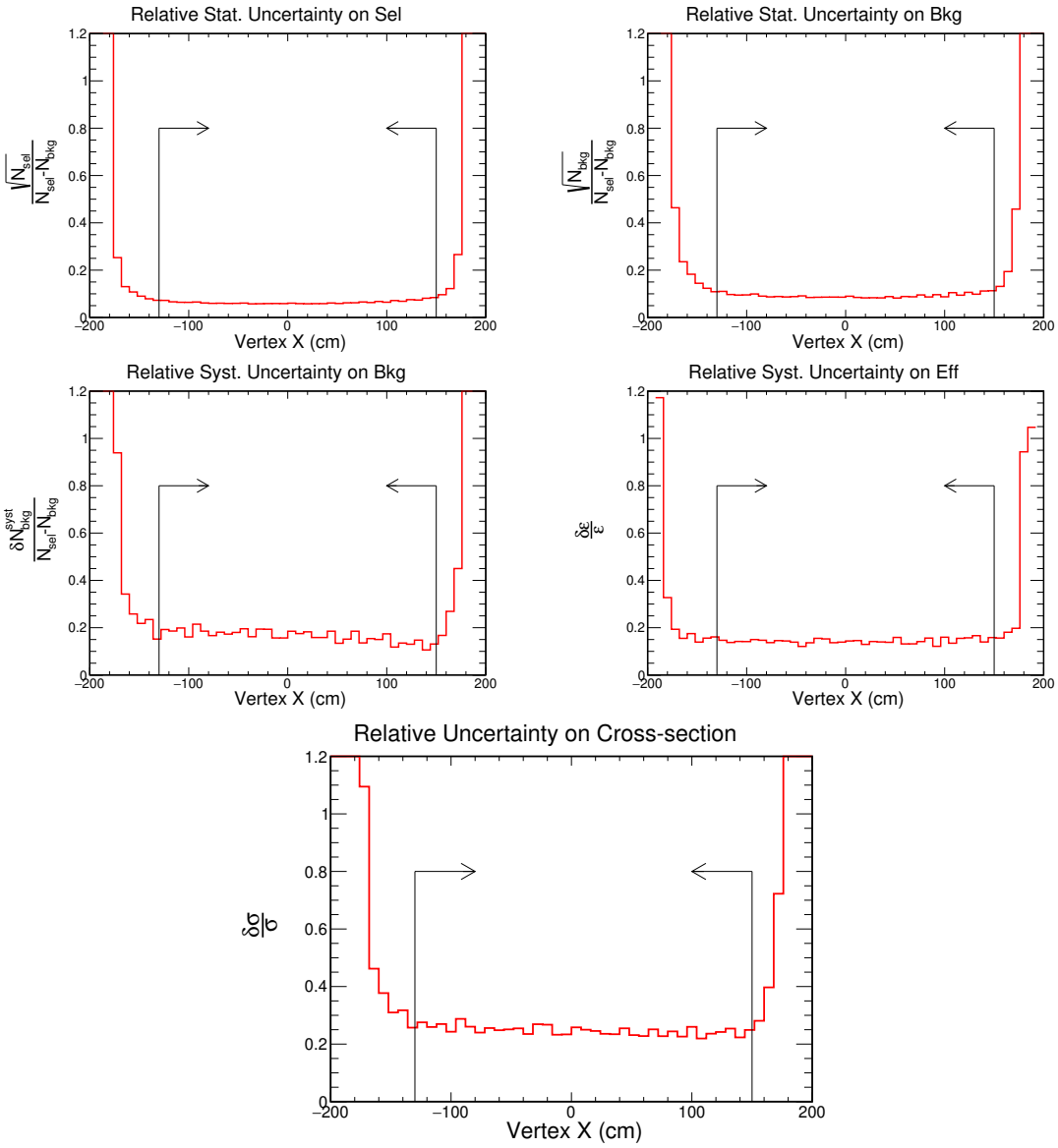

Figure 4.3: Plots of the individual terms of the fractional cross section uncertainty (Equation 4.7) used for the optimization of the fiducial volume with respect to the vertex x position. Arrows indicate the fiducial volume boundaries for this analysis.

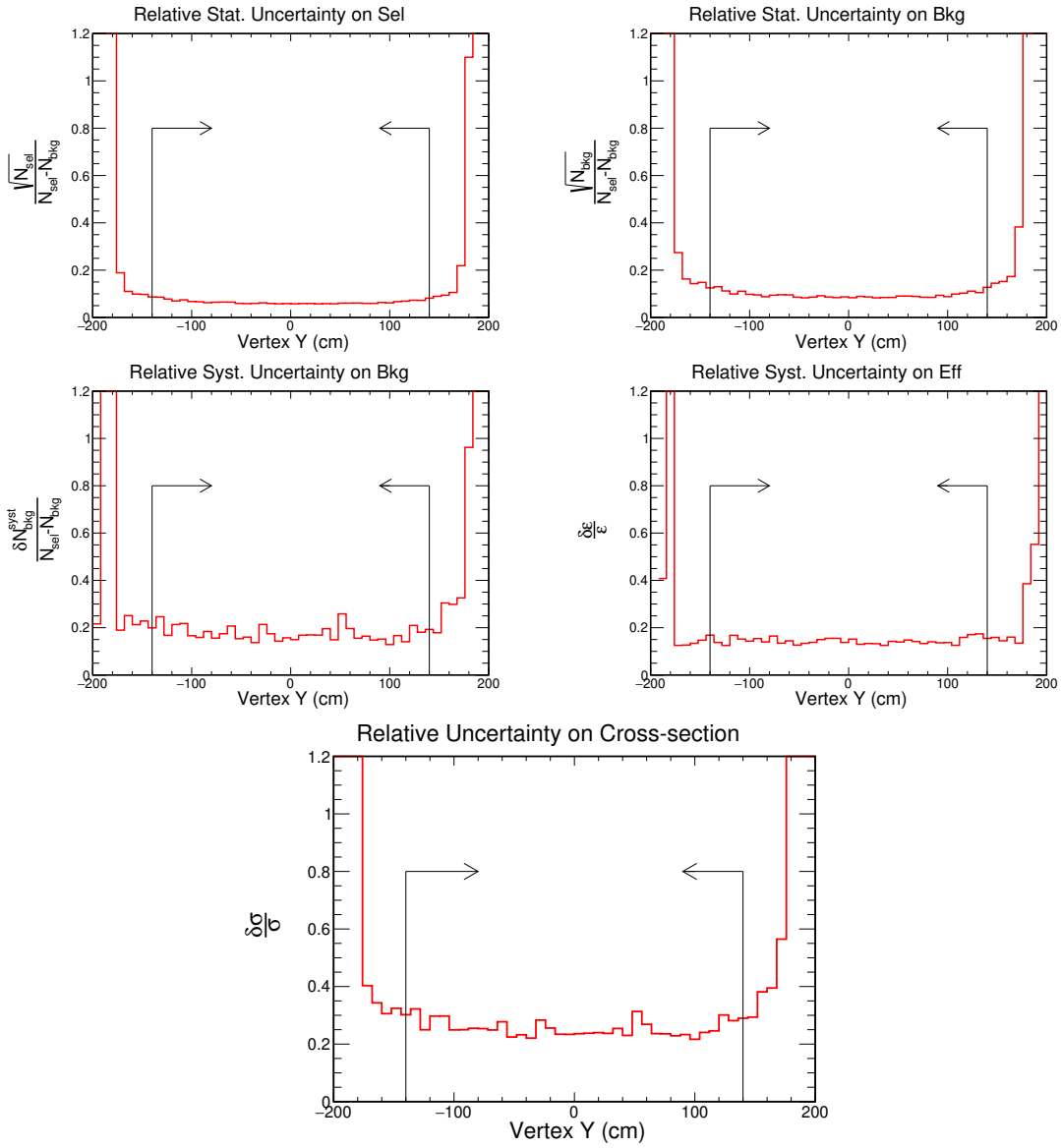

Figure 4.4: Plots of the individual terms of the fractional cross section uncertainty (Equation 4.7) used for the optimization of the fiducial volume with respect to the vertex y position. Arrows indicate the fiducial volume boundaries for this analysis.

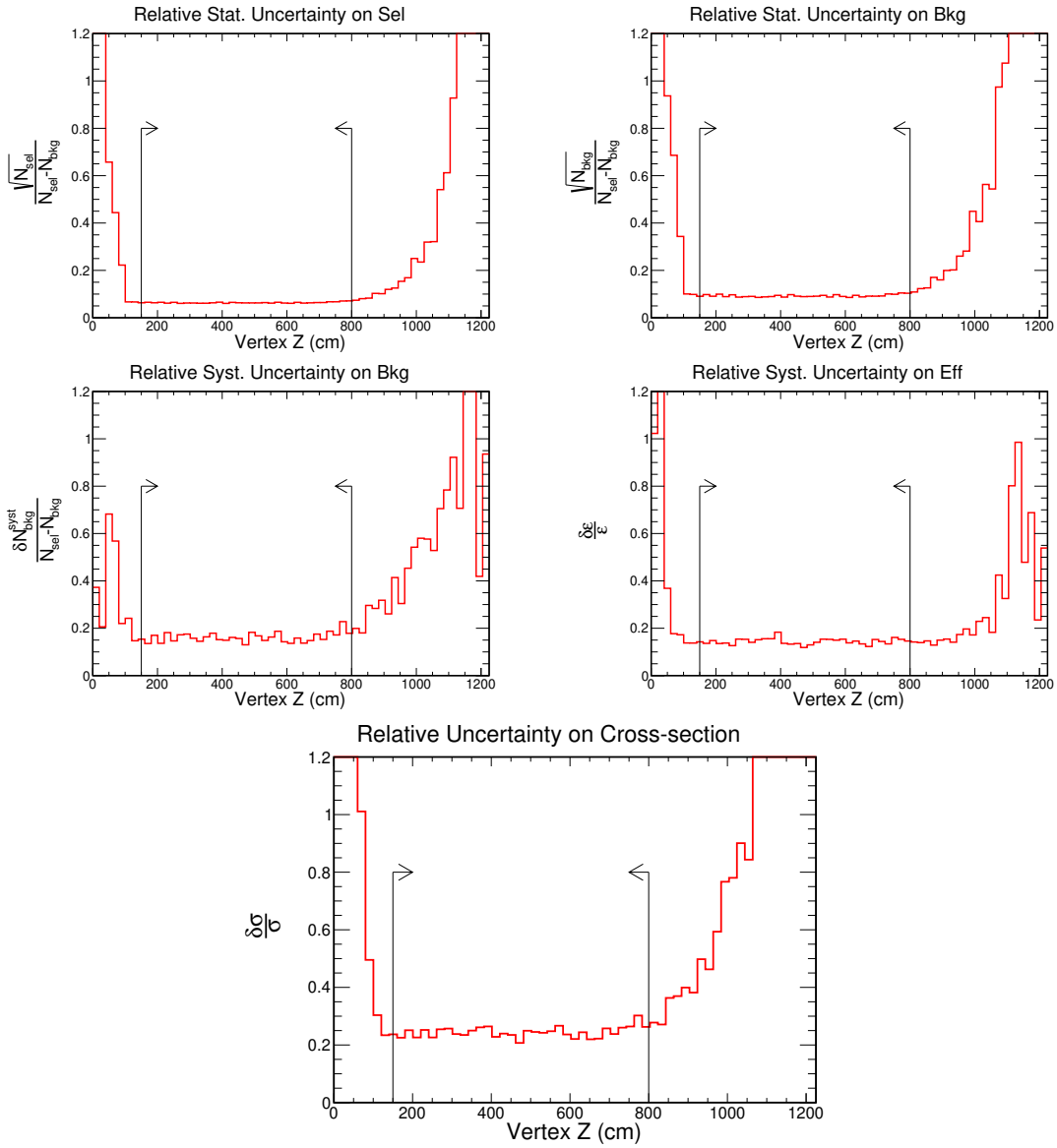

Figure 4.5: Plots of the individual terms of the fractional cross section uncertainty (Equation 4.7) used for the optimization of the fiducial volume with respect to the vertex z position. Arrows indicate the fiducial volume boundaries for this analysis.

Table 4.1: Summary of containment volume definitions and the fractional cross section uncertainties used to determine the volume.

Face of Detector	Minimum Prong Distance (cm)	$\delta\sigma/\sigma$	$\sqrt{N_{\text{sel}}}/(N_{\text{sel}} - N_{\text{bkg}})$	$\sqrt{N_{\text{bkg}}}/(N_{\text{sel}} - N_{\text{bkg}})$	$\delta N_{\text{bkg}}^{\text{syst}}/(N_{\text{sel}} - N_{\text{bkg}})$	$\delta\epsilon/\epsilon$
Upstream	150	0.94	0.13	0.25	0.89	10.17
Downstream	90	0.6	0.16	0.26	0.46	0.20
Eastern	55	0.94	0.13	0.25	0.89	0.17
Western	30	1.01	0.14	0.27	0.89	0.13
Top	50	1.08	0.14	0.26	1.02	0.18
Bottom	30	1.04	0.14	0.26	0.98	0.19

Figure 4.6, shows the individual terms and the fractional cross section uncertainty calculated as a function of the minimum prong distance from all hits within reconstructed prongs from the top face of the detector. The upper-most row of plots show the statistical uncertainties on selected and background events. The middle row plots show the fractional uncertainties on the estimated number of background events and the signal selection efficiency. While the fractional uncertainty on signal selection efficiency is shown to be flat, the fractional uncertainty on the number of background events has a well defined shape. The shape of this distribution is due to detector calibration and modeling uncertainties near the face of the detector wall. The rapid rise at the opposite end of the spectrum is driven by statistical uncertainties, due to the relatively low rate of events that are almost 3.5 meters from any face of the detector after the fiducial volume criteria has been applied. The black arrow indicates the containment boundary for this analysis from the top face of the detector used in this analysis. Table 4.1 provides a summary of the other containment boundaries.

4.3.4 Additional Event Selection Criteria

The following event selection criteria were designed to remove some of the neutrino events with event topologies consistent with backgrounds to the ν_e CC signal.

- **Number of planes to the front of detector $>$ 6**: Removes events reconstructed with a fiducial interaction vertex that were incorrectly sliced and allow charged particles from rock interactions that enter the upstream face of the detector to be included.

- **20 $<=$ Number of Hits in Slice $<=$ 200**: Events with less than 20 hits are more likely to come from neutral-current (NC) interactions, or from random groupings of noise hits. This

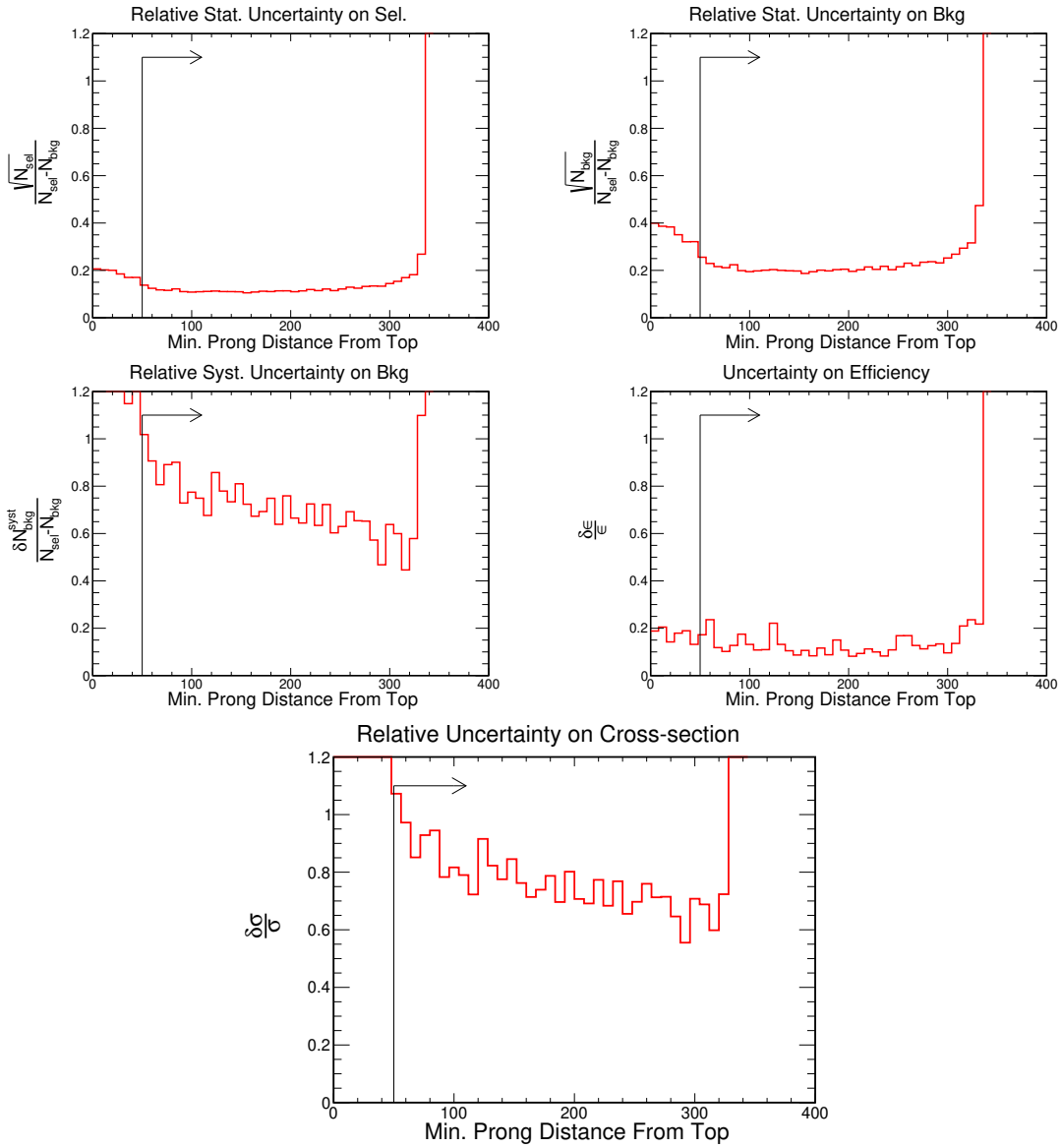

Figure 4.6: Plots of the individual terms of the fractional cross section uncertainty (Equation 4.7) used for the optimization of the containment volume with respect to the minimum distance to the top face of the detector of all hits within reconstructed prongs. The arrow indicates the containment volume boundary for the analysis.

class of events is not often well reconstructed and so are removed. The minimum threshold for recorded hits within the detector is about 20 - 60 MeV, thus this requirement removes events with less than approximately 0.4 GeV in deposited energy. Events with greater than 200 hits are removed due to the low reconstruction efficiency of events with many particles in the final state.

4.3.5 Muon Discrimination

The NOνA neutrino beam is composed of greater than 95% muon neutrinos, so ν_μ CC events make up a large component of the backgrounds for this analysis. The large number of background events is primarily due to ν_μ CC interactions that produce photon-induced electromagnetic showers in the final state, along with the final state muon. Depending on the length of the muon track these events can be misidentified as ν_e CC interactions. Charged-current ν_μ interactions with prominent muon tracks can be easily distinguished from ν_e CC interactions using a multivariate muon identification algorithm. The inputs to this algorithm are:

- **Differential energy loss (dE/dx)**: Log-likelihood differences used to discriminate between muon and pion assumptions.
- **Scattering**: Log-likelihood differences between a muon and pion assumptions used to separate muon produced tracks from the pion induced track background.
- **Average dE/dx in last 10 cm of a track**: Identify the Bragg peak[¶], used to discriminate muons from protons, which typically have a larger Bragg peak
- **Average dE/dx in last 40 cm of a track**: Used to identify the Bragg peak

These variables are used as inputs to a Boosted Decision Tree (BDT)[88], as part of the muon selection. The algorithm is trained on muon (and anti-muon) and background non-muon induced

[¶]A Bragg peak describes the characteristic energy loss as a heavy particle slows down in matter. More energy per unit length will be deposited towards the end of the particles path than at its beginning. [68]

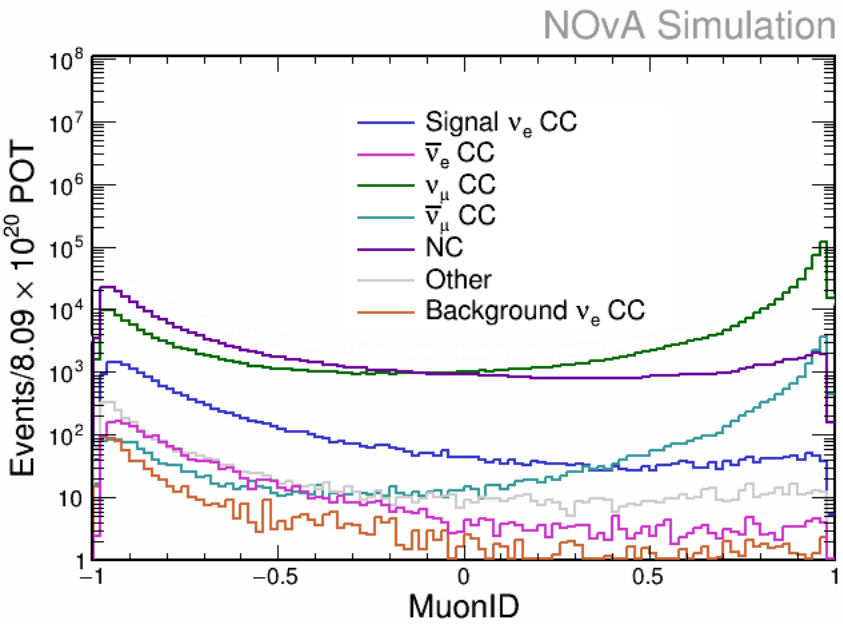

Figure 4.7: Plots of the MuonID distribution following application of all selection requirements. The Y-axis is plotted on a log-scale for ease of visualization of ν_e CC signal events.

.

tracks reconstructed from simulated neutrino interactions. The BDT produces a score corresponding to the likelihood of a track being a true muon. This BDT score is referred to as MuonID and is reported for each reconstructed track.

The distribution of the BDT score for the highest scoring MuonID track in an event is plotted in Figure 4.7. Selected ν_e CC signal events typically have a low BDT score for MuonID while background ν_μ CC interactions are peaked toward high MuonID scores. A requirement on the MuonID score is used for the removal of ν_μ CC background events with clear muon tracks in the final state.

The event selection requirement is optimized using the fractional cross section uncertainty as shown in Figure 4.8. The expected fractional uncertainty is calculated as a function of MuonID cut value, with the dominant systematic contributions to the fractional uncertainty on the selected background events shown in the upper plot. The fractional cross section uncertainty figure of merit is shown in the bottom plot. The shape of the fractional cross section uncertainty is driven by calibration uncertainties at low MuonID score cut values and by neutrino-nucleus interaction

uncertainties at high MuonID score cut values. A flat region in fractional cross section uncertainty occurs from -0.5 to -0.30, the optimal requirement on the highest scoring MuonID track in an event of less than -0.30 is used within this analysis.

4.3.6 Summary of Event Selection

With each of the selection requirements defined, it is helpful to understand the selection of simulated events by interaction type (ν_e CC, ν_μ CC, NC, etc). This breakdown of selected events is depicted in Table 4.2. All numbers within the table are normalized to the protons-on-target recorded for the NuMI dataset collected for this analysis, 8.09×10^{20} POT. In addition to the signal and major background components depicted in the table, several smaller background components are also tabulated. These backgrounds include the number of out-of-detector ν_e CC events where the true interaction vertices are outside of the fiducial volume but that have been reconstructed inside of the fiducial volume. Other events are labeled as "Other", which typically consist of single particles that are in a different reconstructed slice than the true neutrino interaction that produced them or are additional GENIE predicted background processes[‖].

It is worth noting that the event selection for this analysis does not include a traditional signal selection cut, where a final cut is applied to obtain a relatively pure sample of signal events. Instead, the analysis uses the power of machine learning techniques (such as those discussed in Section 3.2) to produce templates to perform data-driven signal and background estimations. While this analysis does not use this type of selection cut, the potential use of CVN to select ν_e signal events is shown in the final row of the table. The inclusion of the CVN requirement illustrates the power of this event identification technique and demonstrates the ability of CVN to discriminate between signal and background events. Although a selection criteria using CVN is not used within the analysis, the CVN classifier forms the basis for the data-driven signal and background estimation

[‖]This can include additional neutrino-nucleus interactions like inverse beta decay or other more theoretical processes[63]

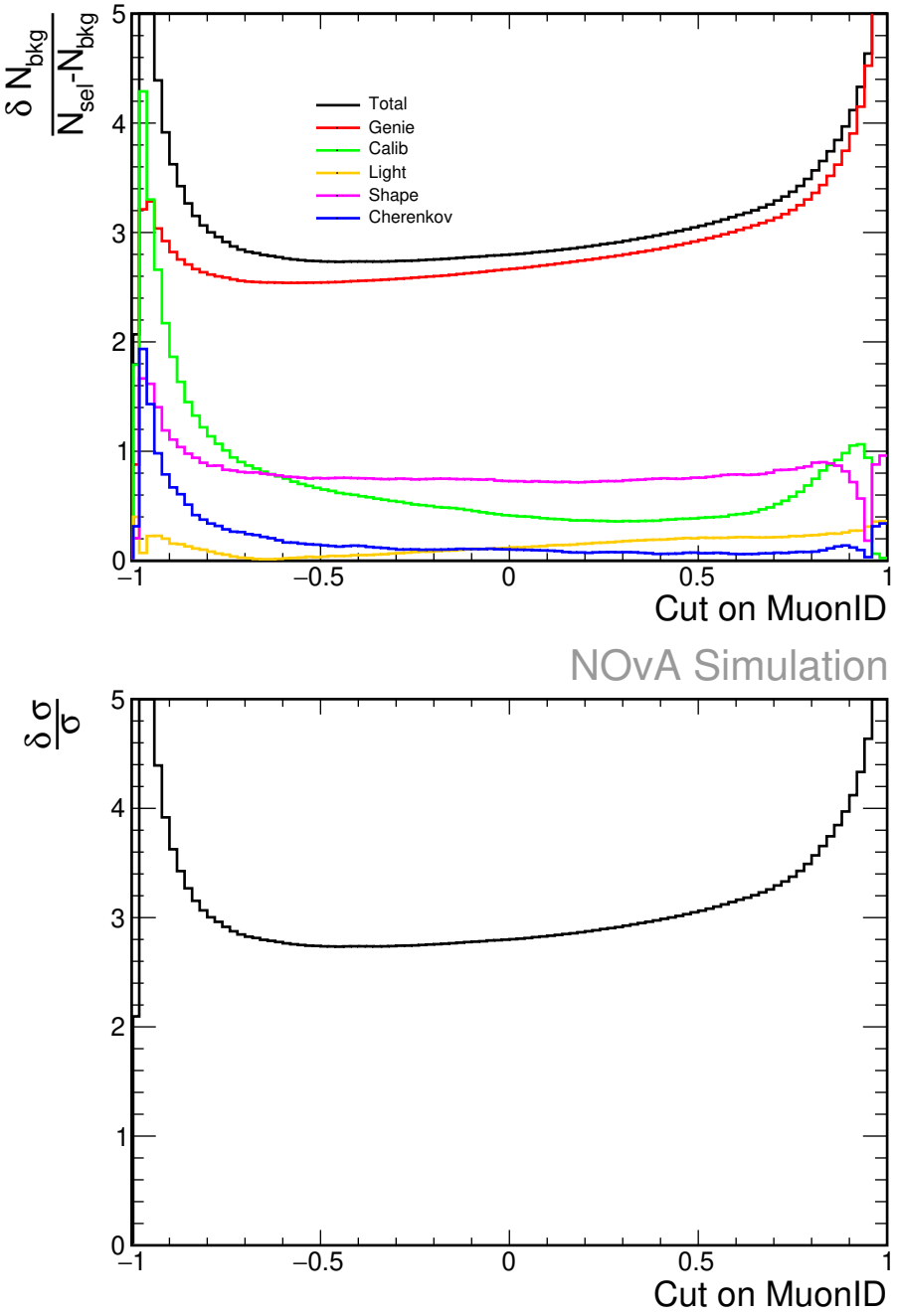

Figure 4.8: Plots used for the optimization of MuonID event selection requirement. Top: The contribution of systematic uncertainties on selected background events. Bottom: The total fractional uncertainty on the cross section. Both plots are made with respect to the MuonID cut value.

Table 4.2: Summary of selected events from simulation, broken down by interaction type. The number of events is normalized to the collected data exposure of 8.09 $\times 10^{20}$ POT.

Cut	**Total MC**	**Signal**	**Backgrounds**						
		ν_e CC	Total	ν_μ CC	$\bar{\nu}_\mu$ CC	NC	$\bar{\nu}_e$ CC	Background ν_e CC	Other
All Events	141,441,000	132,315	141,309,000	113,943,000	4,997,710	16,510,200	142,701	1,484,200	4,230,980
Data Quality	89,835,600	123,389	89,712,200	78,716,600	3,634,130	6,313,330	68,988	636,802	342,414
Fiducial	7,188,850	116,454	7,072,400	5,691,320	223,809	1,120,630	12,184	8,381	16,082
Containment	1,017,510	28,926	988,589	625,159	16,315	335,111	3,746	1,245	7,013
Front Planes	1,009,850	28,813	981,039	619,473	16,061	333,601	3,726	1,218	6,960
NHits	909,639	17,848	891,791	589,699	15,146	280,451	2,019	868	3,607
MuonID	366,574	15,562	351,012	123,147	1,748	220,508	1,807	782	3,019
CVNe	15,918	8,975	6,943	2,615	34	3,287	894	102	10

procedure. The event CVN requirement selects a sample of signal events with a selection purity[**] of 60.8% and an relative efficiency of 35.6% with respect to the preselected sample[††].

Clearly this analysis has no "access" to the true interaction mode (QE, RES, DIS, etc.), however it is helpful to understand the breakdown of selected events from simulation with respect to the true interaction labels. This knowledge is used to prevent any potential selection biases toward particular event topologies. The selected signal events, normalized to data POT, are listed in Table 4.3 for each of the individual selection requirements used within the analysis. Based on the average neutrino energy of the NuMI beam incident on the NOνA near detector most selected events are predicted to be Resonant or DIS interactions, due to the higher average energy of electron neutrinos from the beam. However, due to reconstruction inefficiencies there are similar numbers of QE and Resonant events selected from simulation.

4.3.7 Kinematic Distributions of Selected Events

Once the selection procedure has been defined, it is important to study the characteristics of reconstructed events. The distribution of each of the variables that are important to the cross section measurement are shown in Figure 4.9. As the selected number of signal events is much less than the selected backgrounds and hence hard to see, the same kinematic variables are shown

[**]Selection Purity is defined as # Selected Signal Events / # Total Selected Events.

[††]Relative efficiency is calculated as the ratio of the number of selected events to the number of selected events after a prior selection cut.

Table 4.3: Summary of selected signal events from simulation, broken down by true neutrino interaction mode. Event numbers are normalized to the collected data exposure of 8.09 $\times 10^{20}$ POT. Percentages with respect to the total selected signal events for each selection requirement are reported.

Cut	Signal	QE (%)	MEC (%)	RES (%)	DIS (%)	Coherent (%)
Slicing	132,315	10,479(7.92)	3,652 (2.76)	18,828 (14.23)	98,575 (74.50)	728 (0.55)
DQ	123,389	10,883 (8.82)	4,689 (3.80)	18,792 (15.23)	88,198 (71.48)	777 (0.63)
Fiducial	116,454	12,519 (10.75)	6,894 (5.92)	21,218 (18.22)	75,066 (64.46)	757(0.65)
Containment	28,926	6,234 (21.55)	4,000(13.83)	8,021 (27.73)	10,188 (35.22)	419 (1.45)
Front Planes	28,813	6,229 (21.62)	3,999 (13.88)	8,001 (27.77)	10,098 (35.05)	418 (1.45)
NHits	17,848	4,699 (26.33)	3,264 (18.29)	5,578 (31.25)	3,993 (22.37)	262 (1.47)
MuonID	15,562	4,345 (27.92)	3,045 (19.57)	4,820 (30.97)	3,102 (19.93)	199 (1.28)
CVN > 0.85	8,975	3,099 (34.53)	2,116 (23.58)	2,794 (31.13)	839 (9.35)	96 (1.07)

for signal-only events in Figure 4.10. The selected signal interactions are broken down by neutrino interaction type.

4.4 Determination of Analysis Binning

The analysis is presented in electron kinematics (E_e and $\cos\theta_e$) and neutrino energy, and a determination of bin size was needed. The bin size of each of these variables was determined based on two considerations: the detector resolution and the expected number of signal events. To have physical meaning, the bin width must be greater than the estimated resolution from simulation. To ensure that the statistical errors for each bin are reasonable, statistics are also a consideration when selecting the bin size for an analysis, as areas with low statistics could increase the dependency of the analysis on the neutrino-nucleus interaction models, particularly when performing unfolding or efficiency corrections which are based entirely on the simulated predictions for the analysis.

Figure 4.11 is a plot of the absolute resolution for each analysis variable as a function of truth information from simulation. A Gaussian fit to each 1D projection in the true variable are depicted using the black markers. The Gaussian mean is reported as the central marker and the width is depicted using the vertical error bars in the 2D scatter plots, shown in the left column. Additionally, the resolution (width of each Gaussian fit) is plotted as a function of the true analysis variable in the right column. A resolution of less than 300 MeV is seen up to about 4 GeV in neutrino energy.

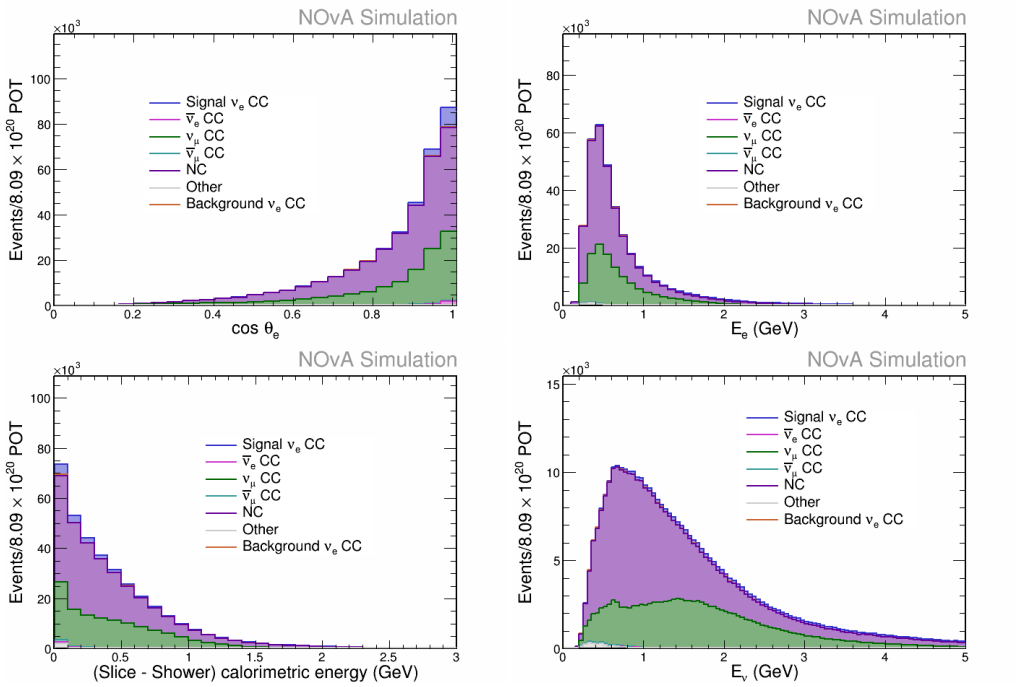

Figure 4.9: Plots of the reconstructed quantities related to the determination of the ν_e CC cross section after all event selection criteria have been applied. (Top Left) Reconstructed $\cos\theta_e$ (Top Right) Electron energy (Bottom Left) Slice - electron shower calorimetric energy (Bottom Right) Neutrino energy.

For electron energy, a resolution of about 200 MeV is seen near 2 GeV. Increases in electron energy resolution at higher values of electron energy require greater bin widths for the measurement. The resolution distribution of $\cos\theta_e$ depicts the need for large bin widths at larger angles from the average beam direction.

The results of these studies in detector resolution, and the requirement that each bin contains about 1000 signal events (corresponding to a 3% statistical uncertainty), led to the following bin definitions:

- 16 bins in neutrino energy (GeV): [1.0,1.25),[1.25,1.50),[1.50,1.75),[1.75,2.0), [2.0,2.25), [2.25,2.75),[2.75,3.0), [3.0,3.25),[3.25,3.5),[3.5,3.75),[3.75,4.0),[4.0,4.5),[4.5,5.0), [5.0,5.5),[5.5,6),[6.0,10.0)

- 11 bins in electron energy (GeV): [1.0,1.4),[1.4,1.65),[1.65,2.0),[2.0,2.5), [2.5,3.0), [3.0,3.5),[3.5,4.1),[4.1,4.7),[4.7,6.0),[6.0,10),[10+)

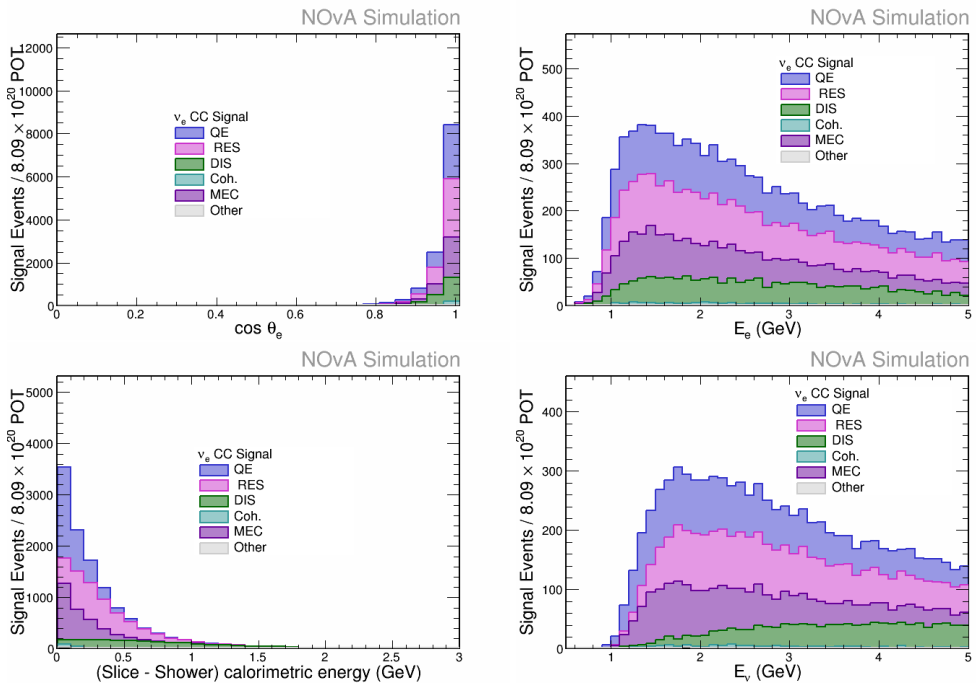

Figure 4.10: Plots of the reconstructed quantities of selected signal events broken down by neutrino interaction mode. (Top Left) Reconstructed $\cos\theta_e$ (Top Right) Electron energy (Bottom Left) Slice - electron shower calorimetric energy (Bottom Right) Neutrino energy.

- 5 bins in cos θ_e: [0.75,0.85),[0.85,0.9),[0.9,0.94),[0.94,0.97),[0.97,1.0]

4.5 Efficiency Corrections

Once the event selection criteria have been determined, the next step in the analysis is to understand how efficiently signal events are selected within detector and correct for any losses due to inefficiencies. This is done by studying the ratio of true signal events that are identified with the event criteria discussed previously to the total number of true signal interactions predicted within the fiducial volume of the detector. The calculated ratio is then used within the cross section calculation to account for the loss of true signal events due to the acceptance of the detector and the signal selection criteria.

As the efficiency correction is determined using only simulated events, the efficiency correction has the potential to introduce model dependence into the analysis. Regions of phase space with low selection efficiency will rely heavily on the neutrino interaction models for the correct estimation

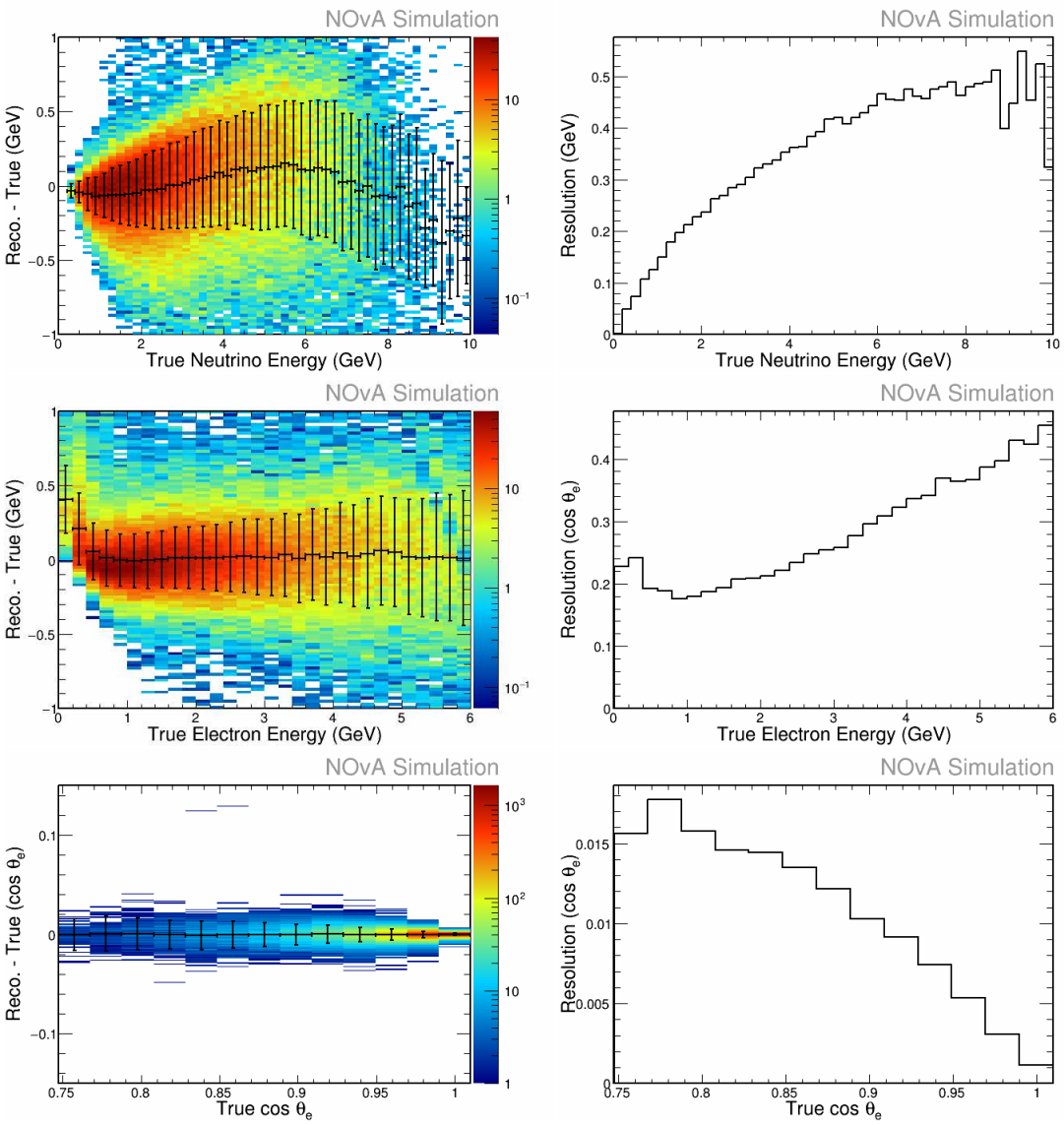

Figure 4.11: Plots of the measured detector resolution of selected signal events from NOνA ND simulation. The left column contains plots of (Reconstructed - True) vs Truth for each analysis variable. The right column contains plots of the width of a Guassian fit to (Reconstructed - True) in each projection of the true variable. The top row contains the resolution of reconstructed neutrino energy. The middle row contains the resolution of electron energy. The bottom row contains the resolution for $\cos\theta_e$.

of the number of signal events. One method for avoiding such model dependence is to impose a restriction on the phase space of the measurement. Another approach is to perform the correction using final-state kinematic variables that adequately describe the detector acceptance for signal events. Final-state electron energy and angle should adequately describe the detector acceptance, but additional limitations are placed on the phase space of the cross section measurement to limit dependence on the neutrino-nucleus interaction models.

Plots in figs. 4.12 to 4.15 show the efficiency of true signal selection as a function of true electron energy, true $\cos\theta_e$ with respect to mean neutrino direction, true neutrino energy, and true inelasticity[‡‡]. The denominator of the efficiency ratio in these distributions is the true signal, defined as true fiducial ν_e CC interactions. The total selection efficiency for the inclusive cross section measurement is shown in Figure 4.12. One-dimensional efficiency distributions in electron kinematic space are contained in Figure 4.14, these show higher selection efficiency for events with electrons traveling co-linear with the incoming neutrino beam. The selection efficiency is reduced as the electrons are emitted at larger angles with respect to the beam direction. The efficiency distributions are further broken down by interaction mode in Figures 4.13 and 4.15. Quasi-elastic and MEC interactions are typically predicted to have higher selection efficiency than Res and DIS interactions. This is primarily due to difficulties reconstructing the complicated final states of these types of interactions.

Figure 4.14 shows several analysis bins with a selection efficiency that is consistent with zero due to large systematic uncertainties on the number of selected events. The final measurement for this analysis will not include these regions of electron kinematic phase space, as they would increase the dependence of the extracted results on the models used to produce the neutrino interaction simulation. The large systematic uncertainties shown in this areas of phase space are primarily driven by uncertainties on neutrino-nucleus interaction models.

[‡‡]Inelasticity refers to the fractional energy loss by the lepton through the scattering interaction.

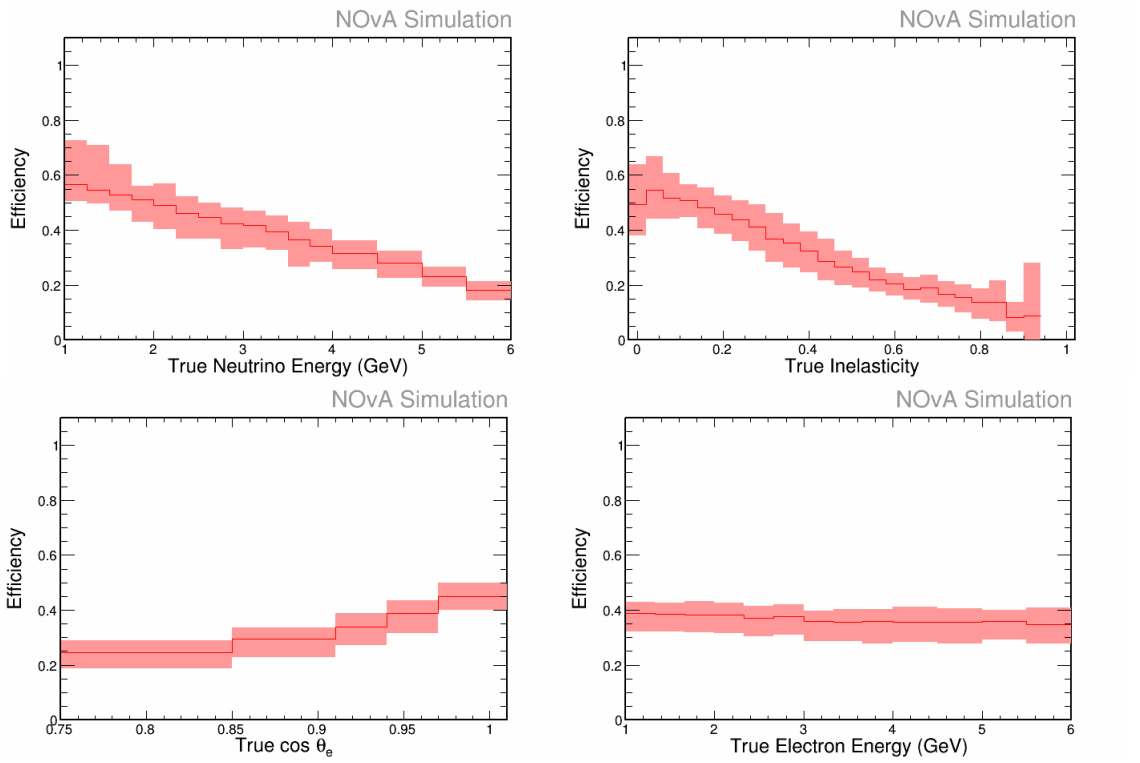

Figure 4.12: Plots of the total selection efficiency as a function of true quantities, neutrino energy (top left), inelasticity (top right), electron $\cos\theta$ with respect to the beam direction (bottom left), electron energy (bottom right). The error band is the systematic uncertainty coming from calibration, light-level, Cherenkov, and neutrino-nucleus cross section models.

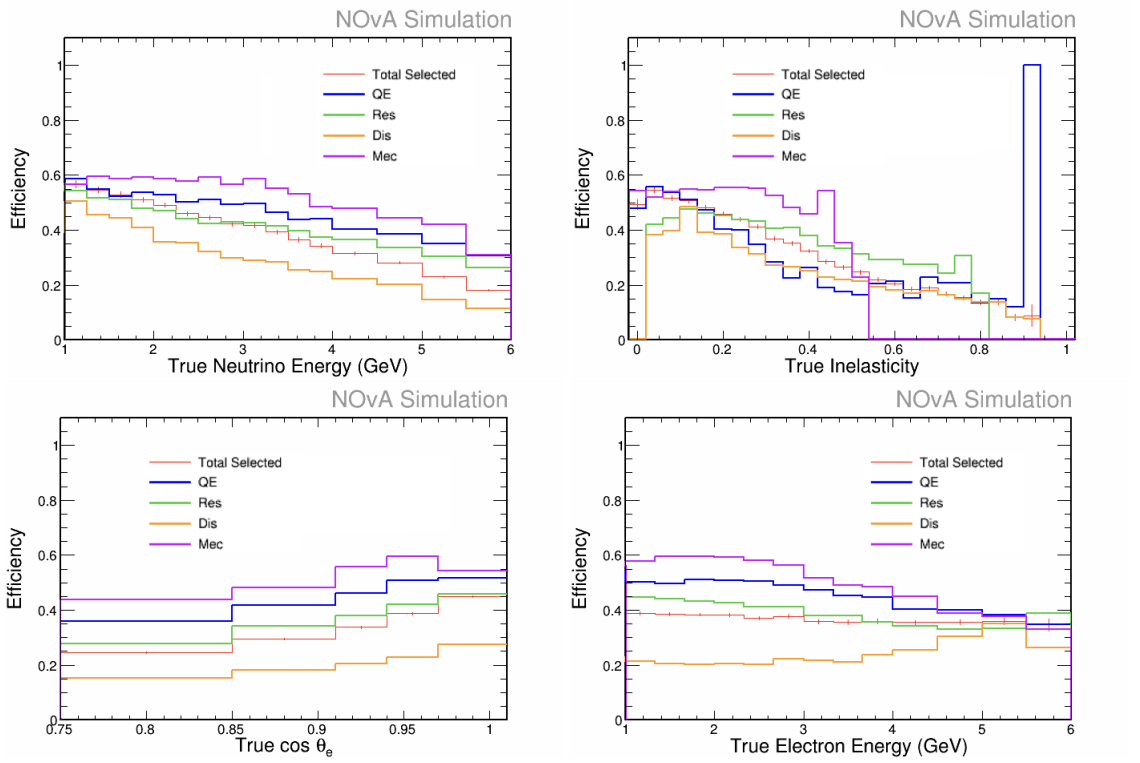

Figure 4.13: Plots of the total selection efficiency as a function of true quantities, neutrino energy (top left), inelasticity (top right), electron $\cos\theta$ with respect to the beam direction (bottom left), electron energy (bottom right). Different interaction types are drawn in different colors. All selection criteria have been applied.

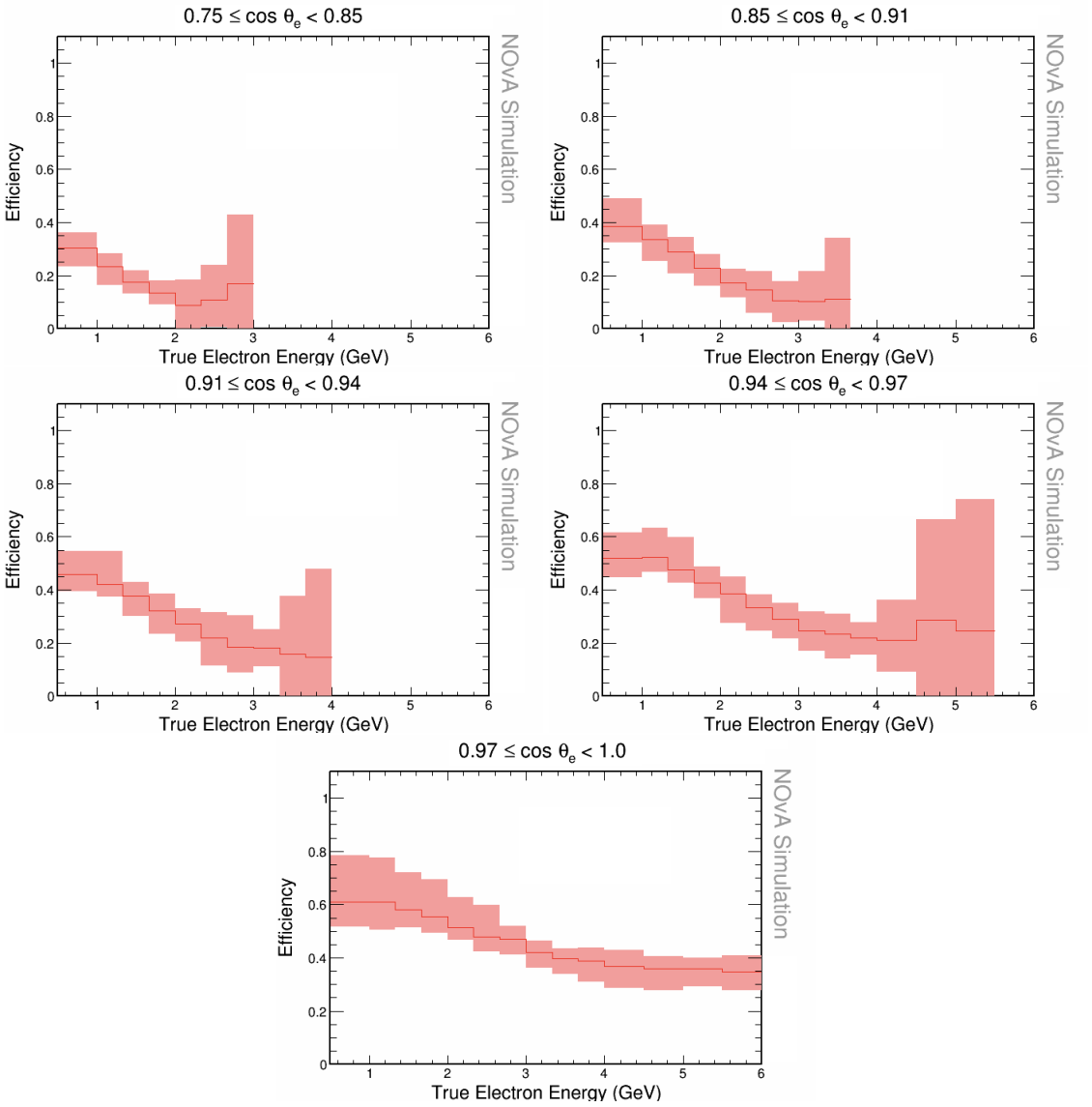

Figure 4.14: Plots of the total selection efficiency as a function of true electron energy plotted in slices of electron $\cos\theta$ with respect to the beam direction. The error band is the systematic uncertainty coming from calibration, light-level, Cherenkov, and neutrino-nucleus cross section model.

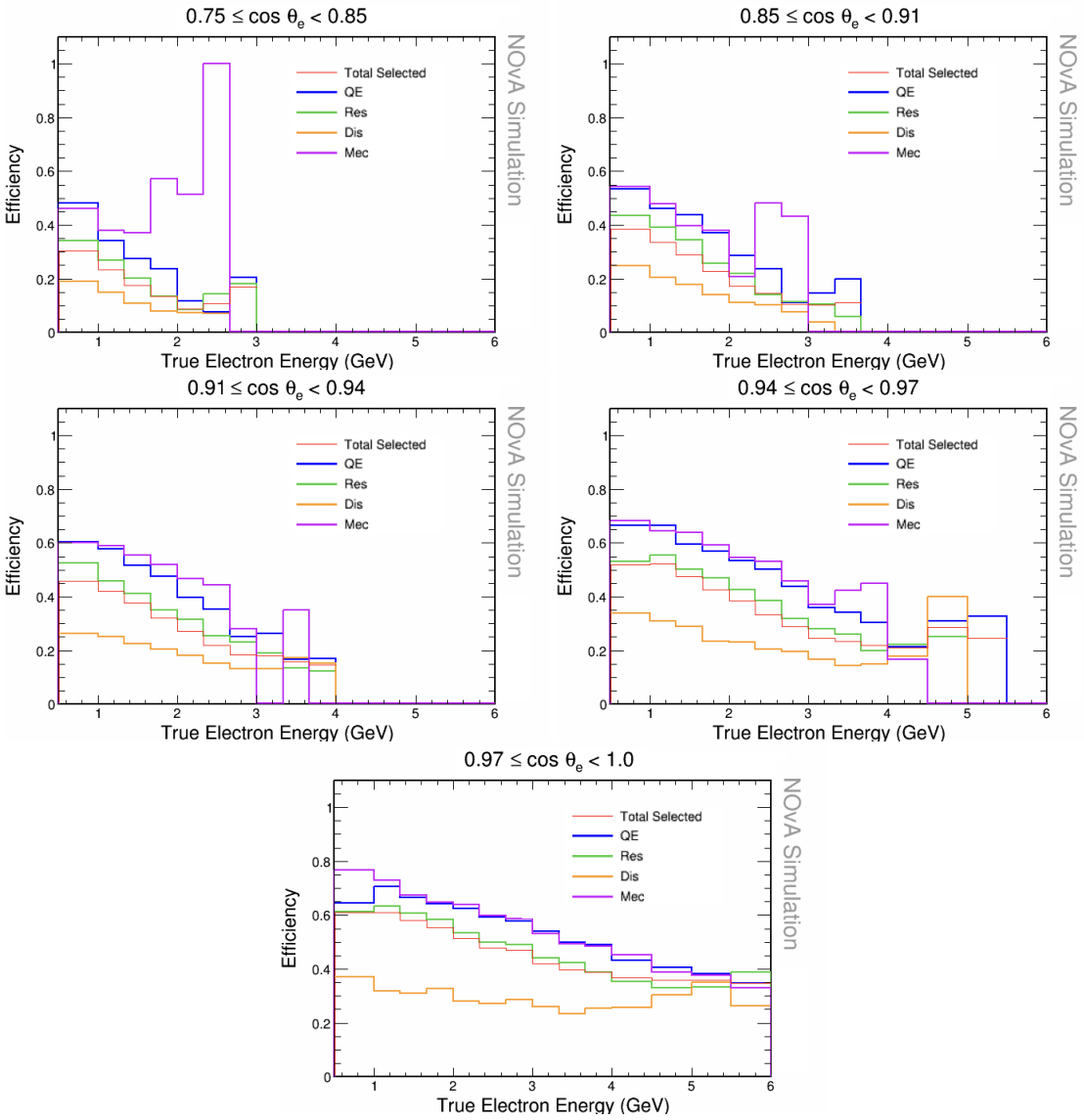

Figure 4.15: Plots of the total efficiency as a function of true electron energy plotted in slices of electron $\cos\theta$ with respect to beam direction. Different interaction types are drawn in different colors. All selection criteria have been applied.

4.6 Data-Driven Efficiency Correction

The predominant type of neutrino interactions that occur within the near detector are ν_μ CC interactions. These interactions can be used to derive a data-driven correction to the signal selection efficiency that is used within this analysis. This is done through the use of a sideband selection criteria, which is defined as highly scoring MuonID events that have passed all other selection criteria used within the analysis.

The sideband events are then studied through a procedure that removes the candidate muon track for the event and replaces it with a simulated electron. This procedure is called the Muon-Removed Electron added (MRE) procedure. The MRE procedure provides a sample of a high statistics sample "ν_e CC" for signal selection efficiency using real detector conditions. By comparing the selection efficiency in this sample to an MRE sample created from simulated events, differences between sideband data and simulated event candidates can be compared. These comparisons can provide a correction that can be applied to signal selection efficiency correction that is applied within the cross section measurement.

Unlike the muon removal procedure discussed in Section 3.6.3, the MRE sample described here is obtained from reconstructed neutrino interactions with highly scoring MuonID tracks. After the muon candidate track has been removed, it is replaced with a simulated electron with the same energy and direction as the removed muon track.

This method combines a well simulated electromagnetic shower with hadronic showers from data since these are not well simulated. Studies of the selection efficiency using these events lead to a better understanding of how the mismodeled hadronic showers impact the signal selection. MRE events can therefore be used to correct the ν_e selection efficiency [89].

Studies of the MRE samples in data and simulation use the same selection criteria discussed in Section 4.3. Figure 4.16 shows the ν_e CVN distribution after the fiducial criteria and pre-selection criteria are applied for both the MRE data and MC events. The ν_e CVN behaves as predicted, assigning high values to most of the MRE pre-selected events. The right plot shows the relative selection efficiency, which is defined as:

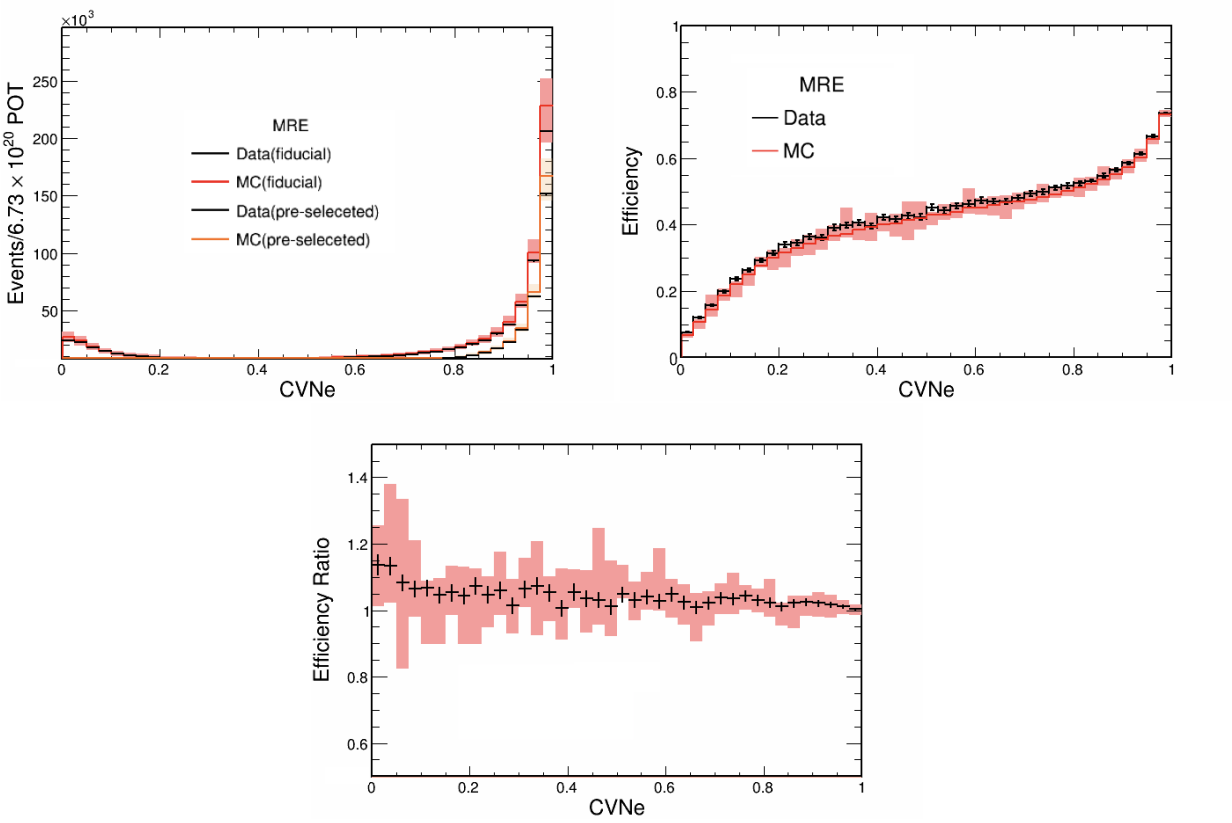

Figure 4.16: Plots of data and MC CVN comparison after fiducial, after all selection criteria have been applied (Left). Selection efficiency in Data and MC (Right). Efficiency ratios (Bottom). The systematic error bands represent, calibration normalization, light modeling, simulated Cherenkov variation, and calibration shape uncertainties.

$$\text{Relative Selection Efficiency} = \frac{\text{Preselected}}{\text{Fiducially Selected}} \tag{4.8}$$

The bottom plot shows the efficiency ratio, which illustrates that the data and MC selection efficiency for a CVN value of about 0.8 is consistent with unity.

Table 4.4 summarizes the number of events passing each set of selection criteria and the corresponding total efficiency. For the full preselection the data efficiency is 53.18% and 52.5% for MC, giving a 1.288% difference between them. The overall selection efficiency is consistent between MRE samples from data and simulation. In order to use this information in the cross section measurement, distributions of analysis variables must be studied. Figures 4.17 to 4.20 show the data and MC distributions corresponding to the full analysis selection, those with only a fiducial

Table 4.4: Total selection efficiency for MC and Data using MRE datasets.

Selection	Sample	Events	Efficiency	Difference(%)
Fiducial	Data	825713	-	-
	MC	877350	-	
Pre-Selection	Data	439126	0.531814	1.288
	MC	460645	0.525052	

selection, the corresponding efficiency, and the data-to-MC efficiency ratio for each of the analysis variables.

The efficiency and data-to-MC ratios illustrate the differences between the relative selection efficiencies as seen in data and MC MRE samples. The largest differences in efficiency are seen as a function of electron energy in Figures 4.19 and 4.20. In the first of these figures the efficiency ratio decreases from low to high electron energy (0.5-3 GeV). This has a fairly strong angular dependence, shown in Figure 4.20, where each grouping corresponds to the electron energy within a particular slice of electron angle (defined in Section 4.4). These discrepancies are consistent with the predicted systematic uncertainties on the MRE samples.

The MRE dataset provides a good proxy for a pure high-statistics charged-current ν_e sample, particularly in the flux peak of the beam. The differences in the selection efficiency between MRE samples produced with ND data and simulation are applied as central value correction to the efficiency calculated in Section 4.5, as depicted in the data-to-MC efficiency ratio plots. Applying this correction is a non-trivial procedure. MRE efficiencies are calculated in reconstructed space, and thus, unfolding is necessary to convert from reconstructed quantities back to the true quantities needed for the efficiency correction. The response matrices necessary for this procedure are shown in Figure 4.21. Another complication comes from the differences in hadron production between ν_μ CC and ν_e CC interactions in the 1-3 GeV neutrino energy region. Major differences in the predictions for these cross sections are expected at the low energy due to the mass difference between electrons and muons. Theoretical predictions suggest that this would only be a 1% difference at our energy scale [36], which is covered by the systematic uncertainties associated with the efficiency correction.

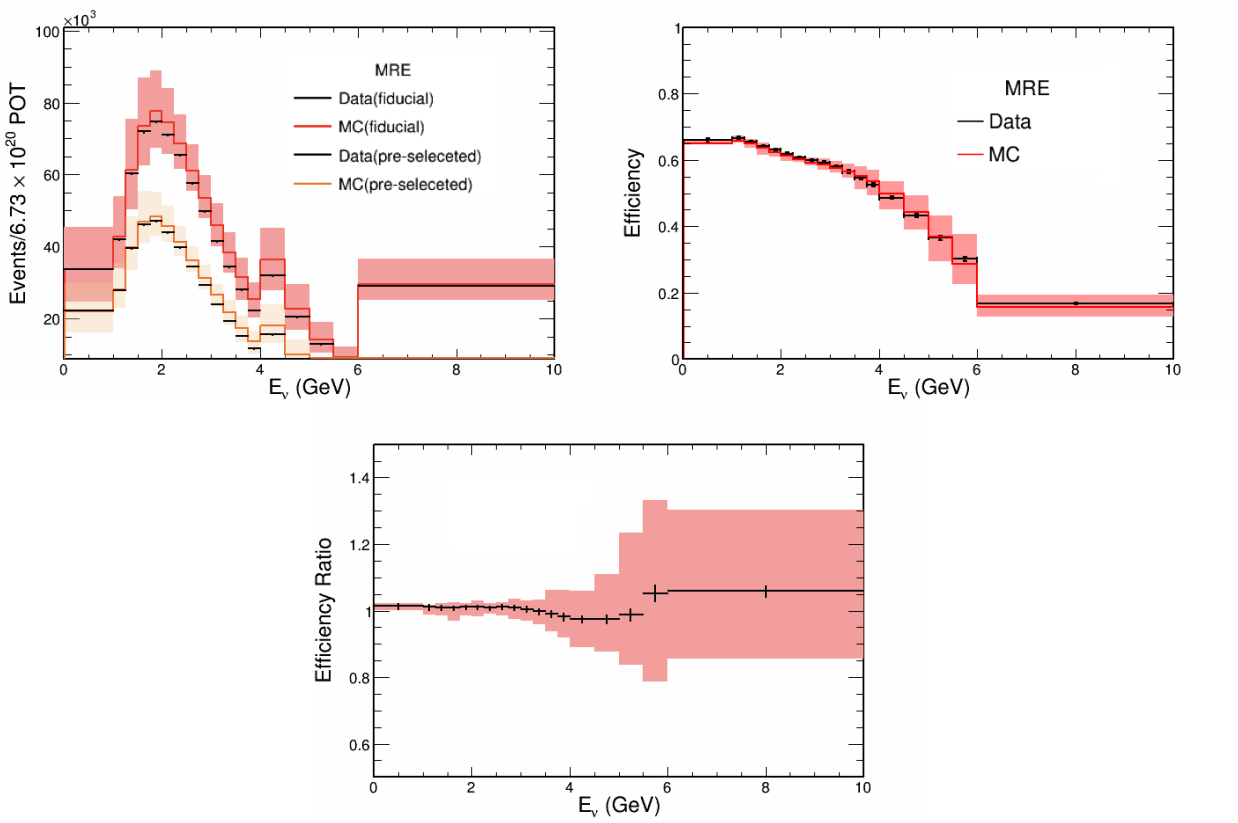

Figure 4.17: Plots of the energy distribution, efficiency for MRE data and MC, and the data-to-MC ratio.

The central value corrections derived from the MRE samples are contained in each of the efficiency ratio plots. These corrections are only applied in areas of electron kinematic phase space that are well covered by the MRE sample. Additionally, these corrections are only applied to the phase space included in the analysis based on the considerations discussed above and within Sections 4.5 and 4.9.

4.7 Flux Calculation

The beam flux incident on the NOνA ND is needed to extract the cross section measurement. The neutrino flux from the NuMI beam is determined through techniques developed by the MINERvA collaboration called the Package to Predict the FluX (PPFX) [90]. This package uses external measurements to constrain the modeling of hadron interactions prior to their decay into neu-

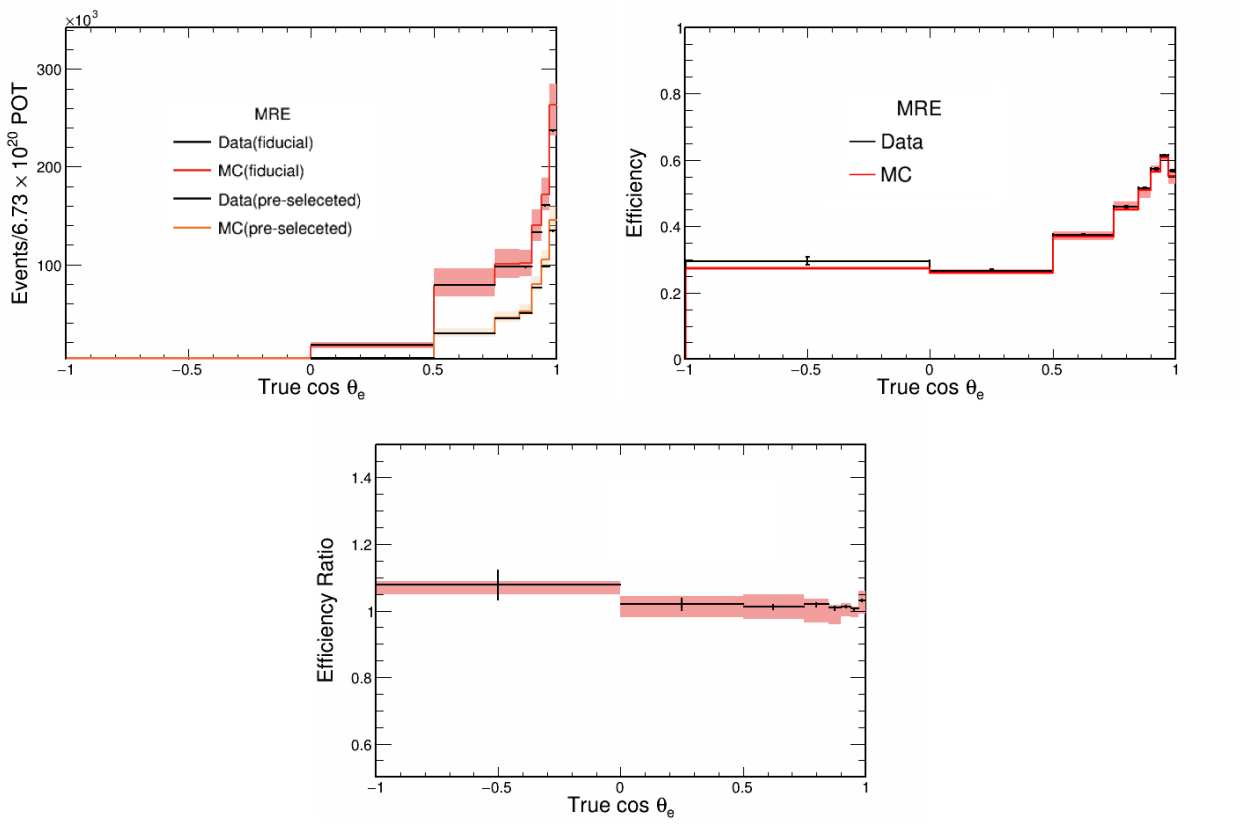

Figure 4.18: Plots of the $\cos\theta_e$ distribution, efficiency for MRE data and MC, and the data-to-MC ratio.

trinos and to produce a weighted flux prediction. This procedure produces a central value tune[§§], that along with several systematic universes are used for the computation of correlations between the fluxes of different types of neutrinos and their energies. In addition to this tune, standard MC techniques are used to determine the electron neutrino flux seen at the ND.

Individual neutrino interactions are produced using the GENIE neutrino event generator, where each simulated event contains information about the cross section for the neutrino interaction, the hadron that decayed to produce the neutrino, and the nucleus that the neutrino scattered off of. Solving for Φ in the relation:

$$N_{\text{Events}}(E) = \Phi(E)\sigma(E)N_{\text{nucleons}} \tag{4.9}$$

[§§]A tune is a procedure to reweight the MC predictions so that they better match well-understood data or simulated samples.

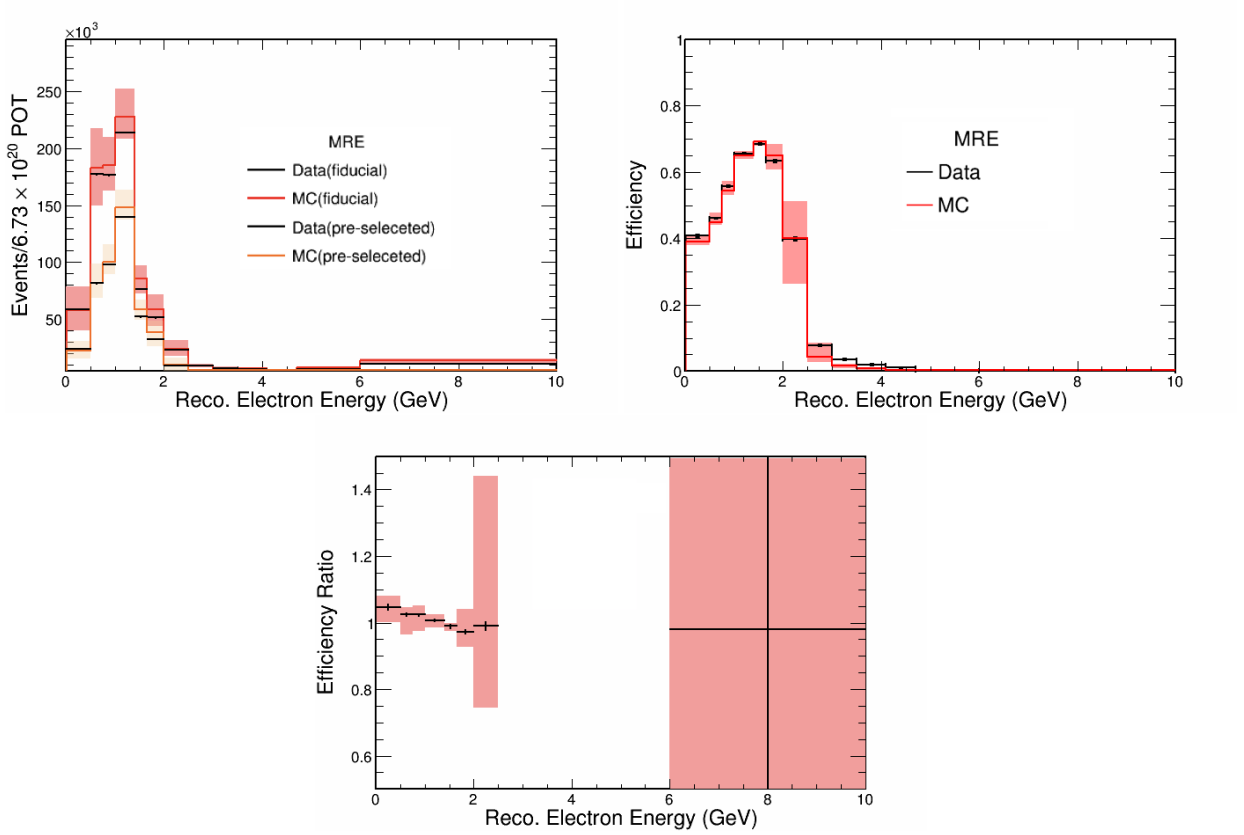

Figure 4.19: Plots of the electron energy distribution, efficiency for MRE data and MC, and the data-to-MC ratio.

gives:

$$\Phi(E) = \frac{N_{\text{Events}}(E)}{\sigma(E) N_{\text{nucleons}}} \tag{4.10}$$

where Φ is the neutrino flux, N_{Events} is the number of observed events, σ is the true neutrino cross section, as predicted by GENIE, and N_{nucleons} is the number of nucleons within a given volume in the detector. This procedure is complicated by the fact that $\sigma(E)$ is different for each scattering process and each target nucleus. To address this only quasi-elastic ν_e CC interactions with carbon are used when calculating the flux. This is an acceptable approximation because the detector is largely made of carbon. The NuMI electron neutrino flux, derived using this technique is shown in Figure 4.22. The plot also contains the flux uncertainties as predicted by PPFX, where the error band corresponds to hadron production and beam focusing uncertainties.

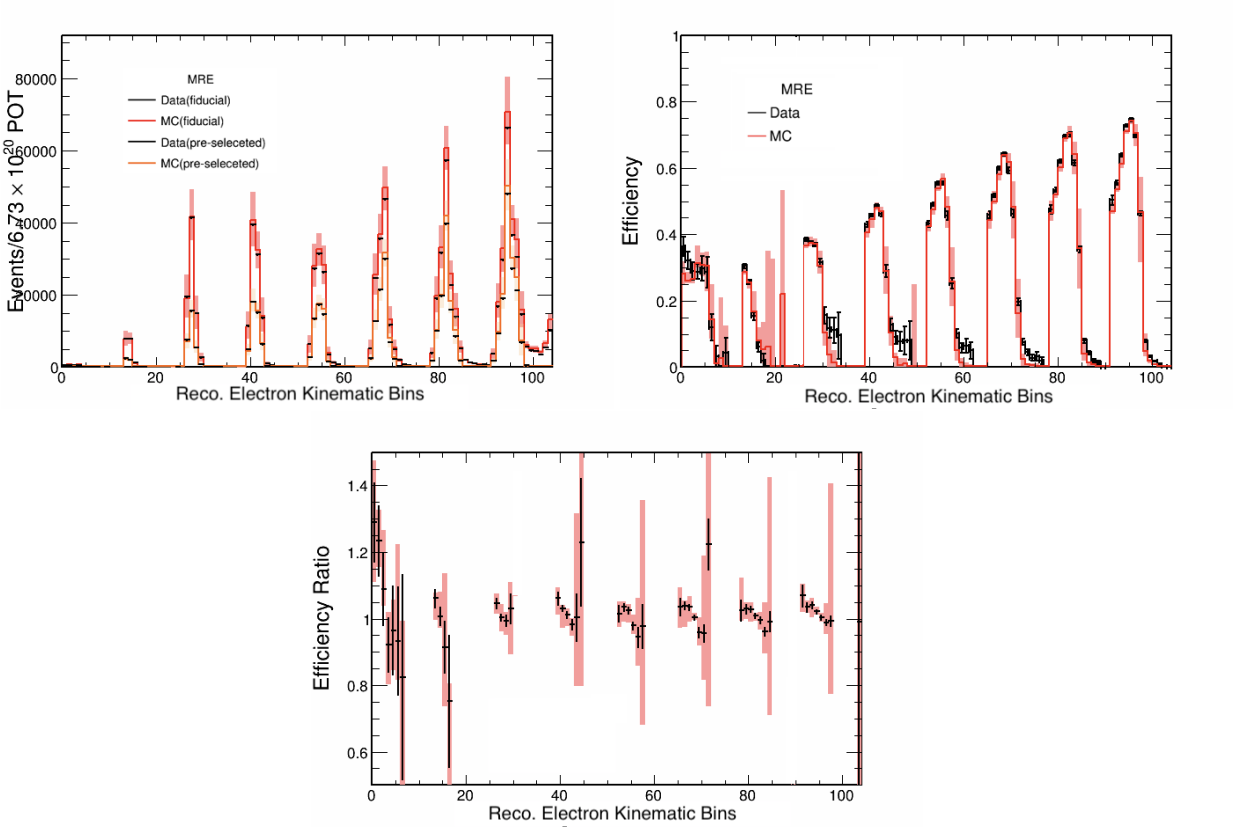

Figure 4.20: Plots of the electron kinematic space distribution, efficiency for MRE data and MC along with the data-to-MC ratio.

4.8 Target Counting

The cross section result is presented per nucleon, enabling comparison with other experiments. Since the ND is not made of a single material, the number of nucleons is determined in simulation using a random sampling within the fiducial volume. For each sampling, a point within the fiducial volume is selected, and the material at that point is determined from the detector geometry used in the simulation. This procedure is performed millions of times to accurately calculate the occurrence of each nuclei within the fiducial volume. The results of the target count estimate are tabulated in Table 4.5. It can be seen that the cross section measurement is being made primarily on hydrogen and carbon, but does include some heavier elements. This gives a total mass of 49,897 $\pm$ 346 kg, with a corresponding nucleon count of 3.02×10^{31}. The error quoted is statistical and

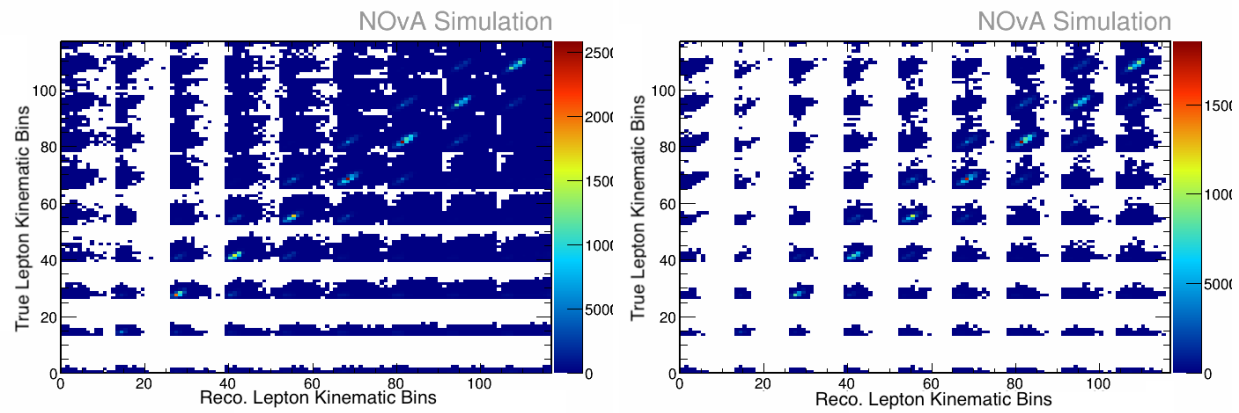

Figure 4.21: MC produced response matrices showing the relationship between true muon kinematics and the reconstructed kinematics of the added simulated electrons. Left: Fiducially selected response matrix. Right: Fully selected response matrix.

comes from sampling the fiducial volume a finite number of times. This error is only a 0.69% contribution.

Table 4.5: The derived mass of the fiducial volume, broken down by element type, used in the calculation of the nucleon count

Element	Z	Mass [kg]	Fraction of Total	Uncertainty [kg]
H	1	5400	0.11	42
C	6	33000	0.67	270
N	7	13	2.6e-04	0.09
O	8	1500	3.0e-02	26
Na	11	1	2.6e-05	0.021
S	16	48	9.5e-05	0.80
Cl	17	8000	0.16	130
Ca	20	13	2.6e-04	0.21
Ti	22	1600	3.2e-02	26
Sn	50	59	1.2e-03	1.0

4.9 Data-Driven Template Fit

As no true signal selection criteria can be applied to the analysis, there will be a large amount of background events present within the selected event sample. These backgrounds can be constrained if the degree of data-to-MC agreement is known. A sideband is used to derive the back-

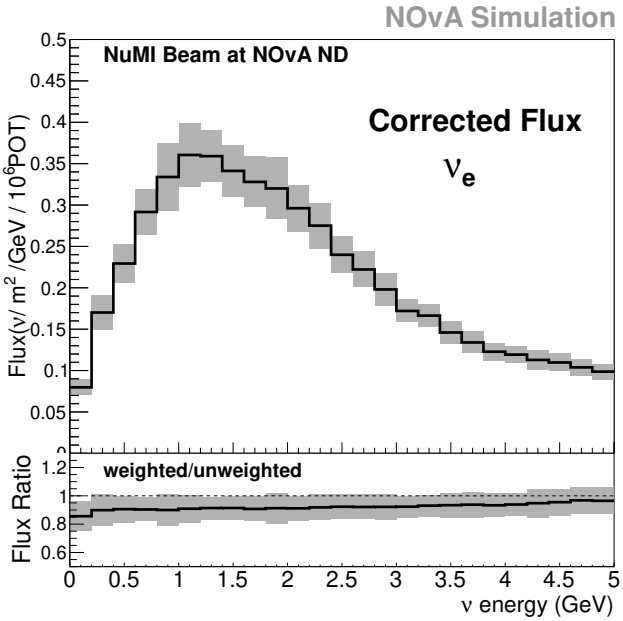

Figure 4.22: (Top) The electron neutrino flux spectrum following flux correction by PPFX. The error band corresponds to the hadron production and beam focusing uncertainties. (Bottom) The ratio between the corrected flux over the prediction without any correction.

ground constraint. This constraint is then used to describe backgrounds within the signal region. For this procedure to be accurate, the sideband data must have similar kinematics to the signal region.

For the measurement of the electron neutrino cross section a sideband was defined by inverting the event ID selection (CVN as discussed in Section 4.3.6). The CVN event identification distribution was divided into three regions, the signal region (CVNe > 0.85), the near sideband (0.6 < CVNe < 0.85), and the far sidebane (CVNe < 0.6). The kinematic distributions for reconstructed electron energy and calorimetric energy, defined as the slice - electron candidate calorimetric energy are shown in Figure 4.23. The distributions in the CVN signal region are shown on the top plots. This region is the most pure region for ν_e CC signal events. The near sideband (shown as the middle row of distributions) shows good coverage of the variables where similarities to the signal region are observed. It can be seen, however, that there is a large amount of signal ν_e CC interactions in this sideband. If there is signal in the sideband region, the sideband will not yield a good

estimate of background-only events. The far sideband region also shows good kinematic coverage, and a small contamination of signal events, but the background events in the signal region (NC with a final-state π^0) do not reflect the backgrounds observed in the far sideband (NC interactions without a final-state π^0). The background events in the far sideband are not a good estimate of those in the signal region.

Event identification techniques typically provide a likelihood distribution that discriminates signal and background events. The differences in the shapes of these distributions can be used to provide a constraint on both the background and signal predictions in an analysis through the use of a template fit. This procedure uses simulated events to produce templates, or the signal and background likelihood distributions from event identifiers, and adjusts the normalization of the templates through a fit to the total likelihood distribution obtained from data.

Template fits are used to provide both the signal and background estimates for the ν_e CC cross section measurement. As this is a differential measurement the template fit is performed in each electron kinematic bin ($\cos\theta_e$, E_e) using templates generated by an electron neutrino event identifier. As the shape of the templates change as a function of electron kinematics, (Figure 4.24) the fitting procedure is performed in each analysis bin separately providing an independent prediction for signal and background in each bin.

The fits are performed under the assumption that the simulation describes the template shapes of both the signal and backgrounds, but not necessarily the normalizations. Uncertainties in template shape are taken into account through the use of a covariance matrix generated using systematic uncertainties on the templates (Section 4.11 contains details about the systematic uncertainties).

The systematic covariance, $V_{ij,\text{syst}}$, between template bins is calculated as:

$$V_{ij,\text{syst}} = \frac{\sum_{n=1}^{U} (s_{n,i} - \mu_i)(s_{n,j} - \mu_j)}{U - 1} \tag{4.11}$$

where the i and j indices are the individual bins in the template distribution, and the n index refers to one of U randomly generated universes, in which the content of each predicted template bin

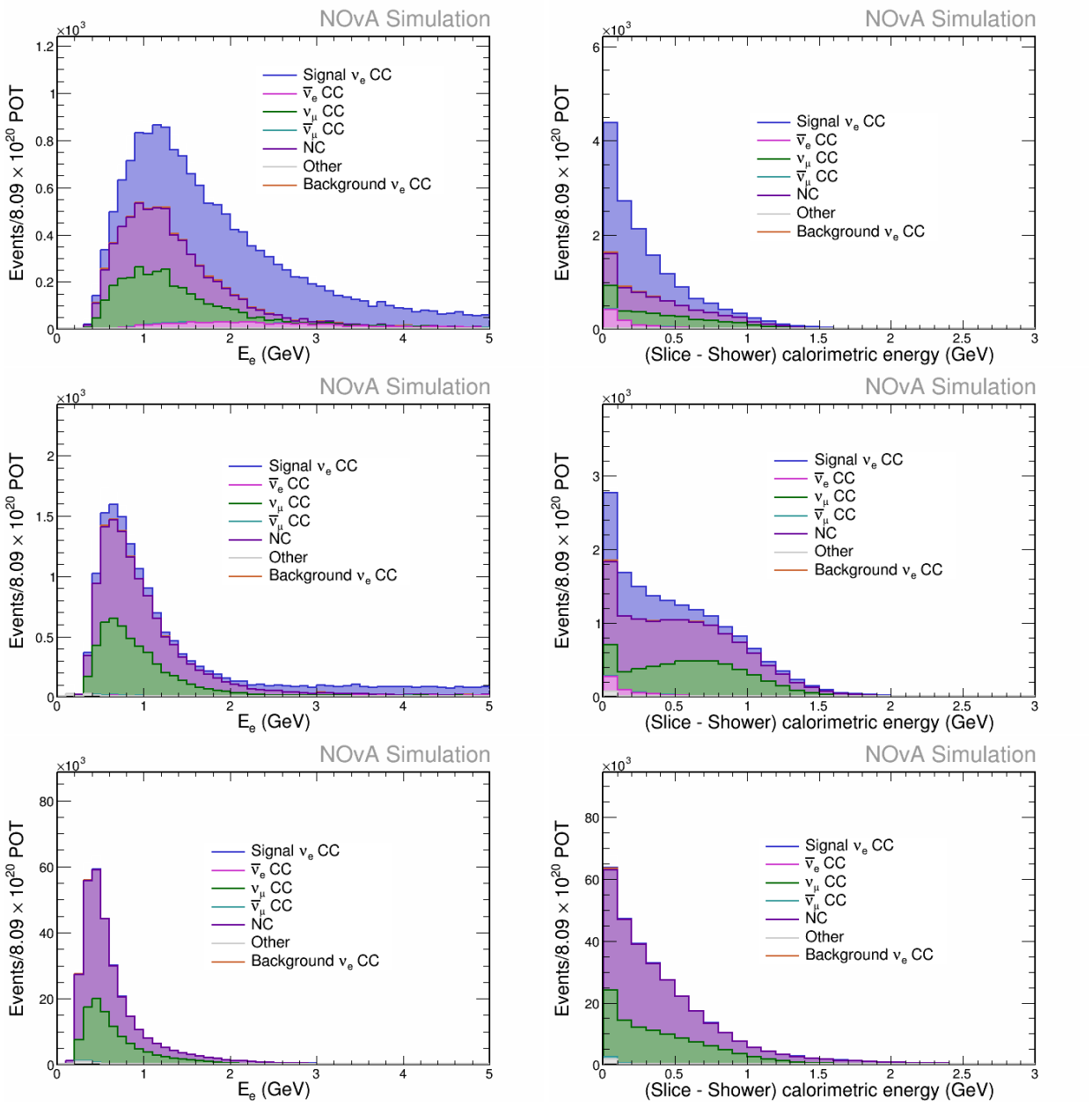

Figure 4.23: Plots of the reconstructed electron energy and calorimetric energy distributions in CVN signal region (top), CVN near sideband region (middle), and CVN far sideband region (bottom). Each region (defined within the text) shows the selected simulated events broken down by neutrino interaction type after all selection cuts within the specified region. Simulated events are normalized to data POT.

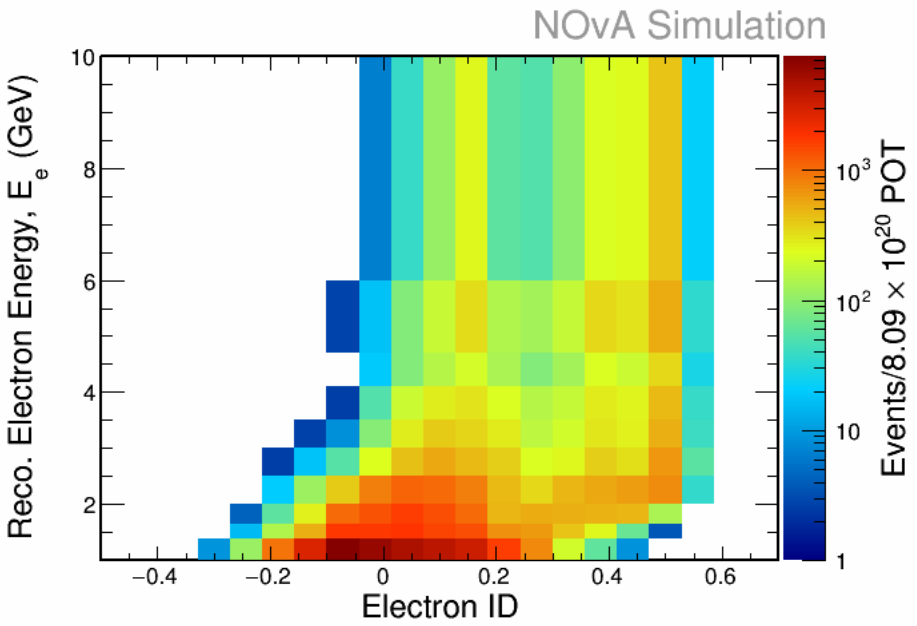

Figure 4.24: Reconstructed electron energy as a function of ElectronID event classifier for the total selected simulated sample. The event count is normalized to 8.09×10^{20} POT.

is systematically shifted to s from the nominal prediction μ. The randomly generated universes are produced in two different ways. To account for the systematic uncertainties describing the neutrino-nucleus interaction models used within the GENIE event generator, all parameters within the models were varied randomly at the same time to produce a single universe. Other universes were generated from simulated samples describing the $\pm 1\sigma$ shifts. The 1σ shift is calculated using:

$$\text{error}_i = |\sigma_i^{\text{shift}} - \sigma_i^{\text{nominal}}| \tag{4.12}$$

or

$$\text{error}_i = \frac{1}{2}(|\sigma_i^{+1} - \sigma_i^{\text{nominal}}| + |\sigma_i^{-1} - \sigma_i^{\text{nominal}}|) \tag{4.13}$$

depending on the number of simulated samples used to described a particular uncertainty. A random universe was obtained by randomly drawing the systematic shift from a Gaussian centered at 1 with a width of 1. Several thousand universes are generated for each of systematic uncertainty.

The signal and background estimates are by fitting the simulated templates to the data distribution using:

$$\chi^2 = (x_i - \mu_i)^T V_{ij}^{-1} (x_j - \mu_j) \tag{4.14}$$

where x refers to a measurement of data in a particular template bin and V_{ij} is the full covariance matrix defined as:

$$V_{ij} = V^{\text{stat}} + V^{\text{syst}} \tag{4.15}$$

where V^{stat} is a diagonal covariance matrix, and each on-diagonal element is the statistical variance in the corresponding event classifier bin. V^{syst} is the systematic uncertainty covariance matrix.

The minimization of Equation 4.14 includes the variation of up to two or three normalization parameters according to:

$$\mu_i^{Predicted} = a_i \cdot (N_{\nu_e} + N_{\bar{\nu_e}})_i + b_i \cdot (N_{\nu_\mu} + N_{\bar{\nu_\mu}})_i + c_i \cdot (N_{NC})_i + (N_{\text{Other}})_i \tag{4.16}$$

or

$$\mu_i^{Predicted} = a_i \cdot (N_{\nu_e} + N_{\bar{\nu_e}})_i + b_i \cdot (N_{\nu_\mu} + N_{\bar{\nu_\mu}} + N_{NC})_i + (N_{\text{Other}})_i \tag{4.17}$$

where N is the number of events in bin i for each of the different estimates of signal and background interactions. In general, the background is decomposed into ν_μ, NC, $\bar{\nu}_\mu$, $\bar{\nu}_e$, and "Other" components. Because the shapes of the $\bar{\nu}_\mu$ and $\bar{\nu}_e$ background components match the shapes of ν_μ and ν_e templates respectively, the normalizations of these components are found simultaneously with the ν_μ and ν_e templates.

The minimization procedure followed several steps as outlined in Figure 4.25. Templates were generated using data (or equivalently fake data) and the nominal simulation were used to produce

the template distributions for each of the signal and background contributions in a single bin of electron kinematic space. The systematic samples were then used to calculate a covariance matrix in the template space of a single bin of electron kinematic space. A three parameter χ^2 minimization procedure was followed using equations 4.14 and 4.16 within the CERN Minuit package [91], which provides a set of minimization tools. The fit was seeded using random starting values for each of the normalization parameters, with values ranging from 0.5 to 1.5. An optimization was then performed several hundred times looking for seeds that produce the lowest values of χ^2, while removing fits with high correlations between the extracted normalization parameters and fits that have non-physical results. If the three parameter fit converged successfully the results were saved and the algorithm moved to the next bin in electron kinematic space. If none of the fits converged successfully, the procedure moved to a two parameter minimization using Equation 4.17. This optimization was seeded using random values ranging from 0.5 to 1.5 and checked for convergence similarly to the three parameter fit. If the procedure results in a successful fit the results were saved and the next electron kinematic bin was examined. If there was no convergence the bin was not used to make a measurement within the analysis.

Additionally, the template fit was only performed using analysis bins with sufficient statistics, i.e. greater than 100 signal events, and with a sufficient ratio of signal events to background events within the signal region of the template distribution, i.e. greater than 0.4. The second requirement is to ensure that an adequate shape discrimination between signal and background template distributions exists. The phase space is plotted for a fit using CVNe as the fitting template in Figures 4.26 and 4.27. Figure 4.26 shows the number of signal events and the S/B ratio for the nominal simulation expected in each analysis bin. The phase space is explicitly outlined in Figure 4.27. The phase space of the fit does change slightly depending on the template used for the fitting procedure, which will be discussed during a comparison of the different event identifiers used to generate templates later in this section.

The fitting procedure is illustrated for a single bin in electron kinematic space in Figure 4.28. A sample of fake data, obtained from the nominal simulation that is statistically independent from

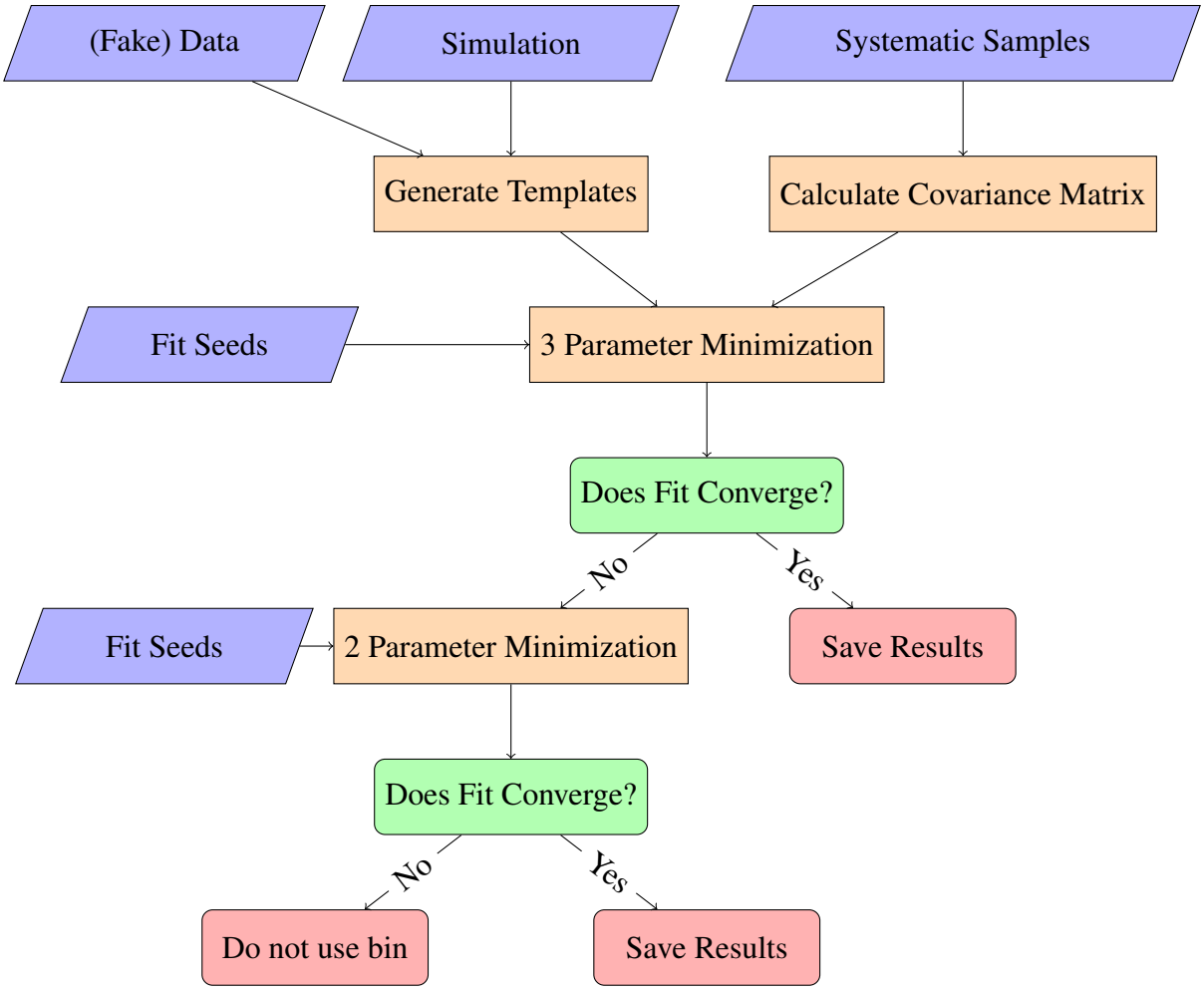

Figure 4.25: Simplified overview of template fit procedure

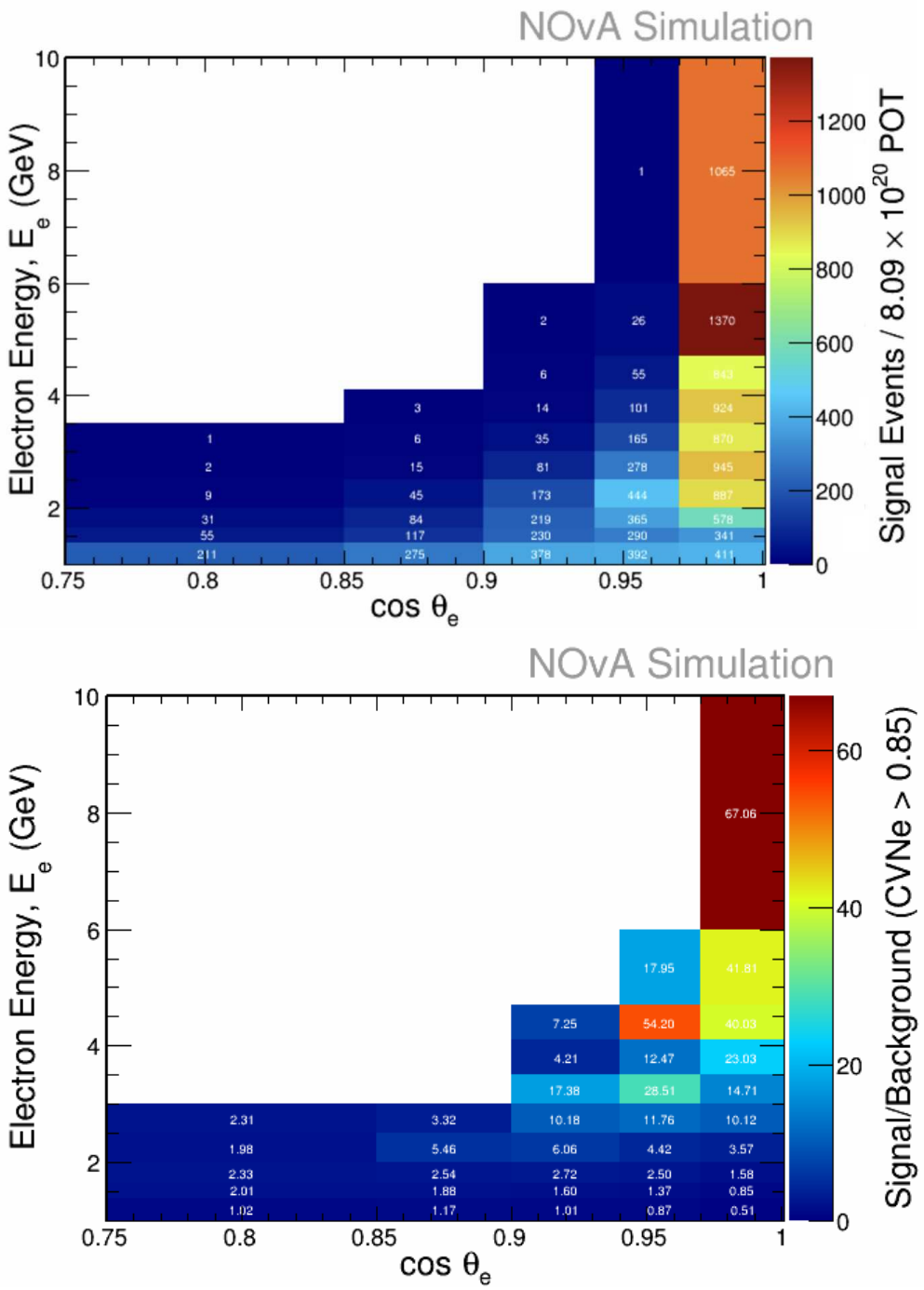

Figure 4.26: The number of signal events (to) in the electron kinematic analysis bins, numbers normalized to Data POT. The S/B in the electron kinematic analysis bins (bottom) in CVN ν_e CC event identifier signal region (CVNe > 0.85).

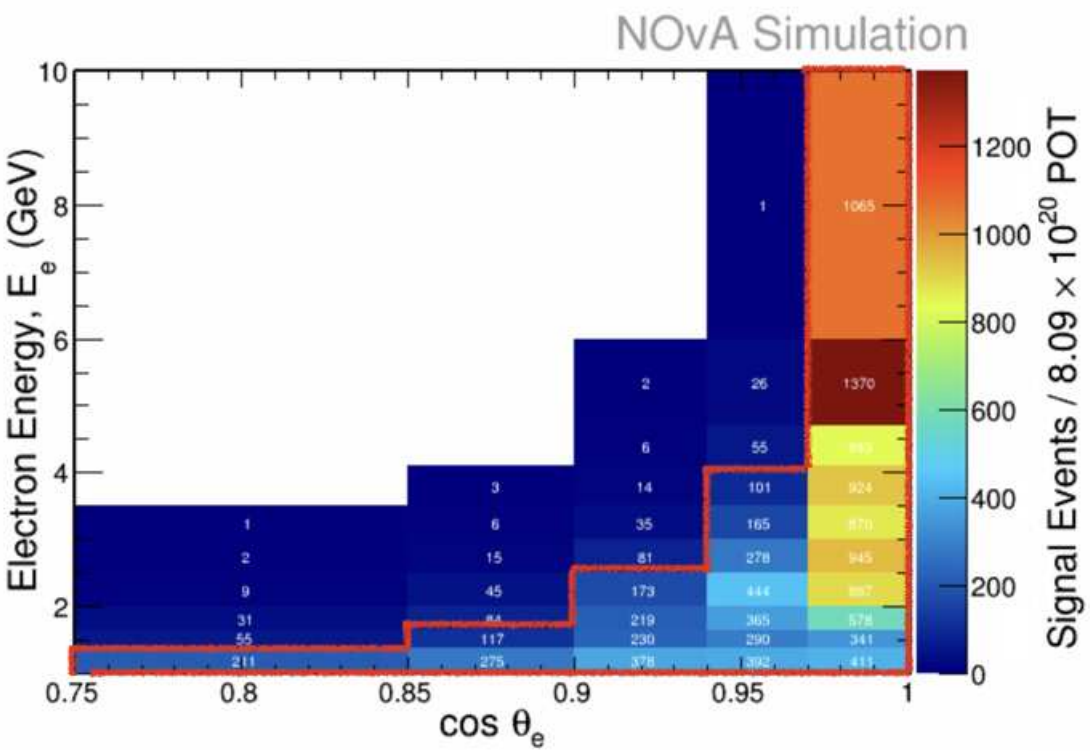

Figure 4.27: The number of signal events in the electron kinematic analysis bins, numbers normalized to Data POT. Red outline shows the phase space that the template fit was performed on.

the sample used to produce the templates, is used for the template fit procedure. The plots show the MC templates for events with $0.94 \leq \cos\theta_e < 0.97$ and $2.0 \leq E_e(GeV) < 2.5$. The signal-like, ν_μ CC-like, and NC template normalizations were free to float within the constraints from the systematic covariance matrix (which is pictured on the right side of Figure 4.28). Systematic uncertainties are implicitly cancelled during the chi-squared calculation.

Figure 4.29 further illustrates the example by showing the predictions in a number of electron energy bins for events with $0.94 \leq \cos\theta_e < 0.97$. The plots contain the results of the template fit for both signal and background contributions on the left and the signal prediction on the right. Error bars in each distribution are the statistical uncertainty in each bin plus the correlated uncertainties on the normalization parameters determined from the fit. The results from the selected sample illustrate that the fitted templates give consistent results with the number of selected events in the

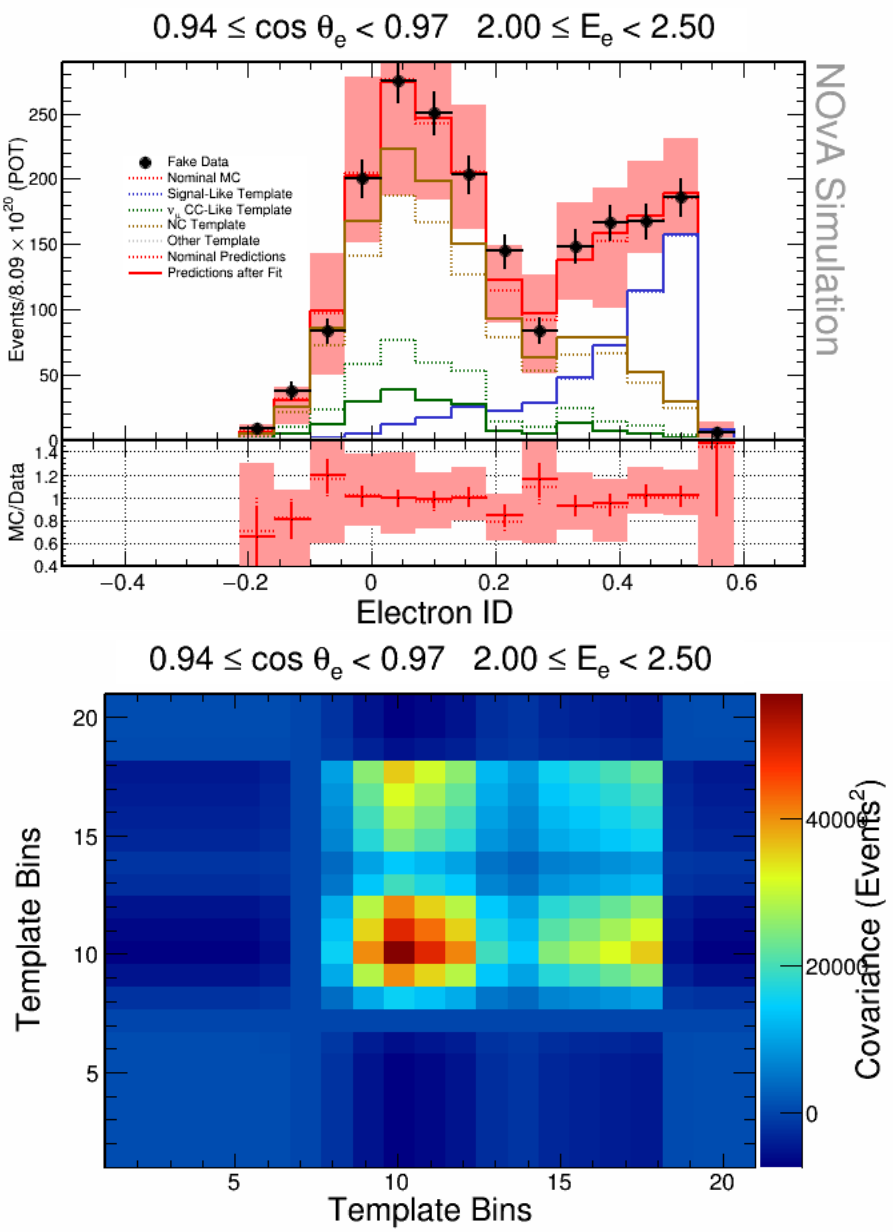

Figure 4.28: An illustrative example of signal extraction via the fitting procedure. Shown are MC templates for events with $0.94 \leq \cos\theta_e < 0.97$ and $2.0 \leq E_e(GeV) < 2.5$. The top plot shows the nominal MC histograms (dashed), the fitted MC histograms (solid), and the fake data. The bottom plot is the systematic covariance matrix.

fake data sample. The signal-only plot illustrates that the results of the template fit reliably extract the correct signal prediction within the systematic uncertainties used in the fit.

4.9.1 Effects of Systematic Uncertainties on the Template Fit

Understanding how the different sources of systematic uncertainty affect the template fit is necessary to ensure the correct interpretation of the template fit results. Figure 4.30 is a plot of the covariance and correlation matrices relating each systematic uncertainty used in the template fit. Each covariance was calculated by creating a multiverse for each systematic uncertainty and then integrating over the entire template fit range in a single electron kinematic bin. This enabled the computation of the covariance between two systematic samples. The systematic uncertainties include: calibration shape, Cherenkov level variations, light level, calibration normalization, neutrino-nucleon interaction, and PPFX multiverse uncertainties. For the electron kinematic bin used to compute the covariance matrix, calibration normalization and the hadron production uncertainties (computed using PPFX [90]) show the largest on-diagonal values of the covariance matrix. Because the variance of the other systematic uncertainties is less than these large uncertainties, the fitting procedure is able to constrain the effects of the large systematics by limiting range of normalization parameters that are consistent with the variances of the other systematic uncertainties. The matrix shows relatively low correlations between all systematic sources. Although only one example matrices shown, it is representative of the matrices generated in other electron kinematic bins.

4.9.2 Tests of the Template Fitting Procedure

Testing of the template fit method is required to confirm that it can be used to extract signal for this measurement and is function as expected. Two such tests were preformed.

Statistical Covariance Matrix

Equation 4.14, is the equation for the χ^2 minimization that was used in the fitting procedure. If the systematic errors are set to zero the results of the fit should be equivalent to using:

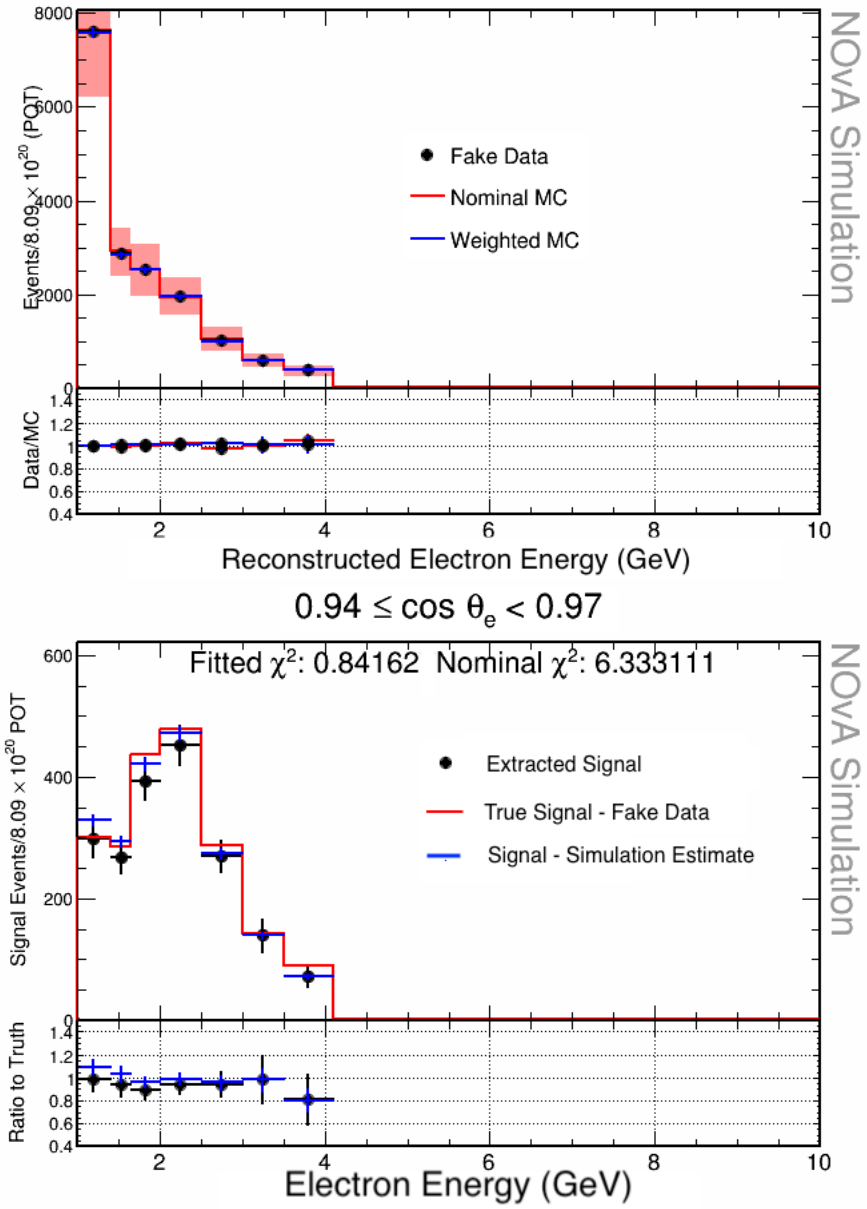

Figure 4.29: An illustrative example of signal extraction via the template fitting procedure, for events with $0.94 \leq \cos\theta_e < 0.97$. The top plot shows the nominal MC prediction, the fitted MC prediction (solid), and the fake data as a function of electron energy in this slice of $\cos\theta_e$. The bottom plot shows the nominal signal prediction, the fitted signal prediction (solid), and true signal distribution from fake data as a function of electron energy in this slice of $\cos\theta_e$.

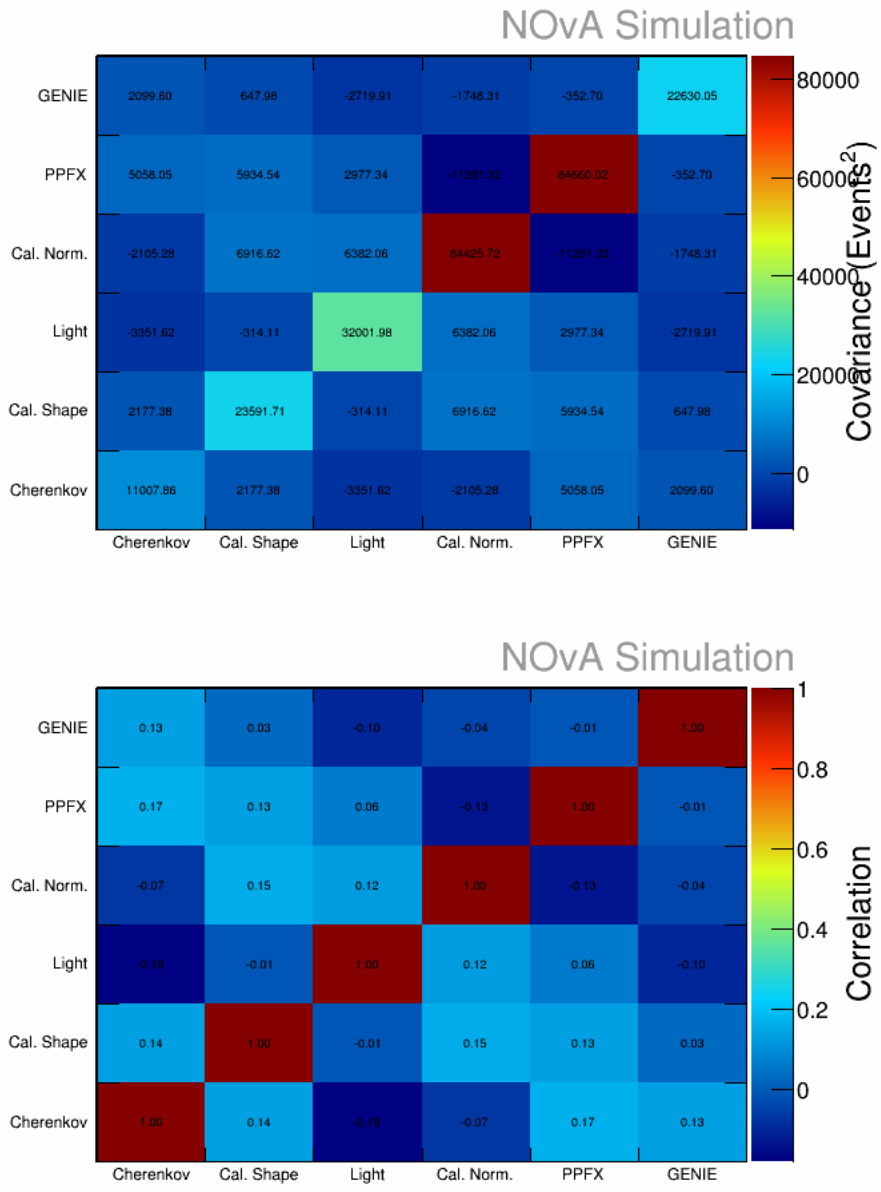

Figure 4.30: The top plot is a matrix showing the covariance between each systematic uncertainty that is used to calculate the systematic covariance matrix used in the template fit. The bottom plot is a matrix showing the correlations between each systematic uncertainty that is used to calculate the systematic covariance matrix used in the template fit. The matrices are calculated for events with $0.94 \leq \cos\theta_e < 0.97$ and $2.0 \leq E_e(GeV) < 2.5$.

Table 4.6: Comparison between the template fit results using only statistical uncertainties in the covariance matrix to the results found using Equation 4.18

	ν_μ CC -Like Normalization		ν_e CC-Like Normalization		NC Normalization	
Energy Bin	Covariance	Standard	Covariance	Standard	Covariance	Standard
$1.0 \leq E_e < 1.4$	0.856	0.856	1.02	1.02	1.06	1.06
$1.4 \leq E_e < 1.65$	1.02	1.02	0.981	0.981	0.990	0.990
$1.55 \leq E_e < 2.0$	1.01	1.01	1.07	1.07	0.993	0.993
$2.0 \leq E_e < 2.5$	0.897	0.897	0.984	0.984	1.08	1.08
$2.5 \leq E_e < 3.0$	1.08	1.08	1.02	1.02	0.917	0.917
$3.0 \leq E_e < 3.5$	0.987	0.987	0.990	0.990	1.01	1.01
$3.5 \leq E_e < 4.1$	1.08	1.08	1.03	1.03	0.924	0.924
$4.1 \leq E_e < 4.7$	0.884	0.884	1.01	1.01	1.09	1.09
$4.7 \leq E_e < 6.0$	1.07	1.07	0.980	0.980	0.963	0.963

$$\chi^2 = \frac{(\text{Data}_i - \text{MC}_i))^2}{\sigma^2_{\text{Data},i} + \sigma^2_{\text{MC},i}} \tag{4.18}$$

The results of this test are shown in Table 4.6. This test shows that the statistical uncertainty covariance matrix is handled correctly by the template fit. Table 4.6 shows the results for all electron energy bins within a single slice of $\cos\theta_e$. The similar results were found across the full electron kinematic phase space used for the template fit.

Comparison of Templates from Alternative Event Identifier Distributions

Comparisons with templates generated from other identifiers were also made. Templates generated from event CVN, LID, ElectronID were used to perform fits to a sample of fake data[¶¶]. The fake data sample consisted of 25% of the nominal simulated sample, which is roughly equivalent to the size of the NuMI data collected with the NOνA near detector for this analysis. This study was designed to assess the impact each event identifier would have on the analysis if it were used within the template fit.

Figure 4.31 shows the event identifier distributions before and after the template fit had been performed to the fake data distribution with the covariance matrix used for the template fit. The

[¶¶]The fake data was generated from a sample of simulation that was statistically independent from the simulated sample used to produce the signal and background templates.

Table 4.7: χ^2 values for the extracted signal resulting from template fit to true signal from fake data.

$\cos\theta_e$ Bin	χ^2 Values From Template Fit		
	CVNe	LID	ElectronID
0.85 - 0.90	0.122	0.113	0.077
0.90 - 0.94	0.567	0.370	0.703
0.94 - 0.97	1.285	1.847	0.858
0.97 - 1.00	2.902	1.454	1.514

plots within the figure show that the choice of event identifier could make a substantial impact on the analysis. The shapes for signal and background templates are substantially different between each of the different classifiers. These shape differences could lead to a better template fit by allowing better constraints on the uncertainties. The covariance matrix for CVNe shows a wide range of bins that can be used to constrain the large uncertainties on the first and final bin within the template, while the matrix for ElectronID has only a few bins that could be used to constrain these uncertainties.

Figure 4.32 shows the distributions of kinematic variables before and after the template fit had been performed to the fake data. These events were from a range of $0.94 \leq \cos\theta_e < 0.97$. The CVNe template fit results shows fluctuations in neighboring electron energy bins on the background estimates in the top row of the figure. ElectronID and LID have background predictions that are consistent with the fake data predictions. An examination of the signal prediction shows that the extracted signal is representative of the true signal from the fake data sample. The CVNe template fit over-predicts the number of true signal events, but is consistent within the uncertainties of the fitting procedure. LID and ElectronID show consistent results across each of the plots.

The χ^2 values for each bin of $\cos\theta_e$ are given in Table 4.7. The χ^2 calculations are always low because they take the uncertainties from the template fit into account. The table shows that each template fit results in similar χ^2 results.

Figure 4.33 is a plot of the extracted signal normalizations and uncertainties on the normalizations from a template fit to the fake data sample. The results using CVNe, LID, and ElectronID are found in the top, middle, and bottom rows, respectively. The phase space that the fit was performed over can be deduced by looking at the fit uncertainty plots. The available phase space for the LID

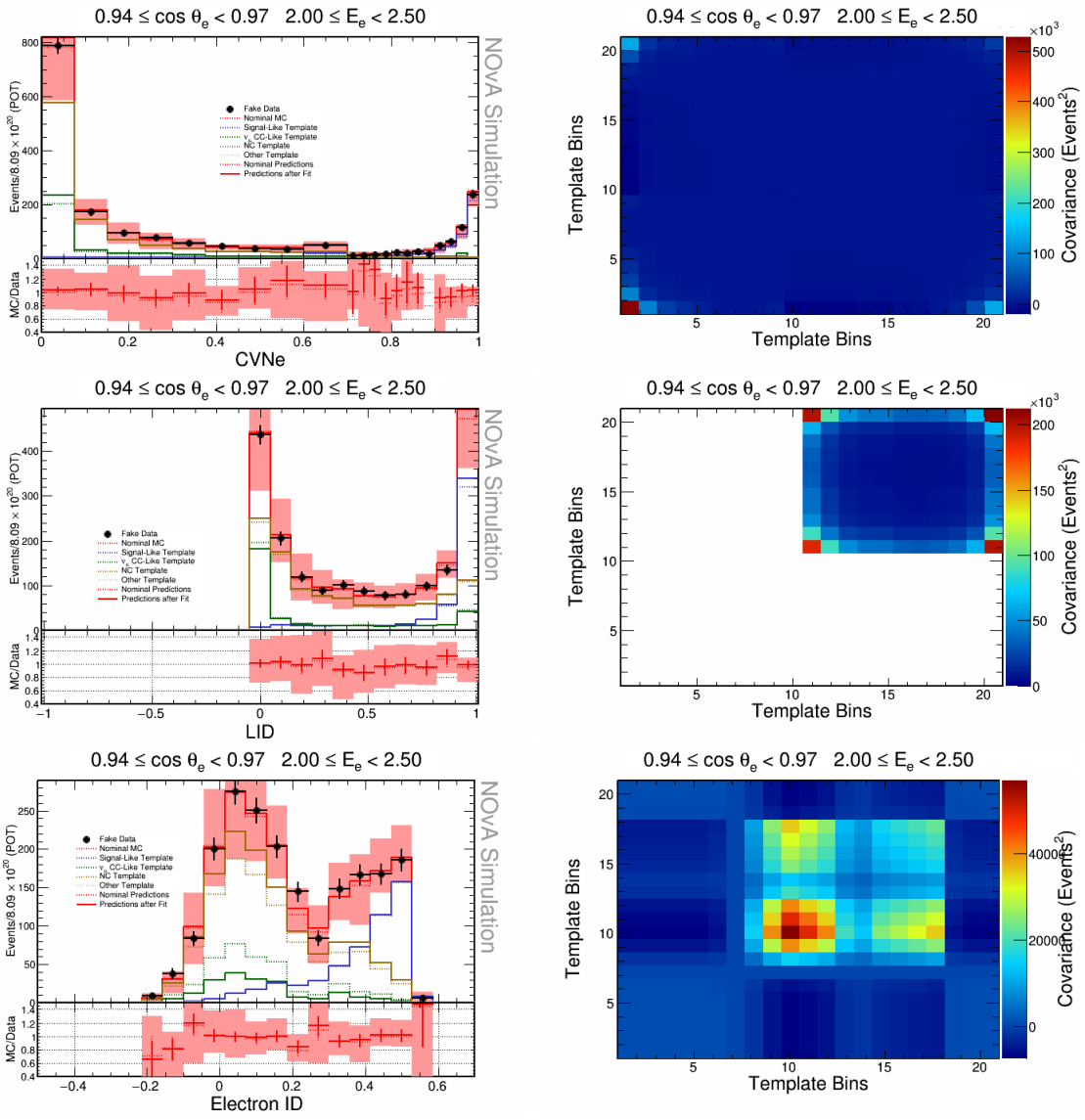

Figure 4.31: An illustrative example of signal extraction via the fitting procedure. Shown are MC templates for events with $0.94 \leq \cos\theta_e < 0.97$ and $2.0 \leq E_e(GeV) < 2.5$. Fake data was produced from nominal MC simulation and was statistically independent from the sample used to produce the templates. (Left Column) Nominal MC histograms (dashed), the fitted MC histograms (solid), and the fake data in template space. (Right Column) Systematic covariance matrix used in template fit. Each row shows the plots for a different event classifier template. (Top) CVNe (Middle) LID (Bottom) ElectronID

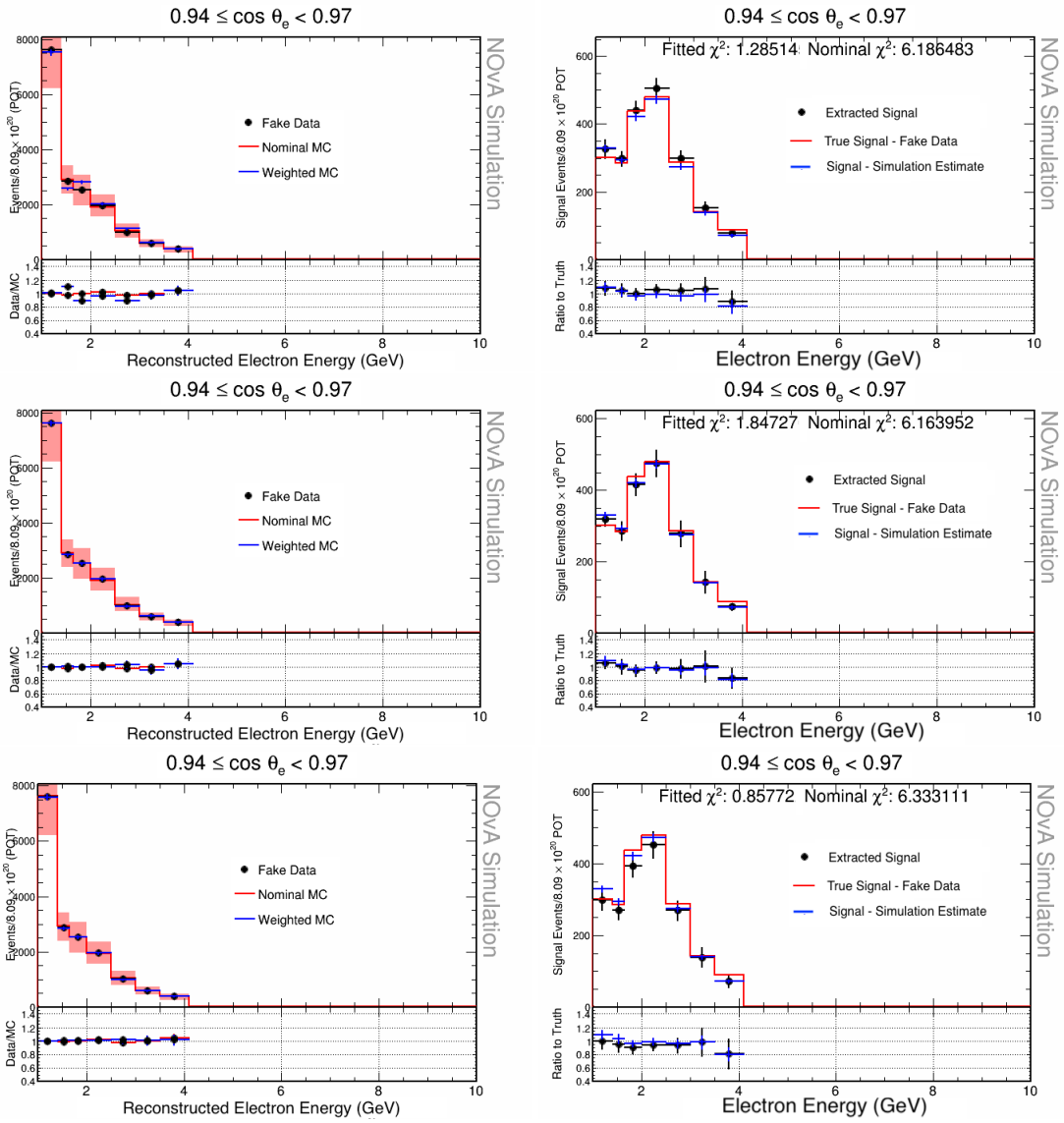

Figure 4.32: An illustrative example of signal extraction via the fitting procedure. Shown are MC predict for events with $0.94 \leq \cos\theta_e < 0.97$. Fake data is produced from nominal MC simulation that is statistically independent from the sample used to produce the templates. (Left Column) Total predicted events from nominal MC, fitted MC, and data as a function of electron energy. (Right Column) Total extracted signal events from nominal MC, fitted MC, and fake data truth as a function of electron energy. (Top) CVNe template fit results (Middle) LID template fit results (Bottom) ElectronID template fit results

template fits is reduced compared to the phase space of either CVNe of ElectronID. Figure 4.33 depicts the expected uncertainty on the number estimated signal events.

4.10 Unfolding

The term unfolding refers to the procedure used to express the results in measurement space back to true space. Measurement space is affected by the limitations of imperfect measurement devices estimating the true particle-level distributions of physical quantities. These techniques seek to answer the question of what a physical distribution would look like in a detector that has perfect resolution and reconstruction capabilities. Observed event counts are different from predictions seen in a "perfect" detector due to three things:

1. Limited acceptance: the probability to observe a given event is limited by detector acceptance. The acceptance is dependent on the kinematic variables in question.

2. Transformation: the ability to reconstruct kinematic variables can be reduced due to non-linear responses of detector components.

3. Finite resolution: the measured quantity is smeared out due to the finite resolution of the detector.

Events may or may not be reconstructed. The process of extracting information of the truth content of reconstructed bins given an observed measurement is called unfolding. This procedure allows for a comparison of the measurement with future theories or comparisons of experiments with different responses. The general problem is formulated through the folding equation [92]:

$$\mathbf{A}\mathbf{x} + \mathbf{b} = \mu \tag{4.19}$$

where μ is a vector of dimension M_y and its components μ_i correspond to the observed detector distribution, the vector $\mathbf{x}$, of dimension M_x, corresponds to the expected number of events in true space. The expected number of background events is described by the vector $\mathbf{b}$ The two vectors

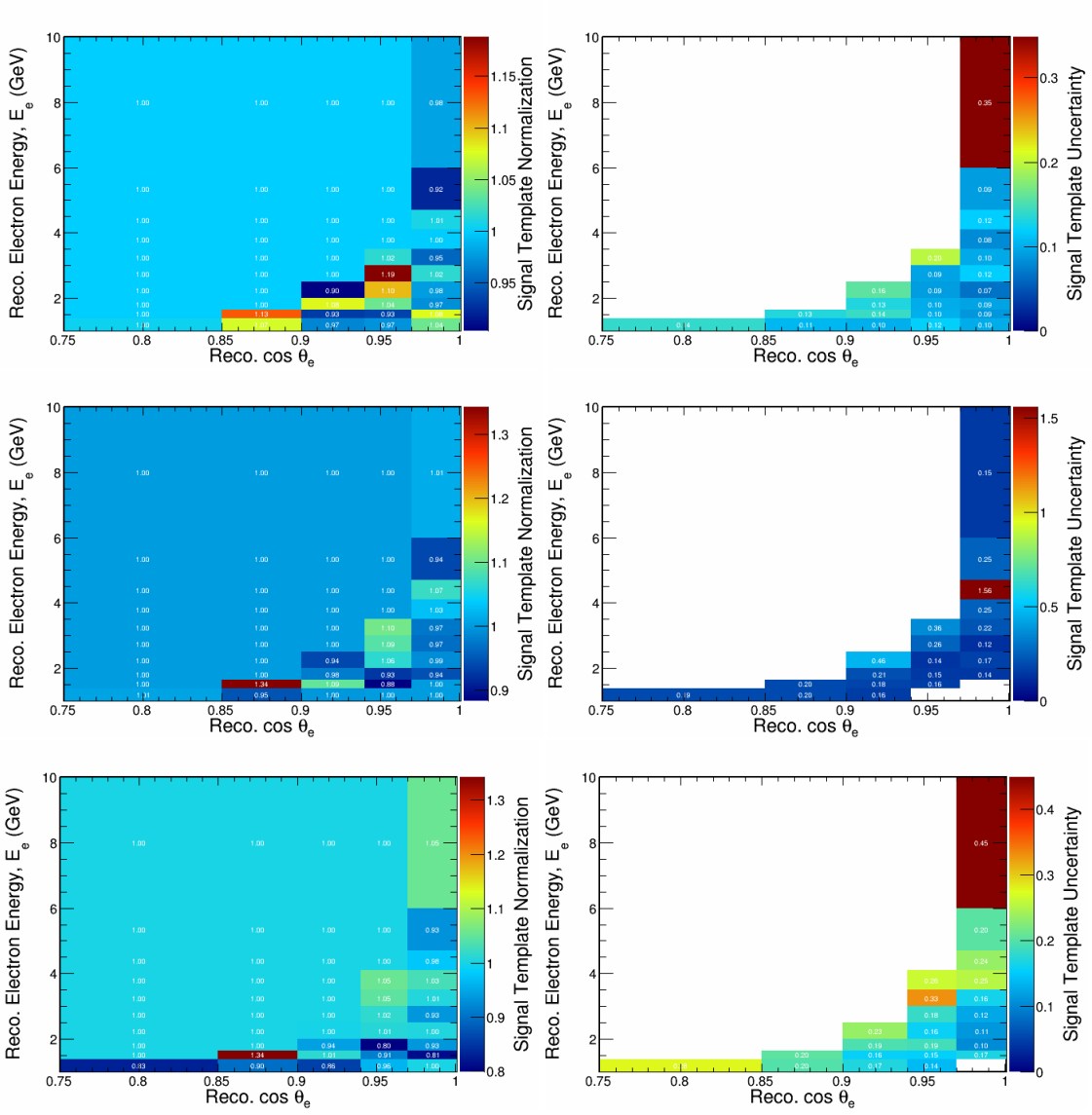

Figure 4.33: Plots of the signal-like template normalizations and uncertainties obtained using various event classifiers as templates within the fitting procedure. (Left Column) Extracted signal template normalization (Right Column) Extracted signal template normalization uncertainty. (Top) CVNe template fit results (Middle) LID template fit results (Bottom) ElectronID template fit results

are related through the folding equation where the elements of $\mathbf{A}$ specify the probability to observe a true event in a specific measured bin.. The matrix $\mathbf{A}$ is called the response (unfolding) matrix. This matrix is dependent on the ability to simulate interactions within the detector and to correctly simulate the response of the detector to these interactions. The response matrices corresponding to reconstructed variables used for the cross section measurement are shown in Figure 4.34. These matrices are built from simulated signal interactions within the ND. The choice of binning used for the analysis plays an important role in the construction of the response matrix. If the bin widths are too small, large off-diagonal elements would be present within the matrices. As the bin widths in this analysis were at least equal to the detector resolution, the matrices show prominent on-diagonal elements.

Generally, experiments attempt to determine $\mathbf{x}$ from the observed distribution $\mathbf{y}$. The simplest solution would typically require the inversion of matrix $\mathbf{A}$ such that:

$$\mathbf{x} = \mathbf{A}^{-1}(\mathbf{y} - \mathbf{b}) \tag{4.20}$$

This solution generally results in unfolded distributions that exhibit large bin-to-bin fluctuations and correspondingly large systematic uncertainties due to high correlations in neighboring bins within $\mathbf{A}^{-1}$. These results are a consistent solution with the unfolding problem, but do not necessarily correspond to the smooth distributions expected for physical processes. The large fluctuations can be avoided through the use of iterative unfolding methods. These methods are regularized using the expected true distribution given by the MC truth and the algorithm is performed a set number of times until an unfolded result is obtained. The analysis presented within this thesis makes use of an iterative unfolding algorithm developed by D'Agoistini that is commonly referred to as D'Agoisitni unfolding or more simply iterative unfolding [93] . The iterative improvement of the unfolding result $x_i^{(n+1)}$, given the result of a previous iteration, $x_j^{(n)}$, is given by:

$$x_j^{(n+1)} = x_j^{(n)} \sum_{i=1}^{M} \frac{A_{ij}}{\epsilon_j} \frac{y_i}{\sum_{k=1}^{N} A_{ik} x_k^{(n)}} \tag{4.21}$$

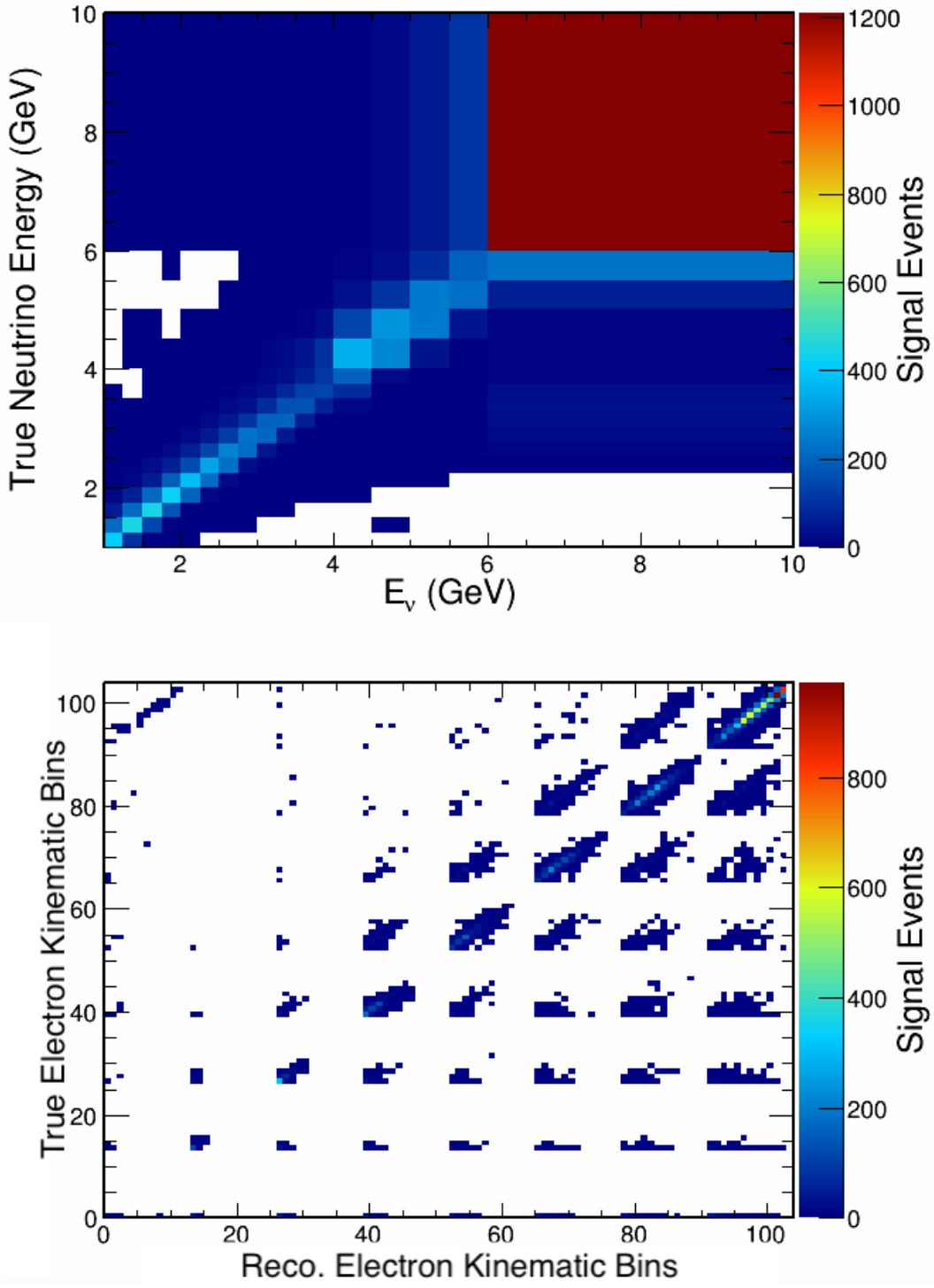

Figure 4.34: Response matrices between reconstructed and true space for neutrino energy (left) and electron kinematic bins (right). All signal events that pass the analysis selection are represented in each plot, using Nominal MC with cross section and flux central value weights.

where the only additional factor is ϵ, which is the reconstruction efficiency, given as, $\epsilon_j = \sum_i A_{ij}$.

The choice of the regularization parameter, which is the number of iterations that are performed before the unfolding procedure is ended, is an important aspect of any analysis that makes use of an unfolding algorithm. Because D'Agositini unfolding starts from the truth distribution predicted through simulation, small regularization parameters bias the unfolding results towards the simulated predictions. At large values for the regularization parameter, the unfolding procedure would reach the unregularized results encountered when using only the inversion of the response matrix, which result in large variances. The choice of regularization parameter is thus an optimization of bias versus variance. If a small regularization parameter is used, the unfolding results will be biased toward the input simulation, whereas a high-valued regularization parameter will result in a large variance, which degrades the significance of the result. Additional unfolding algorithms, like Singular Value Decomposition [94], were also considered and ultimately disregarded due to the prevalent use of D'Agositini in other experiments and the ease of unfolding in multiple dimensions necessary for the double-differential analysis.

Many techniques for requlariza tion parameter optimization were considered for this analysis. The only optimization that will be discussed in detail is the average global correlation coefficient, which is given by:

$$\rho_j = \sqrt{1 - ((V_{xx})_{jj}(V_{xx}^{-1})_{jj})^{-1}} \tag{4.22}$$

where N is the number of bins, $(V_{xx})_{jj}$ is the diagonal covariance matrix (covariance between the truth bins(j)). The average correlation indicates how, on average, each bin is related to all other bins. It is desirable to minimize these correlations as bin-to-bin correlations can result in the large unphysical fluctuations. For iterative unfolding a characteristic curve of ρ_{avg} is observed in Figure 4.35. The shape of the curve is due to the fact that the first iteration produces positively correlated results, through the artificial reproduction of the simulated prediction, where after many iterations, negative correlation coefficients begin to appear. Thus the minimum value of the av-

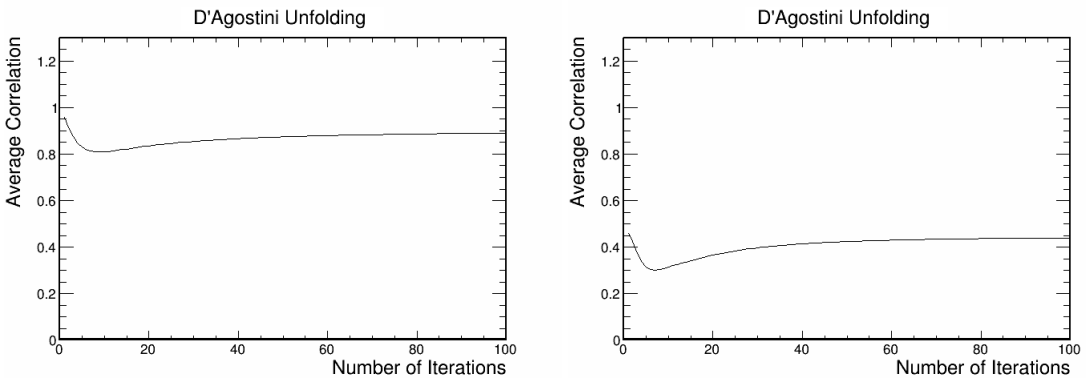

Figure 4.35: The average correlation as a function of iteration for D'Agostini unfolding is shown in each plot. The average correlation as a function of iteration for neutrino energy unfolding is shown in the left plot. The average correlation for electron kinematic unfolding is shown in the right plot. This study was performed using a statistically independent, but otherwise unmodified, fake data set.

Table 4.8: Regularization parameters determined by average global correlation

Analysis Variable	Optimized Regularization Parameter
Neutrino Energy	7
Electron Kinematic Bins (2D)	7

erage global correlation coefficient is largely independent of the starting values of the unfolding procedure [92].

Figure 4.35 shows the average correlation as a function of number of iterations (or regularization parameter) for iterative unfolding both neutrino energy and electron kinematic space. In the unfolding into neutrino energy space a minimum average correlation of about 0.8 is seen after 7 iterations. For unfolding in electron kinematic space a much lower average correlation is seen at a similar number of iterations. The choice of regularization parameter was optimized using 500 fake data samples that were generated from randomly generated Poison fluctuations of the fake data set. The optimization results are shown in Table 4.8.

Figure 4.36 shows a comparison of the unfolding of a statistically independent, but otherwise unmodified, fake data set. The plots contain the reconstructed, true and unfolded analysis variables. Unfolded results show a reasonable match to the truth prediction from the fake data. The results of this test show that after 7 iterations the unfolded distribution is able to describe the true distribution from the fake data sample.

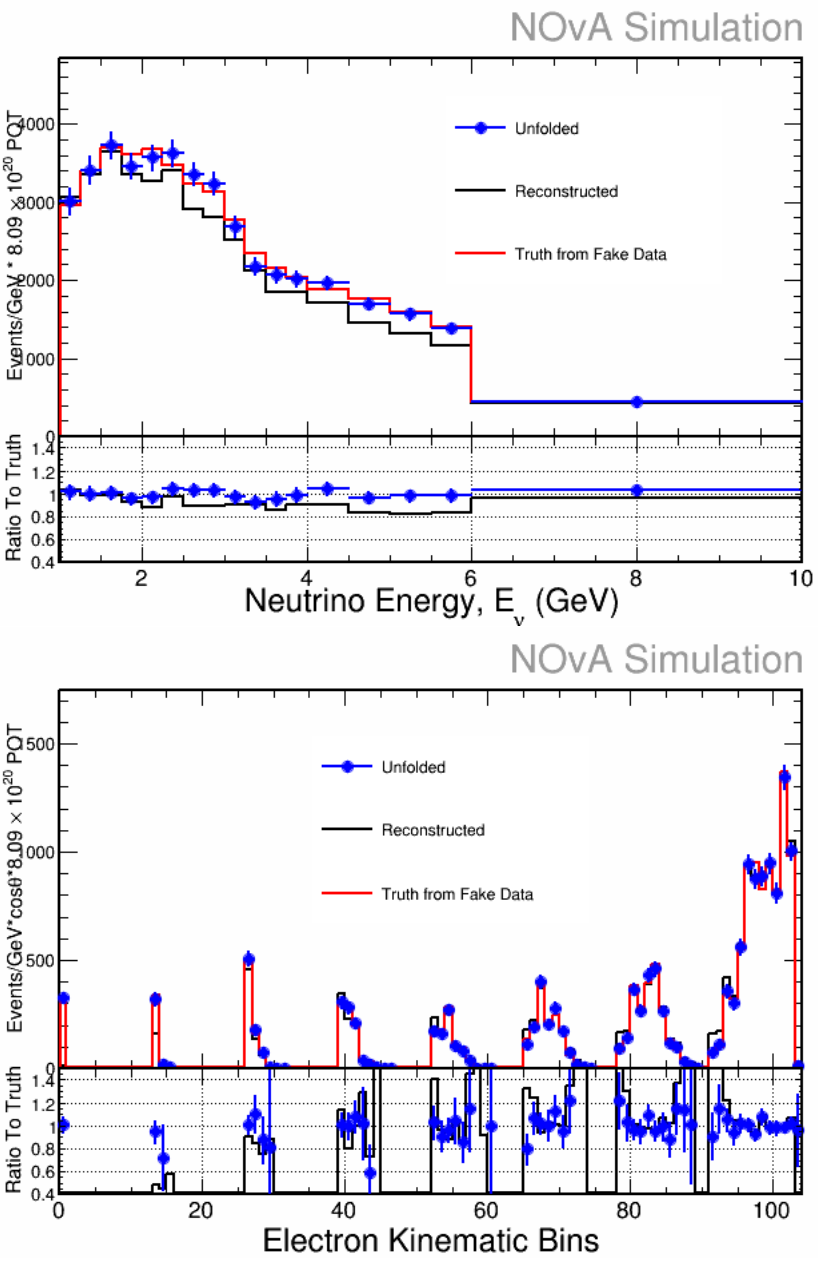

Figure 4.36: A comparison of the unfolding of a statistically independent, but otherwise unmodified, fake data set. Unfolding was done on signal only (perfect background subtraction). Cross section and PPFX central value weights are applied. The plots show the reconstructed, true and unfolded neutrino energy spectra (left) and electron kinematic distribution in 1D (right).

4.11 Systematic Uncertainties

The inclusive ν_e CC cross section measurement accounts for systematic uncertainties in the neutrino cross sections models, final-state interactions, neutrino flux, scintillation model, and the detector calibration. These uncertainties apply specifically to the near detector simulation.

In general, systematic uncertainties are assessed by varying the values in samples about their mean values. This is achieved in two ways. The first is by running the entire simulation chain using a variation in an individual parameter within the simulation. This is typically done for systematic uncertainties that may affect the reconstruction of interactions within the detector. The other approach is to use a reweighting technique to apply permutations to the nominal simulation according to some variation on a specific parameter. An example for the use of the reweighting approach is the assessment of neutrino-nucleus interaction uncertainties associated with the GENIE neutrino event generator. Given the computational resources necessary to produce the several dozen simulated samples associated with each of the adjustable parameters in GENIE a reweighting approach is necessary.

Systematic uncertainties are used several times in the development of the analysis, including the optimization of the criteria used for event selection and in the template fit used to determine signal and background estimates from data. The systematic uncertainties detailed in this section are not the final uncertainties quoted within the result. Tbe systematic uncertainties on the final extracted cross section measurement are calculated by comparing a series of extracted cross sections using the systematically shifted MC to the cross section determined with the standard ND MC (nominal MC). This section describes the various systematically shifted samples used to assess the systematic uncertainties of this analysis

4.11.1 Calibration Systematic Uncertainties

As NOνA is a calorimetric detector all measurements made within the detector depend on being able to accurately read out energy deposits occuring within the detector. Energy calibration systematic uncertainties are designed to account for any residual differences between data and MC

after detector calibration has been performed. The systematic uncertainty due to the calibration is defined by an overall uncertainty in the energy scale and the shape of detector response. The ratios of data over the simulation of calibrated muon energy as a function of distance from the center of a cell are used to define the calibration shape systematic for the XZ and YZ cells independently (Section 3.6).

An uncertainty on the energy scale of hadronic showers is determined by comparing proton energy in data and simulation. This is done by studying the profiles of dE/dx vs the distance to the track end for both protons and muons [95]. The results of this study found that the MC best matched data when scaled by 98% for muon tracks and by 95% for protons. The calibration uncertainty is determined using shifted simulated datasets where the absolute energy scale was shifted up and down by 5%.

Distributions of the hadronic energy, electron energy, neutrino energy and the electron angle are shown for the near detector samples produced from the shifted absolute calibration constants in Figure 4.37. Each plot shows the standard baseline simulation for comparison. Similar distributions are shown for systematic uncertainties associated with a shift in the attenuation correction shape in Figure 4.38.

4.11.2 Light Model

The observed light yield from a scintillator is proportional to the energy loss of the through-going particle. At high dE/dx the light yield, L , becomes non-linear to the energy loss per centimeter but can be modeled as in Reference [96]:

$$L \propto \frac{\frac{dE}{dx}}{1 + k_B \frac{dE}{dx} + k_c \left(\frac{dE}{dx}\right)^2} \tag{4.23}$$

where k_B and k_C are the Birks' constant and a higher order correction constant, respectively.

A fit of this model to near detector data resulted in the constants for the standard simulation used in this analysis. The fit was performed using simulations with various settings for the model parameters and fitting each new simulation with the data. The fit resulted in $k_B = 0.04$ cm/MeV

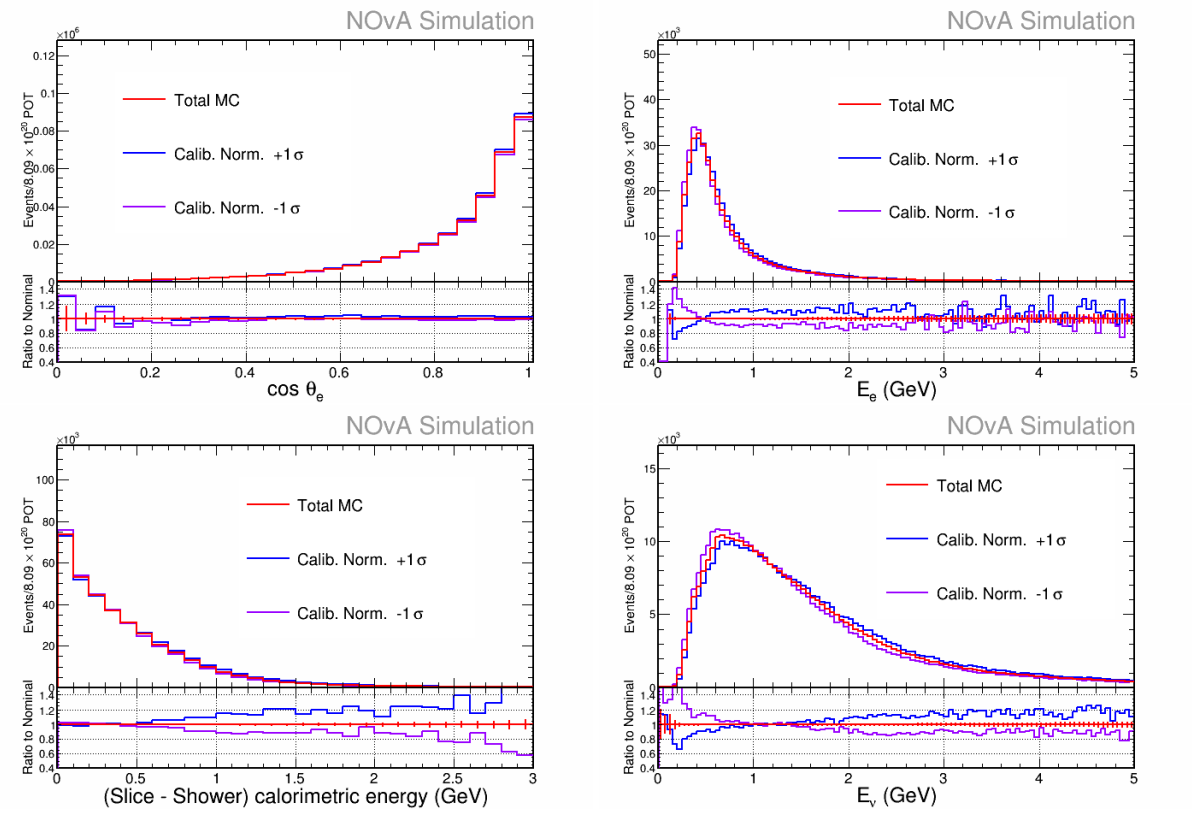

Figure 4.37: Plots of the reconstructed quantities used in the cross section measurement. The standard ND simulation is compared to systematic samples generated using adjustments to the absolute calibration normalization. The simulation is normalized to data POT.

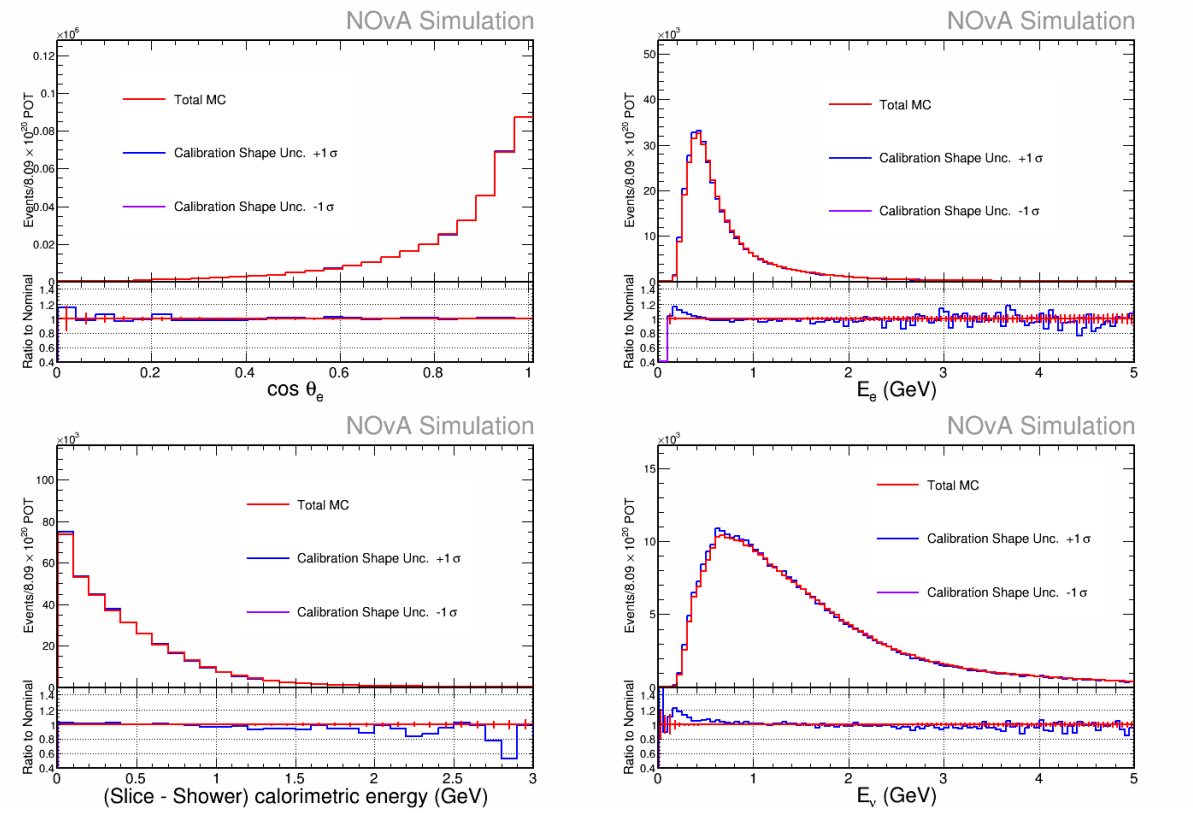

Figure 4.38: Plots of the reconstructed quantities used in the cross section measurement. The standard ND simulation is compared to systematic samples generated using adjustments to the shape of the attenuation correction. The simulation is normalized to data POT.

and $k_C = -0.0005\text{cm}^2/\text{MeV}^2$ [97]. The study and determination of Birks' constant demonstrated that the Cherenkov light could not be neglected in light simulation [98].

Uncertainties in the light levels and thresholds are accounted for by varying the light level by 10% with a compensating change made to the absolute calibration scale discussed previously. Additionally, adjustments to the Cherenkov model were also evaluated by shifting the detector's proton response down by 2.6%.

Distributions of the hadronic energy, electron energy, neutrino energy and (reconstructed-true)/true energy are shown for the near detector shifted samples produced from the shifted light level samples and variation in the Cherenkov model in Figure 4.39. Each plot shows the nominal simulation for comparison.

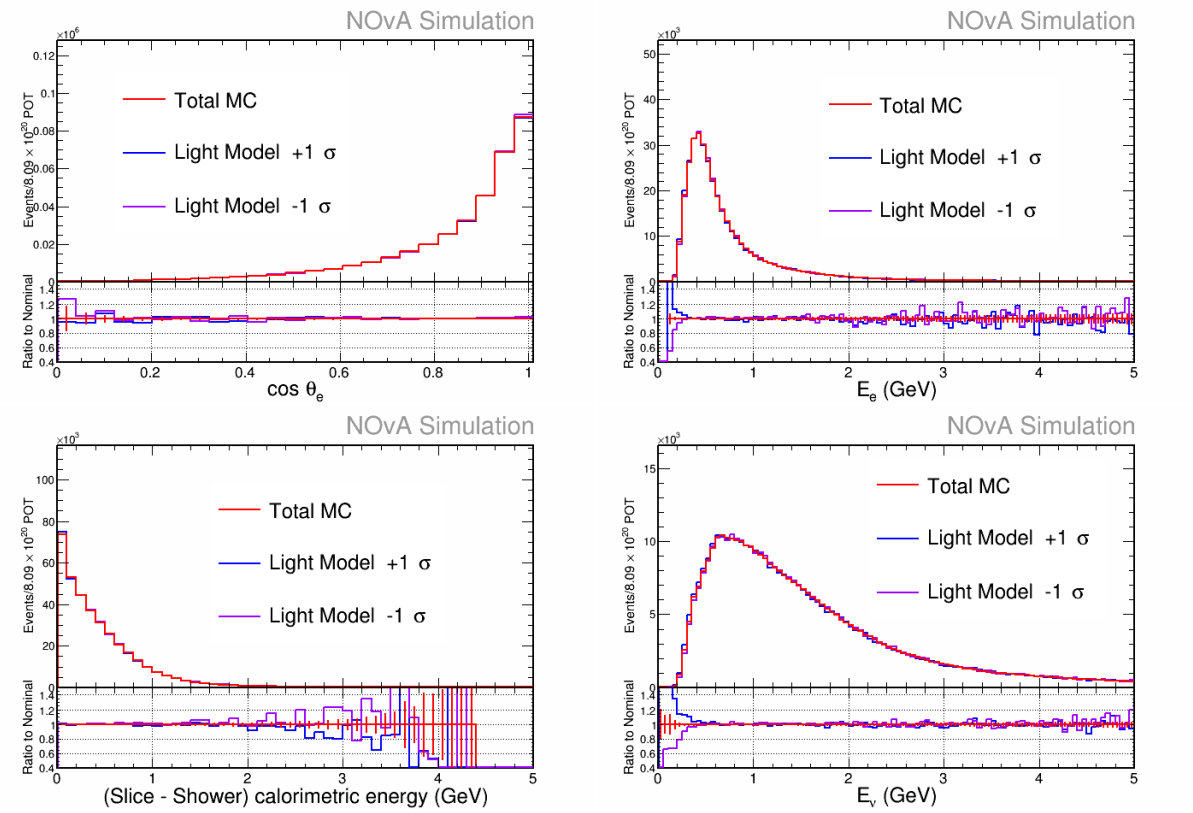

Figure 4.39: Plots of the reconstructed quantities used in the cross section measurement. The standard ND simulation is compared to systematic samples generated using adjustments to the light production model. The simulation is normalized to data POT.

4.11.3 Neutrino-nucleus interactions and FSI Uncertainties

Neutrino-nucleus interaction modeling uncertainties impact both the shape and the normalization of signal and background event distributions. These uncertainties are assessed through the use of reweighted samples created from the nominal simulation. The analysis uses of a "multi-universe" approach where a universe is created by shifting each GENIE reweightable parameter by a random fraction of a standard deviation (the nominal distribution is centered at 0) and the event is reweighted based on the results of these shifts. The cross section is then calculated for each universe using all of the techniques described previously. The width of the distribution of differences between each universe and the nominal cross section result is used to determine the systematic uncertainty associated with the neutrino-nucleus interaction model. The upper and lower bound-

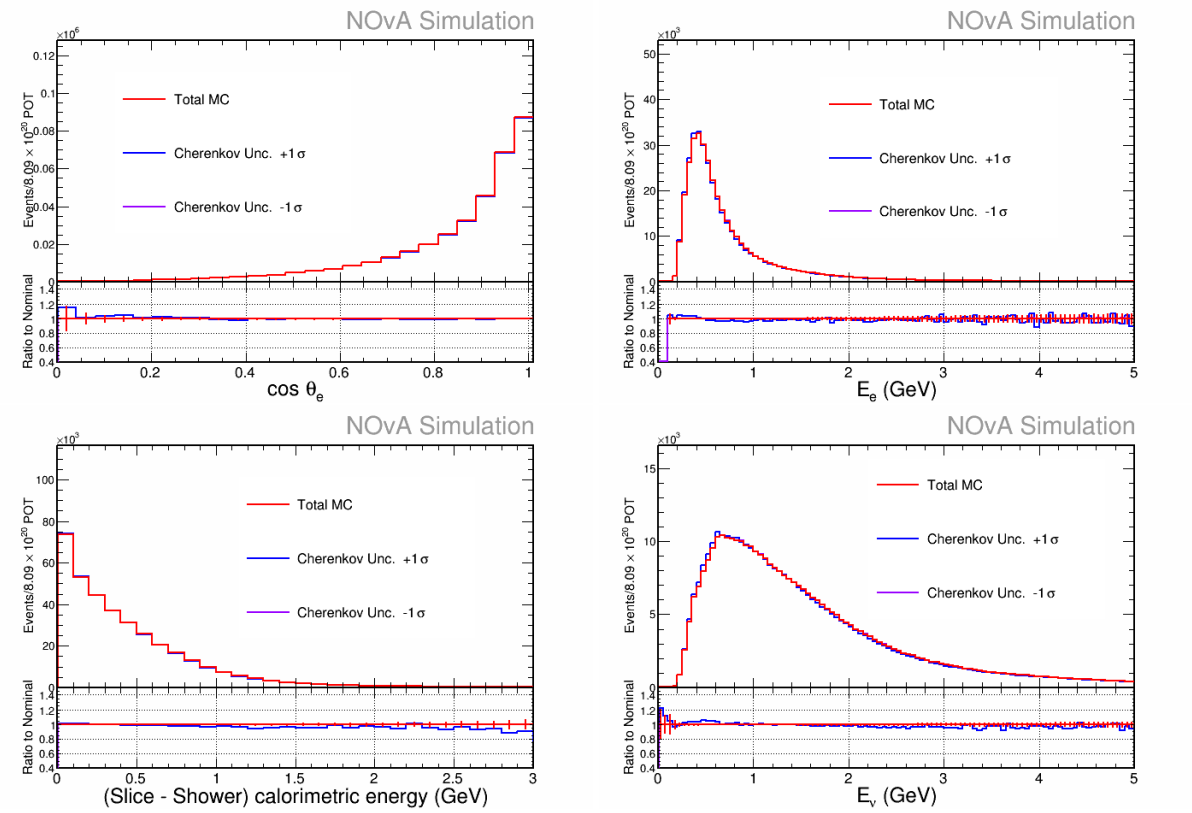

Figure 4.40: Plots of the reconstructed quantities used in the cross section measurement. The standard ND simulation is compared to systematic samples generated using adjustments to the Cherenkov light model. The simulation is normalized to data POT.

aries of the corresponding systematic error band are determined such that 68% of the universes are enclosed between the upper and lower boundaries.

Figure 4.41 shows the nominal simulation and three hundred of the systematically shifted universes for several reconstructed analysis variables. The upper and lower boundaries used within this analysis are shown in blue and red, respectively.

4.11.4 Neutrino Beam Flux

NOvA shares the NuMI beamline with other experiments and therefore benefits from a substantial amount of work that has been previously performed to characterize and understand the beam and the uncertainties associated with it.

NOvA makes use of an external package called the PPFX (Package to Predict the FluX) that calculates a correction for the G4NuMI hadron production models and their uncertainties using

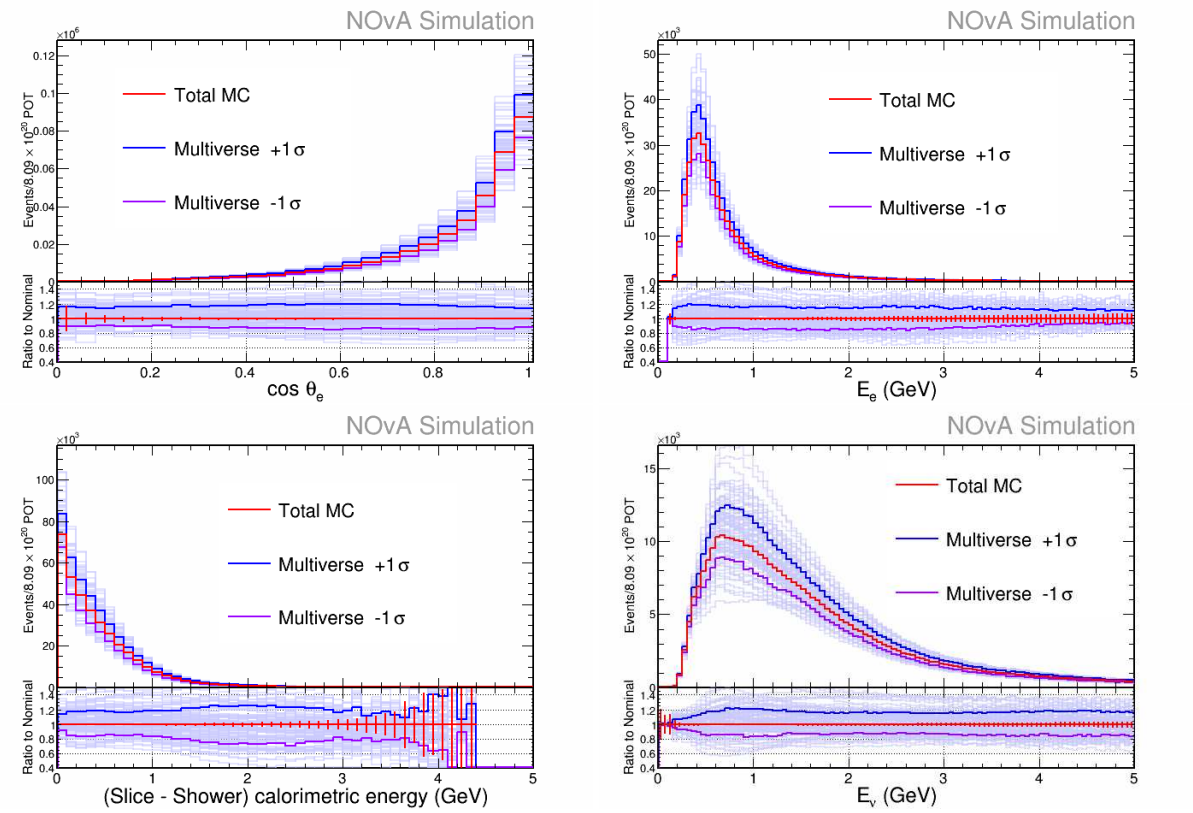

Figure 4.41: Plots of the reconstructed quantities used in the cross section measurement. The standard ND simulation is compared to systematic samples generated using adjustments to the GENIE neutrino-nucleus interaction models. Individual systematic universes are shown in light blue, with the $\pm 1\sigma$ error bands shown in dark blue and red. The simulation is normalized to data POT.

dedicated external hadron production measurements from experimental studies of hadron-nucleus collisions [72]. The output of PPFX is a set of central value weights that represent the best prediction of the neutrino flux. Additionally the package produces additional sets of weights that represent many possible predictions based on the uncertainties on the external hadron production measurements. These weights are then propagated through the entire NOvA analysis framework. A multive-universe approach is used to estimate the hadron production uncertainties associated with nominal near detector simulation of the neutrino flux.

Figure 4.42 shows the fractional uncertainty on the flux with respect to neutrino energy, split into different PPFX components. This figure shows the uncertainties for ν_μ production. The total uncertainty about the beam peak (near 2 GeV) is about 8%, mostly coming from pions created when the primary proton beam interacts with the target, nucleon interactions outside the target,

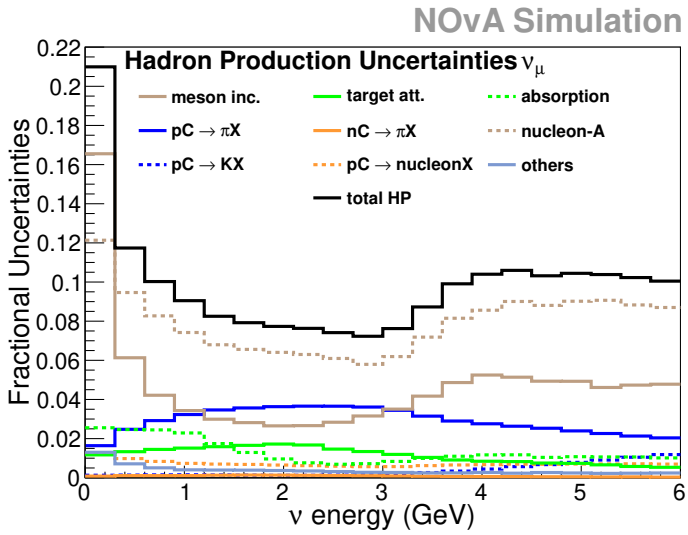

Figure 4.42: Hadron production fractional uncertainties for a muon neutrino beam in the near detector. The total (in black), calculated as the sum in quadrature of every interaction type uncertainty, is around 8% near the peak and increases for higher energies. For very low energies, the uncertainty is higher due to interactions not covered by data (PPFX assumes high uncertainties for these interactions). The uncertainties split into interactions types are also shown. After the pion production type (covered mainly by NA49 data), the meson incident has the higher value.

and interactions with incident mesons. More details regarding these uncertainties can be found in Reference [72]. The total uncertainty in the ν_e flux at the ND is plotted in Figure 4.22. The grey systematic error band shows both the hadron production uncertainties (similar to those shown in Figure 4.42) and the beam focusing uncertainties.

Figure 4.41 contains the nominal simulation and one hundred of the systematically shifted universes for several reconstructed analysis variables. The upper and lower boundaries used within this analysis are shown in blue and red, respectively.

4.12 Validation of the Analysis Framework

This section describes the tests used to further validate that the analysis framework. The tests helped ensure that no significant biases were present in the cross section determination prior to unblinding the data. All fake data samples were made up of a sample of simulated events that was statistically independent from the sample of simulated events that is used to perform the analysis.

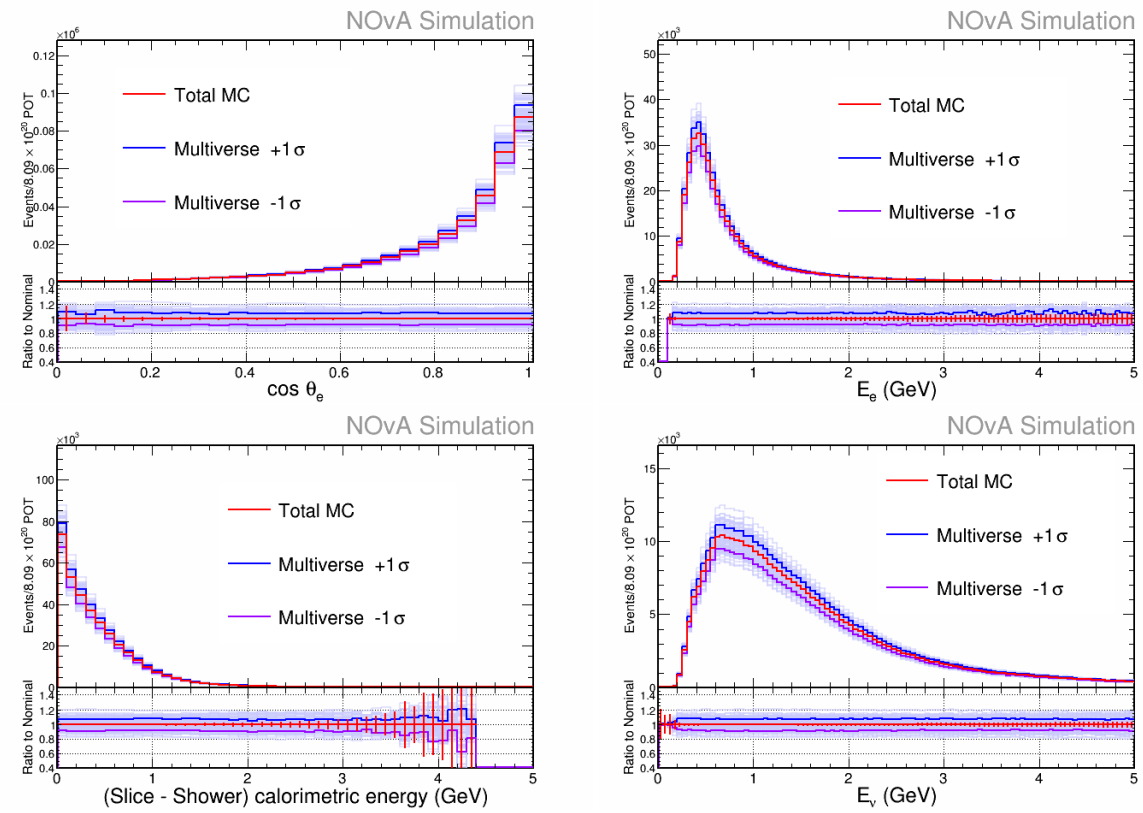

Figure 4.43: Plots of the reconstructed quantities used in the cross section measurement. The standard ND simulation is compared to systematic samples generated using universes generated from the PPFX package. Individual systematic universes are shown in light blue, with the $\pm 1\sigma$ error bands shown in dark blue and red. The simulation is normalized to data POT.

The testing procedure was performed as follows, the simulated fake data sets were analyzed as if they were real data events. This included the use of all selection criteria, efficiency corrections, and data-driven (or in this case, fake data-driven) template fits, as well as the MRE efficiency correction described above. The extracted cross section was compared to the true cross section as observed in the fake data sample. Three fake data sets were used for the testing of the cross section extraction:

1. Statistically Independent: a simulated set of events from nominal ND simulation that comprised 1/4 of the total ND simulation.

2. M_a NC Resonant Shift: a simulated set of events with an adjustment to the axial mass used in the NC resonant interaction model.

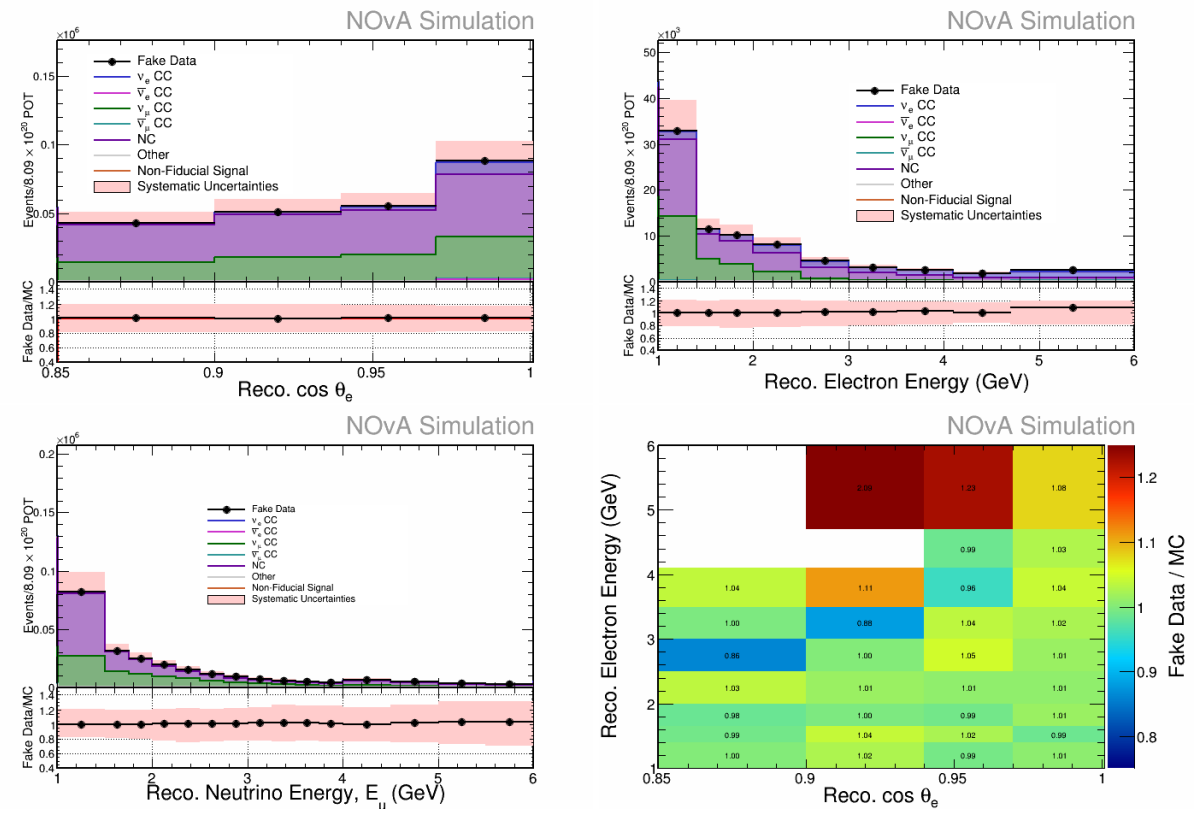

Figure 4.44: The reconstructed distributions from a statistically independent set of simulated events as fake data. Reconstructed $\cos\theta_e$ is shown in the top left plot. Reconstructed electron energy is shown in the top right plot. Reconstructed neutrino energy is shown in the bottom left plot. The bottom panel in each plot shows the ratio of fake data to the nominal simulation. The ratio of selected fake data to nominal simulation in double differential analysis bins is shown in the bottom right plot. The red error band shows the systematic uncertainties for each distribution.

3. MEC Interaction Model Shape Shift: a simulated set of events with an adjustment to the shape of the MEC cross section model.

4.12.1 Statistically Independent Fake Data

The first step of the test was the comparison of fake data to the nominal simulation after all event selection criteria had been applied. These comparisons are shown in Figure 4.44. The data-to-MC ratios show slight statistical variations between the nominal and the fake data sets. The two dimensional ratio plot shows how the selected fake data and nominal simulation differ in the electron kinematic bins used to extract the cross section measurement.

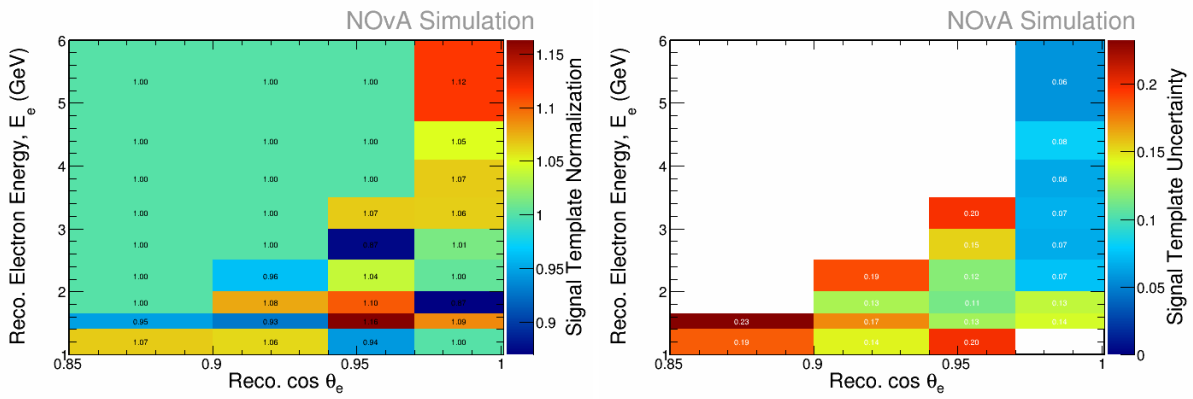

Figure 4.45: The plots of the fitted signal template normalization and the uncertainty parameters from a template fit to statistically independent fake data.

The template fit, performed using the ElectronID event identifier, resulted in the extracted signal normalization parameters and their uncertainties shown in Figure 4.45. Most of the extracted normalization parameters are within 10% of unity, although there are bins that contain normalization parameters that are slightly outside this range. The post-fit event distributions are shown in Figure 4.46. These plots also contain the reduced systematic uncertainties from the template fit, in addition to the flux normalization uncertainty, which corresponds to about 10%.

The extracted signal predictions were compared to the nominal signal prediction (Figure 4.47). Additionally, the extracted and nominal signal predictions were compared in each of the electron kinematic bins (Figure 4.48). Only the extracted signal predictions in the ranges of $0.97 \leq \cos\,\theta_e \leq 1$ and $4.5 \leq E_e < 6$ GeV have values outside of nominal by more than 2σ. However these are still within the normalization uncertainties, which are shown as a blue error band within the figure. This uncertainty was not accounted for within the template fit.

After the signal was determined from the template fit the reconstructed variable distribution was unfolded to the true kinematic variable space. The unfolded distributions in electron kinematic space are shown in Figure 4.49. These plots show the unfolded signal estimate compared to the true fake data electron kinematic distributions. All bins within the measured phase space show good agreement between extracted and true (fake data) signal.

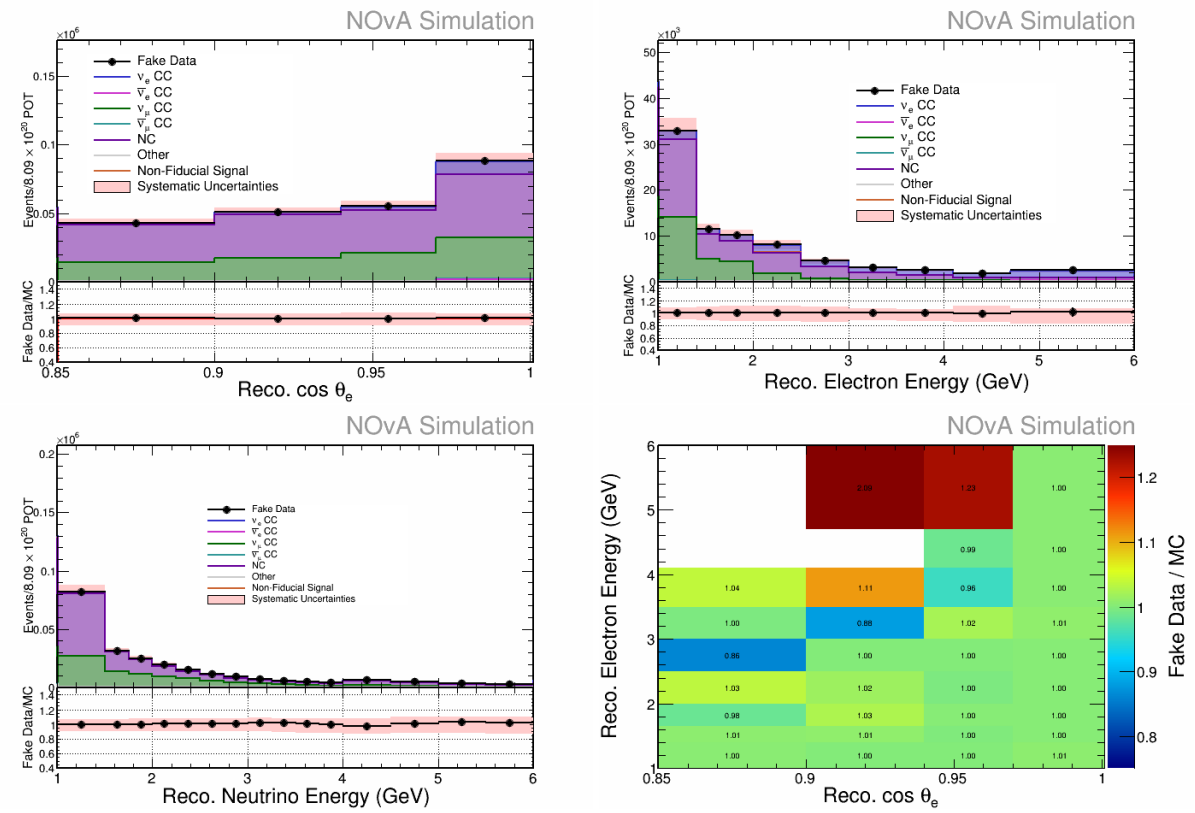

Figure 4.46: The distributions of reconstructed variables using a statistically independent set of simulated events as fake data. Reconstructed $\cos\theta_e$ is shown in the top left plot. Reconstructed electron energy is shown in the top right plot. Reconstructed neutrino energy is shown in the bottom left plot. The bottom panel in each plot shows the ratio of fake data to the nominal simulation. The ratio of selected fake data to nominal simulation in double differential analysis bins is shown in the bottom right plot. The red error band shows the systematic uncertainties for each distribution.

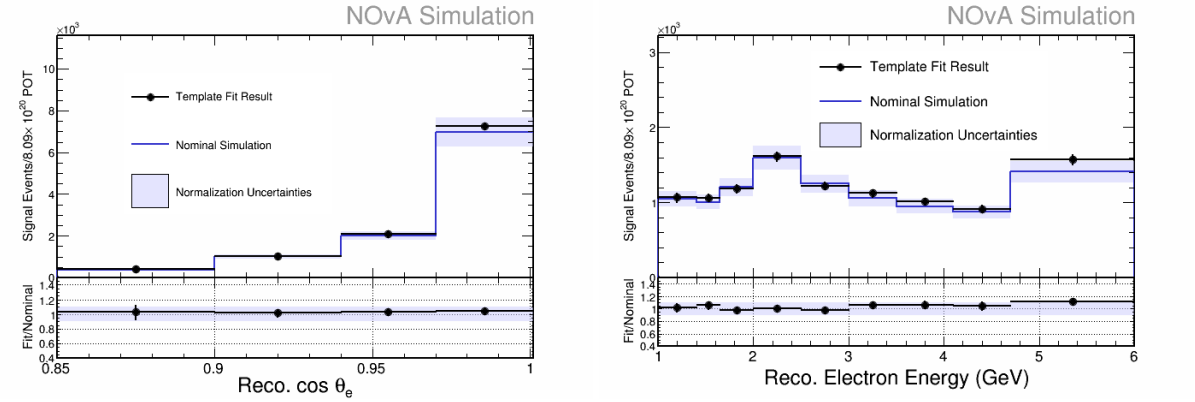

Figure 4.47: The reconstructed electron kinematic variables for signal events extracted from the template fit compared to the standard signal prediction from ND simulation. Error bars show the statistical uncertainty plus the uncertainties from the template fit. The blue error band shows the flux normalization uncertainties not taken into account through the template fit procedure.

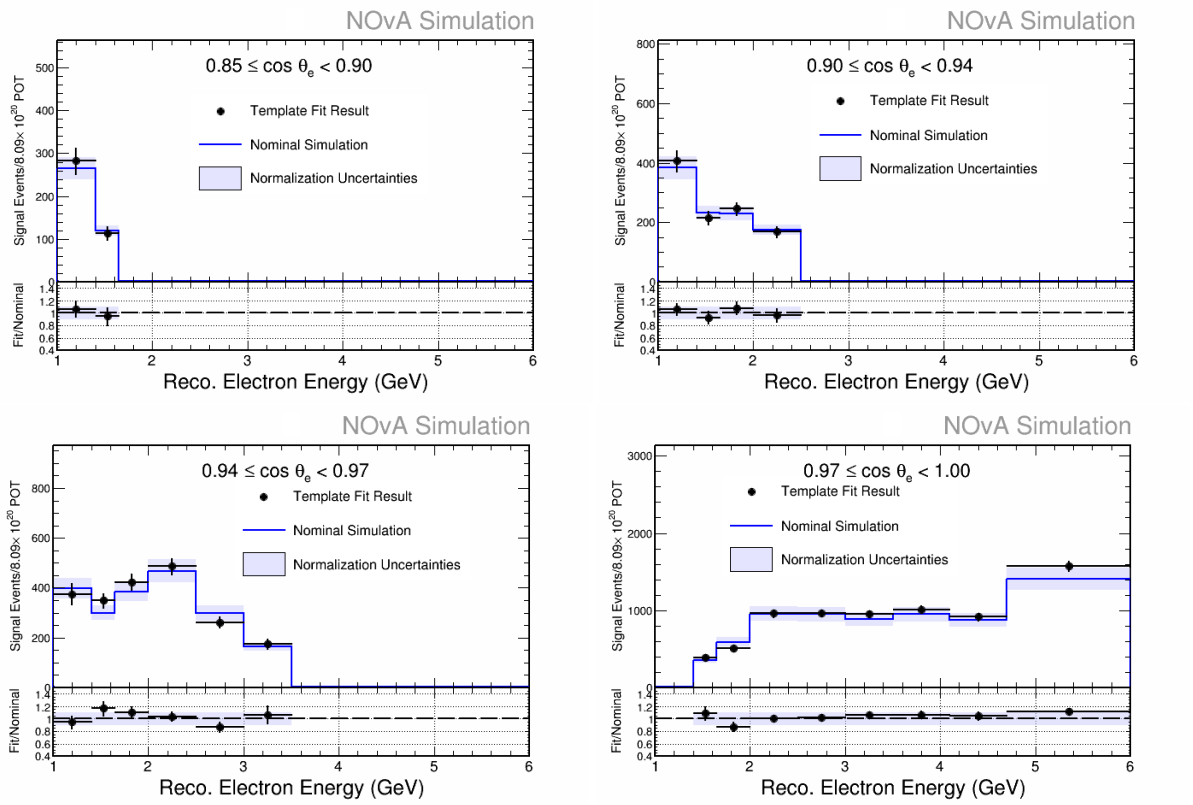

Figure 4.48: The electron kinematic variables in reconstructed space for signal events extracted from the template fit compared to the standard signal prediction from ND simulation in bins of $\cos\theta_e$ as a function of electron energy. Error bars correspond to the statistical uncertainty plus the uncertainties from the template fit. The blue error band corresponds to the flux normalization uncertainties not taken into account through the template fit procedure.

Figure 4.50 shows the extracted cross section from fake data and nominal simulation compared to the true fake data cross section in each of the double differential analysis bins. The right column shows the contribution of each source of systematic uncertainty on the total fractional uncertainty for the extracted cross section. The fractional uncertainty labeled as "Fit" takes into account the statistical uncertainty from the selected number of events, the statistical uncertainty resulting from the fitting procedure, and the systematic uncertainties from the covariance matrix used to produce the fit. This takes all of the systematic uncertainties into account for the signal and background predictions for the analysis. The remaining fractional uncertainty bands correspond to the systematic uncertainty coming from the efficiency correction procedure (ν-N interactions, calibration, light modeling, etc). All of the uncertainties coming from the neutrino beam flux are contained

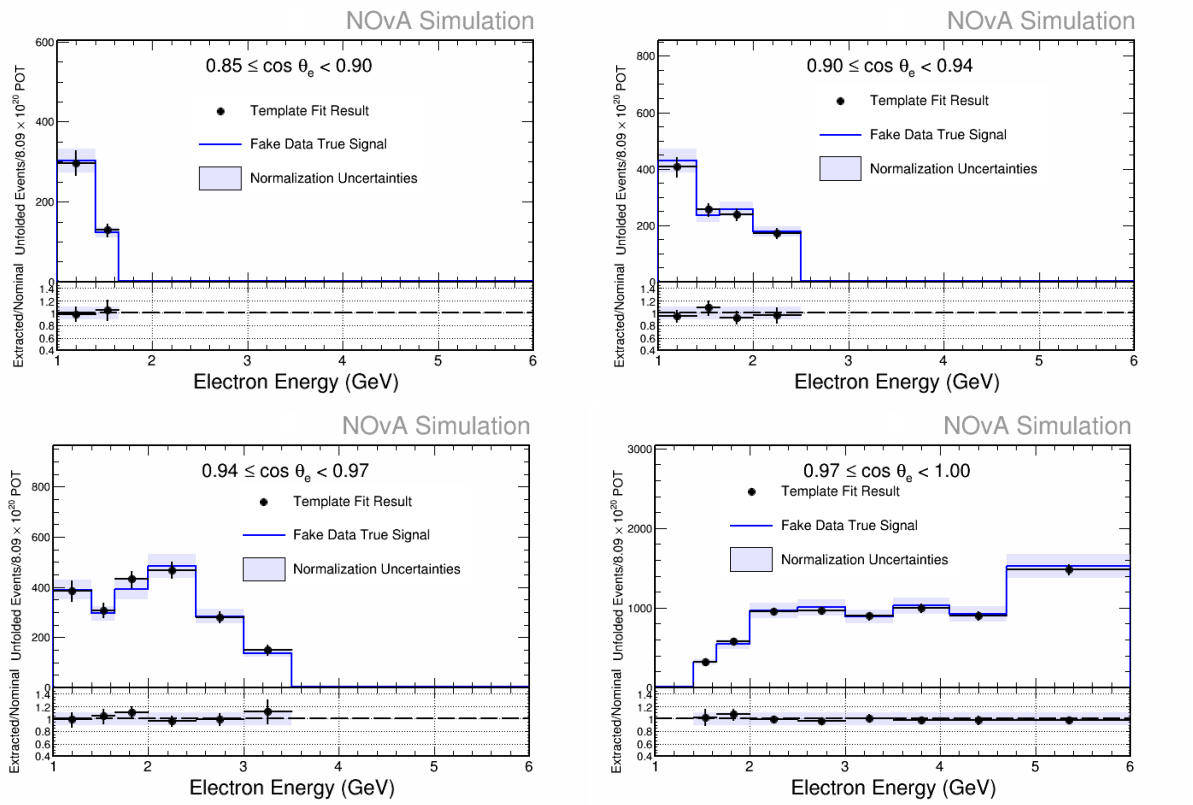

Figure 4.49: The electron kinematic variables in true space for signal events extracted from the template fit compared to the standard signal prediction from ND simulation in bins of $\cos\theta_e$ as a function of electron energy. Error bars correspond to the sum of the statistical uncertainty plus the uncertainties from the template fit. The blue error band corresponds to the flux normalization uncertainties not taken into account through the template fit procedure.

in the flux and beam focusing uncertainty bands. In total most bins show an expected fractional systematic uncertainty of 15 to 20% on the cross section measurement.

4.12.2 Reweighting the Fake Data

The reweighting procedure was described in Section 4.11. The same reweighting procedure was also utilized in the production of fake data sets through perturbations on the standard ND simulation. The following sections describe the cross section extraction procedure using fake data generated with shifts in the NC background prediction (Section 4.12.2) and with shifts on the MEC interaction model used in charged current interactions (Section 4.12.2).

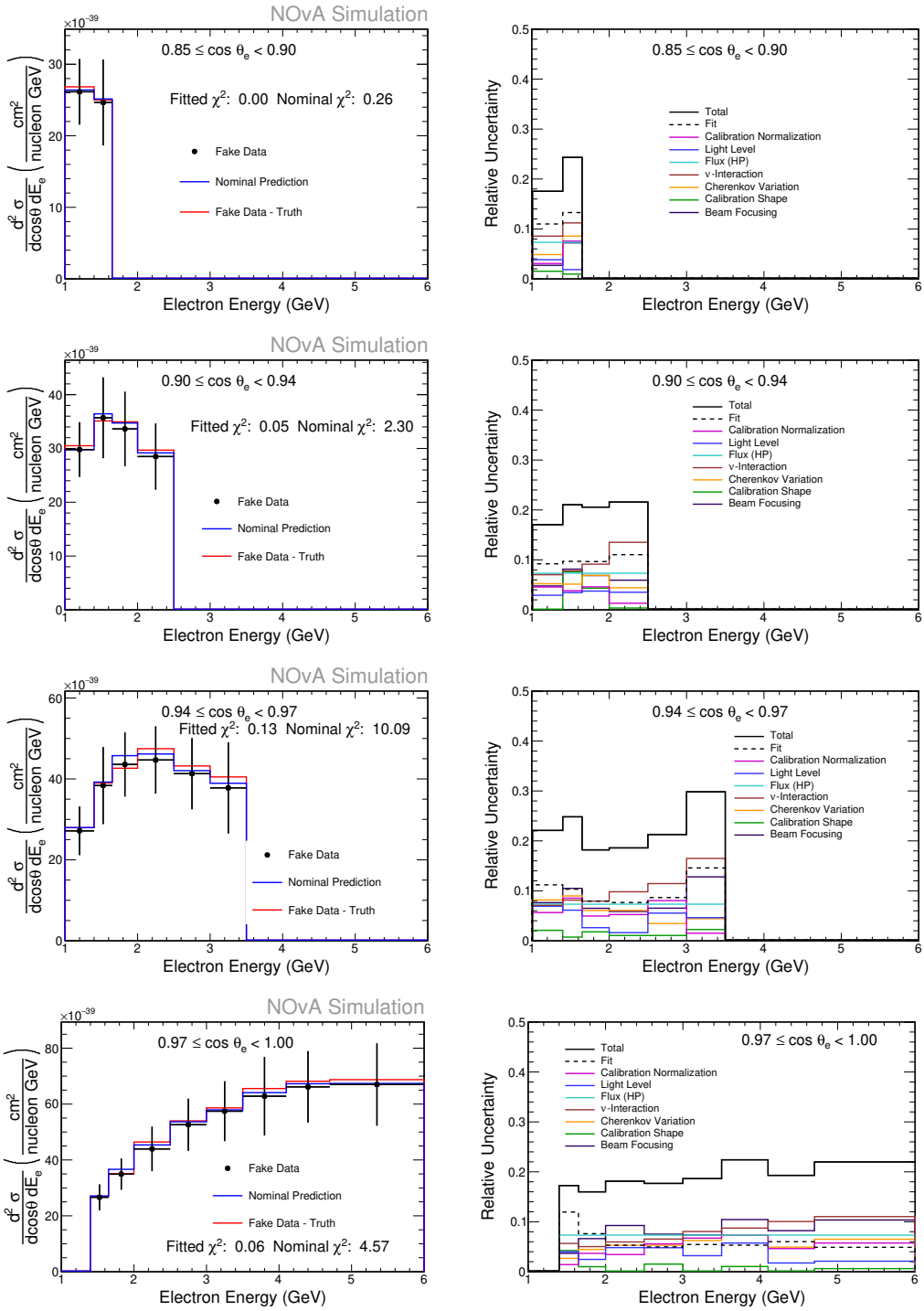

Figure 4.50: The extracted ν_e CC cross section and fractional uncertainties from the analysis of a statistically independent set of simulated events as fake data. The fake data results are shown as one dimensional distributions of the double differential result in the left column. Error bars show the statistical plus all systematic uncertainties on the extracted cross section measurement. The relative contribution of all sources of uncertainty are shown in the right column.

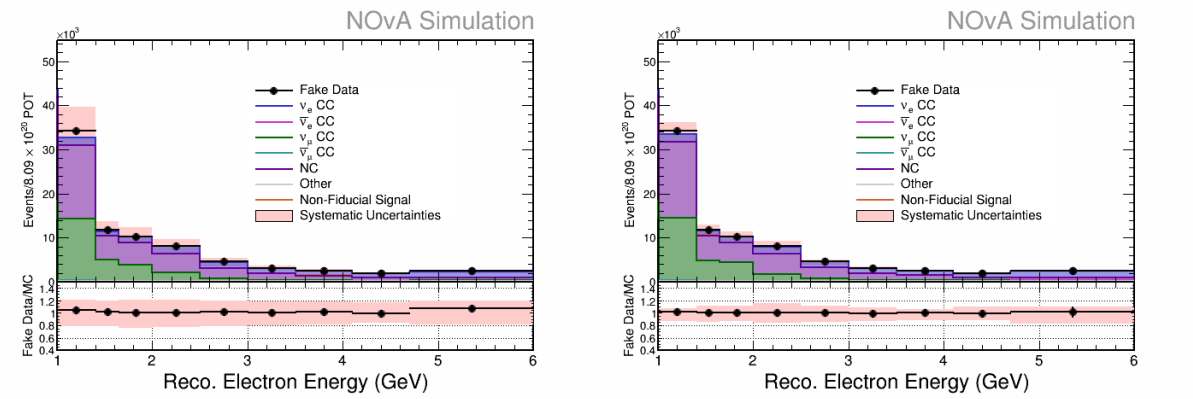

Figure 4.51: The reconstructed electron energy before (left) and after (right) the template fit procedure was performed to a fake data sample produced with a shift on the axial mass of the NC resonant model. The red uncertainty band shows full systematic uncertainties prior to and after the template fit.

M_A NC Resonant Interaction Shift

The fake data used in this section were generated from a statistically independent set of simulated events with a 1σ shift to the axial mass parameter of the NC resonant interaction model. This parameter was chosen as it is one of the few model parameters that affects the event rate of NC events with a final-state π^0. The reconstructed E_e distribution is shown pre- and post- template fit in Figure 4.51. The pre-template fit distribution shows an approximately 5% increase in the selected number of fake data events due to the effect the shift had on the normalization of background events.

The extracted signal distribution was compared to the nominal signal prediction in Figure 4.52. A single plot of the extracted electron neutrino cross section is shown in Figure 4.53. The results are consistent with the nominal prediction and the fake data true cross section, with slight increases in the relative uncertainty on the measurement due to changes in the background normalization prediction.

MEC Interaction Cross Section Shape Shift

The fake data used in this section were generated from a statistically independent set of simulated events with a 1σ adjustment to the the shape of the MEC interaction cross section. This

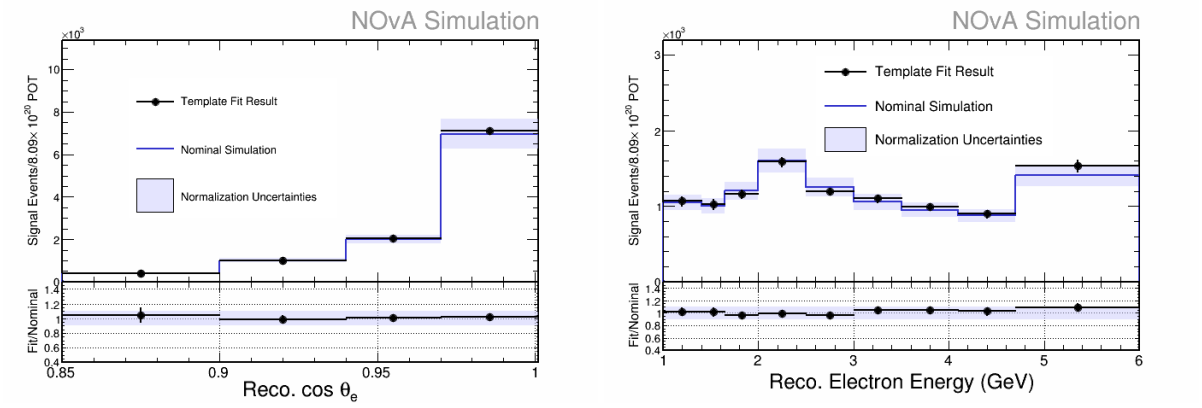

Figure 4.52: The electron kinematic variables in reconstructed space for signal events extracted from the template fit compared to the standard signal prediction. Error bars correspond to the statistical uncertainty plus the uncertainties from the template fit. The blue error band corresponds to the flux normalization uncertainties not taken into account through the template fit procedure.

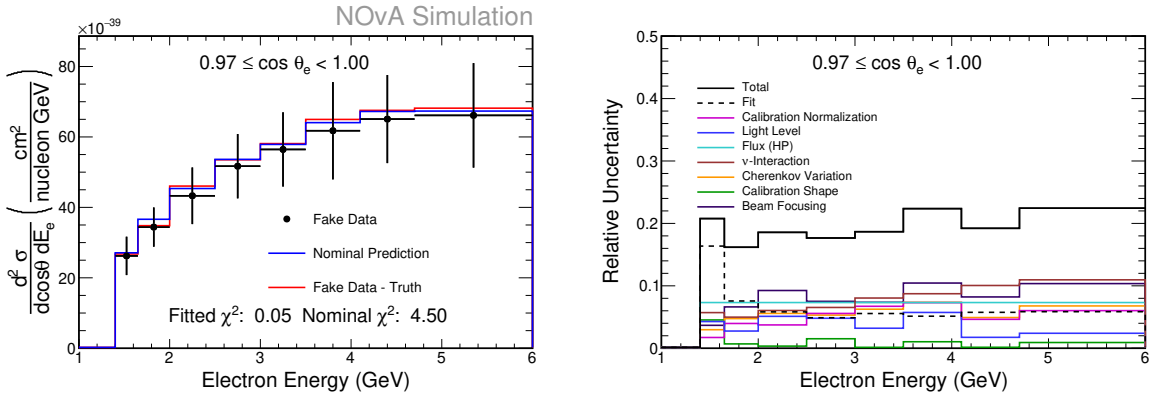

Figure 4.53: The extracted ν_e CC cross section and fractional uncertainties using a sample of fake data produced with a shift on the axial mass of the NC resonant model. Error bars show the statistical plus all systematic uncertainties on the extracted cross section measurement.

adjustment slightly alters the cross sections for charged current ν_μ and ν_e MEC interactions within the fake data sample.

The extracted cross section distributions from this fake data set are shown in Figure 4.54. Good agreement between is seen between the extracted and true cross sections from fake data. This test demonstrates that the analysis may not be sensitive to the extraction of small differences between some cross section models, as all of the results are consistent within the systematic uncertainties of the analysis.

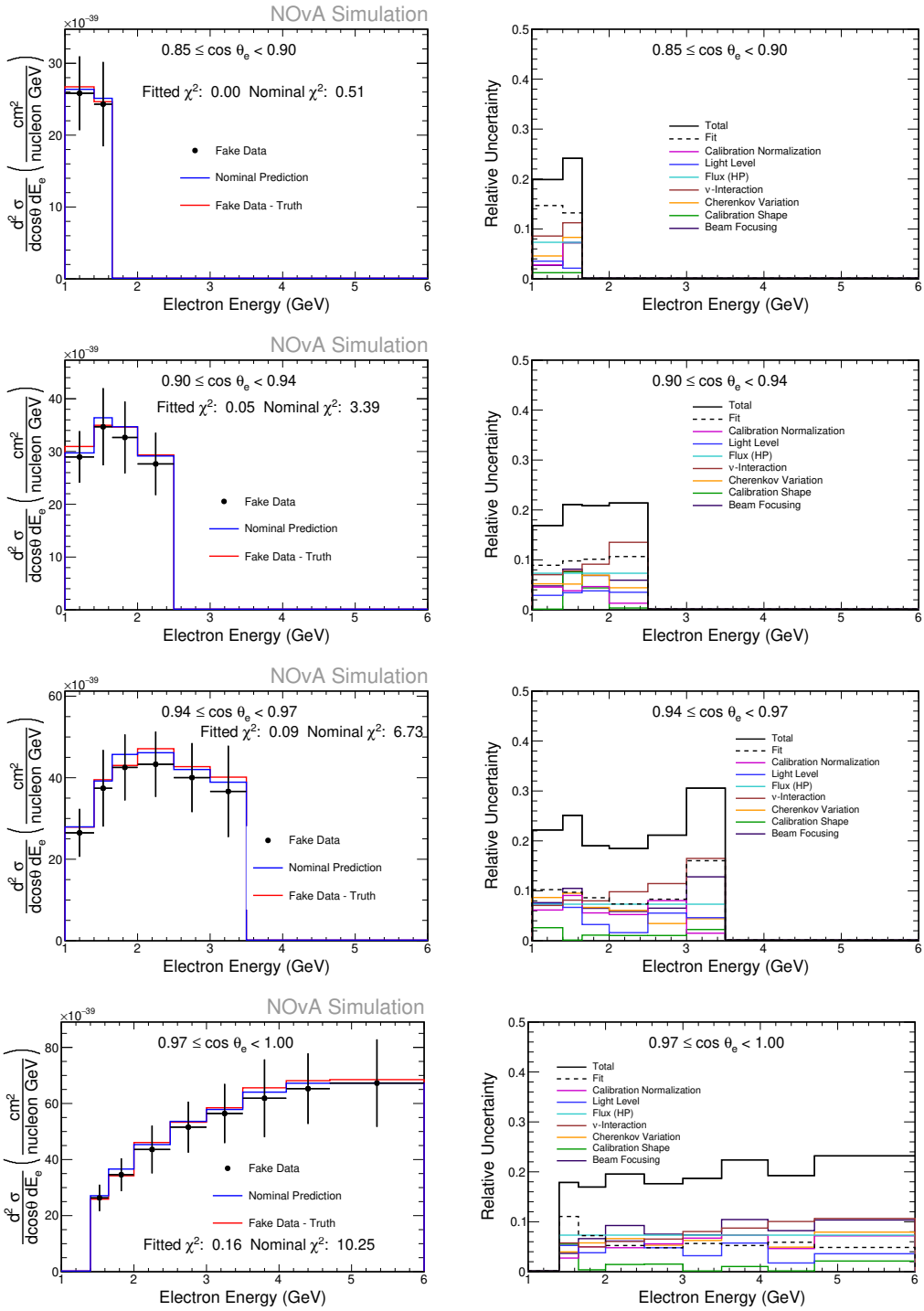

Figure 4.54: The extracted ν_e CC cross section and fractional uncertainties using a sample of fake data produced with a shift on the shape of the MEC interaction cross section. Error bars correspond to the sum of the statistical plus all systematic uncertainties on the extracted cross section measurement.

Chapter 5

Results

This chapter describes the results of the cross section measurement using the NOνA ND data collected between November 2014 to February 2017, corresponding to an exposure of 8.09×10^{20} POT of a primarily neutrino beam. The procedure used to extract the cross section from data was the same as described in Chapter 4.

5.1 Selected Data Events

The total numbers of selected events in data and the simulation are shown in Table 5.1. There is a slight excess of selected data events for each selection criteria used within this analysis. After all selection criteria are applied this excess of only 2% remains, which is covered by the systematic uncertainties of the analysis.

Distributions of vertex position and shower start and end locations for selected data and simulated events after the preselection criteria are shown in Figures 5.1 and 5.2. The plots show comparisons between the number of selected data and simulation events before and after the containment criteria was applied. A substantial deviation between the selected and simulated samples of about 20% after the containment criteria is applied can be seen near 200 cm in the Z position of the shower stop position. This is near the edge of the containment region where such deviations can

Table 5.1: Table featuring the numbers of events remaining following each selection cut. Simulated events are broken down by interaction type and normalized to the data exposure.

Cut	**Data**	**Total MC**	**Signal**	**Backgrounds**						
			ν_e CC	Total	ν_μ CC	$\bar{\nu}_\mu$ CC	NC	$\bar{\nu}_e$ CC	Background ν_e CC	Other
All Events	142,028,000	141,441,000	132,315	141,309,000	113,943,000	4,997,710	16,510,200	142,701	1,484,200	4,230,980
Data Quality	93,109,300	89,835,600	123,389	89,712,200	78,716,600	3,634,130	6,313,330	68,988	636,802	342,414
Fiducial	7,119,780	7,188,850	116,454	7,072,400	5,691,320	223,809	1,120,630	12,184	8,381	16,082
Containment	1,037,390	1,017,510	28,926	988,589	625,159	16,315	335,111	3,746	1,245	7,013
Front Planes	1,033,630	1,009,850	28,813	981,039	619,473	16,061	333,601	3,726	1,218	6,960
NHits	919,790	909,639	17,848	891,791	589,699	15,146	280,451	2,019	868	3,607
MuonID	374,273	366,574	15,562	351,012	123,147	1,748	220,508	1,807	782	3,019
CVNe	16,240	15,918	8,975	6,943	2,615	34	3,287	894	102	10

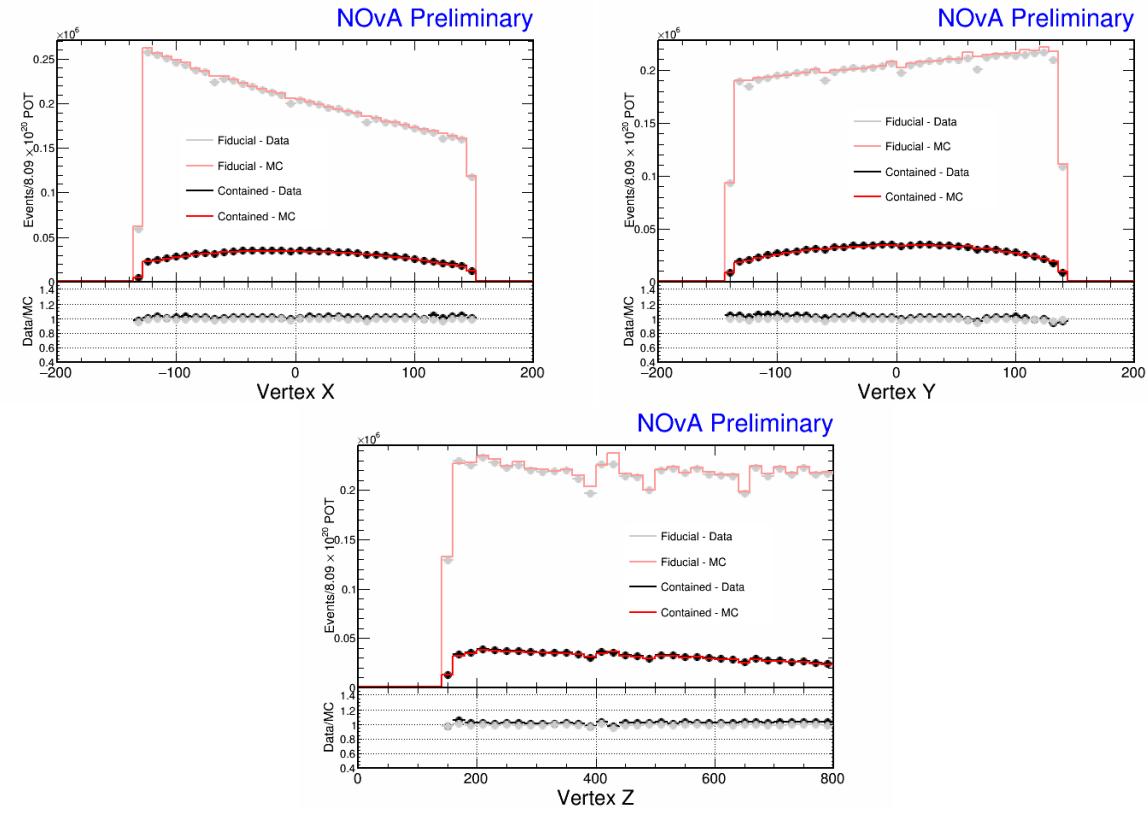

Figure 5.1: Plots of the reconstructed interaction vertex coordinates for selected data and simulated events after fiducial and containment selection cuts have been applied. The ratio of the data to simulation are plotted in the bottom frame of each plot.

be expected. These uncertainties are consistent with the systematic uncertainties on the number of selected events after the containment criteria are applied.

The electron kinematic distributions for selected events prior to the template fit procedure are shown in Figure 5.3. The reconstructed electron angle, or the cosine between the highest scoring electron prong within an event and the beam direction, shows discrepancies starting below about $\cos\theta = 0.8$. Both reconstructed neutrino energy and reconstructed electron energy show data excess near the peaks of the distributions. Each of these discrepancies are well covered by the systematic uncertainties of the analysis and lie outside of the phase space being used in the cross section measurement. Figure 5.4, shows the same reconstructed electron kinematic distributions within the kinematic phase space used in the cross section measurement.

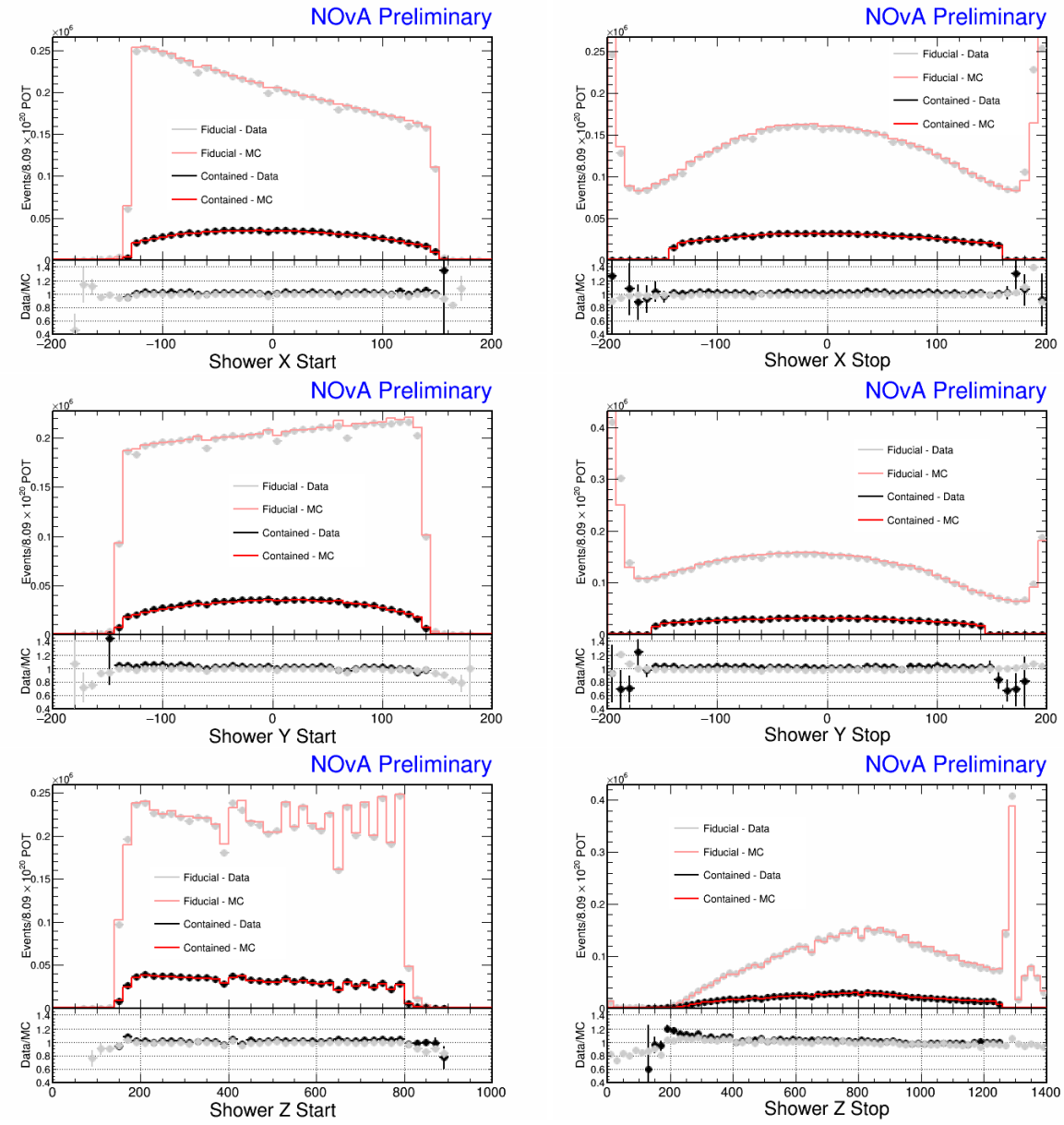

Figure 5.2: Plots of the reconstructed start and stop positions of the highest energy prong for selected data and simulated events after fiducial and containment selection cuts have been applied. The ratio of the data to simulation are plotted in the bottom frame of each plot.

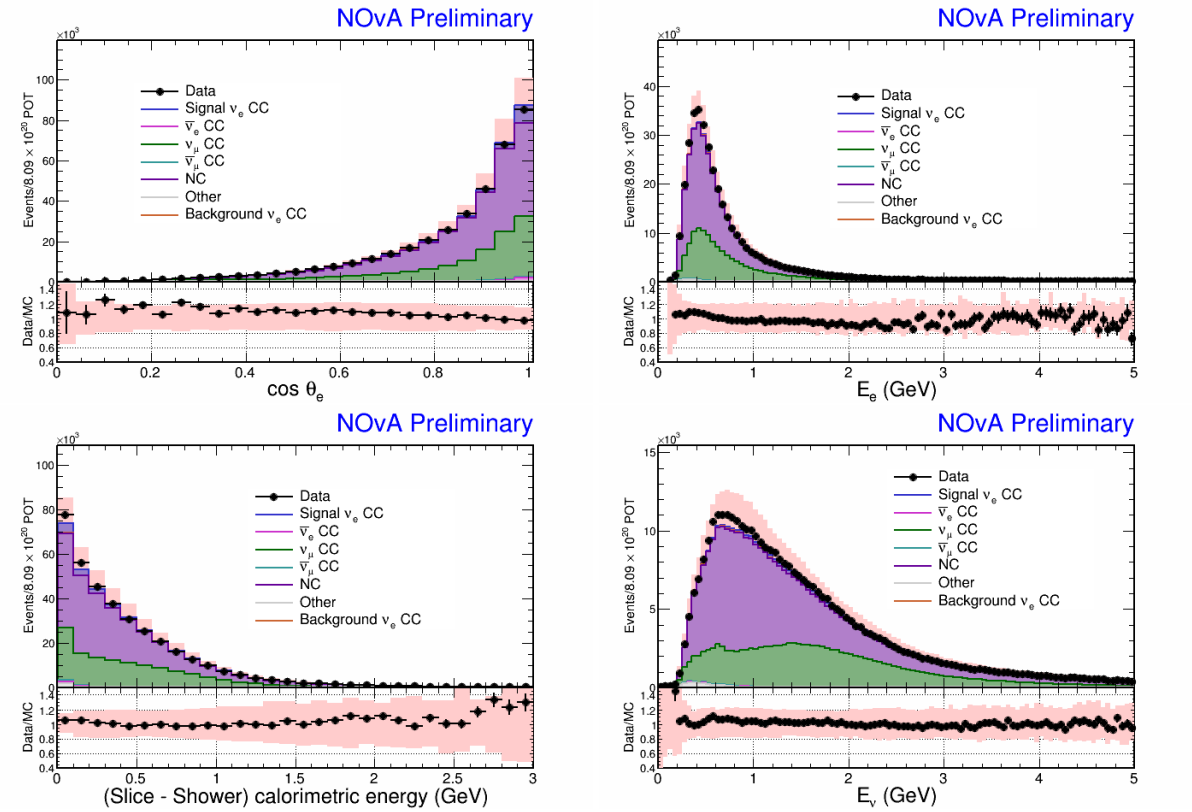

Figure 5.3: Plots in reconstruction space of data compared to nominal simulation. The reconstructed $\cos\theta_e$ is shown in the top left plot. The reconstructed electron energy is shown in the top right plot. The reconstructed slice energy minus the leading shower calorimetric energy is shown in the bottom left plot. The reconstructed neutrino energy is shown in the bottom right plot. Ratio of the data to simulation are plotted in the bottom frame of each plot. Error bars correspond to the statistical uncertainty, while the red band corresponds to the systematic uncertainty.

A plot of the ElectronID variable is shown in Figure 5.5. This distribution shows slight discrepancies along the entire distribution, with the largest focused in the peak of the background region (slightly below ElectronID = 0) and the transition from the background to signal region from 0 to 0.2 in ElectronID. The differences are covered by systematic uncertainties.

5.2 Template Fit Results

To calculate the ν_e CC inclusive cross section template fits were used to extract signal events. The results of the template fits are shown in Figure 5.6. The pink band represents the total extracted uncertainties from the template fit in addition to the remaining normalization uncertainties coming from the neutrino beam flux.

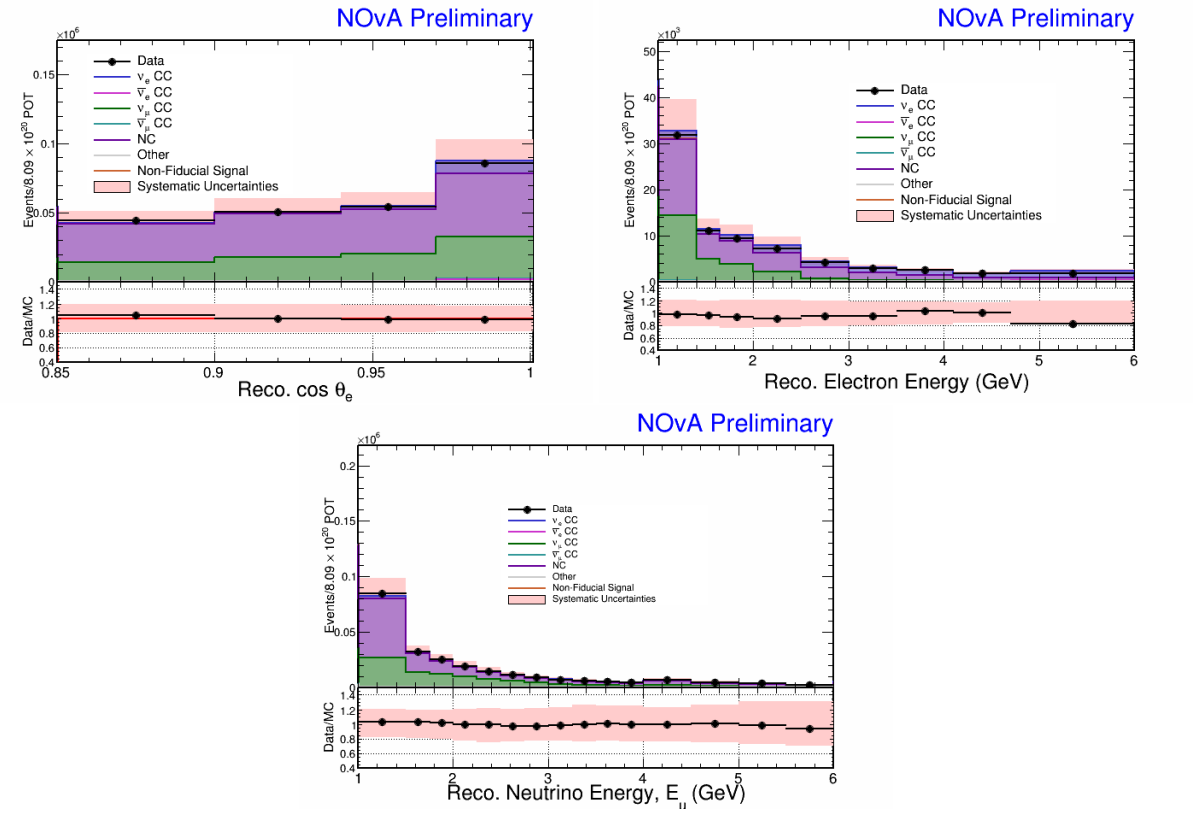

Figure 5.4: Plots of the reconstructed kinematic distributions of data compared to nominal simulation in the binning used for the cross section measurement. The reconstructed $\cos\theta_e$ is shown in the top left plot. The reconstructed electron energy is shown in the top right plot. The reconstructed neutrino energy is shown in the bottom plot. The ratio of data to simulation are plotted in the bottom frame of each plot. Error bars correspond to the statistical uncertainty, while the red band corresponds to the systematic uncertainty.

The extracted signal normalization parameters and uncertainties on the normalization parameters are plotted in Figure 5.7. The 2D normalization distribution show some bin-to-bin fluctuations for the extracted normalization parameters. These fluctuations are nearly all covered by the extracted uncertainties from the template fit and the flux normalization uncertainties (blue band) in Figure 5.8. One data point falls outside of the uncertainty.

The extracted signal normalization parameters and uncertainties on the normalization parameters are depicted in Figure 5.7. The 2D normalization distribution shows some large bin-to-bin fluctuations in the extracted normalization parameters. However, these fluctuations are almost all covered by the extracted uncertainties on the signal parameter, as shown in Figure 5.8. Only one data point falls well outside with two others falling just outside of the extracted template fit and

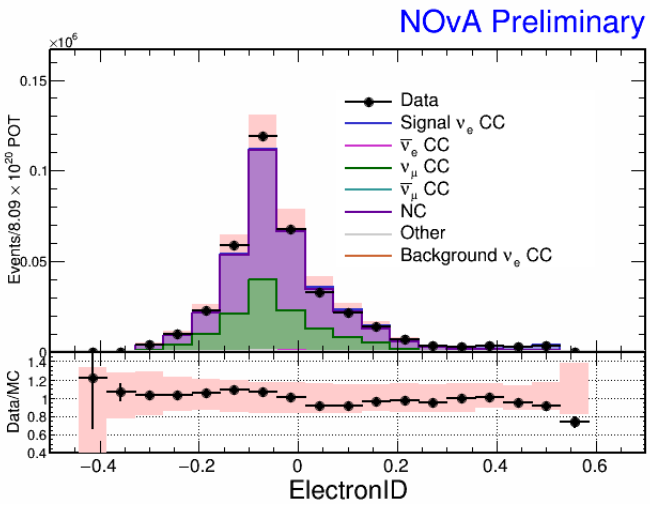

Figure 5.5: Plot of the ElectronID distributions of ND data compared to nominal simulation. Error bars correspond to statistical uncertainty while the pink band corresponds to the systematic uncertainty.

normalization uncertainties. Any of the discrepancies that are related to detector or reconstruction effects are removed through the unfolding of the measured signal distribution to the true electron kinematic phase space. Figure 5.9 contains the results of this procedure.

5.3 Double-Differential Cross Section Measurement

The unfolded double-differential cross section as a function of electron energy and electron angle are plotted in Figures 5.10 and 5.11, the fractional uncertainties on the cross section measurement are plotted in Figures 5.12 and 5.13, and the systematic uncertainty covariance matrix is plotted in Figure 5.14, respectively. No significant disagreements between the extracted cross section and that predicted by the cross section models employed by NOνA were found.

The dominant systematic uncertainties come from the template fit, flux, and the neutrino-nucleus interaction models. The reported fractional uncertainty for the template fit takes the systematic uncertainties on the extracted signal and background predictions and the statistical uncertainty on the estimated number of signal events into account, these uncertainties contribute at about the 10% level in most of the bins. Flux uncertainties related to hadron production (light blue histogram) and the focusing of the hadrons within the NuMI horns (dark blue histogram), combine

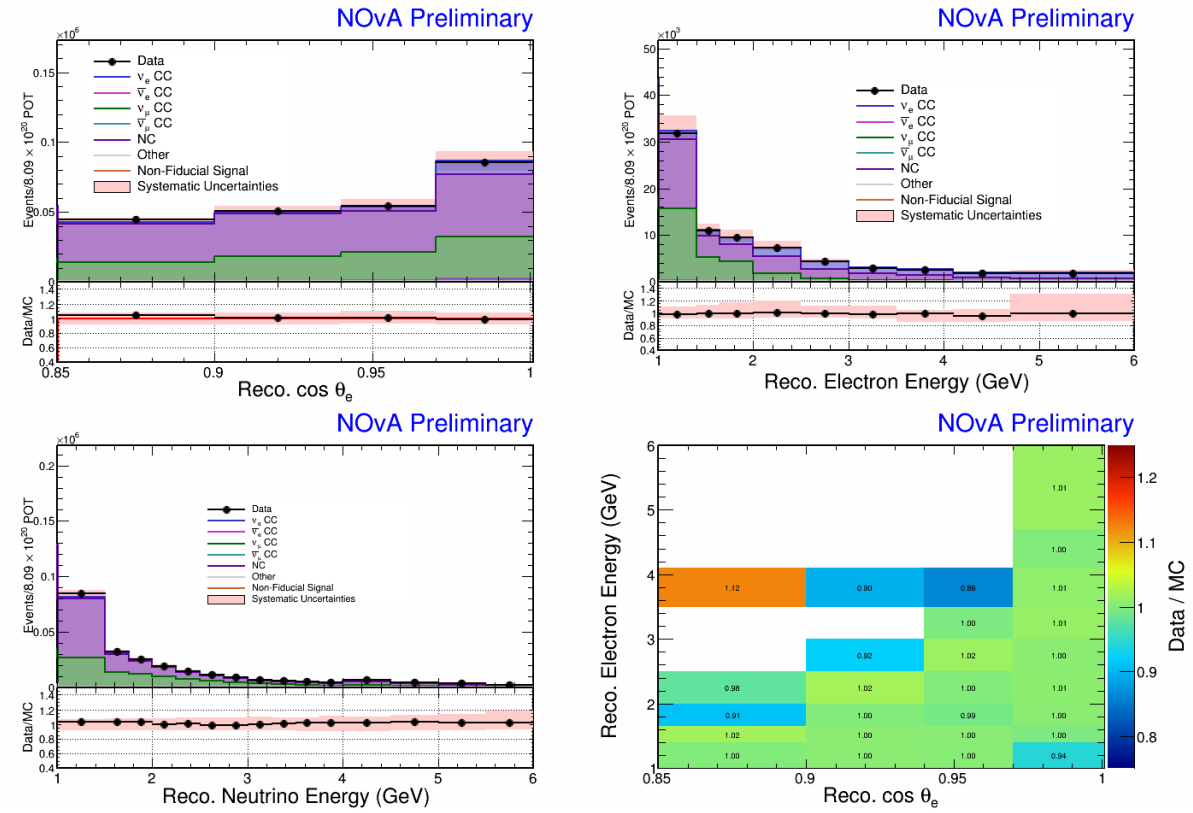

Figure 5.6: The reconstructed distributions of NuMI ND data compared to simulation after template fit weights have been applied. (Top Left) Reconstructed $\cos\theta_e$, (Top Right) Reconstructed electron energy, (Bottom Left) Reconstructed neutrino energy. (Bottom Right) Ratio of data to weighted simulation in electron kinematic bins.

to contribute at the 10% level. At higher electron energy, the beam focusing and neutrino-nucleus interaction model uncertainties become dominant.

5.4 Total Cross Section Result

The template fitting procedure was used to extract signal and background estimates in reconstructed electron kinematic space. To produce the total cross section measurement as a function of neutrino energy, the signal estimates, as a function of electron kinematics, were reformulated into neutrino energy using a three dimensional mapping matrix. The signal estimate as a function of neutrino energy is shown in Figure 5.15. The unfolded signal estimate as a function of neutrino energy is depicted in Figure 5.16

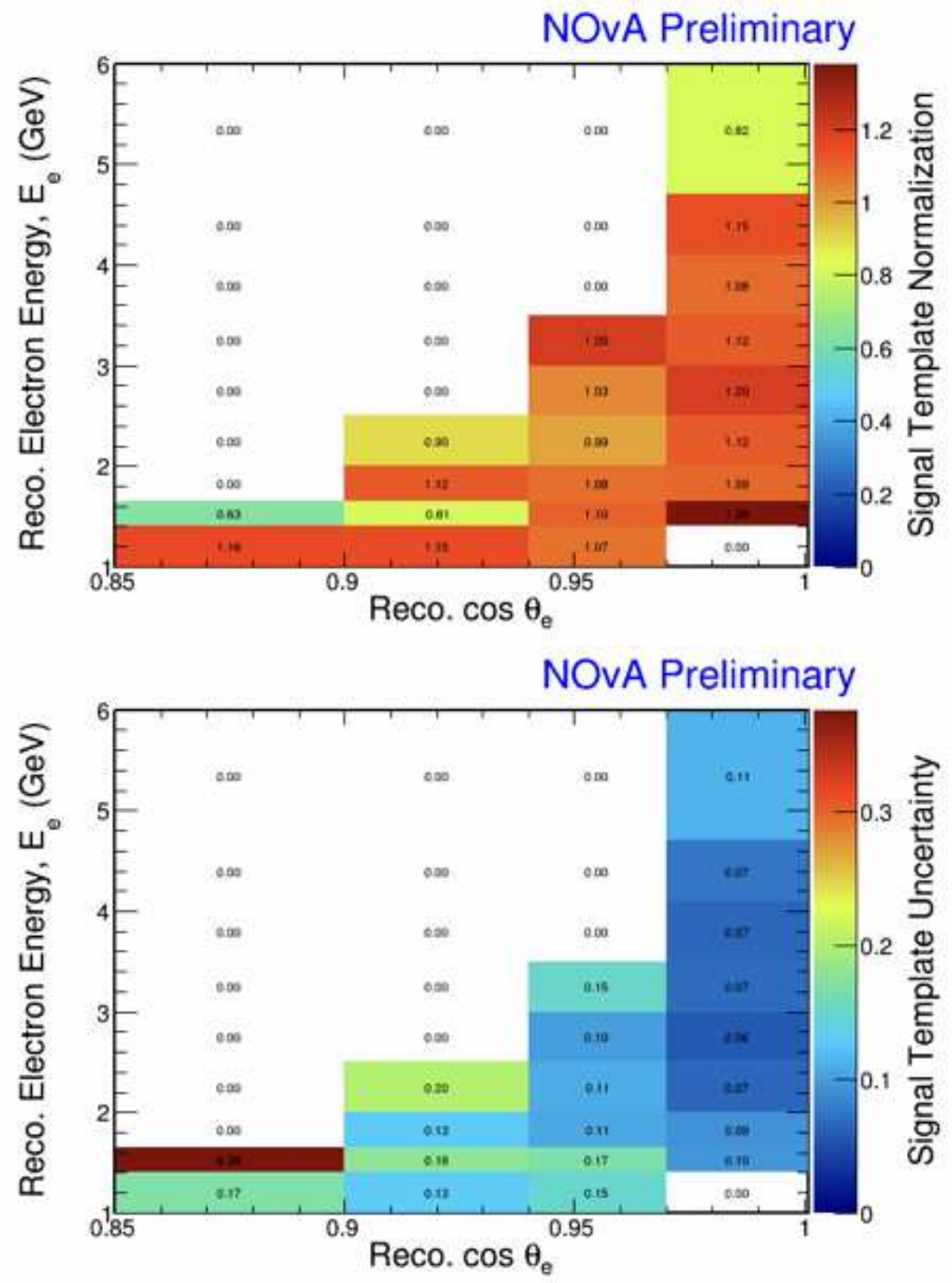

Figure 5.7: The plots of the extracted signal template normalization and uncertainty parameters from a template fit to the NuMI ND data.

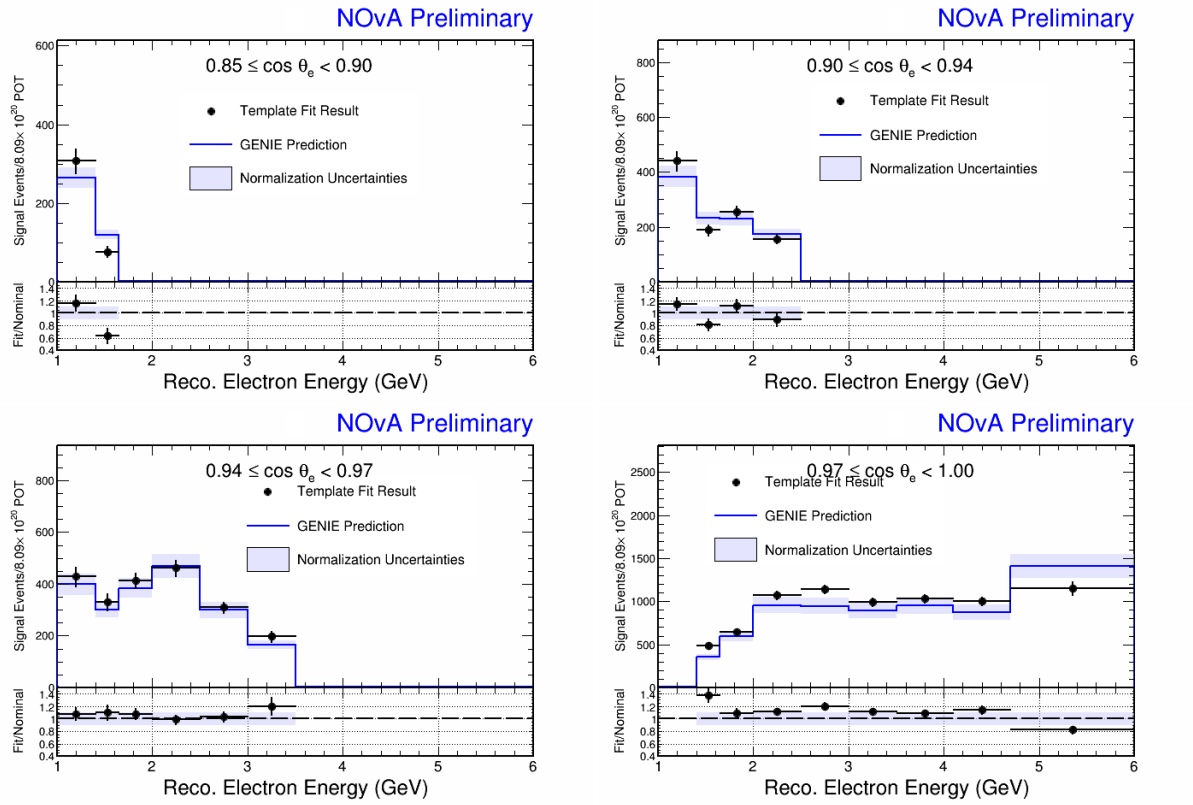

Figure 5.8: The reconstructed distributions the extracted signal from a template fit to NuMI ND data compared to nominal simulated prediction. The plots show one dimensional distributions of the electron kinematic bins used for the double differential cross section measurement. The vertical error bar correspond to the statistical uncertainty plus the systematic uncertainty on the extracted signal prediction. The blue error band depicts the normalization uncertainties not taken into account through the systematic covariance matrix.

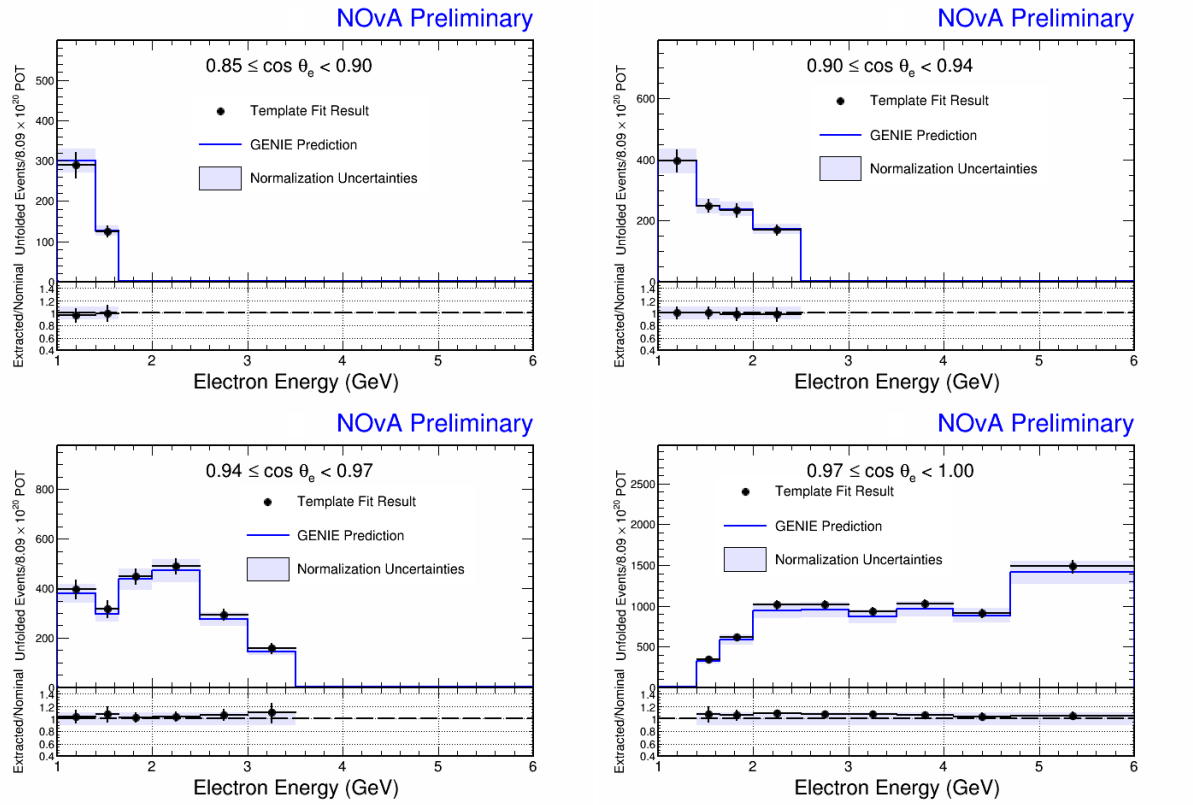

Figure 5.9: The unfolded distributions the extracted signal from a template fit to NuMI ND data compared to nominal simulated prediction. The plots show one dimensional distributions of the electron kinematic bins used for the double differential cross section measurement. The vertical error bar corresponds to the statistical uncertainty plus the systematic uncertainty on the extracted signal prediction. The blue error band depicts the normalization uncertainties not taken into account through the systematic covariance matrix.

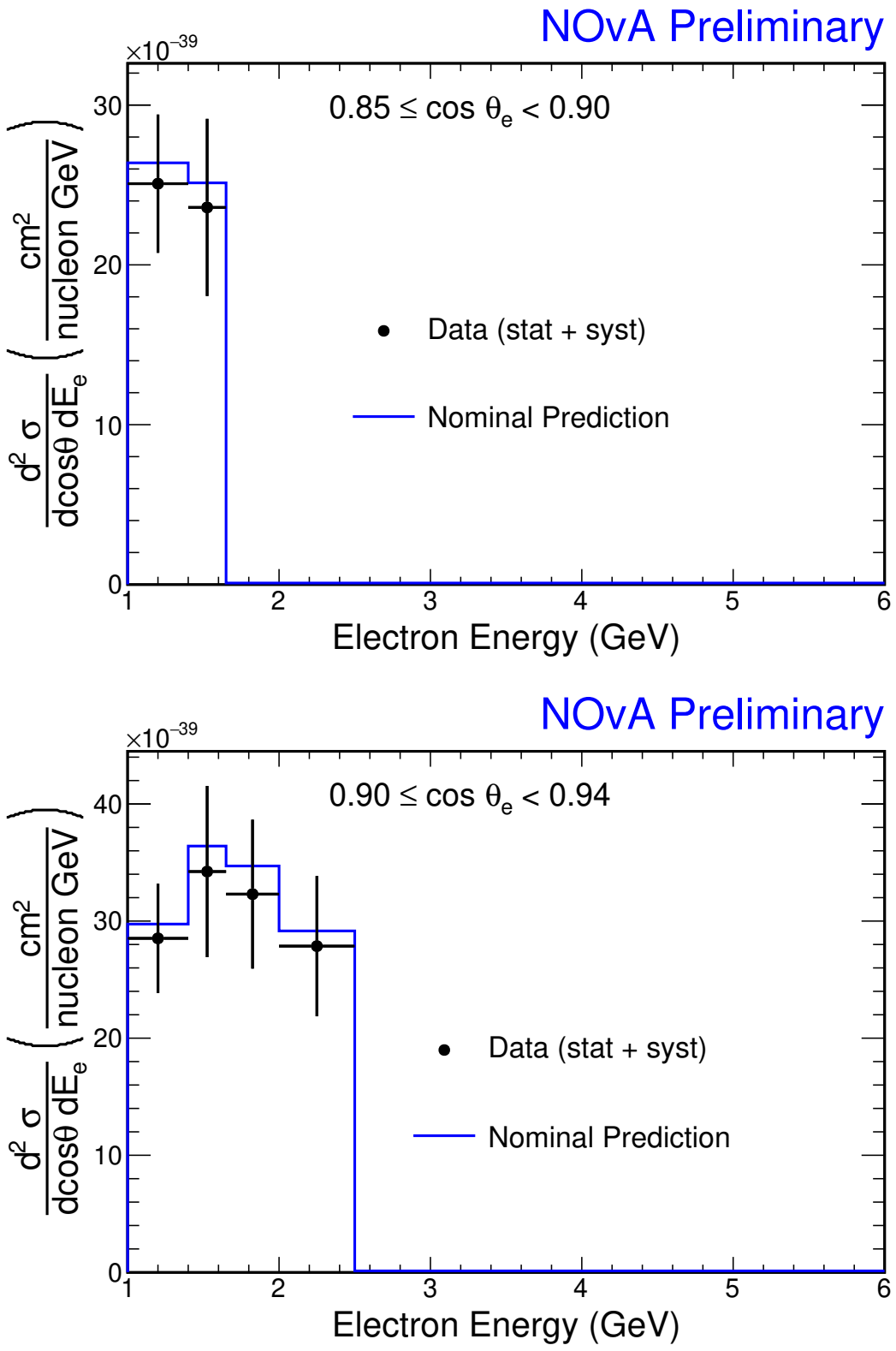

Figure 5.10: The extracted inclusive ν_e CC double-differential cross section from NuMI ND data.

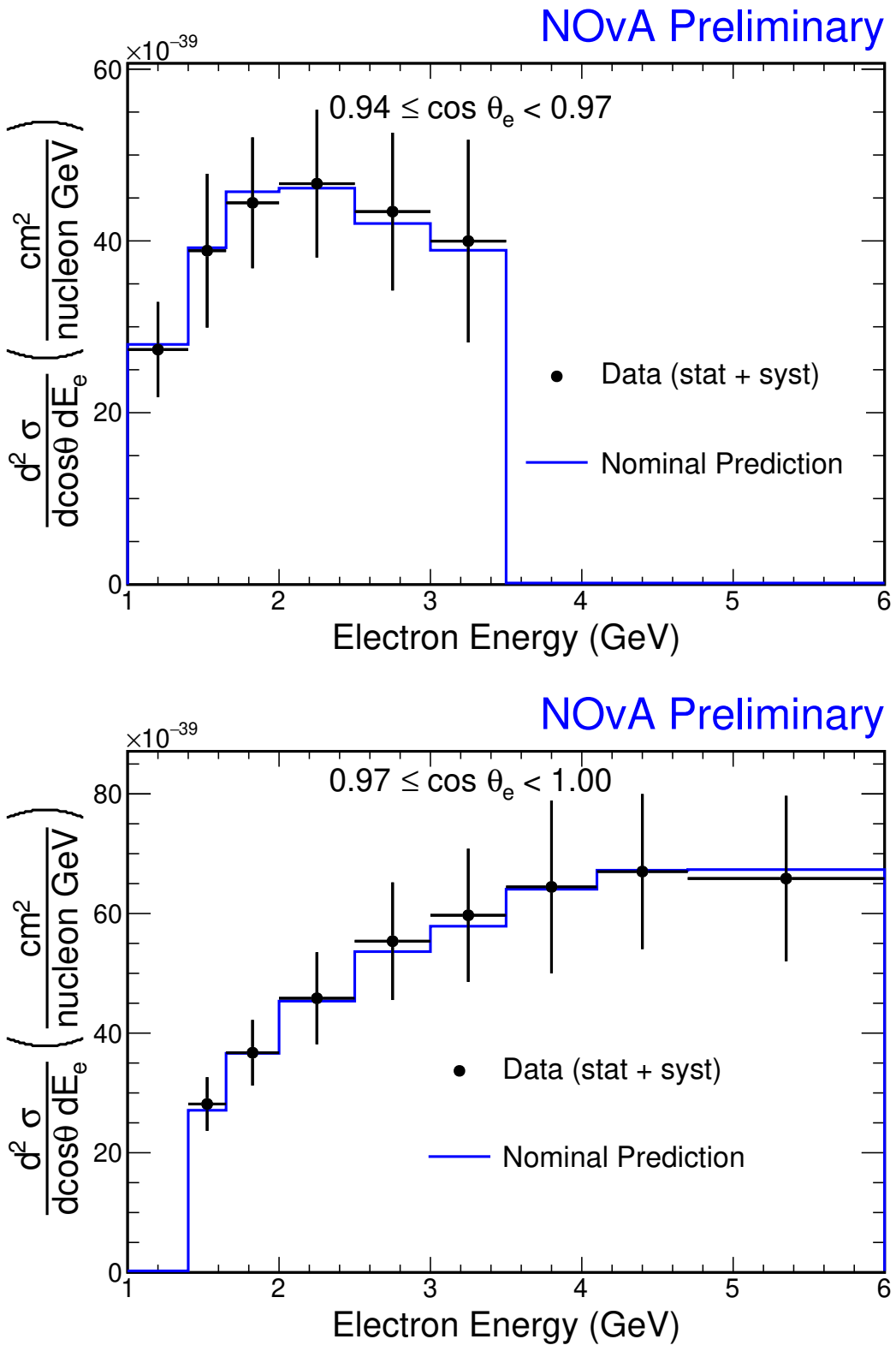

Figure 5.11: The extracted inclusive ν_e CC double-differential cross section from NuMI ND data.

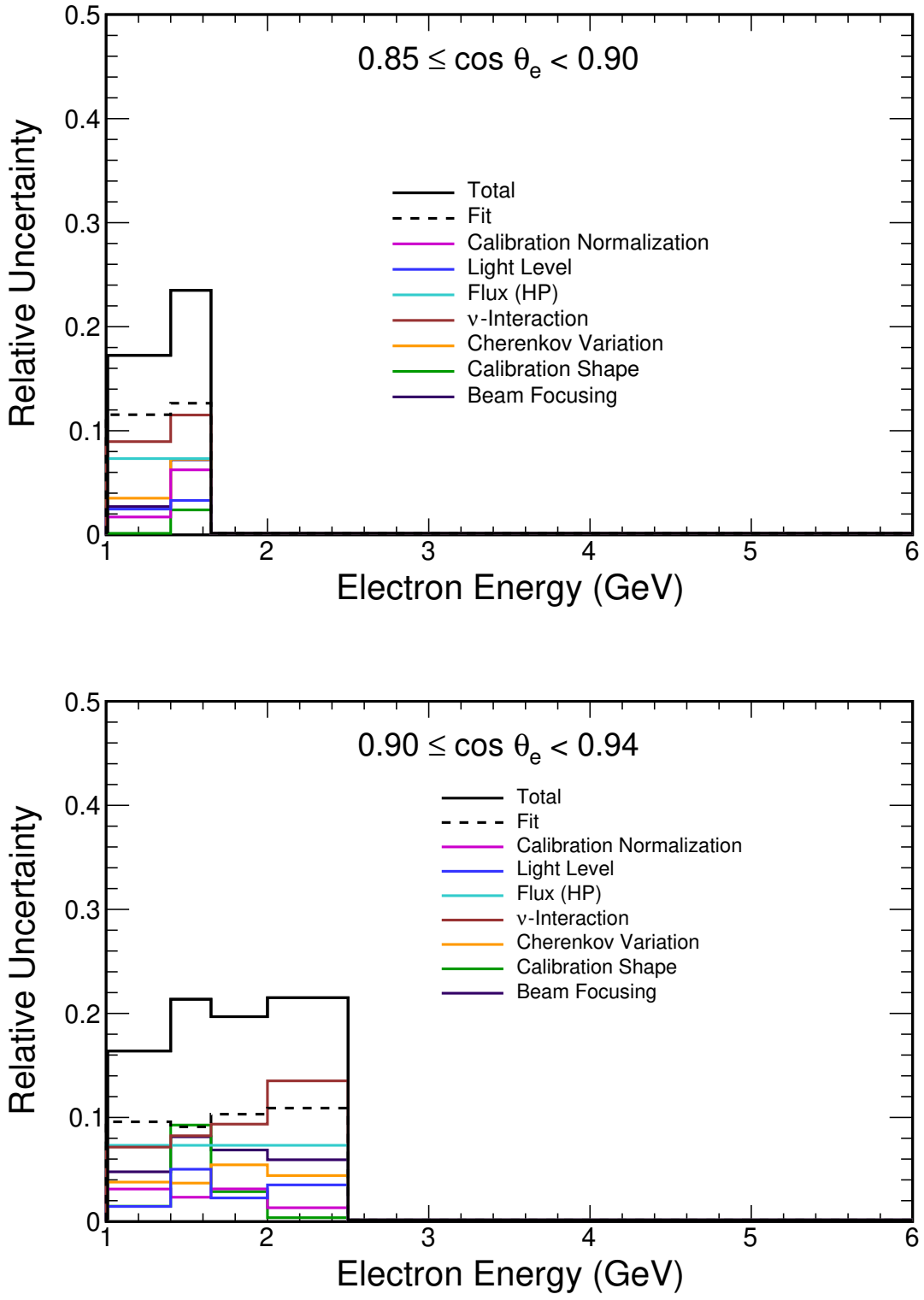

Figure 5.12: The fractional uncertainty on inclusive ν_e CC double-differential cross section from NuMI ND data.

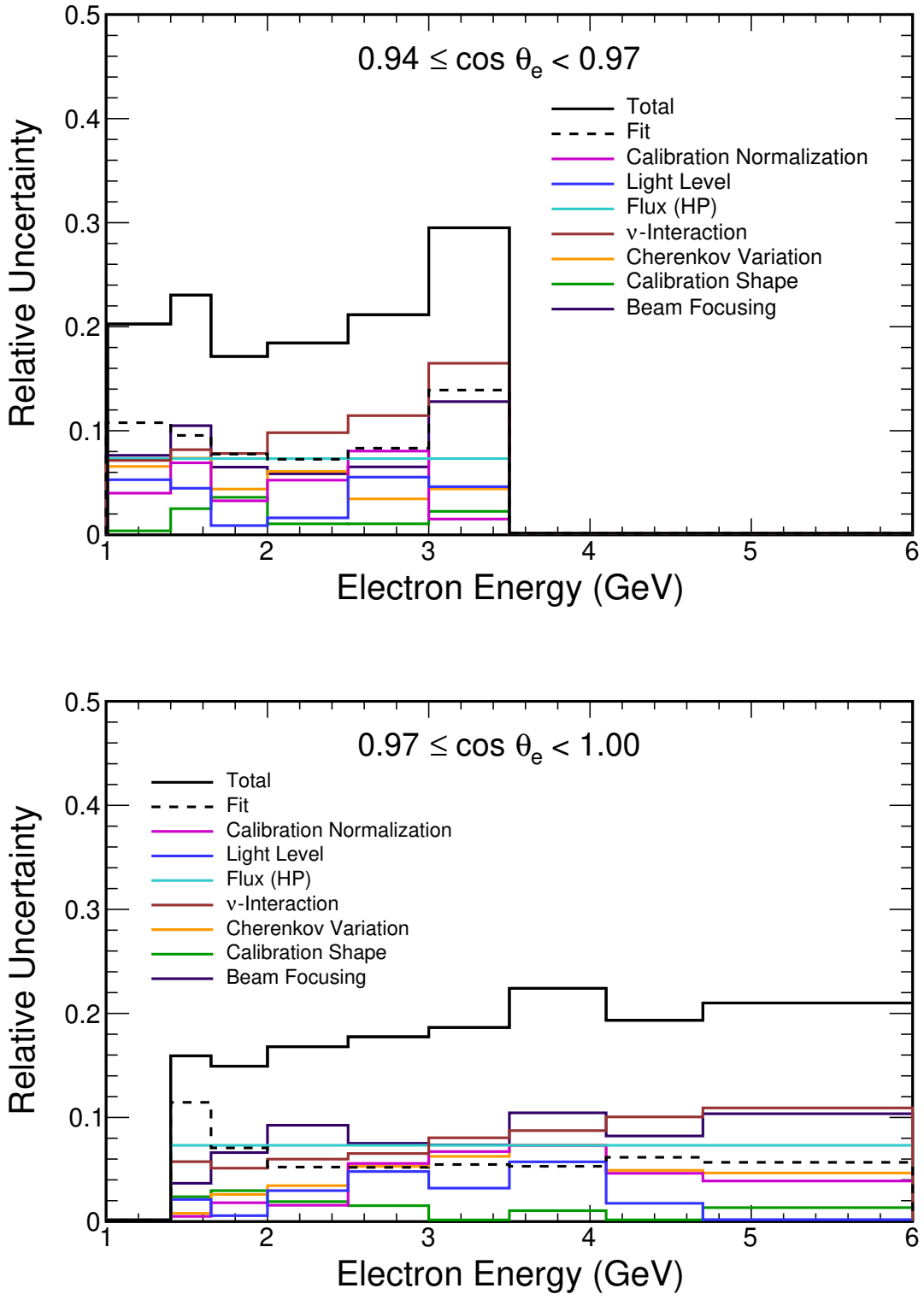

Figure 5.13: The fractional uncertainty on inclusive ν_e CC double-differential cross section from NuMI ND data.

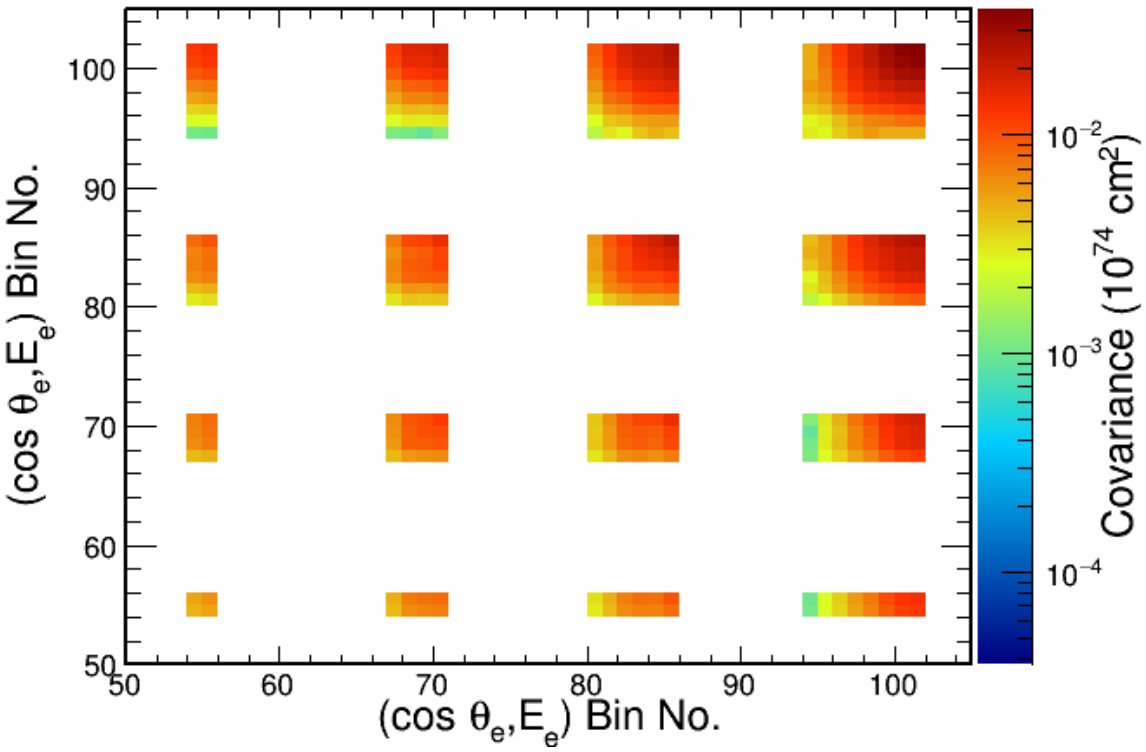

Figure 5.14: The systematic uncertainty covariance matrix for the extracted double differential cross section measurement.

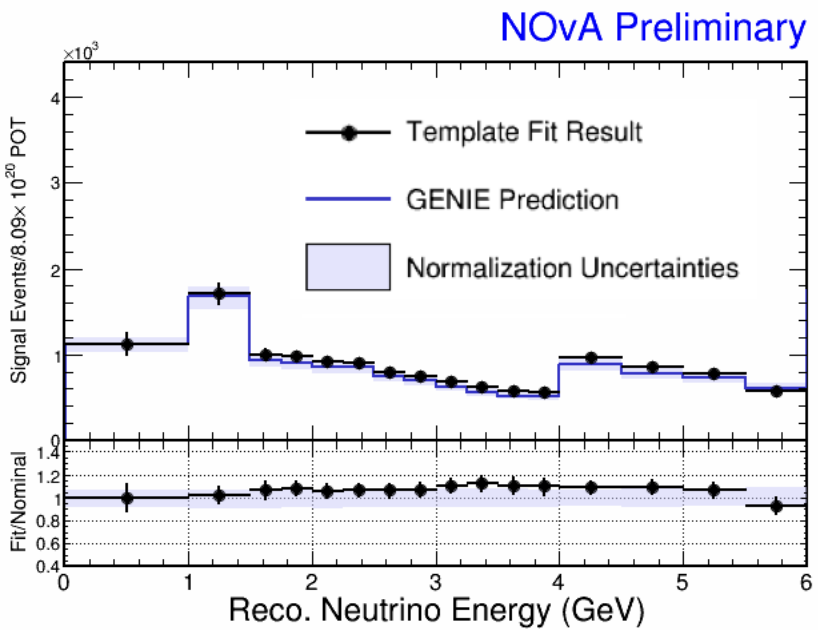

Figure 5.15: The reconstructed neutrino energy distribution comparing the extracted signal from a template fit to NuMI ND data compared to nominal simulated prediction. The blue error band depicts the normalization uncertainties not taken into account through the systematic covariance matrix.

Figure 5.17 contains plots of the extracted electron neutrino cross section as a function of energy from NOνA data. The result is compared to the GENIE prediction and the previous cross section measurements from the Gargamelle and T2K experiments [60, 61]. No significant disagreements between the extracted cross section, that predicted by the cross section models employed by NOνA, or past measurements were found. The dominant systematic uncertainties came from the template fit, flux, and the neutrino-nucleus interaction models.

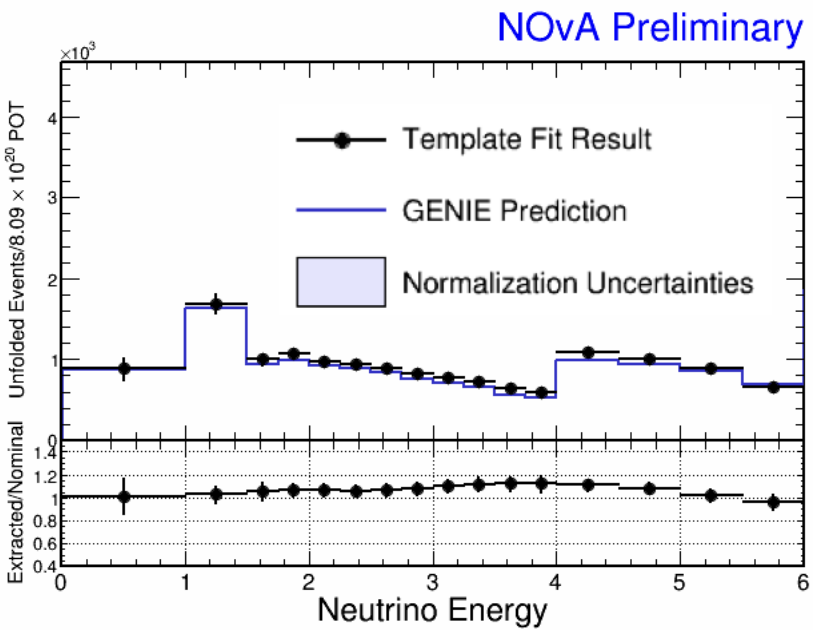

Figure 5.16: The unfolded neutrino energy distribution from the extracted signal prediction compared to the nominal simulated prediction. The blue error band depicts the normalization uncertainties not taken into account through the systematic covariance matrix.

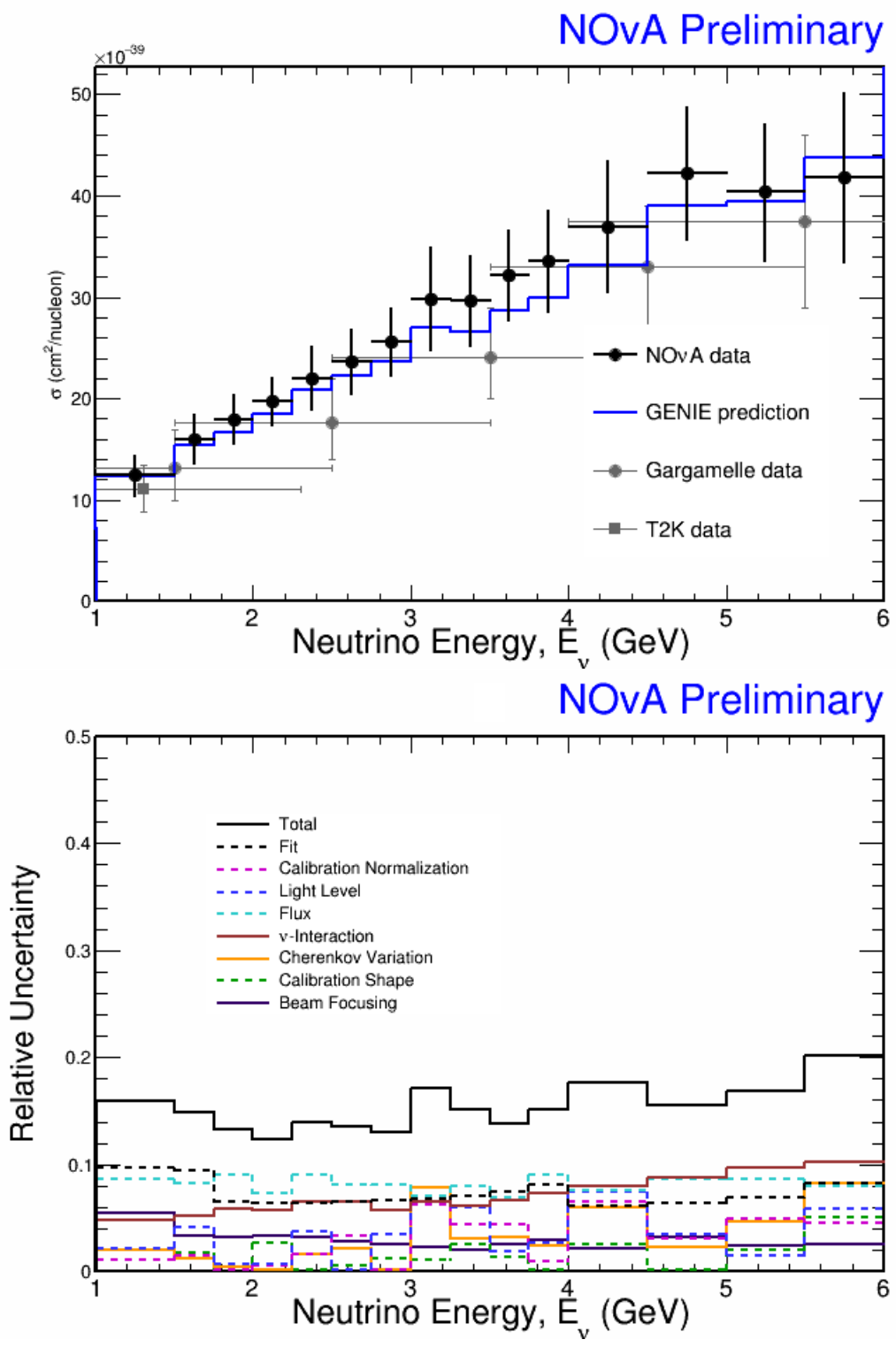

Figure 5.17: The extracted inclusive ν_e CC total cross section as a function of neutrino energy from NuMI ND data is shown in the top plot. Previous measurements from the Gargamelle and T2K experiments are also shown for comparison. The relative uncertainty on the cross section measurement is shown in the bottom plot.

Chapter 6

Additional Contributions to NOvA

Like all high energy physics collaborations, the NOνA collaboration relies on the individual contributions of each member of the collaboration. These contributions can range from maintenance and operation of the detectors to tools required for the production of physics results. This chapter describes two significant examples of additional work that were performed for the NOνA experiment during the development of the analysis presented within this thesis.

6.1 Property Protection of Data Acquisition Hardware

The far detector DAQ computing cluster consists of a few hundred computers housed at the Ash River Computing Center (ARCC) where the FD resides. Each computer works in tandem to process the large amount of data that is read out from the detector every 50 μs. As these computers are operated continuously during data taking, several precautions must be taken to protect the equipment in the event of a loss of communication or in the case of elevated temperatures within the computing center that could damage the computers.

One way to mitigate these potential issues is to continuously monitor each node, or individual computer within the computing cluster, for elevated temperatures or loss of connection with the other machines in the cluster. The monitoring software runs on each node, independently from any of the other nodes, and follows the procedure shown in Figure 6.1. A database is used to store the average node temperature during the summer or winter, which is used as the baseline that elevated temperatures are compared too. This is vital as the average node temperature can vary by several degrees depending on the location of the node within the computing center during different times of the year. The temperature monitor periodically compares the measured motherboard temperature to the baseline temperature to catch any significant temperature increases. If a substantial rise in temperature lasts for several minutes the node is powered off.

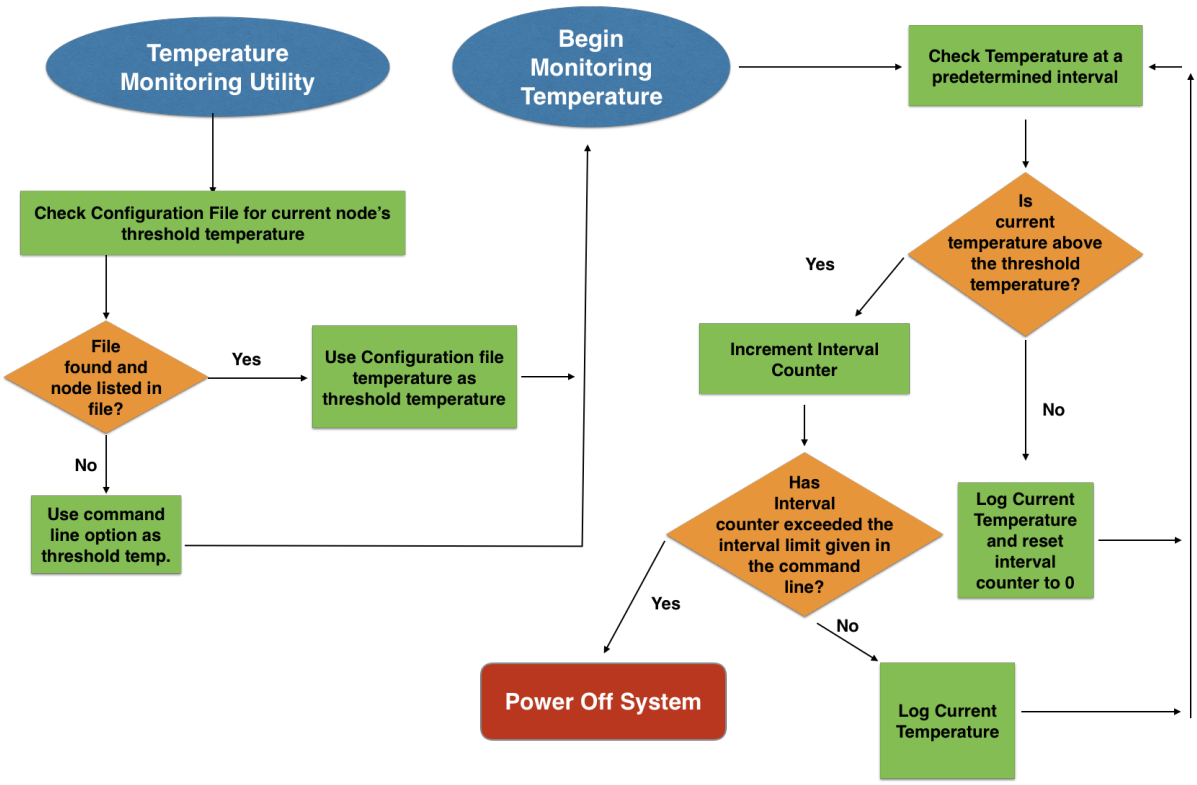

Figure 6.1: A flow chart for the procedure followed within the single node temperature monitor deployed at the NOνA far detector DAQ computing cluster.

The development of this system was brought about by a high-temperature event. During this event, the ARCC cooling system malfunctioned causing the temperature of the room to become elevated, which eventually led to the activation of the fire protection systems within the computing center. This resulted in the loss of dozens of nodes due to water damage.

6.2 Development of a Michel Electron Trigger

Section 2.4.5 described the data-driven trigger system used within the NOνA experiment. This system scans all data read out for particular conditions that are consistent with unique event topologies. Electrons resulting from the decay of stopped muons, called Michel electrons, provide useful low energy calibration sample for the NOνA detectors. Michel electrons have a well-studied energy spectrum with a peak below 53 MeV [99]. A pure sample of Michel electrons can be used to provide an improved energy calibration of the NOνA detectors using low energy events. These

electrons can also be used to study the response of parts of the NOνA FD that is not well sampled during normal operation.

The process of finding events containing Michel electrons consists of finding cosmic tracks that terminate within the fiducial part of the detector and identifying hits near the stopping point. Clustering is then performed on low energy hits requiring the hits to occur within 10 ns and within 3 planes from each other. The final cluster is required to contain at least one hit in each view of the detector. The last requirement reduces the amount of candidate clusters coming from adjacent noisy channels in an APD. An event display for a Michel electron candidate event in the FD is shown in Figure 6.2.

As the detector readout is continuous, the Michel trigger can be used to select a sample of Michel electrons within certain regions of the detector where typical calibration samples (like the cosmic pulser) are unlikely to obtain many events. This was done through the implementation of a geometric prescale map, which is a weighting factor that reduces the number of triggers that are accepted. The geometric prescale map was developed using the cosmic pulser data to obtain the rate of muon track termination in different regions of the detector. This rate map was then inverted and normalized to create the geometric prescale map. The far detector geometric prescale map is shown in Figure 6.3.

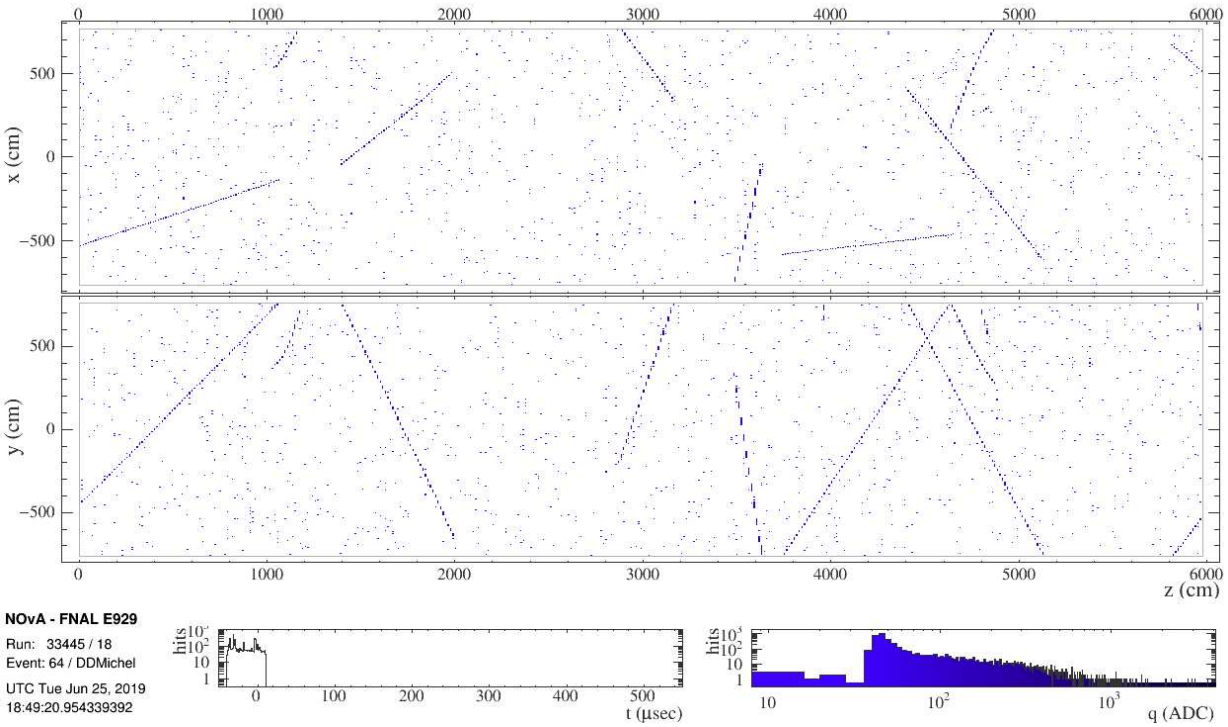

Figure 6.2: A data-driven Michel electron trigger candidate in the NOνA far detector.

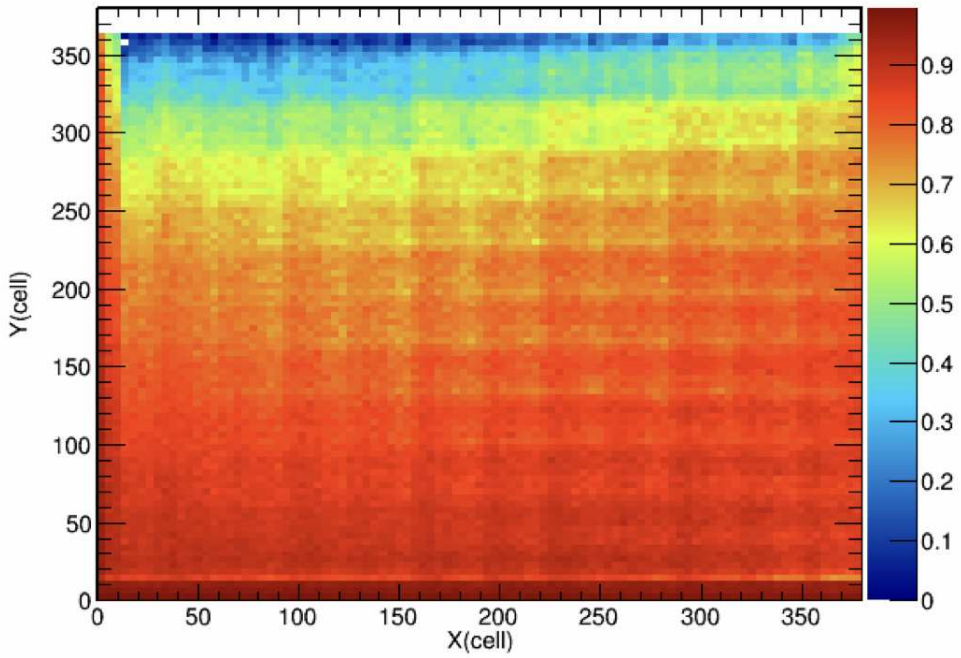

Figure 6.3: The Michel electron trigger geometric prescale map. The Z axis depicts the probability that a trigger is issued based on the cluster location within the far detector.

Chapter 7

Conclusion and Outlook

Neutrino-nucleus interactions and the models used to predict them have become increasingly important as long-baseline oscillation experiments are used to probe fundamental questions in physics. Measurements of the charged-current electron neutrino cross section will improve oscillation measurements through the reduction of systematic errors related to the neutrino-nucleon interaction models and constraining the ν_e component of the neutrino beam flux. This thesis has presented a measurement of the first double-differential electron neutrino cross section made in the energy range relevant to long-baseline neutrino oscillation experiments. A number of novel analysis techniques were used as a part of this analysis. Particle identification utilizing machine learning played a crucial role in this challenging analysis. A CVN classifier was used to enhance the identification of final-state electrons in charged-current ν_e interactions. A template fitting approach was used to estimate the signal events along with the background events for this measurement. Utilizing these techniques, no significant disagreements between the extracted cross section and that predicted by the cross section models employed by NOνA were found.

The NOνA experiment will continue to provide an excellent platform in the continued study of electron neutrino interactions with matter. This analysis will be used as a baseline analysis for the measurement of electron antineutrino interactions with nuclei. The results will also be utilized in the ν_μ to ν_e and ν_e to $\bar{\nu_e}$ cross section ratio measurements which will probe the differences between ν_μ and ν_e interactions and neutrino and antineutrino interactions, respectively. These and future ν_e CC measurements will benefit from increased statistics as NOνA continues to take data and from the reduction of systematic uncertainties through NOνA's test beam program and improvements in the analysis techniques.

Bibliography

[1] W. Pauli, "Letter to the physical society of tubingen." Letter, 1930.

[2] J. Chadwick, "Distribution in intensity in the magnetic spectrum of the β-rays of radium," *Ver. Dtsch. Physik. Ges*, vol. 16, pp. 383–391, 1914.

[3] F. Reines and C. L. Cowan, "The neutrino," *Nature*, vol. 178, pp. 446–449, 1956.

[4] D. Griffiths, *Introduction to elementary particles*. 2008.

[5] P. W. Higgs, "Broken symmetries, massless particles and gauge fields," *Phys. Lett.*, vol. 12, pp. 132–133, 1964.

[6] P. W. Higgs, "Broken symmetries and the masses of gauge bosons," *Phys. Rev. Lett.*, vol. 13, pp. 508–509, Oct 1964.

[7] E. Fermi, "Tentativo di una teoria dei raggi β," *Il Nuovo Cimento (1924-1942)*, vol. 11, pp. 1–19, 1934.

[8] G. Danby, J.-M. Gaillard, K. Goulianos, L. M. Lederman, N. Mistry, M. Schwartz, and J. Steinberger, "Observation of high-energy neutrino reactions and the existence of two kinds of neutrinos," *Phys. Rev. Lett.*, vol. 9, pp. 36–44, Jul 1962.

[9] M. L. Perl *et al.*, "Evidence for anomalous lepton production in $e^+ - e^-$ annihilation," *Phys. Rev. Lett.*, vol. 35, pp. 1489–1492, Dec 1975.

[10] D. Decamp *et al.*, "A Precise Determination of the Number of Families With Light Neutrinos and of the Z Boson Partial Widths," *Phys. Lett.*, vol. B235, pp. 399–411, 1990.

[11] K. Kodama *et al.*, "Observation of tau neutrino interactions," *Phys. Lett.*, vol. B504, pp. 218–224, 2001.

[12] S. Schael *et al.*, "Precision electroweak measurements on the Z resonance," *Phys. Rept.*, vol. 427, pp. 257–454, 2006.

[13] R. Davis, D. S. Harmer, and K. C. Hoffman, "Search for neutrinos from the sun," *Phys. Rev. Lett.*, vol. 20, pp. 1205–1209, 1968.

[14] K. S. Hirata *et al.*, "Observation of ^{8}b solar neutrinos in the kamiokande-ii detector," *Phys. Rev. Lett.*, vol. 63, pp. 16–19, 1989.

[15] P. Anselmann *et al.*, "Solar neutrinos observed by gallex at gran sasso.," *Phys. Lett. B.*, vol. 285, pp. 376–389, 1992.

[16] A. I. Abazov *et al.*, "Search for neutrinos from the sun using the reaction $^{71}\mathrm{Ga}(\nu_e,e^-)^{71}\mathrm{Ge}$," *Phys. Rev. Lett.*, vol. 67, pp. 3332–3335, Dec 1991.

[17] B. Pontecorvo, "Neutrino experiments and the problem of conservation of leptonic charge," *Sov. Phys. JETP*, vol. 26, pp. 984 – 988, 1968.

[18] B. P. V.N. Gribov, "Neutrino astronomy and lepton charge," *Phys. Lett. B*, vol. 28, p. 493, 1969.

[19] S. S. Z. Maki, M. Nakagawa, "Remarks on the unified model of elementary particles," *Prog. Theor. Phys.*, vol. 28, pp. 870–880, 1962.

[20] Q. R. Ahmad *et al.*, "Direct evidence for neutrino flavor transformation from neutral-current interactions in the sudbury neutrino observatory," *Phys. Rev. Lett.*, vol. 89, p. 011301, Jun 2002.

[21] Y. Fukuda *et al.*, "Evidence for oscillation of atmospheric neutrinos," *Phys. Rev. Lett.*, vol. 81, pp. 1562–1567, 1998.

[22] P. Adamson *et al.*, "First measurement of muon-neutrino disappearance in nova," *Phys. Rev. D*, vol. 93, p. 051104, Mar 2016.

[23] C. Giganti, S. Lavignac, and M. Zito, "Neutrino oscillations: the rise of the PMNS paradigm," *Prog. Part. Nucl. Phys.*, vol. 98, pp. 1–54, 2018.

[24] L. Wolfenstein, "Neutrino oscillations in matter," *Phys. Rev. D*, vol. 17, pp. 2369 – 2374, 1978.

[25] S. P. Mikheyev and A. Y. Smirnov, "Resonant amplification of ν oscillations in matter and solar-neutrino spectroscopy," *Il Nuovo Cimento C*, vol. 9, pp. 17–26, Jan 1986.

[26] P. F. De Salas, S. Gariazzo, O. Mena, C. A. Ternes, and M. Tórtola, "Neutrino Mass Ordering from Oscillations and Beyond: 2018 Status and Future Prospects," *Front. Astron. Space Sci.*, vol. 5, p. 36, 2018.

[27] E. K. Akhmedov, "Neutrino physics," in *Proceedings, Summer School in Particle Physics: Trieste, Italy, June 21-July 9, 1999*, pp. 103–164, 1999.

[28] H. Nunokawa, S. J. Parke, and J. W. F. Valle, "CP Violation and Neutrino Oscillations," *Prog. Part. Nucl. Phys.*, vol. 60, pp. 338–402, 2008.

[29] S. Glashow, "The renormalizability of vector meson interactions," *Nucl. Phys.*, vol. 10, p. 107, 1959.

[30] A. Salam and J. Ward, "Weak and electromagentic interactions," *Nuovo Cimento*, vol. 11, pp. 568–577, 1959.

[31] S. Weinberg, "A model of leptons," *Phys. Rev. Lett.*, vol. 19, pp. 1264–1266, 1967.

[32] F. Hasert *et al.*, "Observation of neutrino like interactions without muon or electron in the gargamelle neutrino experiment," *Phys.Lett. B*, vol. 46, pp. 138–140, 1973.

[33] J. A. Formaggio and G. P. Zeller, "From eV to EeV: Neutrino Cross Sections Across Energy Scales," *Rev. Mod. Phys.*, vol. 84, pp. 1307–1341, 2012.

[34] C. L. Smith, "Neutrino reactions at accelerator energies," *Phys. Rept.*, vol. 3, pp. 261–379, 1972.

[35] O. L. Trinhammer, "On cabibbo angle from theory," *EPL (Europhysics Letters)*, vol. 124, p. 31001, dec 2018.

[36] M. Day and K. S. McFarland, "Differences in Quasi-Elastic Cross-Sections of Muon and Electron Neutrinos," *Phys. Rev.*, vol. D86, p. 053003, 2012.

[37] K. N. and, "Review of particle physics," *Journal of Physics G: Nuclear and Particle Physics*, vol. 37, p. 075021, jul 2010.

[38] A. Bodek *et al.*, "Extraction of the axial nucleon form-factor from neutrino experiments on deuterium," *J. Phys. Conf. Ser.*, vol. 110, p. 082004, 2008.

[39] G. Z. H. Gallagher, G. Garvey, "Neutrino-nucleus interactions," *Ann. Rev. Nucl. Part. Sci.*, vol. 61, pp. 355–378, 2011.

[40] D. Rein and L. Sehgal, "Neutrino-excitation of baryon resonances and single pion production," *Annals Phys.*, vol. 133, pp. 79 – 153, 1981.

[41] J. Bjorken, "Asymptotic sum rules at infinite momentum," *Phys. Rev.*, vol. 179, pp. 1547 – 1553, 1969.

[42] S. L. Adler, "Tests of the conserved vector current and partially conserved axial-vector current hypotheses in high-energy neutrino reactions," *Phys. Rev.*, vol. 135, pp. B963–B966, Aug 1964.

[43] K. Saraswat, P. Shukla, V. Kumar, and V. Singh, "Coherent pion production in neutrino-nucleus scattering," *Phys. Rev. C*, vol. 93, p. 035504, Mar 2016.

[44] D. Rein and L. M. Sehgal, "Coherent pi0 Production in Neutrino Reactions," *Nucl. Phys.*, vol. B223, pp. 29–44, 1983.

[45] T. Golan, "Modeling nuclear effects in nuwro monte carlo neutrino event generator," *Ph.D thesis, University of Wroclaw*, 2014.

[46] H. D. Vries, C. D. Jager, and C. D. Vries, "Nuclear charge-density-distribution parameters from elastic electron scattering," *Atomic Data and Nuclear Data Tables*, vol. 36, no. 3, pp. 495 – 536, 1987.

[47] D. Rohe *et al.*, "Correlated strength in the nuclear spectral function," *Phys. Rev. Lett.*, vol. 93, p. 182501, Oct 2004.

[48] P. K. A. de Witt Huberts, "Proton spectral functions and momentum distributions in nuclei from high-resolution (e,e'p) experiments," *Journal of Physics G: Nuclear and Particle Physics*, vol. 16, no. 4, p. 507, 1990.

[49] O. Benhar and A. Fabrocini, "Two-nucleon spectral function in infinite nuclear matter," *Phys. Rev. C*, vol. 62, p. 034304, Aug 2000.

[50] R. Shneor *et al.*, "Investigation of proton-proton short-range correlations via the C-12(e, e-prime pp) reaction," *Phys. Rev. Lett.*, vol. 99, p. 072501, 2007.

[51] J. Nieves, I. R. Simo, and M. J. V. Vacas, "Inclusive charged-current neutrino-nucleus reactions," *Phys. Rev. C*, vol. 83, p. 045501, Apr 2011.

[52] J. Nieves, I. Ruiz Simo, and M. J. Vicente Vacas, "The nucleon axial mass and the MiniBooNE Quasielastic Neutrino-Nucleus Scattering problem," *Phys. Lett.*, vol. B707, pp. 72–75, 2012.

[53] M. Martini, M. Ericson, G. Chanfray, and J. Marteau, "Unified approach for nucleon knockout and coherent and incoherent pion production in neutrino interactions with nuclei," *Phys. Rev. C*, vol. 80, p. 065501, Dec 2009.

[54] G. Co', "Random phase approximation and neutrino-nucleus cross sections," *Acta Phys. Polon.*, vol. B37, pp. 2235–2242, 2006.

[55] J. Nieves, J. E. Amaro, and M. Valverde, "Inclusive quasi-elastic neutrino reactions," *Phys. Rev.*, vol. C70, p. 055503, 2004. [Erratum: Phys. Rev.C72,019902(2005)].

[56] R. Gran, "Model Uncertainties for Valencia RPA Effect for MINERvA," 2017.

[57] S. Boyd, S. Dytman, E. Hernández, J. Sobczyk, and R. Tacik, "Comparison of models of neutrino-nucleus interactions," *AIP Conference Proceedings*, vol. 1189, no. 1, pp. 60–73, 2009.

[58] L. Alvarez-Ruso *et al.*, "NuSTEC White Paper: Status and challenges of neutrino–nucleus scattering," *Prog. Part. Nucl. Phys.*, vol. 100, pp. 1–68, 2018.

[59] A. De Rujula, R. Petronzio, and A. Savoy-Navarro, "Radiative Corrections to High-Energy Neutrino Scattering," *Nucl. Phys.*, vol. B154, pp. 394–426, 1979.

[60] J. Blietschau *et al.*, "Total cross sections for ν_e and $\overline{\nu}_e$ interactions and search for neutrino oscillations and decay," *Nuclear Physics B*, vol. 133, no. 2, pp. 205 – 219, 1978.

[61] K. Abe *et al.*, "Measurement of the Inclusive Electron Neutrino Charged Current Cross Section on Carbon with the T2K Near Detector," *Phys. Rev. Lett.*, vol. 113, no. 24, p. 241803, 2014.

[62] J. Wolcott *et al.*, "Measurement of electron neutrino quasielastic and quasielasticlike scattering on hydrocarbon at $\langle E_\nu \rangle$ = 3.6 GeV," *Phys. Rev. Lett.*, vol. 116, no. 8, p. 081802, 2016.

[63] C. Andreopoulos *et al.*, "The GENIE Neutrino Monte Carlo Generator," *Nucl. Instrum. Meth.*, vol. A614, pp. 87–104, 2010.

[64] Fermilab, "Fermilab accelerator complex." https://www.fnal.gov/pub/science/particle-accelerators/accelerator-complex.html, cited July 2019.

[65] P. Adamson *et al.*, "The NuMI Neutrino Beam," *Nucl. Instrum. Meth.*, vol. A806, pp. 279–306, 2016.

[66] D. S. Ayres *et al.*, "The NOvA Technical Design Report," 2007.

[67] C. Patrignani *et al.*, "Review of Particle Physics," *Chin. Phys.*, vol. C40, no. 10, p. 100001, 2016.

[68] W. R. Leo, *Techniques for Nuclear and Particle Physics Experiments: A How to Approach*. 1987.

[69] L. Suter, "Extrapolation Techniques and Systematic Uncertainties in the NOνA Muon Neutrino Disappearance Analysis," in *Proceedings, Meeting of the APS Division of Particles and Fields (DPF 2015): Ann Arbor, Michigan, USA, 4-8 Aug 2015*, 2015.

[70] B. Behera, "Tracking Detector Performance and Data Quality in the NOvA Experiment," in *Proceedings, Meeting of the APS Division of Particles and Fields (DPF 2017): Fermilab, Batavia, Illinois, USA, July 31 - August 4, 2017*, 2017.

[71] A. Norman, "The nova data acquisition system," *Journal of Physics: Conference Series*, vol. 396, no. 1, p. 012035, 2012.

[72] L. Aliaga *et al.*, "Neutrino Flux Predictions for the NuMI Beam," *Phys. Rev.*, vol. D94, no. 9, p. 092005, 2016. [Addendum: Phys. Rev.D95,no.3,039903(2017)].

[73] T. Böhlen *et al.*, "The fluka code: Developments and challenges for high energy and medical applications," *Nuclear Data Sheets*, vol. 120, pp. 211 – 214, 2014.

[74] A. Ferrari, P. R. Sala, A. Fasso, and J. Ranft, "FLUKA: A multi-particle transport code (Program version 2005)," 2005.

[75] A. S. Meyer, M. Betancourt, R. Gran, and R. J. Hill, "Deuterium target data for precision neutrino-nucleus cross sections," *Phys. Rev.*, vol. D93, no. 11, p. 113015, 2016.

[76] O. Altinok *et al.*, "Measurement of ν_μ charged-current single π^0 production on hydrocarbon in the few-GeV region using MINERvA," *Phys. Rev.*, vol. D96, no. 7, p. 072003, 2017.

[77] C. L. McGivern *et al.*, "Cross sections for ν_μ and $\bar{\nu}_\mu$ induced pion production on hydrocarbon in the few-GeV region using MINERvA," *Phys. Rev.*, vol. D94, no. 5, p. 052005, 2016.

[78] A. A. Aguilar-Arevalo *et al.*, "Measurement of Neutrino-Induced Charged-Current Charged Pion Production Cross Sections on Mineral Oil at $E_\nu \sim 1$ GeV," *Phys. Rev.*, vol. D83, p. 052007, 2011.

[79] M. Ester, H.-P. Kriegel, J. Sander, and X. Xu, "A density-based algorithm for discovering clusters a density-based algorithm for discovering clusters in large spatial databases with noise," in *Proceedings of the Second International Conference on Knowledge Discovery and Data Mining*, KDD'96, pp. 226–231, AAAI Press, 1996.

[80] M. Baird, J. Bian, M. Messier, E. Niner, D. Rocco, and K. Sachdev, "Event reconstruction techniques in NOvA," *Journal of Physics: Conference Series*, vol. 664, p. 072035, dec 2015.

[81] M. Gyulassy and M. Harlander, "Elastic tracking and neural network algorithms for complex pattern recognition," *Computer Physics Communications*, vol. 66, pp. 31–46, 07 1991.

[82] M. Ohlsson *et al.*, "Track finding with deformable templates — the elastic arms approach," *Computer Physics Communications*, vol. 71, no. 1, pp. 77 – 98, 1992.

[83] P. Adamson *et al.*, "First measurement of electron neutrino appearance in NOvA," *Phys. Rev. Lett.*, vol. 116, no. 15, p. 151806, 2016.

[84] Y. Bengio, "Learning deep architectures for ai," *Found. Trends Mach. Learn.*, vol. 2, pp. 1–127, Jan. 2009.

[85] A. Krizhevsky, I. Sutskever, and G. E. Hinton, "Imagenet classification with deep convolutional neural networks," *Neural Information Processing Systems*, vol. 25, 01 2012.

[86] A. Aurisano, A. Radovic, D. Rocco, A. Himmel, M. D. Messier, E. Niner, G. Pawloski, F. Psihas, A. Sousa, and P. Vahle, "A Convolutional Neural Network Neutrino Event Classifier," *JINST*, vol. 11, no. 09, p. P09001, 2016.

[87] P. Adamson *et al.*, "Constraints on oscillation parameters from ν_e appearance and ν_μ disappearance in nova," *Phys. Rev. Lett.*, vol. 118, p. 231801, Jun 2017.

[88] A. Hoecker, P. Speckmayer, J. Stelzer, J. Therhaag, E. von Toerne, and H. Voss, "TMVA: Toolkit for Multivariate Data Analysis," *PoS*, vol. ACAT, p. 040, 2007.

[89] K. Sachdev, "Muon Neutrino To Electron Neutrino Oscillation in NOvA," 2015.

[90] L. Aliaga, "Package to predict the flux in nova," *NOvA Internal Document*, vol. DocDB-23441-v3, 2017.

[91] F. James, "MINUIT Function Minimization and Error Analysis: Reference Manual Version 94.1," 1994.

[92] S. Schmitt, "Data Unfolding Methods in High Energy Physics," *EPJ Web Conf.*, vol. 137, p. 11008, 2017.

[93] G. D'Agostini, "Improved iterative Bayesian unfolding," *arXiv e-prints*, p. arXiv:1010.0632, Oct 2010.

[94] A. Hocker and V. Kartvelishvili, "SVD approach to data unfolding," *Nucl. Instrum. Meth.*, vol. A372, pp. 469–481, 1996.

[95] S. Lein, "Summary of dE/dx plots for Muons/Protons," *NOvA Internal Document*, vol. DocDB-15028, 2016.

[96] C. N. Chou, "The nature of the saturation effect of fluorescent scintillators," *Phys. Rev.*, vol. 87, pp. 904–905, Sep 1952.

[97] D. Pershey, "Birks-Chou Post Tuning," *NOvA Internal Document*, vol. DocDB-13233, 2015.

[98] A. Aurisano, "Detector Simulations," *NOvA Internal Document*, vol. DocDB-20717, 2017.

[99] M. Bardon, P. Norton, J. Peoples, A. M. Sachs, and J. Lee-Franzini, "Measurement of the momentum spectrum of positrons from muon decay," *Phys. Rev. Lett.*, vol. 14, pp. 449–453, Mar 1965.

List of Abbreviations

ADC	Analog-to-digital units.
APD	Avalanche Photodiode.
BDT	Boosted Decision Tree.
CC	Charged-Current Interaction.
CNN	Convolutional Neural Network.
COH	Coherent Scattering.
CVN	Convolutional Visual Network.
CVNe	ν_e CC CVN event identifier.
DAQ	Data Acquisition.
DBSCAN	Density-based clustering algorithm.
DCM	Data Concentrator Module.
DDT	Data-Driven Trigger.
DIS	Deep Inelastic Scattering.
FD	NOνA Far Detector.
FEB	Front End Board.
FNAL	Fermi National Accelerator Laboratory.
FSI	Final State Interactions.
GFG	Global Fermi Gases.
LFG	Local Fermi Gases.

LID	Likelihood-based Identifier.
MC	Monte Carlo Simulation.
MEC	Meson Exchange Current.
MIP	Minimum Ionizing Particle.
MRE	Muon Removed - Electron Added.
NC	Neutral Current Interaction.
ND	NOνA Near Detector.
NOνA	NuMI Off-Axis Electron Neutrino Appearance Experiment.
NuMI	Neutrinos at the Main Injector.
PCAC	Partially Conserved Axial Current.
PID	Particle Identification.
PMNS	Pontecorvo-Maki-Nakagawa-Sakata.
PPFX	Package to Predict the FluX.
PVC	Polyvinyl chloride.
QE	Quasi-Elastic Scattering.
RES	Resonant Scattering.
ROC	Receiver Operating Characteristic Curve.
RPA	Random Phase Approximation.
SF	Spectral Function.
SVD	Single Value Decomposition.